Microstructural Characterisation of Laser Shock Peening Processed Commercially Pure Titanium

By

Uthman Mahmud

A thesis submitted to the University of Birmingham for the degree of

Doctor of Philosophy

School of Metallurgy and Materials
College of Engineering and Physical Sciences
University of Birmingham
March 2024

Preface

This research was carried out by Uthman Mahmud in the School of Metallurgy and Materials, University of Birmingham and The MTC Coventry from October 2019 to March 2024, under the supervision of Prof. Yu-Lung Chiu and Prof. Ian Jones from the University of Birmingham, and Dr. Yijun Liu and Dr. David Gilbert from The MTC.

The present work is original, and no part of the work has been submitted for another degree at any other university. Wherever other researcher's work has been drawn or cited, it is acknowledged in the text and the references cited.

Abstract

Laser shock peening can be applied on a wide range of materials with real-world applications, including many aerospace and automotive components. In this work, the microstructure evolution during laser shock peening of commercially pure titanium with large grain size (well exceeding 100 µm) was studied.

The study focused on the microstructural features observed as a result of laser shock between 1 and 20 times, with a beam of laser of 2 J power, 1.5 µm spot size and 10 ns pulse duration, giving a power density approximating 11.32 GW cm^{-2}. The samples were studied using optical profilometry, scanning electron microscopy, transmission Kikuchi diffraction, and transmission electron microscopy.

It was found that an increase in the number of shocks increases the plastic deformation zone underneath the shock spot. Twinning was observed in the 3, 5, 10 and 15-shock samples at a distance of 142 µm, 339 µm, 570 µm, and 805 µm, respectively from the surface. A similar increase in total twinning area was also observed. The near-surface (typically $\sim$10 µm) twins were identified to be of $\{10\bar{1}1\}$-type, and the rest are primarily of $\{11\bar{2}1\}$-type, extending to the afore-mentioned depths. This is atypical for HCP structures, with the $\{11\bar{2}1\}$ twin production most likely being a result of the large twin shear caused by the deformative shockwave. It is proposed that the near-surface twins in the LSP without coating (LSPwC) regime are indicative of tensile residual stresses, and those found over the majority of the samples indicate compressive residual stresses, characterised by microstructural presentation.

The collection of findings in this study develops a picture of the mechanisms of deformation introduced through LSP, and the resultant microstructural analysis allows us to make assertions as to the reasons behind the effect on component performance. This contributes a step towards building a process parameter - mechanical property relationship, allowing us to predict the mechanical performance improvement of components as a result of laser inputs, based on the materials involved.

Acknowledgements

I begin in the name of God, the most beneficent, the most merciful, without whose grace and bestowal of honour I would not be in this position of favour. [See Al-Quran 2:152]

My sincerest gratitude to my academic supervisors. Prof. Yu-Lung Chiu, who's longstanding relationship has always extended past that of a supervisor, and Prof. Ian Jones, whose retirement I am yet to witness due to his unending attention to my work.

I'd like to thank all of my colleagues from the research fellows and PhD students in the department, especially: Xinyu Lu, Bo Pang, Shanshan Si, Yu Lu, Gnanavel Thirunavukkarasu, Subash Rai, Ubaid Ur Rehman Ghori, Yang Lyu, Zhaoxuan Wu, Alexandra Dickinson-Lomas, Iulia Ipatova, Manmath Dash, Longfangdi Shi, Liam Hughes, Jinming Lin, Louis Butt, Jianing Jiang, and any I may have missed. A special thanks is needed for Minshi Wang. I have appreciated the company of the many master's students that have passed through. The CEM centre staff have helped profusely with the microscopes, namely Paul, Theresa and Ludwig, and the workshop assistance with their sample resizing at short notice, Tony, Jag and Tony.

My Industrial supervisors, Dr. Yijun Liu and Dr. David Gilbert have also assisted significantly, in addition to facilitating site visits and equipment usage (thanks Annie!). This project was partially funded by *The MTC*, and we acknowledge their support with gratitude.

I lastly thank everyone who encouraged me in my PhD, and dedicate this thesis to my family and parents, without whose love and support I could not have begun this journey; and by extension, my grandfather, who paved the way for more than just me.

Abbreviations and Notes

EB	Electron Beam
EM	Electron Microscopy
FIB	Focused Ion Beam
IB	Ion Beam
OM	Optical Microscopy
PFIB	Plasma Focused Ion Beam
SEM	Scanning Electron Microscope
TEM	Transmission Electron Microscope
LS	Laser Shock
LSP	Laser Shock Peening
LSPwC	Laser Shock Peening without Coating
SP	Shot Peening
BCC	Body Centered Cubic
FCC	Face Centered Cubic
HCP	Hexagonal Close Packed
OR	Orientation Relationship
SFE	Stacking Fault Energy
BSE	Backscattered Electron
EBSD	Electron Backscattered Diffraction
EDS / EDX	Energy Dispersive X-ray Spectroscopy
SE	Secondary Electron
TKD	Transmission Kikuchi Diffraction
B / BD	Beam Direction
BF	Bright Field
DF	Dark Field
DP	Diffraction Pattern
g	g-vector
CP	Commercially Pure
CRS	Compressive Residual Stress(es)
HEL	Hugoniot Elastic Limit
HP	High Purity
RS	Residual Stress(es)
TRS	Tensile Residual Stress(es)
CRSS	Critically Resolved Shear Stress

These works involve orientational studies of HCP structures. This is often reliant upon knowledge of the LSP samples and the orientation of TEM and SEM cutouts relative to the bulk SEM samples. For this reason, a co-ordinate system is employed. **The negative z direction indicates the shock direction.** The other axes may be inferred through the diagrams and schematics explained in *Chapter 3 Experimental Methodologies*.

Regarding twins, this study refers to extension twins and contraction twins. Other works may refer to these as tension twins and compression twins, respectively. This work avoids this terminology so as not to confuse the reader when discussing tensile and compressive twins; that is to say, twins indicating the presence of tensile residual stresses and compressive residual stresses, respectively.

Contents

1 Introduction

Laser shock peening (LSP) is an advanced surface processing technique employed primarily to improve fatigue resistance in metallic components, such as aero-engine fan blades and connecting rods. Although established in the aerospace industry, there is significant potential to broaden the application of LSP techniques for use in other industries, such as biomedical implants or workplace machinery, and any other parts which commonly undergo cyclic stresses. Fatigue resistance is achieved through the introduction of compressive residual stresses in a substrate, produced from the shockwave induced from the confined ablation of material struck by the laser. The ultra-high strain-rate (over 10^7) causes severe plastic deformation to the target material, causing many microstructural changes.

However there has been a lack of systematic study of the effects of LSP on the resultant microstructures. The project aims to characterise the microstructural evolution of specific laser processed material, namely, a commercially pure titanium which can be used as biocomponents and in chemical processing yet possesses a relatively simple HCP α-Titanium microstructure.

The following section will start with a review of the LSP process and the relationship between various processing parameters established. The experimental procedure was then designed attempting to maintain a simplified approach to LSP with fewer variables, changing only the number of laser shocks, and predominantly focusing on experiments performed without a coating. The results obtained will then be presented including those from the "strain-free" material to the severely plastically deformed. The importance of the features are seen, the implications of the technique are discussed, and conclusions drawn.

2 Literature Review

2.1 Laser Shock Peening and Processing

2.1.1 Introduction and Procedure

Shot Peening (SP), initially termed shot blasting when first employed in the 1920's, is a metal processing technique that has been commonly used in industries such as automotive and aerospace since the 1940's after being applied experimentally to armour and aircraft in WWII [1]. The SP process involves the acceleration of fragments at a usually metallic substance which upon collision will generate compressive residual stresses in the surface. Residual stresses are internal stresses that exist through an absence of external load. When formed through plastic deformation (as in this case) this often causes microstructural changes which lead to enhanced mechanical properties, most notable of which is improved fatigue resistance. However, the process is not without limitations such as the poor post-processing surface quality for applications where smooth surfaces are desired, and lack of precision when attempting to improve performance of complex geometries. The increased roughness is suggested to lead to a larger number of possible crack initiation sites. The subsequent necessary machining often results in alleviation or reduction of the intentionally generated compressive residual stresses [2]. Other peening techniques are increasingly being employed to tackle these issues, and further the magnitude and depth of compressive residual stresses (CRS) generated in the material. Examples include water and oil jet peening, ultrasonic impact/shot peening (UIP/USP), and laser shock peening (LSP) (see Figure 1).

Research first began on pulsed laser irradiation of materials in the 1960's after the discovery of the generation of shockwaves resulting from an incident laser beam upon a material. Research conducted in the *Battelle Institute* (Columbus, OH, USA) generally concentrated these efforts upon materials such as aluminium and steel for use in the aerospace industry [2]. This along with many other works was developed into LSP, which became known to the industry under two patents, the first developed by *Industrial Materials Limited* in 1973 and the second in 1983 from *Battelle Development Corporation* [3].

LSP is a more versatile and effective process than conventional shot peening, primarily due to increased depth (potentially four times) and arguably magnitude of CRS, but also due to its speed, versatility, and precision [4]. LSP can target sections of material in complex geometries where SP is not possible. The microstructural changes caused by peening are many. Whilst SP causes severe plastic deformation (SPD) (enabling hardening and introducing CRS), it also can damage the microstructure, particularly on the edges of the impacted region. LSP causes SPD with significantly less microstructural damage. Due to the short timescale of the laser pulse (often from 1 -50 ns) LSP induces an ultrahigh strain rate in materials [5], often beyond the order of 10^6 s^{-1}, whilst in comparison SP produces at most 10^5 s^{-1}. The grain refinement that ultrahigh strain induces is an important strengthening mechanism, that has gained recent attention due to the surface hardening effect. In some situations nanocrystalline structures form, potentially providing additional ductility and strengthening, [6] although the mechanism for this is unclear, and will be discussed in section [*2.6 LSP Influence on Microstructure*].

LSP is usually carried out at room temperature with a coating known as the ablative layer. This is an opaque layer which absorbs the laser energy in a short space of time, generating plasma and a shockwave that propagates through the material from the shocked surface. The schematic in Figure 2 depicts the process. The blue layer, termed the transparent overlay, is a confining medium which is transparent to allow the laser light to pass through to reach the opaque ablative layer. When the plasma is formed and expands, the transparent medium allows for greater force to be directed upon the sample material by restricting the expansion of plasma into gas, thus increasing the force of the shockwave transmitted. The resultant pressure is of the order of GPa [7]. (See section 2.1.2.2.1 Confining Medium.)

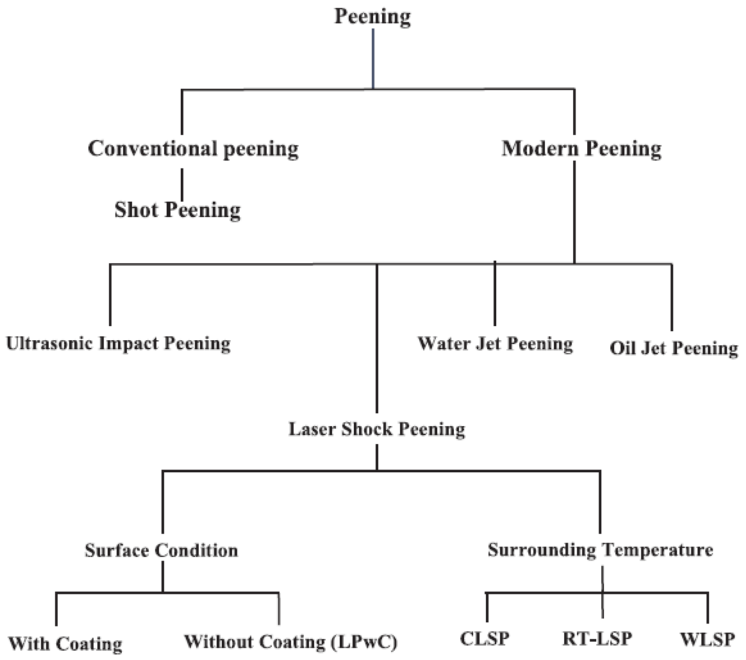

Figure 1. Flow chart of the classification of peening. Surrounding temperature variations for LSP can be categorised as cryogenic (CLSP), room temperature (RT-LSP) or warm LSP (WLSP).
(Dhakal & Swaroop, 2018)

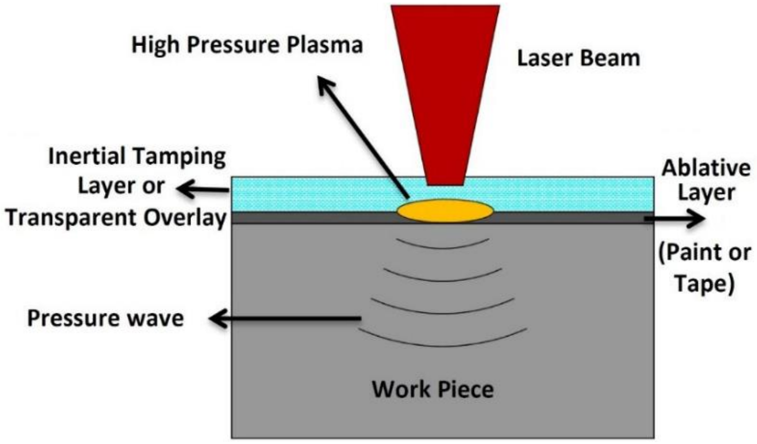

Figure 2. Schematic of the Laser Shock Peening (LSP) Process.
(Gujba & Medraj, 2014)

2.1.2 Process parameters

There are many process parameters that determine the effectiveness of LSP. The majority of the literature focuses on the effect on CRS generated, however some comments on microstructure and surface roughness are common. This section will be split into three sections (i) the laser parameters (wavelength, power, power density, pulse duration, spot size, spot shape and temporal pulse shape), (ii) the physical layers and materials used for the confining medium and ablative layer and (iii) other variables from a practical standpoint such as repetition of the process for multiple laser shocks, overlaps in these shocks, as well as comments on how material geometry may affect the component. It is also worth clarifying that the resultant microstructure and stress state of the material are primarily a function of the induced plasma pressure, *P*. This is the pressure generated when plasma is formed on the material surface, regardless of whether this is confined and what the plasma is generated from; it will be discussed in section [*2.1.2.2.2 Ablative* layer].

2.1.2.1 Laser Parameters

2.1.2.1.1 Wavelength

Lasers commonly have one of three primary wavelengths, 355 nm, 532 nm and 1064 nm, hence these are the most common operating wavelengths for LSP equipment. The literature on this is slim, although the data suggests that higher wavelengths may cause greater residual stresses in some Al Alloys, such as 6061-T6 [8]. Wavelength does have multiple effects, and *Berthe et al.* [9] demonstrated that interactions with water of 355 nm photons and 1064 nm photons show a significant difference in absorption levels and as such changed the generated pressure pulse. Figure 3 [2] shows that for the same energy density, photons of lower wavelengths form greater pressure pulses resulting from the increased photon-metal interaction, but they also have a lower peak pressure threshold due to dielectric breakdown [9]. The resultant CRS is primarily a function of the plasma pressure generated from the absorption of laser energy in the ablative layer; this disparity (the theoretical potential that greater wavelength increases CRS generation, vs the greater efficiency of lower wavelength lasers) is most likely due to the interaction depending on the tape or sacrificial layer used in the experiment and cannot be calculated in isolation of the ablative and confining layers. For example, when using water as a confining layer, a laser energy of 1064 nm is much more likely to be absorbed; less energy is transmitted through to the ablative layer beneath, reducing the peak pressure of the impulse. It is therefore more favourable to use 355 nm or 532 nm photons, but such laser technology is more expensive and less cost-effective relative to the difference in CRS generation.

2.1.2.1.2 Power and Power Density

Although a summary is provided here, the nature of shock-waves is expounded upon in section [*2.4.1 Shock-wave Responses of Materials*]. The shock wave pressure, *P*, from the plasma, is proportional to the laser power intensity, which is related to the laser power density, *I*. As CRS magnitude and depth increase with shock wave pressure, this demonstrates that the magnitude and depth of the CRS are dependent upon the laser energy density [10]. Equations relating pressure and laser power density vary, but most agree that pressure is proportional to the square root of laser power density ($P \propto \sqrt{I}$) (see section [*2.1.2.2.2 Ablative* layer]). This relationship only exists between two thresholds. The lower threshold is bounded by the Hugoniot Elastic Limit (HEL). The volume of material affected by the shock wave is plastically strained to a depth beyond which the peak pressure is no longer greater than the HEL, which is calculated according to equation (1):

$$HEL = \frac{1-\nu}{1-2\nu}\sigma_{y} \tag{1}$$

where ν is Poisson's ratio and σ_{y} is the yield strength (at high strain rates) of the material [11], [2]. The upper threshold is often determined by the target's stress saturation point. Applying stresses above this point can actually *decrease* the CRS due to release waves; hence the CRS will be decreased after successive shocks after this point is reached [12]. Another upper threshold can be due to interactions of the laser beam with water. A water confined ablation laser intensity below 0.5 GW cm^{-2} is ineffective; it has a linear relationship with shock wave pressure until 30 GW cm^{-2} whereupon it reaches saturation [13]. This, however, seems to contrast with Figure 3 [2], which suggests a saturated power of 10 GW cm^{-2}. Section [*2.1.2.2.1 Confining Medium*] gives more detail on this discrepancy.

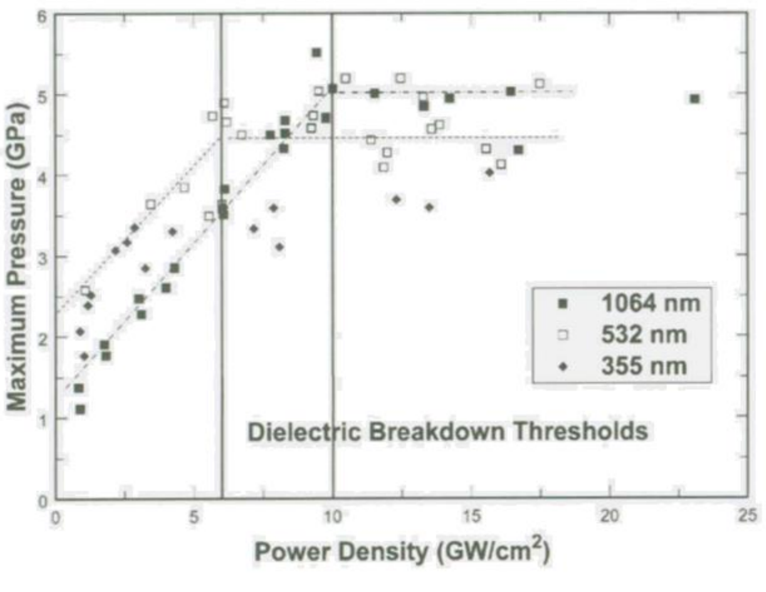

Figure 3. Peak pressures obtained in the water confining regime as a function of laser power density at 1.064µm, 0.532µm and 0.355µm laser wavelengths, and a laser pulse duration of 25 -30 ns
(Berthe, et al., 1999) in *(Montross, et al., 2002)*

2.1.2.1.3 Pulse Duration

Whilst too short a pulse duration is ineffective in producing sufficient shockwave pressure to cause severe plastic deformation, a long pulse may melt the material surface [2]. The pulse duration heavily relates to the shock wave pressure due to increased time over which material may absorb laser energy increasing overall pressure magnitude, and hence this affects the residual stress profile. The laser pulse duration is similar to the pressure pulse duration in direct ablation mode (where there is no confining medium over the pulsed spot), but in confined ablation the pressure pulse duration is 2-4 times larger [7]. Fournier *et al.* [14] demonstrate that CRS is increased with longer pulse duration. Such evidence can be seen in later sections (Figure 7) where 2.5 ns pulse durations lead to a CRS depth of 0.5 - 1 mm whilst 25 ns pulses caused an increase to 2 - 3 times greater. This also caused a reduction in the magnitude of surface compressive stress by approximately 25 %, which may indicate surface damage from localised tensile regions caused by heating and fast cooling of material.

2.1.2.1.4 Beam Shape

Circular beams are, as expected, more commonly used than other beam shapes, although square beams are also used. Circular beams are used for convenience, although the evidence suggests that square beams provide improved characteristics. This is due to the decrease in overlap when performing multiple shots in close proximity to each other. This allows for greater uniformity in the final surface microstructure. The beam size also has significant impact. Smaller beams tend to increase the near-surface CRS, whilst larger beams increase the depth of CRS. Evaluated along depth, a larger beam size is more effective, however this is largely dependent on sample geometry as illustrated on T651 Al alloy [15]. Some claim that larger beams also increase the CRS on the surface layers [12], although this discrepancy may be due to varying responses of differing materials and their pre-processing surface conditions. Comparing and interpreting these measurements are tricky as there may be microstructural variation over the surface analysed due to overlap issues. Also, many researchers study different locations on their samples because of the destructive nature of many CRS measurement techniques such as incremental hole drilling and TEM sample excavation.

2.1.2.2 Confining medium and ablative layer

2.1.2.2.1 Confining Medium

The confining medium is a layer transparent to the photon beam which restricts the free expansion of plasma into the environment after vaporisation. This restriction allows for greater force to be directed upon the sample material, thus increasing the force of the shockwave transmitted. The resultant pressure is around 5-10 GPa [3] and has a pressure pulse duration 2-4 times larger and amplitude 4-10 times greater than when unconfined (also known as direct ablation mode) [7][9].

Historically, the transparent overlay was quartz or glass, although water provides numerous benefits including abundance and formability of liquid around complex sample geometries. This provides cooling and is much more practical for industrial processing. It also possesses an increased dielectric breakdown threshold [13], (an example of dielectric breakdown is seen in Figure 3, at 6 and 10 GW cm^{-2} for different wavelengths [2]) allowing for the use of increased plasma density, enabling greater maximum plasma pressure. From an industrial perspective, the water thickness may be difficult to maintain and control. This means that industrialised peening must maintain a power density, pulse duration and pulse shape allowing for a power density within the dielectric strength limits of water.

2.1.2.2.2 Ablative layer

The primary purpose of the ablative (or sacrificial) layer is to heat up, becoming a plasma causing a high enough pressure to induce a shockwave. This requires the layer be opaque to the given operating wavelength such that the laser energy is absorbed effectively. The paint or tape then vaporises, expanding rapidly, generating a shockwave through the target and thus CRS. Although it is possible to laser peen without a coating (LSPwC), peening intensity is reduced. In this case, the vaporised layer is the surface of the target material causing surface geometry alteration. The remaining surface will undergo thermal changes due to melting, potentially causing embrittlement or compositional changes. Figure 4 shows that the near-surface residual stress of unpainted Al-6061-T6 alloy is reduced compared to that obtained from painted processing [16]. This can create tensile residual stresses in the surface which counteract the beneficial peening effect, as shown in Figure 5 [17]. The effect of the LSPwC process is therefore thermo-mechanical, whilst effective coated LSP can be considered purely mechanical [16].

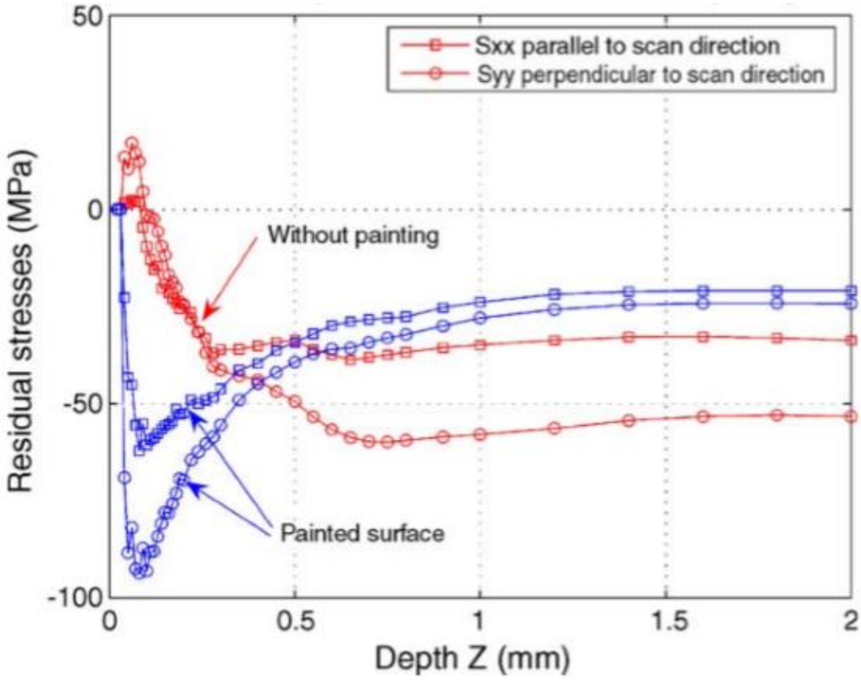

Figure 4. Residual stress distribution on Al-6061-T6 samples treated using LSP with and without coating. LSP incident at 2500 pulses cm^{-2} whilst samples are held in a water bucket. *(Rubio-González, et al., 2006)*

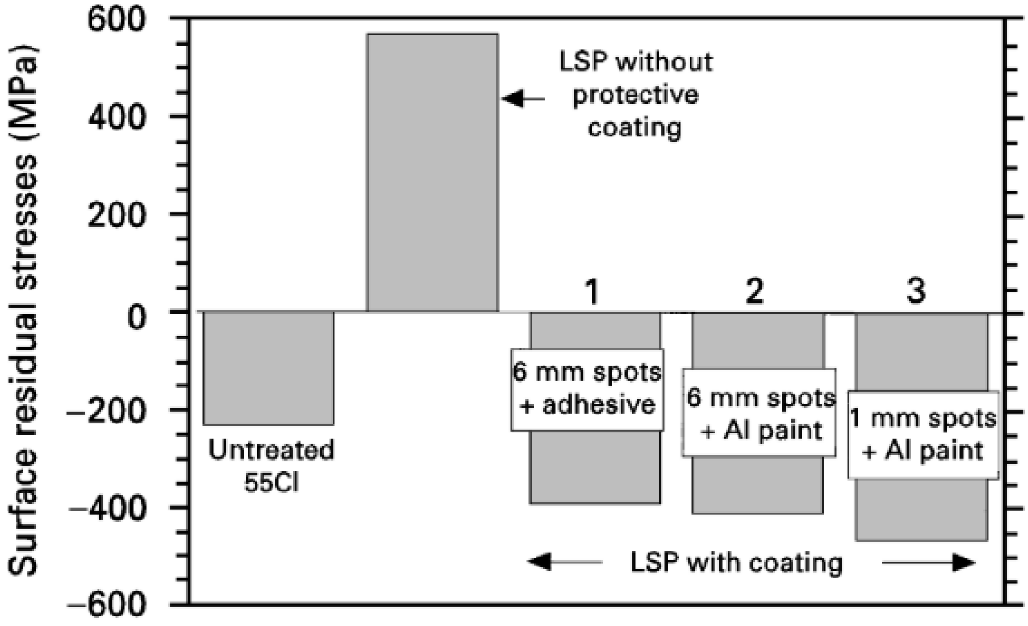

Figure 5. Average residual stress values determined at the surface of notched fatigue samples of 55C1 Steel with different LSP conditions at 5 GW cm^{-2} in the water-confining regime: (1) 6 mm impacts + aluminium adhesive, (2) 6 mm impacts + aluminium paint, (3) 1 mm impacts + aluminium paint.
(Peyre et. al., 1998)

Many kinds of coatings have been used, such as aluminium, zinc, lead, black vinyl tape and black paint. Commercially, black paints and tapes are most common, with some opting for aluminium tape [18]. In early studies on laser peening (late 1970s) it was thought that there were significant differences between the effects of various coatings on the magnitude of the pressure pulse. This has been attributed to the acoustic impedance (*Z*) (opposition a material system presents to acoustic flow, equal to the speed of sound through the medium multiplied by its density) relationship between the target material (of Z_2) and the ablative layer (of Z_1), as explained by Fabbro *et al*. as per equation (2) [7].

$$\frac{2}{Z} = \frac{1}{Z_1} + \frac{1}{Z_2} \qquad (2)$$

This, coupled with equations (3) and (4), shows that the acoustic mismatch between the ablative layer and target material will increase the peak pressure, *P*, but decrease the length (depth in the shock direction) of the plasma interface, *L*. This reduction causes less effective LSP overall, and more irregularity in the deformation layer. I_0 is the laser power density, α is the ratio of thermal to internal energy and τ is pulse duration.

$$P\ (GPa) = 0.01\sqrt{\frac{\alpha}{2\alpha+3}}\sqrt{Z\ (g\ cm^2\ s^{-1})\ I_0\ (GW\ cm^{-2})} \qquad (3)$$

$$L\ (\mu m) = 2.10^5\,\frac{P\ (GPa)\ \tau\ (ns)}{Z\ (g\ cm^{-2}\ s^{-1})} \qquad (4)$$

Equation (3) is one example of possible peak pressure formulae; many others, however, are mentioned in the literature, as compiled by Gujba and Medraj [3], where Equation (4) can also be found.

For manufacturing, paints are often fast drying, and of a low viscosity to allow the paint thickness to be optimised. It is also beneficial for the paint to have low solubility in water when used as the confinement layer, hence oil and rubber-based paints are suitable. Better quality processing is possible when there is more complete adhesion of paint to the sample surface and reduced air gaps. This increases pressure on the target as there is less compressible space for the plasma to expand and escape into.

2.1.2.3 Practical Parameters

2.1.2.3.1 Multiple Laser Shocks and Overlap

The LSP intensity is based upon the power per unit area applied to the coating or target material, which is limited, often by the laser maximal power output. This hurdle can be overcome by performing multiple shots over the same location. This improves the effect of LSP (see Figure 6, shown for AZ31B Mg Alloy, [19]) until the stress saturation point is reached. Additional laser shocks provide increased residual stress magnitude deeper in the target, as implied by Figure 7 [14]. Information regarding the microstructural effects of multi-shock LSP can be found in section [*2.6 LSP Influence on Microstructure*].

It is necessary to address the difficulty in providing uniform shocking to the target due to differences in plasma formation, because of residual paint from, and proximity to, previous pulses. These interferences can reduce the pressure pulse intensity with too much paint or cause thermal effects where there is too little paint. As circular lasers have a large percentage overlap, square laser spot shapes can be used. During many automated peening processes, it is common to provide an overlap value which determines the distance the beam centre will travel relative to the initial position. For a circular beam, a 0 % overlap will cause two successive shots to be adjacent. A 50% overlap will have the centre of each point on the perimeter of the adjoining shot. This can be used to successively laser shock a single location, although the ablative layer may need to be re-applied. As a result, some peening equipment has in-situ paint application, but this slows the process, reducing the repetition rate of the machine.

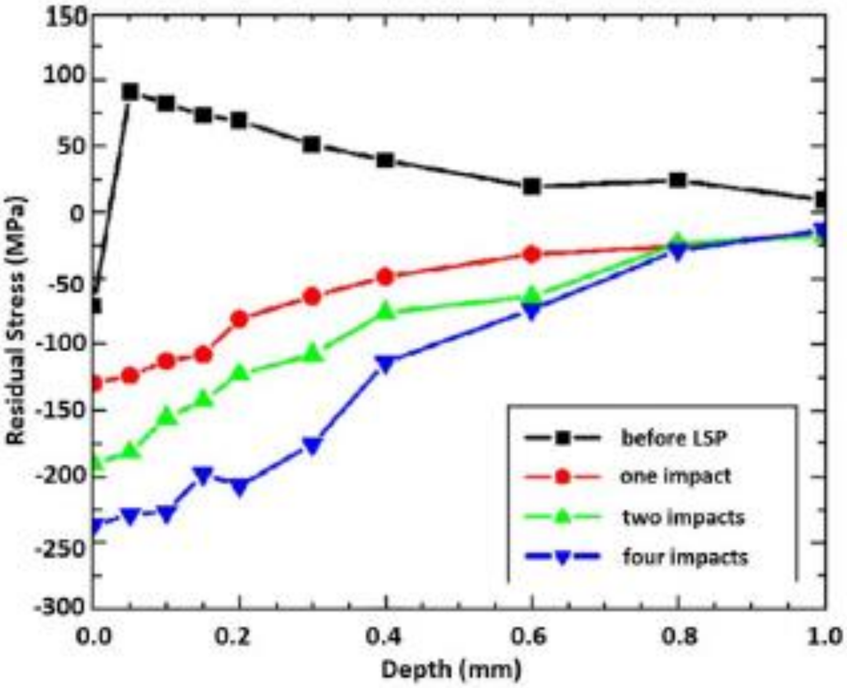

Figure 6. Residual stress variation with depth in AZ31B Mg alloy after different numbers of laser impacts.
(Zhang, et al., 2010)

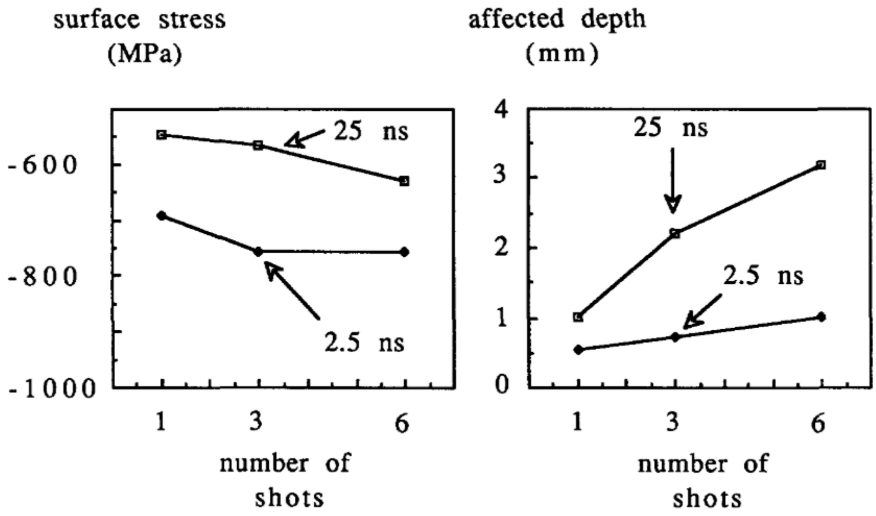

Figure 7. Residual stress parameters as a function of the number of shots incident on low alloy steel at optimum laser intensities for pulse durations of 25 nm and 2.5 nm.
(Fournier et. Al., 1991)

2.1.2.3.2 Target Material Geometry

The vast majority of experimental data covers flat surfaces. Attempts to predict the effect of LSP for more complex geometries have been made, mostly via modelling. Correa *et al.*, [20] report simulations of residual stresses in Ti-6Al-4V hip replacements. Complex geometries can have especially variable effects on the residual stress state due to existing microstructural features and release wave interactions.

When performing LSP on thin pieces, specimens have a tendency to distort, bending the specimen as a result of the residual stress distribution [21]. This is noticeable on components such as gas turbine compressor blades and plate valves. Although the peened face will be in compression, the opposing side will be in tension. This can be solved either by carefully attaching samples onto larger pieces, or by peening both sides. Process parameters must be altered accordingly for the application. The surface condition will also affect the final RS distribution and overall effectiveness of LSP.

2.2 Effect of LSP on Mechanical Properties

The LSP process is employed due to its beneficial effect on many mechanical properties, including but not limited to fatigue resistance, crack corrosion resistance, wear resistance and surface hardening [12]. The majority of available research covers fatigue resistance, as this is the predominant reason why LSP is employed.

2.2.1 Fatigue Resistance

The aim of many surface processing methods, from conventional shot peening to carburisation, is to increase the fatigue resistance of materials via the compressive residual stress embedded in the material. An example of this can be seen in Figure 6, where successive laser shocks increase CRS. Although the extent of improvement that LSP provides depends on the material history, in the vast majority of cases LSP will drastically improve the fatigue resistance of materials.

Examples of this can be found in Figure 8 and Figure 9. Figure 8 demonstrates how LSP has been used to increase the fatigue life of notched steel specimens, whilst comparing varying laser spot sizes. Not only do the cycles to failure increase, but the increase in fatigue limit from 380MPa to 470MPa-490MPa is highly significant. Figure 9 illustrates the effects of high cycle fatigue on damaged Ti-6Al-4V fan blades after different peening-based methods. It can be seen that the fatigue strength after LSP has more than doubled when compared with the shot peening alternatives.

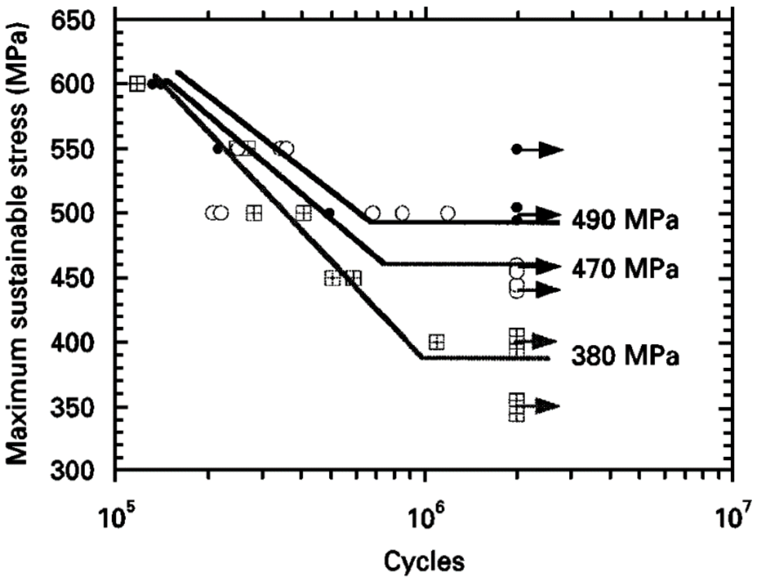

Figure 8: S-N curves of 55C1 - notched samples; bending test at R=0.1. Effects of laser-shock processing with small or large impacts at 5 GWcm-2 in the water-confined mode. (●) 1 mm impacts, (□) base material; (◯) 7 mm impacts. *(Peyre, et al., 1998)*

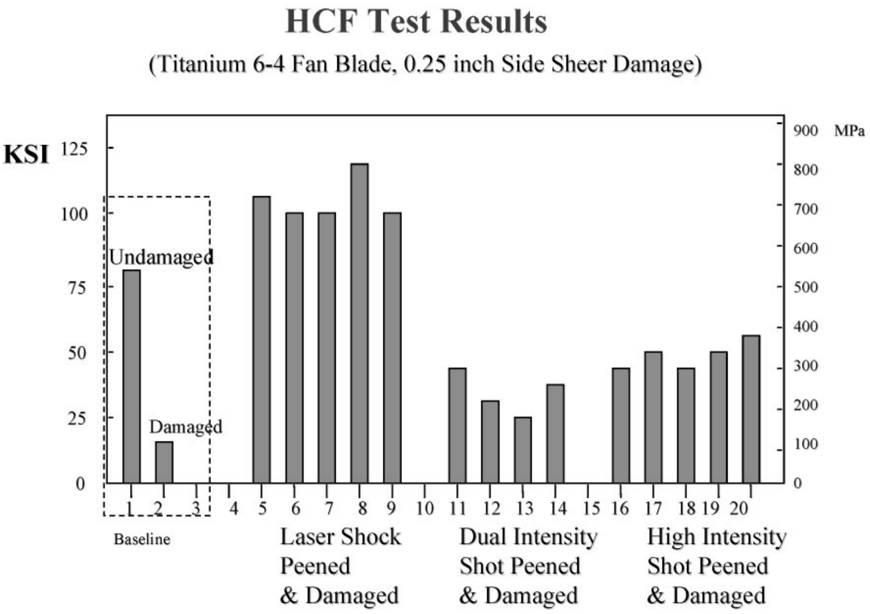

Figure 9: High cycle fatigue test results * titanium fan blades (Hammersley, et al., 2000)

It is possible, however, that for samples which already possess high residual stresses that approach the stress saturation point, as well as those which possess existing fatigue, LSP may reduce the CRS, or may create extreme local area stresses from the propagation of the stress wave, thereby reducing fatigue and wear resistance. The effect of this, and over-processing in general, is internal rupture [3,12]. These cause internal cracks to manifest which leads to component failure. Examples of partial over-processing can be found in a 7050-T74 Al alloy [22]. The damage is described as similar to spall fracture in armour materials. The mechanism proposed relates to the fact that when compressive stress waves propagate through materials they are balanced with tensile waves, which together make up the shockwave. When the shockwave is reflected on the opposing surface this couples with a change in sign of the shockwave components such that this causes the tensile wave to lead the compressive wave. Where the reflection takes place, there is a short time where the leading wave is reflected and the trailing wave is not, and they are both tensile. When this occurs, if the total tensile stress the material is subjected to exceeds the tensile or fracture strength of the material, a fracture occurs. This phenomenon is of interest because it makes a component undergoing ultra-high strain more susceptible to internal cracking, if the technique is misused.

2.2.2 Crack Corrosion Resistance

Studies have indicated nominal improvements to corrosion resistance of materials after LSP, particularly in conjunction with stresses. Lim et al. [23] found the corrosion rates of duplex stainless steel (22.6-Cr 5.5-Ni 3.1-Mo 1.9-Mn by wt.%) in 0.35 wt.% NaCl to decrease from 3.37×10^{-3} mm/year to 0.869×10^{-3} mm/year after LSP treatment, demonstrating an improvement of 74.2 %. Austenitic stainless steel exhibited a reduction in average corrosion potential with an increase in laser pulses per area, as indicated in Figure 10 [24], although this was only after an increase in corrosion current density following early exposure to the 3.5

wt.% NaCl solution (Table 1), indicating swift passivation of the outer material, protecting the sub-surface. This effect was in conjunction with a reduction of pitting corrosion in laser peened specimens.

In AZ31B Mg alloy it has been shown that LSP retards SCC crack initiation and propagation in a 1 wt.% solution of NaOH [19]. The results of the accompanying bent-beam specimen tests show a significant reduction of crack propagation in the LSP specimen at a crack length of 237µm (as seen in Figure 11) compared to the unpeened specimen crack which exceeded the measurements used in the study. Most significantly, during these bending tests the LSP specimen extended the pre-crack by 10 - 24 % with the unpeened specimen crack well exceeding a 100 % increase.

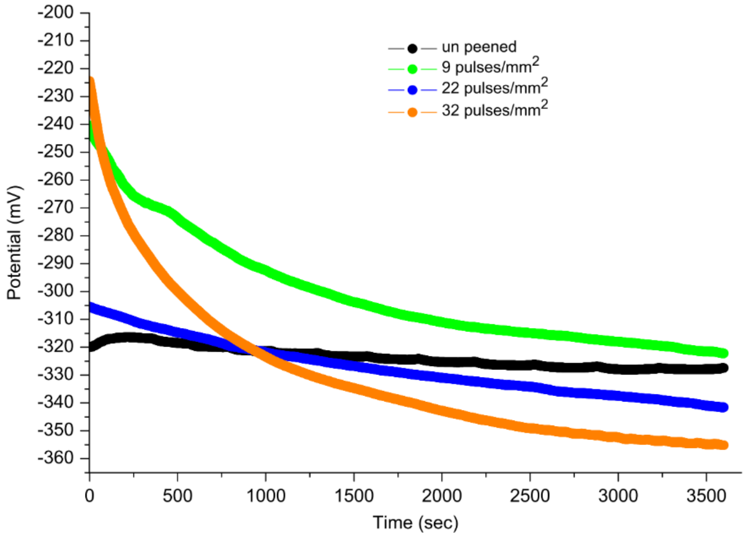

Figure 10: Variation of open circuit potential with time. Potential, and thereby risk of corrosion, is reduced at the beginning of testing, when corrosive solutions are closer to the sample surface. This becomes more susceptible to corrosion deeper into the sample. The effect is continuously beneficial for 9 pulses mm^{-2} but once the outer layer is corroded, significant LSP can cause increased corrosion rates.
(Kalainathan, Sathyajith and Swaroop, 2012)

Table 1: Variation of open circuit potential and corrosion current density over different pulse density. Open circuit potential is reduced for samples with greater LSP density.
(Kalainathan, Sathyajith and Swaroop, 2012)

Specimen	I_{corr} (mA/cm^2)	E_{corr} (mV)
Untreated	2.3793	−406.71
9 pulses/mm^2	2.3035	−369.42
22 pulses/mm^2	2.4827	−384.78
32 pulses/mm^2	2.6339	−351.87

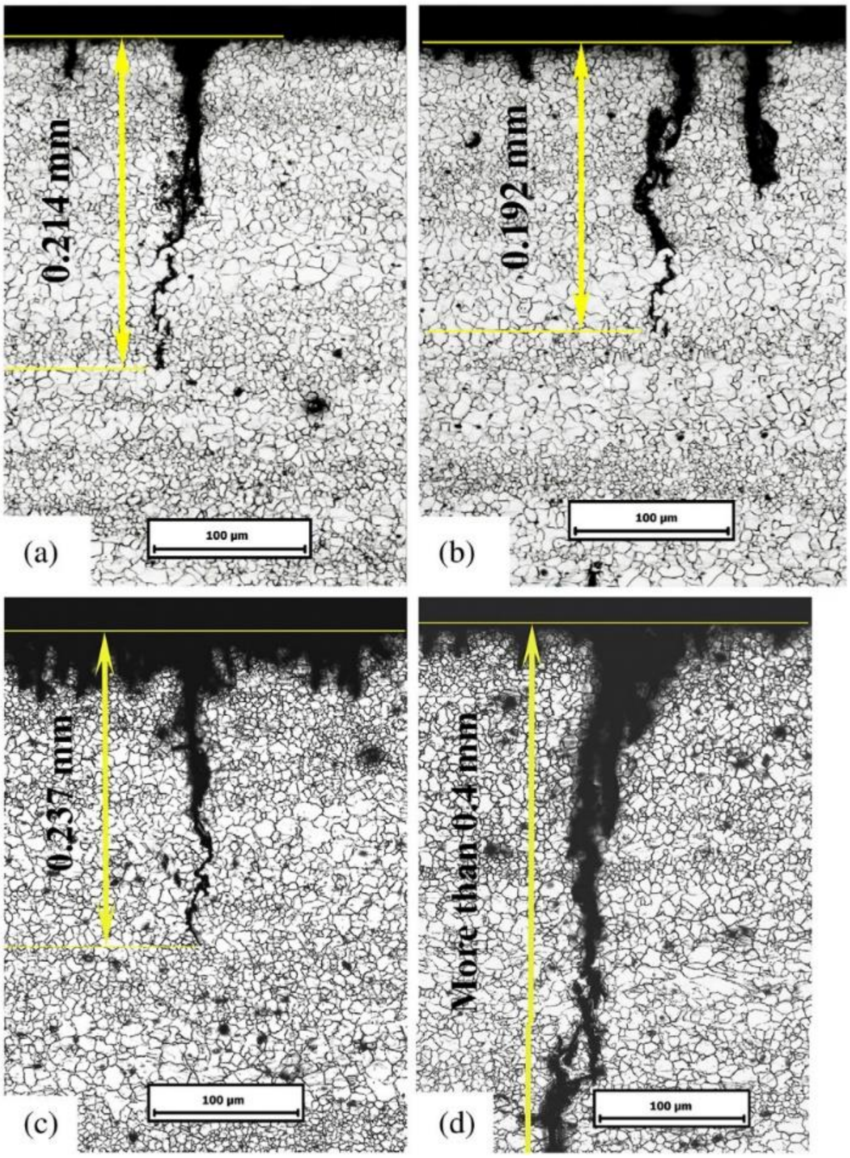

Figure 11: The distributions of the maximum crack depth in AZ31B Mg alloy samples after immersion in 1 wt.% NaOH solution for 500h: (a, b) pre-cracked specimens without further processing; (c) Laser shock peened specimen after bent-beam type stress testing; and (d) unpeened specimen after bent-beam type stress testing. (Zhang, *et al.*, 2010)

2.2.3 Wear Resistance

Wear resistance may be improved with the use of laser shock peening, although this is also dependent on the surface condition of the metal after LSP. Surface roughness will increase, although this change is minimal when compared to earlier methods such as shot peening. Figure 12 [23] shows the changes to the wear volume (material lost over wear testing) of duplex stainless steels, and Vickers hardness of LSP material with different protective coatings, with wear testing at 3 kg and 160 rpm for 30 minutes. Wear volume reduction has also been demonstrated by Kumar et al. on Ti-6Al-4V, [25] as shown in Figure 13d. Figure 13 also shows the increase in surface roughness with increasing laser fluence (b) and related increases to the coefficient of friction (c). A confinement layer of water significantly reduces these effects which is beneficial to the surface finish of the material. A useful summary of various properties can be seen in (e), such as the reciprocal relationship between hardness and wear volume, corroborating Figure 12.

Figure 14bi [26] shows that this improvement to wear rates in the case of TC11 Ti alloy is not limited to room temperature, but had even more significant changes at 600 °C, providing an improvement of around 73% over the non-LSP counterpart. LSP shows consistent improvement for multiple wear tests (Figure 14ii).

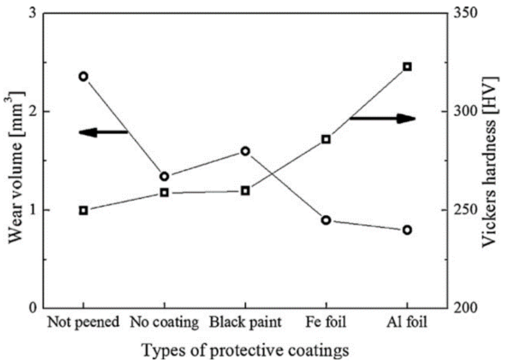

Figure 12: Effects of the protective coating on wear volume and micro-Vickers hardness. (LSP conditions: 10 GW/cm^2, 75 pulse/mm^2, Wear test conditions: 3 kg, 160 rpm, 30 min.)
[23] (Lim et al., 2012)

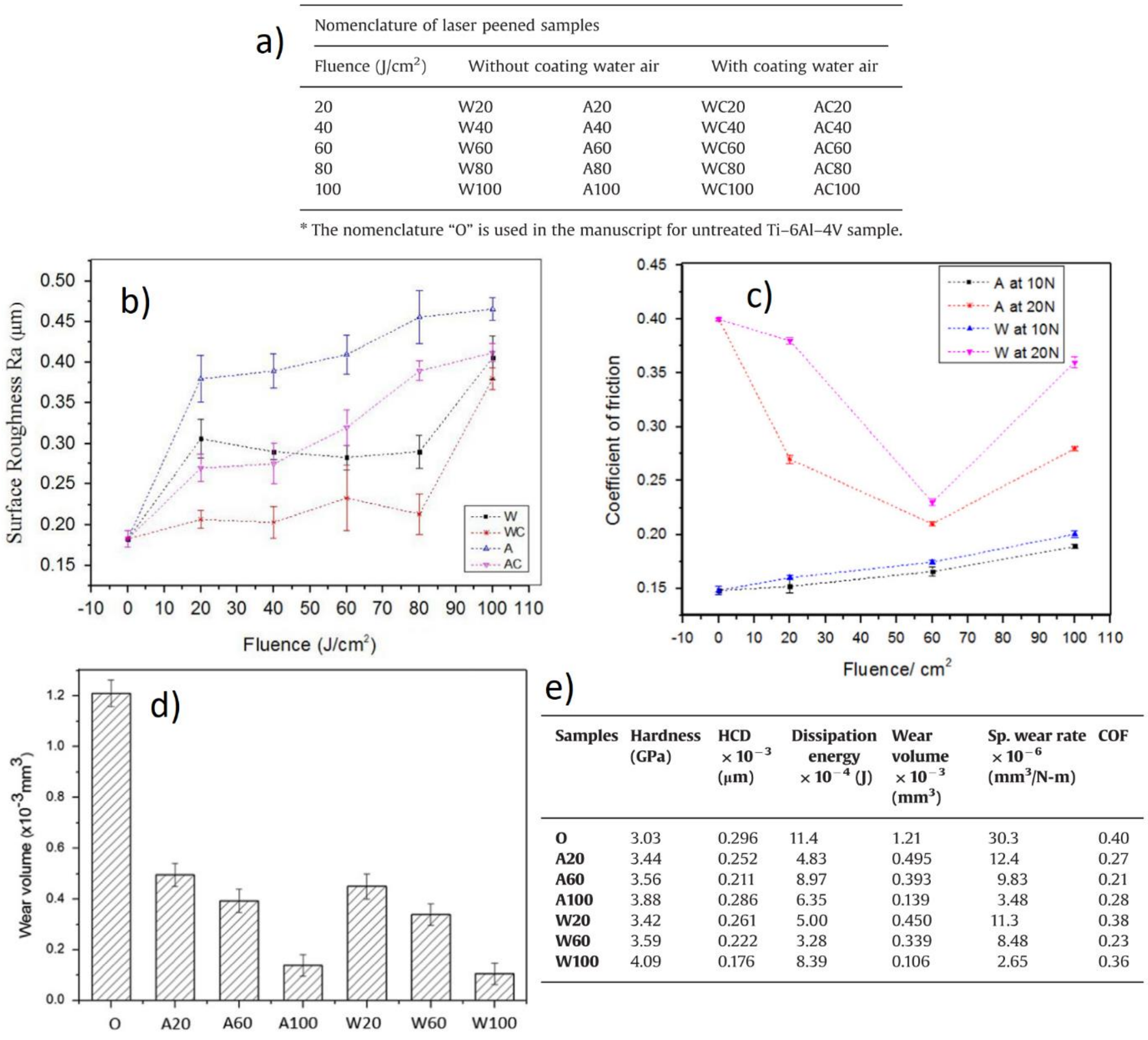

Nomenclature of laser peened samples

Fluence (J/cm^2)	Without coating water air		With coating water air	
20	W20	A20	WC20	AC20
40	W40	A40	WC40	AC40
60	W60	A60	WC60	AC60
80	W80	A80	WC80	AC80
100	W100	A100	WC100	AC100

* The nomenclature "O" is used in the manuscript for untreated Ti–6Al–4V sample.

Samples	Hardness (GPa)	HCD $\times 10^{-3}$ (μm)	Dissipation energy $\times 10^{-4}$ (J)	Wear volume $\times 10^{-3}$ (mm^3)	Sp. wear rate $\times 10^{-6}$ (mm^3/N-m)	COF
O	3.03	0.296	11.4	1.21	30.3	0.40
A20	3.44	0.252	4.83	0.495	12.4	0.27
A60	3.56	0.211	8.97	0.393	9.83	0.21
A100	3.88	0.286	6.35	0.139	3.48	0.28
W20	3.42	0.261	5.00	0.450	11.3	0.38
W60	3.59	0.222	3.28	0.339	8.48	0.23
W100	4.09	0.176	8.39	0.106	2.65	0.36

Figure 13: Various tribological properties of Ti-6Al-4V in relation to different laser peening parameters, as shown with a) table of nomenclature of laser peened samples under different ablative and confinement layers and fluence (e.g.: WC60 means a sample undergoing LP at fluence of 60 J cm^{-2} whilst coated, with a water transparent overlay). b) Surface roughness at different fluences and media. c) variation of coefficient of friction (COF) of titanium at different normal loads (of 10 N and 20 N) at fixed stroke length of 100 μm, frequency 10 Hz, and 10,000 Cycles. d) Plot of wear volume at laser peening with different fluences. e) Summary table of correlation between material properties in experiments at 20 N load.
(Kumar *et al.*, 2015)

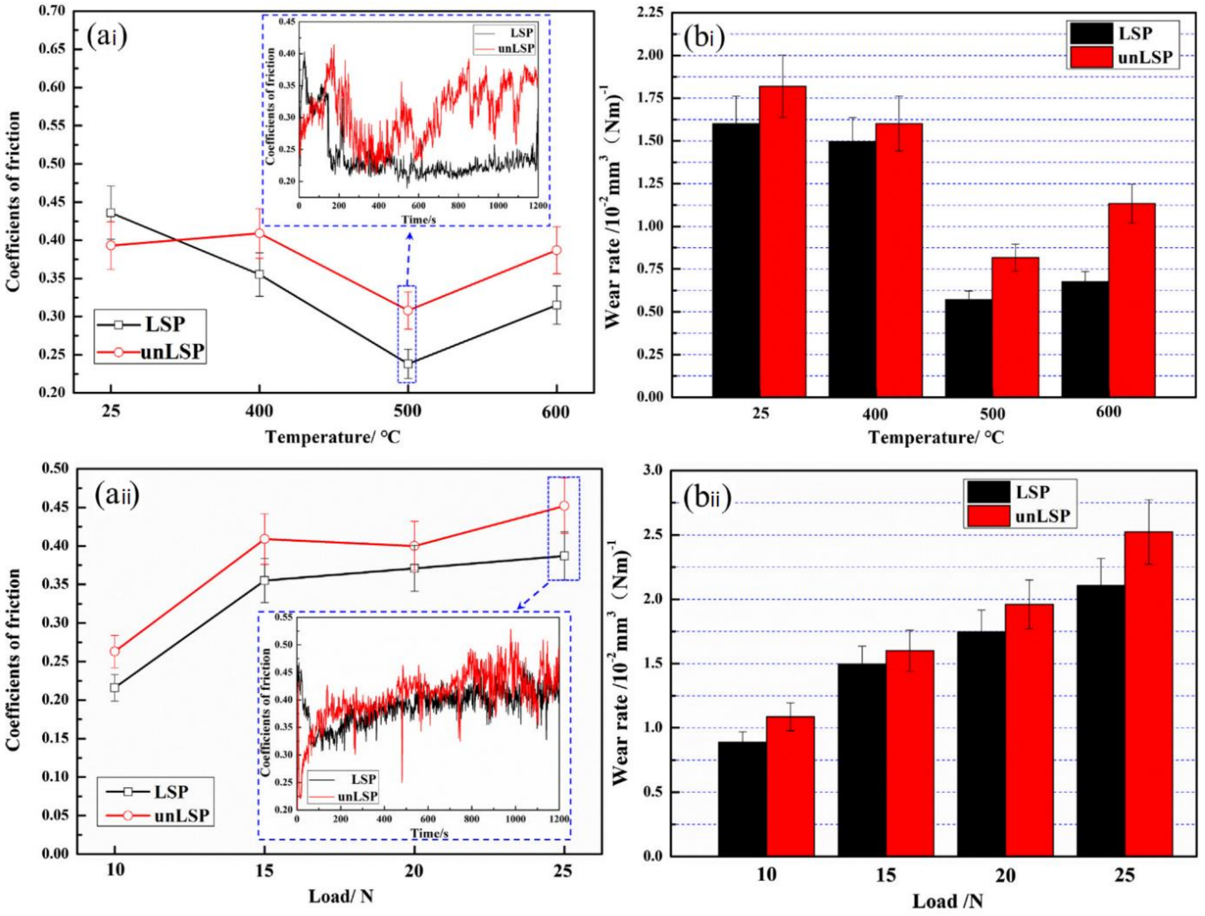

Figure 14: a) Friction coefficients and b) wear rates of specimens at different i) temperatures under 15 N load and ii) applied loads at 400 °C.
(Tong *et al.*, 2019)

2.2.4 Surface Hardening

Many of the results discussed so far have involved indentation techniques to evaluate the surface hardening of LSP materials. Other works focusing on indentation directly on the LSP surface include Ganesh et al. [27], and Zhang et al. [28]. The nano-indentation of fatigued steel spring components with and without laser shock peening yielded a hardness increase of 22 %. The yield strength was also improved by 20 % (Table 2 [27]). Figure 15 [28] shows how the micro-hardness of Ti-6Al-4V changes after localised LSP, establishing a significant increase in hardness over this processed region.

Indentation has also been performed across cross sections of LSP materials to evaluate the depth of peening effect on TC11 titanium alloy [29,30], and various other materials, such as steels [31,32]. An example from CP-titanium in Figure 16 is shown to have decreasing hardness when travelling away from the LSP surface. It should be noted that often when LSP is performed without a protective ablative layer (LSPwC) the top surface may be softer due to the fast heating and subsequent supercooling of the surface layer. As the damage layer is thin, this may not be picked up by micro-indentation but can often be seen with nano-indentation.

Table 2: Summary of results obtained from nano-indentation of pre-fatigued stainless steel spring components with and without laser shock peening. Test-pieces and testing regions taken from and on three separate bulk specimens. (Ganesh *et al.*, 2014)

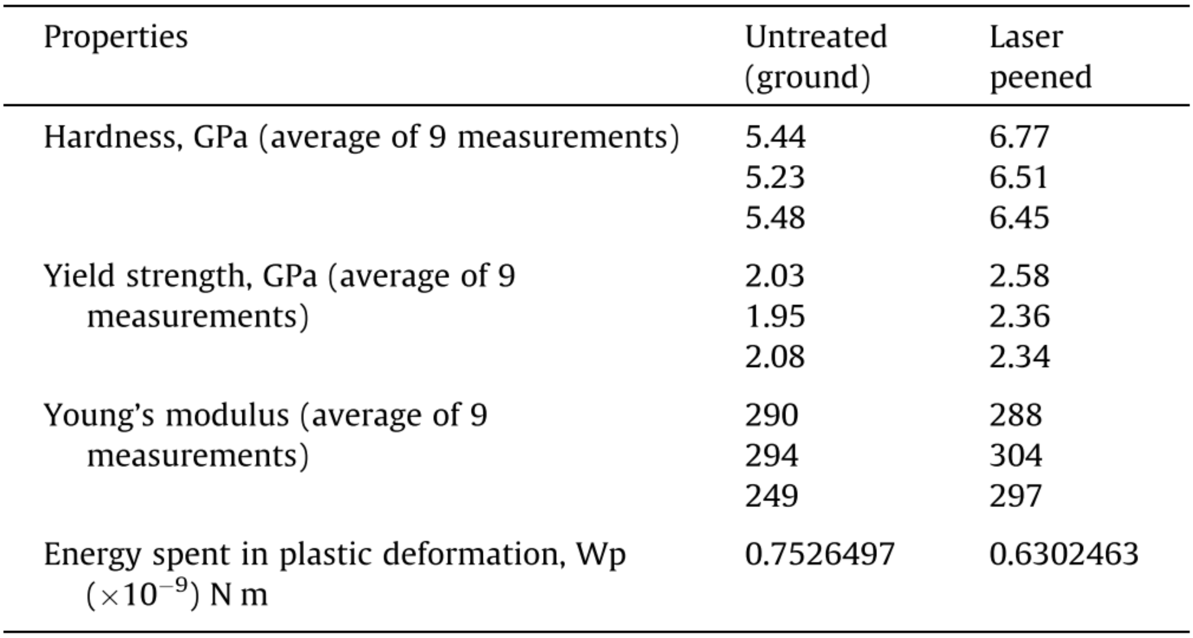

Properties	Untreated (ground)	Laser peened
Hardness, GPa (average of 9 measurements)	5.44	6.77
	5.23	6.51
	5.48	6.45
Yield strength, GPa (average of 9 measurements)	2.03	2.58
	1.95	2.36
	2.08	2.34
Young's modulus (average of 9 measurements)	290	288
	294	304
	249	297
Energy spent in plastic deformation, Wp ($\times10^{-9}$) N m	0.7526497	0.6302463

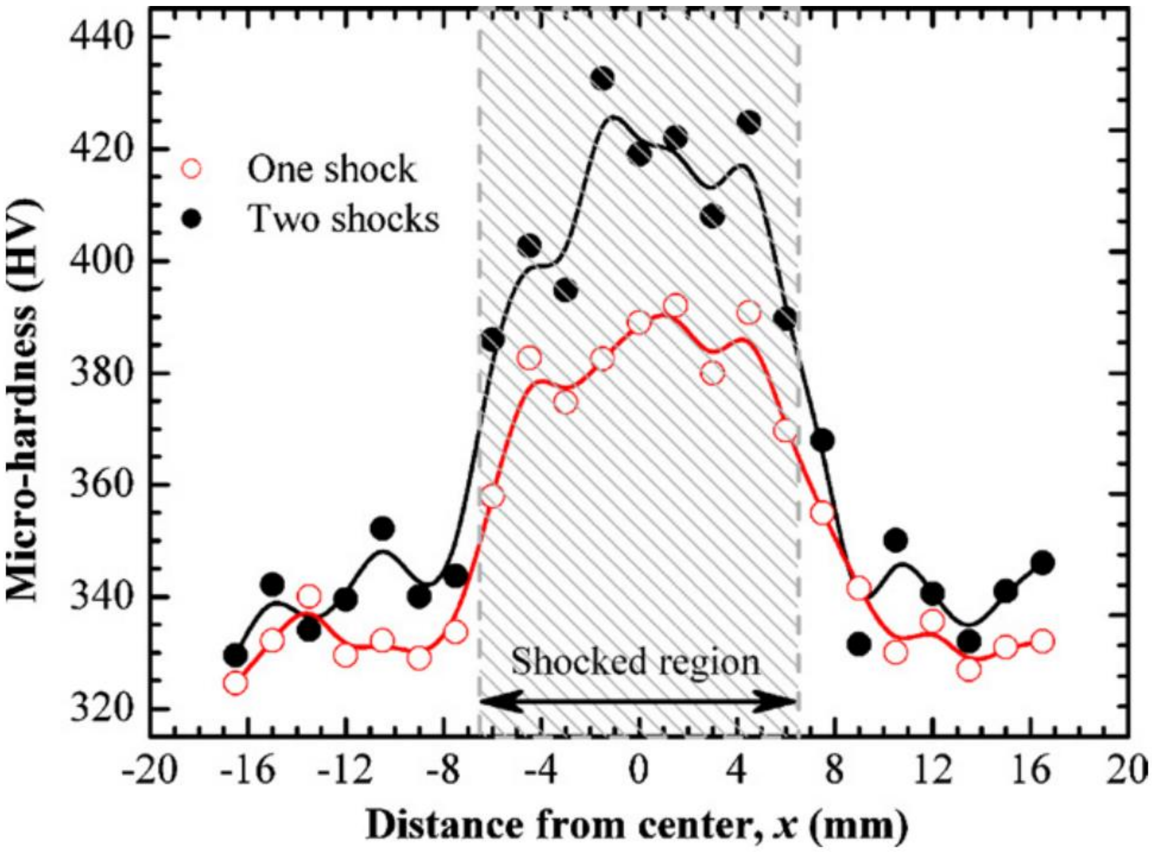

Figure 15: Micro-hardness profiles at the surfaces of two Ti-6Al-4V specimens shocked with three overlapped spots (5 mm spot size with 40% overlap). Power density of 5 GW/cm^2.
(X. C. Zhang et al., 2010)

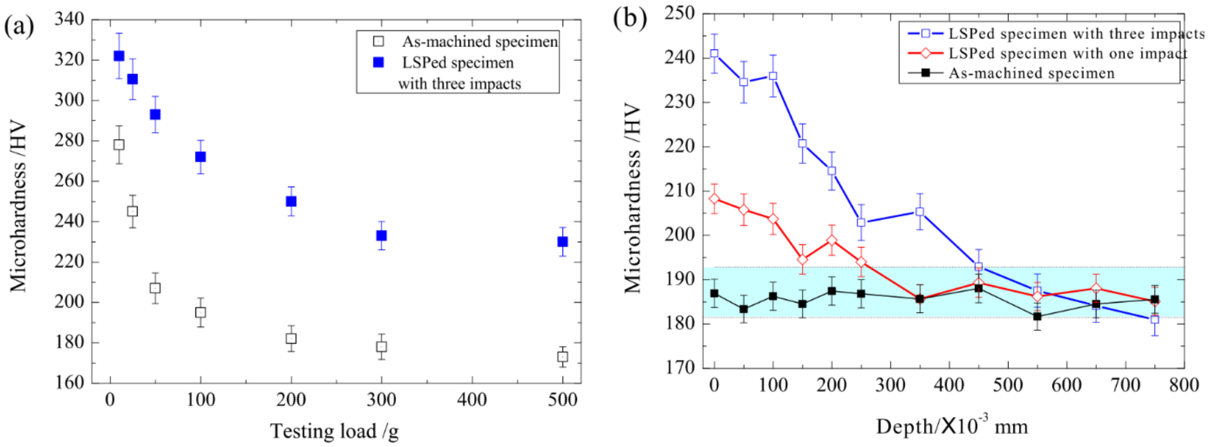

Figure 16: Surface micro-hardness of as-machined and LSPed commercially pure titanium samples under a) different testing loads and b) in-depth micro-hardness curves with different LSP shock numbers under a 200 g load.
(Lu *et al.*, 2017)

2.3 Deformation mechanisms in α-Titanium

There are four mechanisms by which metallic materials accommodate strain. At the smallest scale, slip occurs by creating and moving dislocations. Where slip mechanisms are insufficient, twinning can occur, which is also dependent on dislocation activity. These two mechanisms, slip and twinning, are often considered competing mechanisms depending on the application. It is also possible to trigger phase transformations through mechanical deformation, with martensitic transformations being most common. If none of these internal mechanisms are capable of accommodating the introduced strain, fracture follows, either locally, leading to cracking, or at a macro scale, resulting in component failure. [33].

Much of this discussion is concerned with twinning, whilst also covering slip. Phase transformations after LSP are not widely reported (although some reasons why this is the case will be covered further in section [*2.4.2 Shock-wave Responses of HCP Titanium*]) and fracture is typically discussed in relation to pre-fatigued components or over-processing of LSP material. A generalised attempt at predicting the mechanical response of materials based on shear strain rate and temperature can be seen in the Weertman-Ashby map [34] (Figure 17, [33]) for large grained (100 µm) Titanium with assumed 0.1% Oxygen mimicking low levels of impurity.

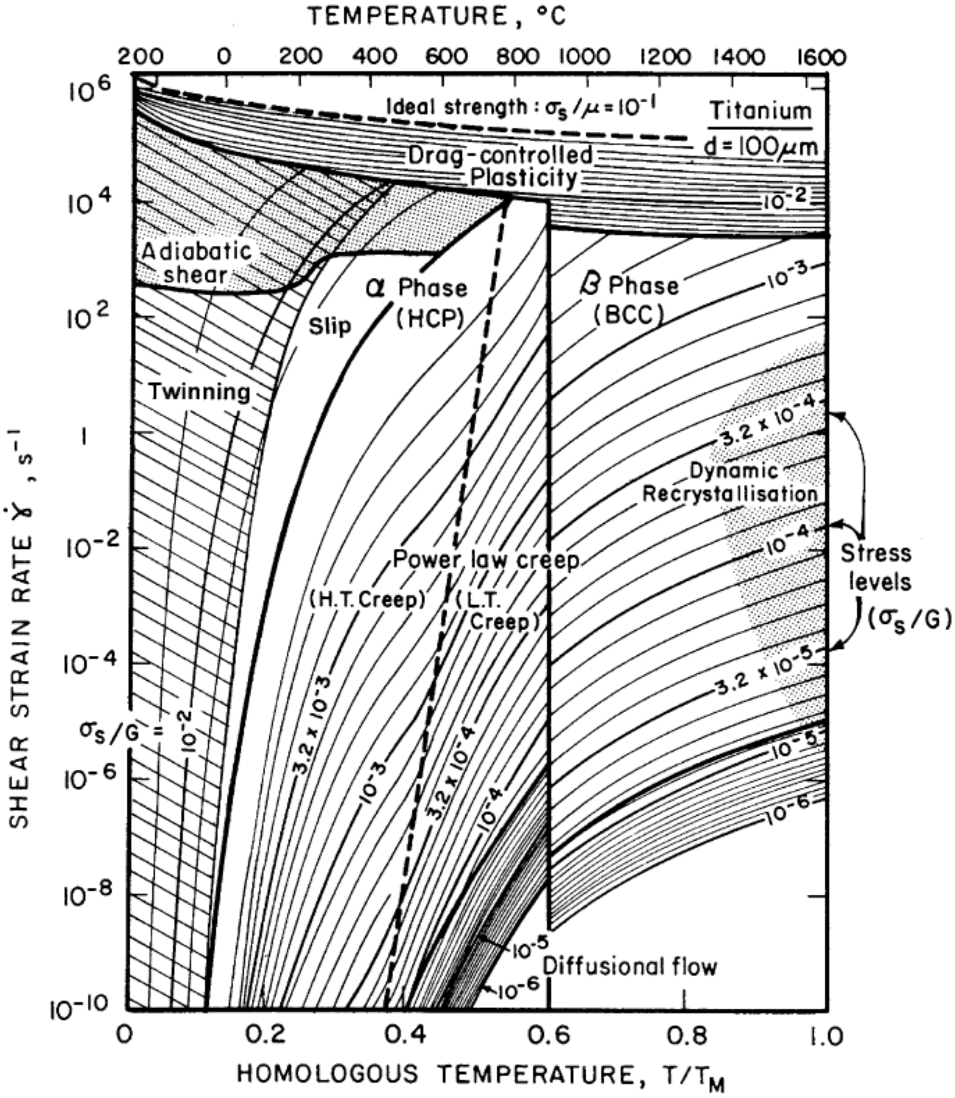

Figure 17: Weertman-Ashby map for 0.1% oxygen equivalent for titanium with d = 100 μm, in which a twinning domain has been inserted.
Adapted by (*Meyers, Vöhringer and Lubarda, 2001*) from (*Frost & Ashby, 1982*)

2.3.1 HCP Slip

Dislocations in HCP are characterised by the plane in which they glide and by their slip, or Burgers, vector. $< a >$ type dislocations have a Burgers vector $\frac{1}{3} < 11\bar{2}0 >$. These can glide on basal, prismatic and pyramidal planes. The von Mises criterion states that at least five independent slip systems are required for extensive ductility in polycrystalline materials. As seen in Table 3, the number of independent modes for $< a >$ type dislocations are insufficient to satisfy the von-Mises criterion [35]. $< c + a >$ type dislocations have five independent slip systems. These have Burgers vector $\frac{1}{3} < 11\bar{2}3 >$ and can glide on the prismatic and first order pyramidal planes. These are illustrated in Figure 18 [36].

The most common slip systems in α-Titanium are $< a >$ on the prismatic plane [37], and $< c + a >$ on the first order pyramidal plane [38,39]. Twinning has a similar stress threshold to many of these slip mechanisms (apart from prismatic $< a >$ type dislocations, which are much easier to produce) and as such twinning is common in low alloy α-Titanium. This will be discussed further in section [*2.3.3.1 CRSS and TCRSS*].

Table 3: Independent modes of deformation in HCP crystals.
(*Yoo et al., 1981*)

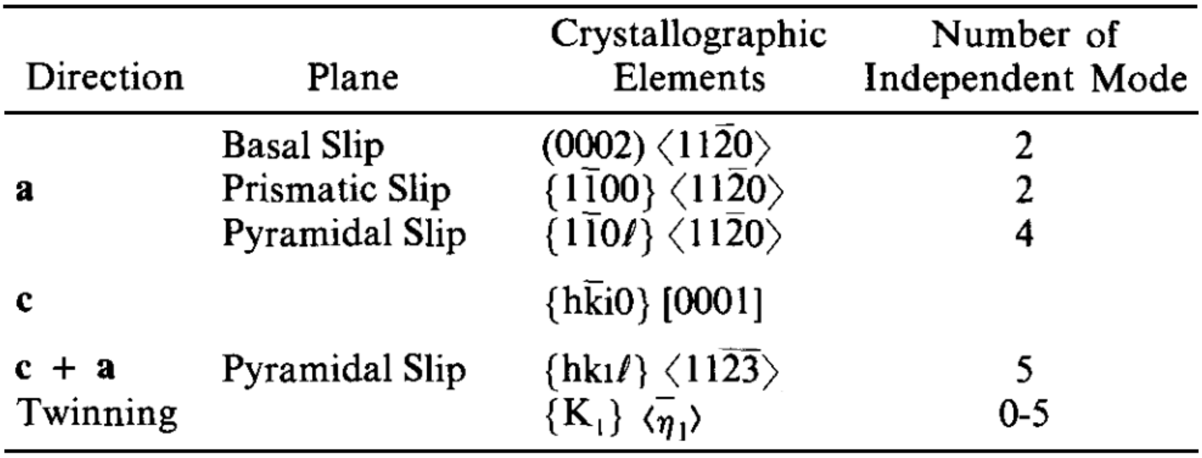

Direction	Plane	Crystallographic Elements	Number of Independent Mode
a	Basal Slip	$(0002)\ \langle 11\bar{2}0 \rangle$	2
	Prismatic Slip	$\{1\bar{1}00\}\ \langle 11\bar{2}0 \rangle$	2
	Pyramidal Slip	$\{1\bar{1}0\ell\}\ \langle 11\bar{2}0 \rangle$	4
c		$\{h\bar{k}i0\}\ [0001]$	
c + a	Pyramidal Slip	$\{hki\ell\}\ \langle 11\overline{23} \rangle$	5
Twinning		$\{K_1\}\ \langle \bar{\eta}_1 \rangle$	0-5

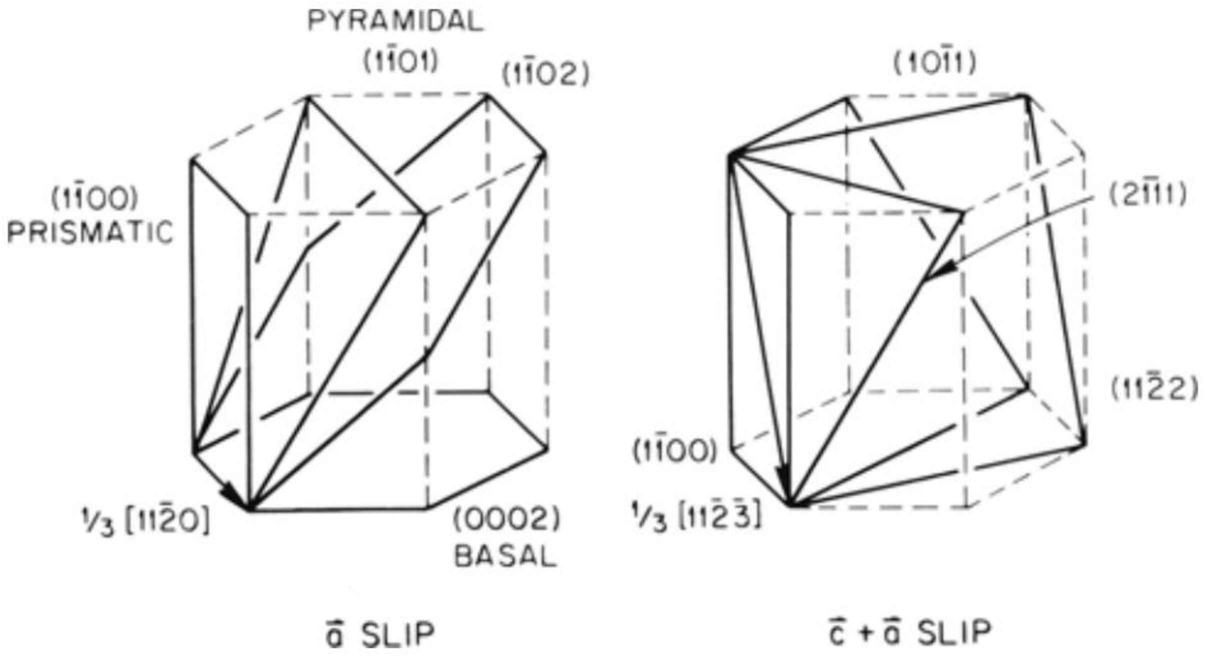

Figure 18: Basal, prismatic, and pyramidal slip systems with $< a >$ Burgers vector, and four possible pyramidal slip planes with $< c + a >$ Burgers vector.
(*Yoo et al., 1981*)

2.3.2 HCP Twinning

Annealing twins are characterised by their large structure (relative to the grains) and parallel nature of their boundaries. These form during slow cooling of low SFE materials. In contrast, deformation twins are usually thin, and their boundaries are not always parallel. These are more likely to form when deformation is performed at lower temperatures, and at high strain rates. In the case of some crystal structures, it has been commented that ultra-high strain rates (>10^6 s^{-1}, as exhibited by LSP) reduce the likelihood of twinning [40], but this has not been shown for HCP titanium. Mechanical twinning subdivides grains and increases the barriers to slip along with the work hardening rate. This twinning also contributes to work hardening as the twinning shear causes plastic deformation, which decreases the work hardening rate [33].

Deformation twins may also be described according to the relative compression of the HCP unit cell along the c axis. Contraction twins such as $\{11\bar{2}2\}$ and $\{10\bar{1}1\}$ type cause compression along the c-axis, whilst extension twins of $\{10\bar{1}2\}$ and $\{11\bar{2}1\}$ type cause compression along the a-axes (see section [*2.3.2.2 Types of Twinning*]). Depending on the orientation of the grain, these can be indicative of compressive or tensile residual stresses. For example, if a grain undergoes compression along the $[11\bar{2}0]$ direction via an extension twin $\{11\bar{2}1\}$, this should correspond to compressive residual stresses in the system.

2.3.2.1 Mechanisms and Nomenclature

Twins are defined according to K_1, the shared plane between the twin and the matrix, also known as the invariant plane of twinning shear. K_2 Is the undistorted conjugate twinning plane, with K_2' being the plane after twinning. These K_2 planes make an angle ϕ with K_1. The shear plane, S is the plane on which lattice sites move to produce twins. These atomic movements are achieved through shear and shuffle. d is the interplanar spacing of lattice planes parallel to K_1 with q being the total number of K_1 planes in the unit cell. The matrix unit cell is defined according to $\boldsymbol{\eta_1}, \boldsymbol{\eta_2}\ and\ \boldsymbol{S}$ located within the $K_1, K_2\ and\ S$ planes, respectively, with $\boldsymbol{\eta_2}$ and K_2 replaced by $\boldsymbol{\eta_2'}$ and K_2' for the twin unit cell. $\boldsymbol{\eta_1}$ is the direction of shear, and $\boldsymbol{\eta_2}$ is the conjugate shear direction.

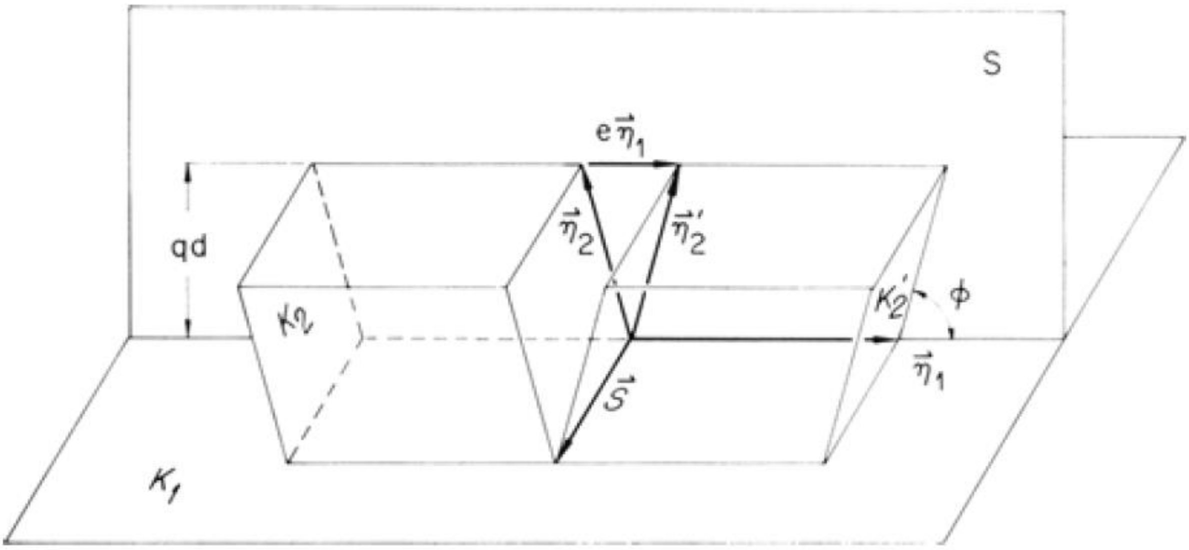

Figure 19: Crystallographic elements of twinning. The unit cell defined by $\boldsymbol{\eta_1}, \boldsymbol{\eta_2}$ and $\boldsymbol{S}$ Is homogeneously sheared to the unit cell defined by $\boldsymbol{\eta_1}, \boldsymbol{\eta_2'}$ and $\boldsymbol{S}$.
(M. H. Yoo, 1981)

On the atomic level, twinning necessitates the shear of crystal planes and shuffling of lattice points to the new twinned planes. The balance of the proportion of strain accommodated through each mechanism is related to the number of shear plane repetitions in the unit cell, defined as q. If q Is equal to 1 or 2, then the shift is accommodated entirely by shear and there is no need for lattice shuffles. Greater q values increase the probability of shuffle. The lattice interface will move forward by a distance qd such that the atomic displacements are repeated in each successive group of q planes [41].

The magnitude of shear, s, is calculated as a function of axial ratio, providing a theoretical basis for the difference in stress required to induce different types of twinning. This gives rise to the critical resolved shear stress of twinning, henceforth termed TCRSS, which, similar to the CRSS for slip, provides values based on experimental evidence for the onset of twinning (see section [*2.3.3 HCP Slip and Twinning*]). It is also worth noting that the stress required for the growth of twins is significantly less than that required for twin nucleation.

2.3.2.2 Types of Twinning

Many types of twinning have been theorised according to their K -planes and $\boldsymbol{\eta}$ -vectors. These are listed in Table 4 [41]. Of these, only a handful have been experimentally observed, an even smaller number of which have been confirmed in α-Titanium, the predominant ones having been summarised in Table 5 [36].

The most common twins found in commercially pure titanium are the $\{11\bar{2}2\}$ and $\{10\bar{1}2\}$ type twins in c-axis compression and tension respectively [42]. This relates to the twinning shear, s required to produce said twins. As seen in Figure 20 [36], $s < 2.5$ for these twins. Although the lowest s-value twin is the $\{10\bar{1}1\}$ type, these do not appear as regularly, and are most seen in second order twinning (formation of twins inside pre-existing twins). Nishiyama et. al., reported that these twins are often found beside stacking faults and dislocations, and can be considered common components of martensitic transformation [43]. Hence, they were considered not as deformation twins but as transformation twins. $\{10\bar{1}1\}$ twins have been reported in deformed materials but they are uncommon in isolation to other faults, such as dislocations and stacking faults, which suggests they may be more aptly described as deformation assisted twins.

The q-factor, as previously discussed, is one possible variable which determines the amount of shear or shuffle the atoms undergo to produce the twin. The only $q \leq 2$ is the $\{11\bar{2}1\}$ type twin. This suggests that the twinning is accommodated entirely by shear force as shuffles are not required. Another feature of this twin is that $\boldsymbol{\eta}_2$ and K_2 are the only such twin identifiers that correspond to an observed slip plane, $\{0002\}$, and slip direction $\frac{1}{3} < 11\bar{2}0 >$. $\{11\bar{2}1\}$ are much less common than all previously mentioned twins. This is also the twin with the greatest s as seen in Figure 20, more than double that for other twins in titanium. It is possible to promote the production of such twins by compression or tension along favourable axes, such as tension from 47 – 60 ° away from the c-axis [44].

Table 4: Predicted and observed twinning modes in HCP structures.
Adapted from table compiled by *(Christian and Mahajan, 1995)*

$\mathbf{K}_1$ { }	$\mathbf{K}_2$ { }	η_1 ⟨ ⟩	η_2 ⟨ ⟩	s	q	Observed by supporting experimental studies
$10\bar{1}2$	$\bar{1}012$	$10\bar{1}\bar{1}$	$\bar{1}01\bar{1}$	$(\gamma^2-3)/3^{\frac{1}{2}}\gamma$	4	Mg, Ti, Co, Zr, Zn, and Be
$22\bar{4}1$	0001	$1,1,\bar{2},\bar{1}\bar{2}$	$11\bar{2}0$	$1/2\gamma$	4	
$10\bar{1}1$	$10\bar{1}3$	$10\bar{1}\bar{2}$	$30\bar{3}2$	$(4\gamma^2-9)/4(3)^{\frac{1}{2}}\gamma$	8	Mg and Ti
$10\bar{1}1$	i	i	$41\bar{5}3$	$(4\gamma^4-17\gamma^2+21)^{\frac{1}{2}}/2(3)^{\frac{1}{2}}\gamma$	4	
$20\bar{2}1$	0001	$10\bar{1}\bar{4}$	$10\bar{1}0$	$3^{\frac{1}{2}}/2\gamma$	4	
$11\bar{2}1$	0001	$11\bar{2}\bar{6}$	$11\bar{2}0$	γ^{-1}	2	Re, Ti, Zr, Co and graphite
$10\bar{1}\bar{3}$	$10\bar{1}1$	$30\bar{3}2$	$10\bar{1}2$	$(4\gamma^2-9)/4(3)^{\frac{1}{2}}\gamma$	8	Mg
$10\bar{1}3$	i	i	$21\bar{1}\bar{3}$	$(4\gamma^4-17\gamma^2+21)^{\frac{1}{2}}/2(3)^{\frac{1}{2}}\gamma$	4	
i	i	i	i	$(4\gamma^4-21\gamma^2+36)^{\frac{1}{2}}/4(3)^{\frac{1}{2}}\gamma$		Mg
({$10\bar{1}3$} 'double twinning')						
$13\bar{4}0$	$\bar{1}100$	$7\bar{5}\bar{2}0$	$11\bar{2}0$	$3^{-\frac{1}{2}}$	4	
$13\bar{4}1$	$\bar{1}101$	i	$11\bar{2}0$	$(4\gamma^2+3)^{\frac{1}{2}}/2(3)^{\frac{1}{2}}\gamma$	4	
$13\bar{4}2$	$\bar{1}102$	i	$11\bar{2}0$	$(4\gamma^2+3)^{\frac{1}{2}}/2(3)^{\frac{1}{2}}\gamma$	4	
$22\bar{4}3$	0001	$11\bar{2}\bar{4}$	$11\bar{2}0$	$3/2\gamma$	4	
$10\bar{1}4$	$10\bar{1}0$	$20\bar{2}1$	0001	$\gamma/3^{\frac{1}{2}}$	4	
$11\bar{2}2$	$11\bar{2}\bar{4}$	$11\bar{2}\bar{3}$	$22\bar{4}3$	$2(\gamma^2-2)/3\gamma$	6	Ti and Zr
$11\bar{2}\bar{4}$	$11\bar{2}2$	$22\bar{4}3$	$11\bar{2}\bar{3}$	$2(\gamma^2-2)/3\gamma$	6	
$30\bar{3}4$	—	—	—			
$11\bar{2}3$	—	—	—			

Notes: i denotes an irrational plane or direction. Some of the reported modes have not been confirmed and appear doubtful. For greater clarity, each mode and its conjugate are listed separately. The table includes the eleven predicted modes which have $s \leqslant 1$ and $q \leqslant 4$ for the ideal axial ratio, and also the more probable $q = 8$ modes for $\{10\bar{1}1\}$ and $\{10\bar{1}3\}$ and the $q = 6$ modes for $\{11\bar{2}2\}$ and $\{11\bar{2}4\}$.

Table 5: Crystallographic elements and parameters of commonly observed twin systems in HCP structures, particularly Titanium.
(Yoo, 1981)

K_1	K_2	η_1	η_2	S	q	s	$e/2$ η_1	$e/2$ η_2
$\{10\bar{1}2\}$	$\{10\bar{1}\bar{2}\}$	$\pm\langle 10\bar{1}\bar{1}\rangle$	$\pm\langle 10\bar{1}1\rangle$	$\pm\frac{1}{3}\langle 1\bar{2}10\rangle$	4	$\frac{\gamma^2-3^*}{\gamma\sqrt{3}}$	$\frac{\gamma^2-3^*}{\gamma^2+3}$	
$\{10\bar{1}1\}$	$\{10\bar{1}\bar{3}\}$	$\langle 10\bar{1}\bar{2}\rangle$	$\langle 30\bar{3}2\rangle$	$\frac{1}{3}\langle 1\bar{2}10\rangle$	8	$\frac{4\gamma^2-9}{4\gamma\sqrt{3}}$	$\frac{4\gamma^2-9}{4\gamma^2+3}$	$\frac{4\gamma^2-9}{4\gamma^2+27}$
$\{11\bar{2}2\}$	$\{11\bar{2}\bar{4}\}$	$\frac{1}{3}\langle 11\bar{2}\bar{3}\rangle$	$\frac{1}{3}\langle 22\bar{4}3\rangle$	$\langle 1\bar{1}00\rangle$	6	$\frac{2(\gamma^2-2)}{3\gamma}$	$\frac{\gamma^2-2}{\gamma^2+1}$	$\frac{\gamma^2-2}{\gamma^2+4}$
$\{11\bar{2}1\}$	(0002)	$\frac{1}{3}\langle\bar{1}\bar{1}26\rangle$	$\frac{1}{3}\langle 1120\rangle$	$\langle\bar{1}100\rangle$	2	$\frac{1}{\gamma}$	$\frac{1}{4\gamma^2+1}$	1

*Absolute value of the difference.

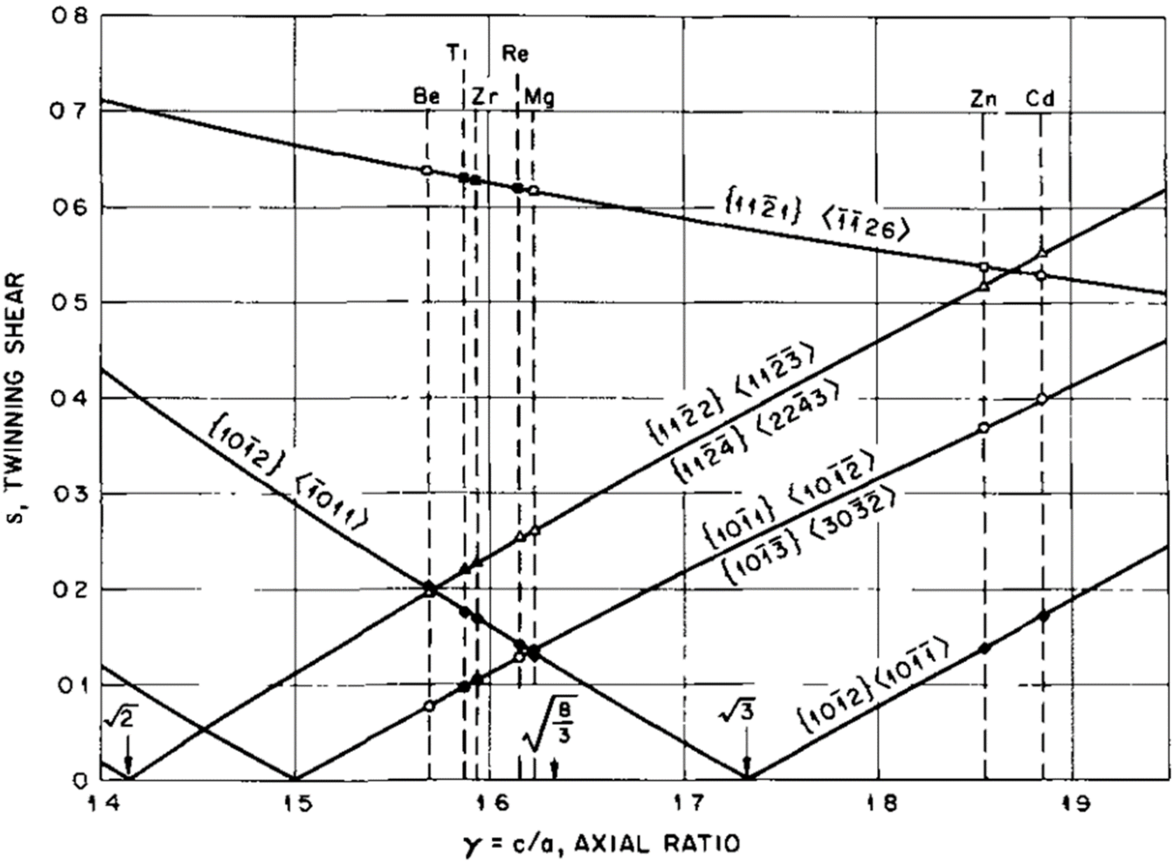

Figure 20: Variation of twinning shear with the axial ratio. For the seven hexagonal metals, a filled symbol indicates that the twin mode is an active mode.
(*Yoo, 1981*)

2.3.3 HCP Slip and Twinning

Slip and Twinning are often considered competing mechanisms. An example of which is seen in Figure 21 [33]. This quantifies the general trend that decreased temperature and increased strain rate promotes the likelihood of twinning, whilst increased temperature and decreased strain rate increases the likelihood of slip. However, the presence of dislocations from slip provides nucleation sites for twin initiation. In many cases the presence of dislocations is a necessary precondition for twinning. Increasingly higher stresses are required to produce increased amounts of twinning, although the stress required for growth of twins is much less than for twin nucleation. When twins are produced this often leads to a shielded region surrounding these twins where the dislocation density is reduced [33].

It is important to note that the total number of twins per grain is a function of stress, and independent of temperature and strain rate [45]. It is suggested that generalised plastic deformation and microplasticity are described by separate mechanisms. Twinning is associated with microplasticity – that is, dislocation activity taking place before generalised plastic deformation [46].

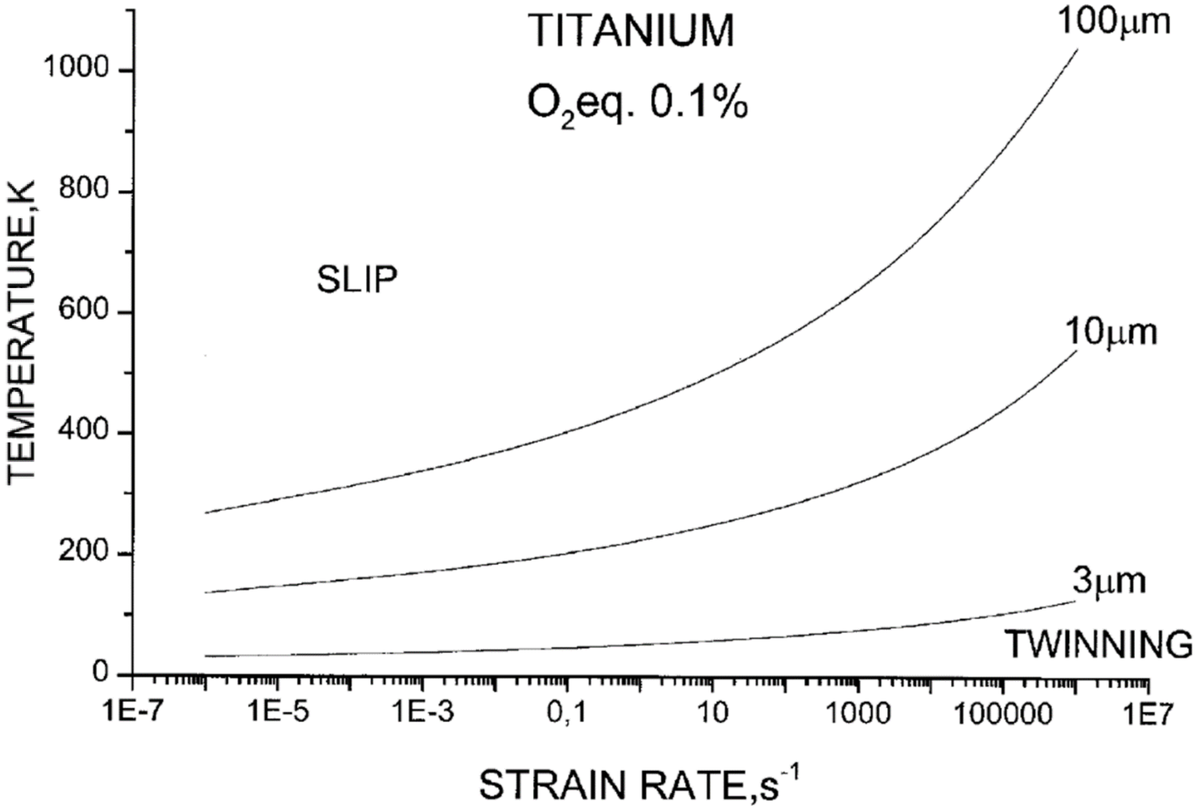

Figure 21: Calculated slip-twinning transition ith respect to temperature for titanium of different grain sizes. 0.1% Oxygen equivalent impurities.
(*Meyers, Vöhringer and Lubarda, 2001*)

2.3.3.1 CRSS and TCRSS

CRSS is the critical resolved shear stress. This is the minimum stress required to cause plastic deformation. This is usually considered in connection with dislocation production; however, we may apply a similar approach to twinning. The TCRSS is the critical resolved shear stress for twinning, defining the threshold stress above which a twin is produced. Dislocations of different types have different CRSS values. This is the same with twinning types. As all twins are dependent on compression or tension angle relative to the c-axis, all twin types must be assessed independently. This differs from dislocations in the material response to compression or tension. Dislocations move in the opposite sense when the applied stress is reversed. Twinning has a definite sense in which it shears, is heavily dependent on texture and may not form at other compression angles [33]. Due to these complications, the literature makes many simplifications in attempting to deduce such values, with a number of studies assuming polycrystalline microstructures, negating the textured response of crystals entirely.

Experiments by Salem *et al.*, [47] assessed the strain hardening responses of α-titanium in simple compression, plane-strain compression and simple shear (Figure 22). Coupling this with micro-graphical data, we can see what stresses allow for slip and what allows for twinning by assuming the onset of various deformation mechanisms with changes in the strain hardening response after experimental studies have verified the presence of dislocations and twins in these different regimes. Wu *et al.*, [48] uses this experimental data as the basis for predicting texture evolution based on previous techniques and assumptions. Leading methods include: 1) Predominant twin reorientation where twinning is treated as a pseudo-slip mechanism, and the twin volume fraction is tracked in each grain. Total number of possible grain orientations are constant; 2. Volume fraction transfer, using weighted bins of orientations, where the weights are modified to represent the changes caused by twinning; 3. Total Lagrangian approach, a complex method expanding upon Lagrangian crystal plasticity frameworks, previously validated for study of slip. This is useful as it can account for the relationship between slip and twinning in deformation. However, this is numerically cumbersome, particularly in the study of HCP metals relative to their cubic counterparts. Studies such as those by Qin *et al.*, [49] use these conclusions to compare back to experimental results to determine the critical strain for twinning in order to engineer ideal microstructures.

It is seen in Table 6 [48] that prismatic $< a >$ slip has the smallest barrier, whilst this is much greater for pyramidal $< c + a >$ and basal $< a >$ slip. The TCRSS for the simple common twin types $\{11\bar{2}2\}$ and $\{10\bar{1}2\}$ are similar to the CRSS of pyramidal $< c + a >$ and basal $< a >$ slip. Looking at Figure 22, predictions for slip were made by fitting the stage A of the strain hardening plot and the stress-strain curve in simple shear (where twinning is not significant). Slip-twin hardening parameters were determined by fitting stage B of the hardening plot where strain hardening rate increases (and is determined to be due to the increased twin volume fraction). The determination of the initial resistance for twinning was given by the beginning of stage B on the strain hardening plot in simple compression. As this data is empirically obtained, this has not been extended to other less common twin types, such as $\{11\bar{2}1\}$ or $\{11\bar{2}4\}$, and as such no TCRSS value for $\{11\bar{2}1\}$ has been reported. This would be more challenging as it is not a commonly produced twin type.

Figure 22: Normalised strain hardening responses of α-titanium in simple compression, plane-strain compression and simple shear.
(*Salem, Kalidindi and Dohery., 2003*)

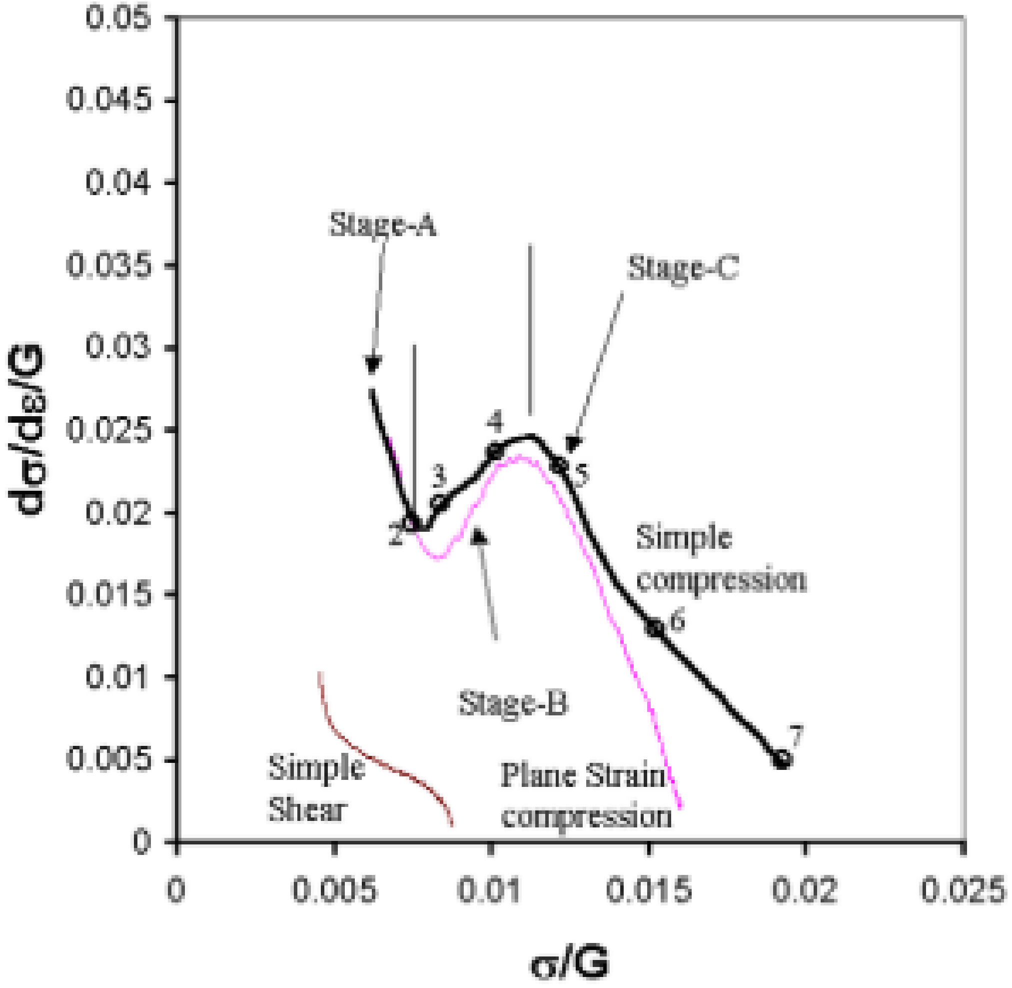

Table 6: Main slip and twinning systems in titanium.
(*Wu et al., 2007; Qin et al., 2014*)

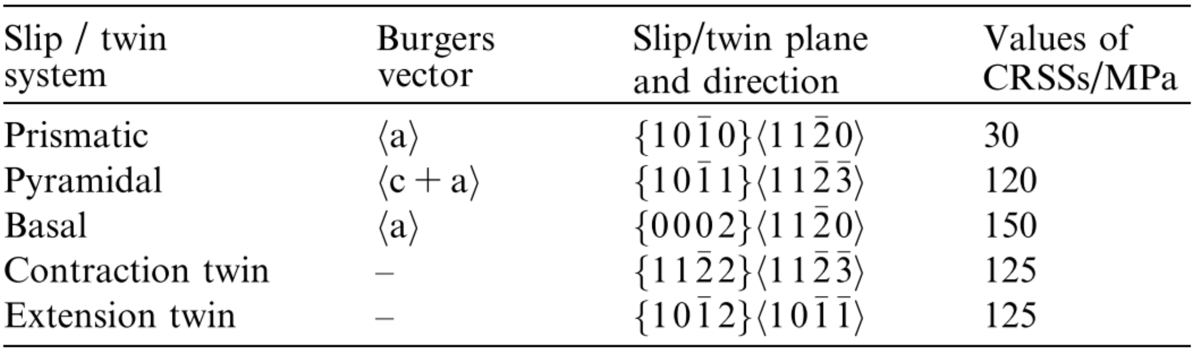

Slip / twin system	Burgers vector	Slip/twin plane and direction	Values of CRSSs/MPa
Prismatic	⟨a⟩	$\{10\bar{1}0\}\langle 11\bar{2}0\rangle$	30
Pyramidal	⟨c + a⟩	$\{10\bar{1}1\}\langle 11\bar{2}\bar{3}\rangle$	120
Basal	⟨a⟩	$\{0002\}\langle 11\bar{2}0\rangle$	150
Contraction twin	–	$\{11\bar{2}2\}\langle 11\bar{2}\bar{3}\rangle$	125
Extension twin	–	$\{10\bar{1}2\}\langle 10\bar{1}\bar{1}\rangle$	125

2.4 Shock-wave Responses

2.4.1 Shock-wave Responses of Materials

A brief explanation of a shock wave, is a discontinuous change of state, such as a change in pressure, density or temperature, which propagates through a material [50]. This is a common occurrence when a material is impacted with projectiles, or through physical or chemical detonations of part of the material itself. The LS procedure generates a shock wave from the expansion of laser heated plasma either on (LSPwC) or close to (Coated LSP) the target surface.

A material under shock compression may be described according to a number of equations of state such as through conservation of energy, mass and momentum. These relate the pressure, P, density, ρ, Energy, E, velocity of the source projectile, v_p, and the velocity of the resulting shockwave v_s. Combining the equations of state allows us to establish a pressure-volume relationship, where:

$$P = \frac{C_0^2 (V_0 - V_1)}{[V_0 - S(V_0 - V_1)]^2} \tag{5}$$

where C_0 and S are constants that relate the projectile velocity to the shockwave velocity in the form $v_s = C_0 + S\, v_p$. This $P - V$ equation is valid assuming a one-dimensional pressure state. Proceeding in the uniaxial strain regime, the theoretical value of the Hugoniot elastic limit (HEL) may be obtained by resolving Hooke's laws and applying the von-Mises yield criterion where $\sigma_x - \sigma_y = \sigma_Y$ (longitudinal stress in y minus longitudinal stress in x is equal to the yield strength). The resulting equation is as follows:

$$\sigma_{HEL} = \frac{1-v}{1-2v} \sigma_Y \tag{1}$$

where υ is the Poisson's ratio and σ_Y is the yield strength (Equation 1, as seen in section [2.1.2.1.2 Power and Power Density]) [51].

This description is flawed for multiple reasons. Firstly, there is significant challenge in ensuring conditions for uniaxial strain. Many shock loading experiments, such as the Hopkinson-bar and other gas compression methods, are designed to mimic this one-dimensional strain regime. In the case of general compression or tensile testing, or in the case of laser shock loading, we are instead much closer to conditions of one-dimensional stress. Next, the Hugoniot curve as labelled in Figure 23 [51] assumes the material response to the shockwave will not change over time (curve 1, which shares the trajectory of the Hugoniot curve with a small displacement to account for elastic strain). In practice, materials sometimes soften (curve 2), and in most cases they harden (curve 3)[51]. Another reason is that even after the rapid increase in stress to the HEL, another linear increase is found which reaches the incident shock-wave pressure. This shock-wave discontinuity is due to the trailing part of the shock-wave which travels marginally faster than the front of the shock-wave which encounters more resistance from the localised pressure and density. This is described according to the Rayleigh Line, intersecting a stress-strain curve (Figure 23, curve 1) at the HEL and the localised shock-wave pressure. When the trailing part contracts onto the leading part, this creates the strong peak pressure of the shock-wave [52]. A comprehensive description of shock-wave mechanics can be found in *Dynamic Behaviour of Materials*, by M. A. Meyers [51]

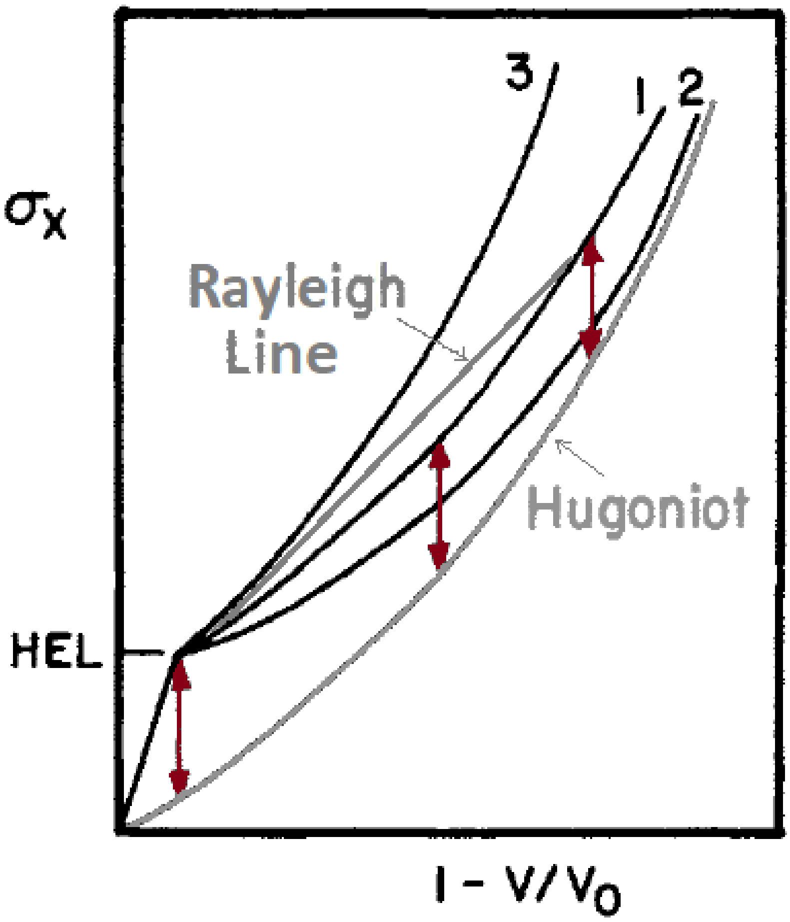

Figure 23: Theoretical stress-strain curve for material undergoing shock deformation. The Hugoniot is active from the point of plastic deformation. As such, the Hugoniot curve offset in stress by the Hugoniot elastic limit (HEL), as seen in curve 1. Curves 2 and 3 represent a softening and hardening of the material as a response to shock compression, respectively.

(Adapted from *Dynamic Behaviour of Materials, Chapter 4* by M. A. Meyers, 1994)

2.4.2 Shock-wave Responses of HCP Titanium

A summary of the responses of common metallic crystal structures can be found in Ch.5 of *Materials in Mechanical Extremes*, by N. Bourne [53]. Many HCP materials, namely Ti, Zr and Hf, under shock or hydrostatic loading conditions are sometimes found to induce a phase transformation from α (hexagonal close packed) to ω (simple hexagonal) [54,55] . The conditions conducive to these changes are well characterised, often via modelling, based on temperature, pressure and in some cases alloying elements. [55–60]. Other contributions, as proposed by *Sikka, Vohra and Chidambaram* [55], are the pre-shock microstructure, and the hydrostatic nature of the pressure experienced by the sample. The commonly reported orientation relationship (OR) between the two phases are variant I, with $(0001)_{\alpha}||(01\bar{1}1)_{\omega}$ $[\bar{1}010]_{\alpha}||[\bar{1}011]_{\omega}$, and variant II, with $(0001)_{\alpha}||(11\bar{2}0)_{\omega}$ $[11\bar{2}0]_{\alpha}||[0001]_{\omega}$ [61].

Measurements of shockwaves through materials are studied through a VISAR (velocity interferometer system for any reflector). After a shock event of a material, the measurement of free surface velocity over time is taken. The graph demonstrates a constant gradient for a given sample phase with increasing incident pressure. When an inflection occurs on the graph, a phase transformation may be noted (Meyers, Ch8 [51]). If the phase transformation is stable, the sample may be sectioned and analysed through EM techniques such as EBSD and TEM, or through other diffraction methods, to ascertain the proportion of the new phase(s).

In the case of pure Ti, the peak pressure found to induce the α-ω phase transformation was found to be approximately 10 GPa through modelling [62]. This is different from Ti-6Al-4V which in the same study does not observe this α-ω phase transformation. One variable found to have considerable influence over this value is the oxygen content of the material. For high purity titanium (HP Ti) of O < 80 ppm and O = 360 ppm, the α-ω phase transformation occurred at 10.1 GPa [63] and 10.4 GPa [61] respectively. In these studies, ω-phase was retained to 65 % (via EBSD with poor hit-rate giving a large margin for error) and 28 % (reliably understood through neutron diffraction), respectively. If we take these values at face value, this demonstrates the significant influence of Oxygen on the phase transition not only in the increase in transition stress, but also the reduction in retained ω-phase.

The atomic radius of Oxygen is 0.65 Å, matching closely to the octahedral interstitial site of space 0.61 Å, as opposed to the tetrahedral site with space 0.33 Å [64]. As the octahedral interstitial site is marginally smaller than the atomic radius of oxygen, this causes internal stress in the HCP lattice. This raises the stress requirement of the α-ω phase transformation. This means that commercially pure titanium (CP Ti), and many other higher alloy content variations, are not readily seen to undergo the α-ω phase transformation when under shock conditions, even up to 35 GPa [61,63]. Some alloys still allow for the α-ω phase transformation, such as in Ti-10at.%V [58].

2.5 Techniques to measure the effect of LSP

Many attempts have been made to accurately characterise the changes made as a result of LSP. Different methods are applied depending on the nature of the test material, and the type of test component that has been improved via the shock processing, such as complex geometries, weld zones, or pre-fatigued specimens. Most techniques can be classified under three different general types:

1. Diffraction-based methods. These are useful because they are able to provide residual stress and strain data without compromising the sample integrity. Diffraction techniques often make sample preparation on the required area more challenging, and the information is limited to elastic strain.

2. Imaging. Many initial assessments can be made through imaging with optical microscopy, with further study being performed through advanced electron microscopy techniques. This provides greater understanding of microstructural changes and can provide answers for the mechanical response of materials after LSP. Often, however, these results are subjective and require detailed analysis.

3. Mechanical testing. This provides reliable understanding of components in industry-applicable environments, allowing us to assess the benefit of LSP to material properties. Although these tests are often cheaper to perform, time is required to manufacture test pieces and use large quantities of material. This increases processing time. Apart from some small localised deformation methods, mechanical testing procedures are destructive. Therefore, components are not usually able to be used in service environments post-testing.

Combining these different methods can enable us to understand the changes LSP makes to materials and develop a mechanistic understanding that enables us to, in the future, relate the LSP processing parameters to the mechanical response in the service environment. A table to summarise the methods discussed can be seen below.

Table 7: Summary of technique advantages and disadvantages.

Method	Description	Advantages and Disadvantages	Literature
1. **Diffraction**		+ Non-Destructive + Data analysis is quantitative - Measures elastic strain only - Usually requires surface preparation	[65]
EBSD (+TKD)	Uses Electron diffraction to test for misorientation and strain	+ Automation and analysis tools readily available + High Resolution - Greater surface preparation required - Poor penetration depth	[40,66–70]
XRD	Uses X-rays to test for strain	+ Easy to perform + Low cost - Limited sample size - Poor spatial resolution	[66,68,71,72]
HE XRD + Synchrotron	Uses High energy X-rays to test for strain	+ Good Penetration + High resolution + Depth profiling - Special facility required with limited availability - High Cost	[10,73–75]
Neutron Diffraction	Uses Neutrons to test for strain	+ Excellent penetration + Good resolution + 3D Mapping - Special facility required with limited availability - High Cost - Samples may become radioactive (hot)	[73,76,77]

2. **Imaging**		+ Studied area is non-destructive + Much more information may be acquired - Limited volumetric understanding (maximally 300 nm) due to poor penetration depth - Analysis is largely subjective	
OM+SE	Provides imaging using visible light photons and secondary electrons, respectively	+ Extremely easy + Low financial and time cost - Only able to provide qualitative stress analysis, and only in limited situations	[72,78,79]
Optical Profilometry	Uses visible light variation to measure topography	+ Low time cost - Limited residual stress analysis capability	[66,80]
BSE / ECCI	Images using the channelling effect of backscattered electrons	+ Can provide initial information with low time + High special resolution - Some sample preparation required - Comprehensive analysis can take time	
TEM + related	Images using transmitted electrons and provides diffraction-based contrast.	+ Very high special resolution + Specific understanding of microstructure and mechanisms of residual stress may be obtained. - Image acquisition and analysis require extended time - Sample preparation also requires time	[26,29,71,79,81,82]
3. **Mechanical Testing**		+ (generally) cheaper to perform + Direct measurement of mechanical properties, useful for industrial application - Destructive (sometimes only locally) - Often requires manufacture of specific test-pieces, extending time required	
Indentation	Utilises hard indenter to obtain Hardness	+ Low sample destruction (negligible on nano scale) + Quick and easy - Limited mechanical property acquisition	[27–29,31,32,83]

Compression	Measures compressive stresses over given strain	+ Provides information on multiple mechanical properties + Easier than tensile tests (particularly when compared to micro-scale tensile testing) - Test-pieces require manufacturing (testing not applied directly to component)	[67]
Tensile	Measures tensile stresses over given strain	+ Highly relevant for components where compressive stress is desirable due to being able to obtain yield strength, UTS, strain hardening and more information. + Provide information on multiple mechanical properties - Test-pieces require manufacturing (very challenging on micro-scale) - Equipment cost can be greater, depending on specific method chosen.	[31,81,82,84–86]
Fatigue	Measures cycles to failure over given loading regime	+ Highly relevant for components where compressive stress is desirable - Test-pieces require manufacturing (testing not applied directly to component)	[27,28,84]
Strain Gauge testing (and similarly principled techniques)	Measures release of residual stress after material removal.	+ Cheap to acquire all necessary equipment and perform + Direct mapping of residual stress + Can be performed at different scales, including use of FIB - Highly destructive	[2,30,40,87]

2.6 LSP Influence on Microstructure

Some microstructural analysis has been performed on a variety of materials. Many alloys used in aerospace have been studied, such as 2195 aluminium lithium alloy [5], and magnesium alloys AZ91D [88] and AZ31B [89]. Various stainless steels, due to their applicability to high fatigue environments, are useful in the automotive and nuclear industries [69,70,72]. There has been an increasing amount of study of titanium alloys [26,29,30,66,90–98], with many focusing on Ti-6Al-4V [40,71,99–102] due to their wide variety of applications across industry. More research is emerging on characterisation of laser peening strengthening mechanisms with commercially pure titanium [79,86] and pure titanium [103,104] as its focus. Some involve novel processing forms such as in the cryogenic regime (CLSP) of TC6 Ti Alloy [92] and pure titanium [103].

A widely acknowledged structure outlining the microstructural evolution of materials subjected to LSP can be seen in [70]. There are some differences regarding the number of shots required to induce the relevant microstructural changes, but this can be explained by the different mechanical properties of unprocessed components, the alloys used and the variation in processing techniques. For example, Lainé *et al.* [40] produced nanocrystalline features after 3 shots; few changes were visible in Zhou *et al.* [71] until 5 shots despite both studies being on Ti-6Al-4V. Nie *et al.* demonstrated that artifacts generated in TC11 titanium alloy from 2.83 GW cm^{-2} laser shocks displayed less progression towards nanocrystallisation (see Figure 24) than those generated from greater power densities of 4.24 and 5.66 GW cm^{-2} [30]. Hence, grain refinement increases with the amount of laser energy injected into the material [29].

In the initial stages of shocking (typically 1 - 2 impacts) the wave propagation causes dislocations at the wave front. These tend to follow specific directions, and are described as planar dislocations, also termed dislocation lines [40], characterised by repetition along successive planes whilst observed in a direction approximately perpendicular to these planes. If the dislocation density is great enough, these may concentrate and tangle. Further into the sample the wave propagation can lose some direction and the dislocations are more evenly spread around the plastic zone. Additional peening (2 - 4 shocks) increases the quantity of dislocations, producing dislocation tangles. The increased energy can allow tangles to collect into dislocation walls, leading to the formation of dislocation cells. An example of a dislocation cell can be seen in Figure 25 from [90], which appears to have been created with the right wall formed from a pre-existing grain boundary, and the left wall forming from dislocation tangles. When the dislocation density at the boundaries is great enough, the cells form into sub-grains. The sub-surface depth of dislocation lines and walls increases. After further laser shocks (3 – 5, sometimes many more) remaining dislocation cells are broken down into sub-grains and subsequent nanostructures. Successive shocks will further the grain refinement process, however there may be additional effects which are undesirable [12]. As the strain rate decreases below the surface, from potentially 10^7 s^{-1} to zero in the strain-free matrix, the structure evolution process should be described by the microstructural characteristics at different depths [79,87,105].

In addition to the widely reported dislocation tangles and dislocation cells reported in literature, some also highlight the presence of deformation twins (such as [26,79,100,106]). Jia *et. al.* and Pan *et. al*. report the presence of dislocation arrays [91,99], which constitute dislocations forming in bands which can be argued to constitute stacking faults. Li, Jia and Ji reports twinning arrays on the nano-scale [107], which constitutes fine twins that form parallel to each other, often within a pre-existing twin, or thin (> 200 nm) lamella boundary.

As the majority of LSP induced features are on the micro to nano scale, most material referenced has involved transmission electron microscopy (TEM). Residual stress measurement by x-ray diffraction (XRD) is also common (see Table 7 for references). An example of the microstructural progression is seen in Figure 26, which shows Ti-6Al-4V post LSP after increasing number of shocks [71]. After a single shock (Figure 26a), dislocation lines can be found particularly distinguishable in the HCP-α phase, with a higher density of dislocations in the BCC-β, forming tangles. Following 3 shocks (Figure 26b), the dislocation density of the β grains has increased, with α grains beginning to show mechanical twinning. The number of twins increases when increasing the number of shocks to 5 (Figure 26c), with dislocations concentrating at twin boundaries. After 10 shocks (Figure 26d), sub-grain boundaries have formed, with features 200 - 300 nm wide. There are extremely dense dislocation tangles in the β and α phases, with substantial apparent grain refinement in the α grains. The dislocation tangles have been pinned by phase and grain boundaries.

A point of interest in Figure 26 is the difference between the dislocation concentration and mechanical twin density between the α-HCP and β-BCC phases. The abundance of dislocations in the β titanium is due to the high stacking fault energy (SFE), which allows dislocations to adequately accommodate the induced strain, and that BCC structures contain many more slip systems when compared with other crystal structures. The HCP structure contains only 4 primary (and easily available) independent slip systems, which, in line with the von-Mises rule, makes it more difficult for the structure to accommodate the plastic strain through dislocations alone; it must then accommodate this strain through mechanical twinning. Hence, it can be concluded that the evolution described by Lou *et al*. in Figure 24 is likely limited to high SFE materials.

It is also claimed by various authors that LSP limits the potential for twinning. Experiments reported in Lainé *et al.* [40] demonstrate that ultrahigh strain rates (> 10^6) did not induce mechanical twinning whereas high strain rates ($10^3 – 10^5$) (from [metallic] shot peening) did. It is suggested that the ultrahigh strain regime allows for high-speed dislocations to accommodate strain. In the case of Zhou *et al*. [71], no mechanical twinning was observed after the first shock, and only subsequent shocks induced twinning. This twinning was only induced in the Low SFE HCP α phase. Lainé *et al.* did not apply additional shocks to the samples.

It is commonly accepted that grain refinement induced by successive LSP treatments are due to dislocation evolution [70,88]. Twinning in low SFE materials provides additional sub-division of grains. It is also noted, however, that the grain refinement produced by LSP may not provide enough misorientation to produce different grains [40]. Luo *et al.* adds that an amorphous layer (as demonstrated via SAED patterns, Figure 27C [29]) produced in TC11 Ti-alloy was only 10 nm thick and was the result of fast heating and cooling of the alloy during the LSP process. This does not discount the SAED from Figure 27A, which demonstrates nanocrystallisation for up to 350 nm from the surface.

To fully understand the impact of the ultra-high strain rate introduced by LSP and to uncover the underlying mechanisms, it is essential to identify the various resultant microstructural features - the dislocation evolution, twin production, and potential nano-crystallisation. The existing literature focuses on research on LSP in relation to improvement of component performance. This often discusses pre-processed alloys with small initial grain sizes, which influences the shockwave progression through reflection and refraction of the shockwaves by grain boundaries. LSP of larger grains may exhibit slightly different results and be of interest as this will remove many other variables when attempting to map the direction of the shockwave progression through the crystal.

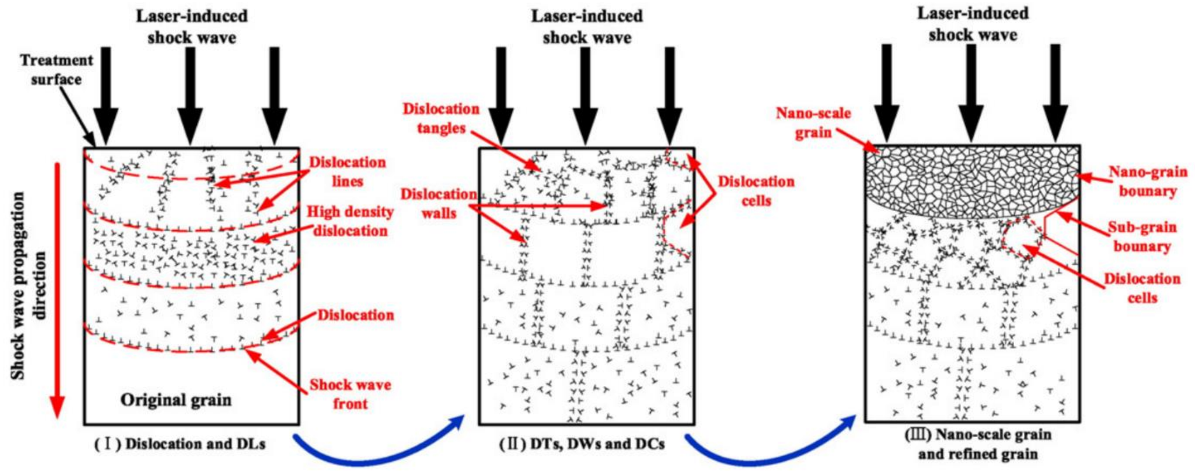

Figure 24. Schematic illustration showing progressive microstructural evolution after multiple laser shocking of the high stacking fault energy TC6 titanium alloy resulting in nanocrystallisation.
(Lou et al., 2016)

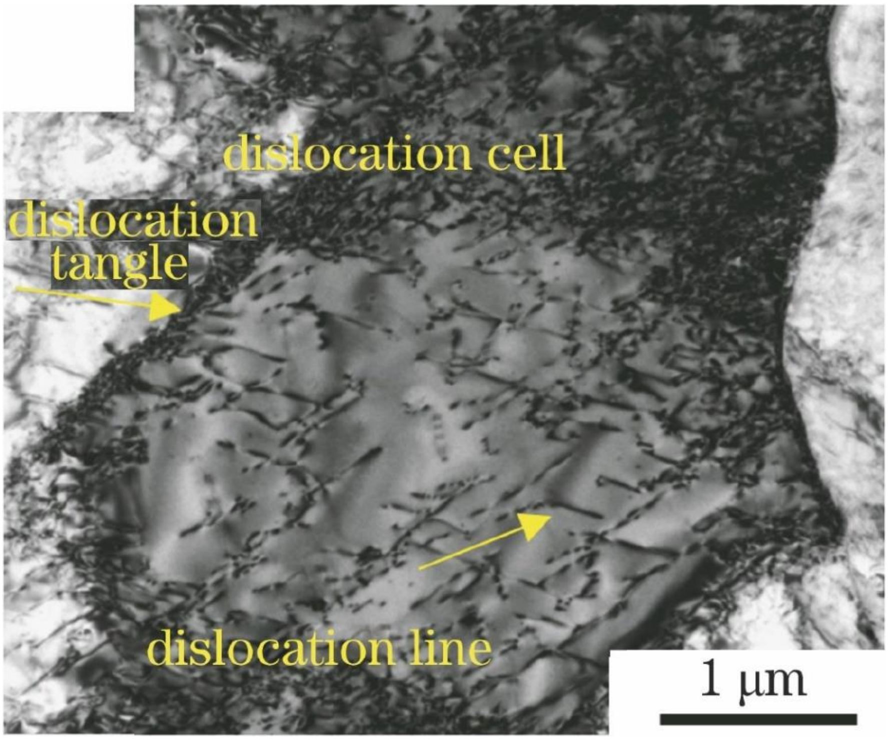

Figure 25: Features found in Ti-6Al-3Nb-2Zr-1Mo Titanium Alloy after LSP (Power Density of 4.95 GW cm^{-2}, 50 % Overlap). This shows a dislocation cell, which appears to be bounded on the left with dislocation tangles, and on the right with a grain boundary. Many dislocations are seen inside the cell, at a lower density than the boundary tangles.

(Gaoli et al., 2022)

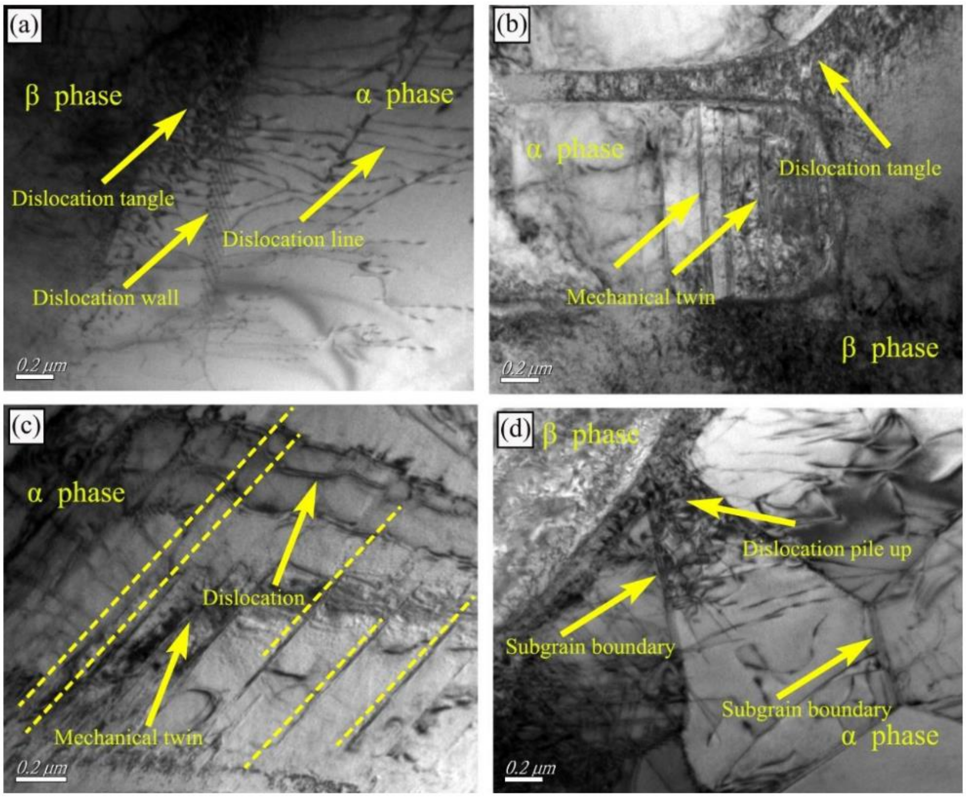

Figure 26. TEM images taken after a)1 b) 3 c) 5 and d) 10 laser impacts on Ti-6Al-4V.
(W. Zhou et al., 2016)

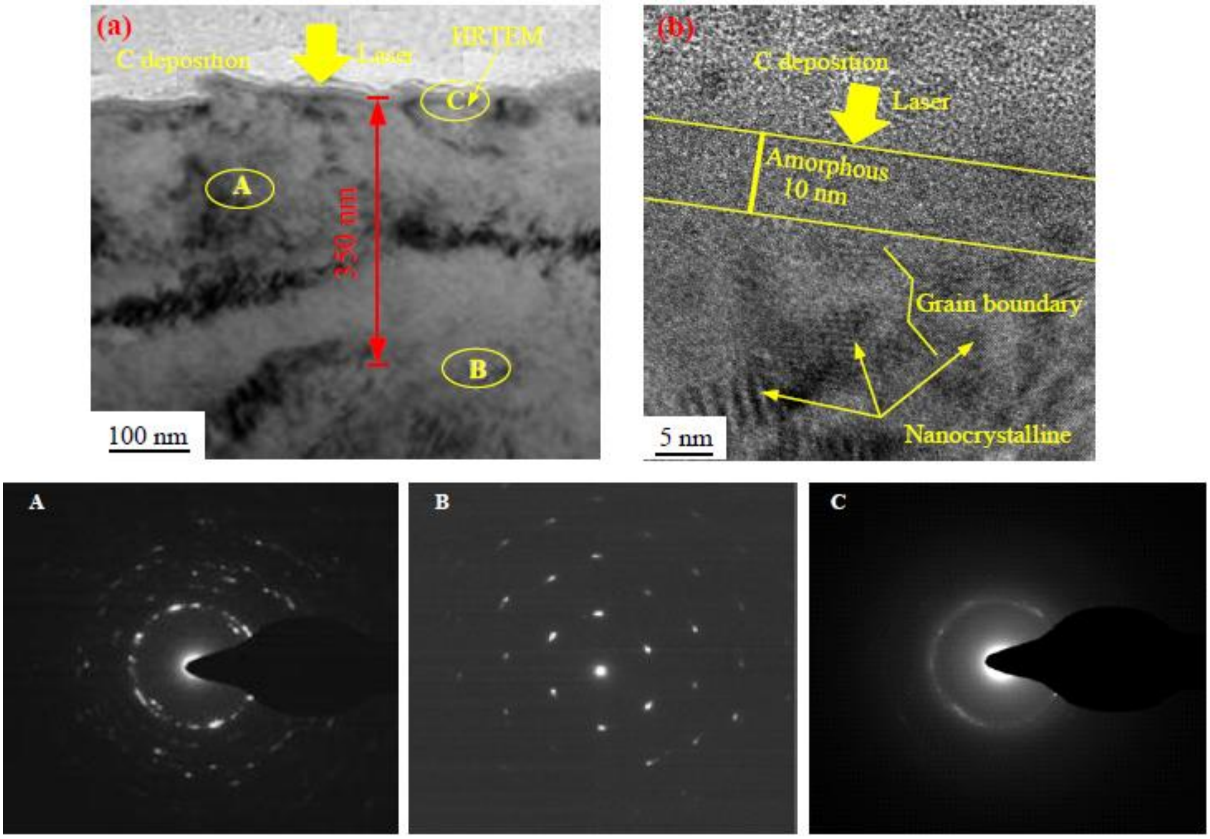

Figure 27: HRTEM and corresponding SAED patterns of different regions (A) heavily affected region (B) unaffected region (C) nanocrystalline region.
(Luo et al., 2018)

3 Methodology

3.1 Preparation of Laser Shock Peened Samples

3.1.1 Chemical Composition and Heat Treatment

A 9 mm x 9 mm x 53 mm block of commercially pure titanium (Ti-0.1Fe-0.1Al-0.1Si wt%) was heat treated via homogenisation at 1050 °C for 14 hours, and two holds at 880 °C and 825 °C for a total of 12 hours. The aim for this was to hold just below the α-β transus temperature of 882 °C [108]. There were later holds to mimic slow cooling, with final furnace cooling taking place from 750 °C. This treatment is depicted in Figure 28.

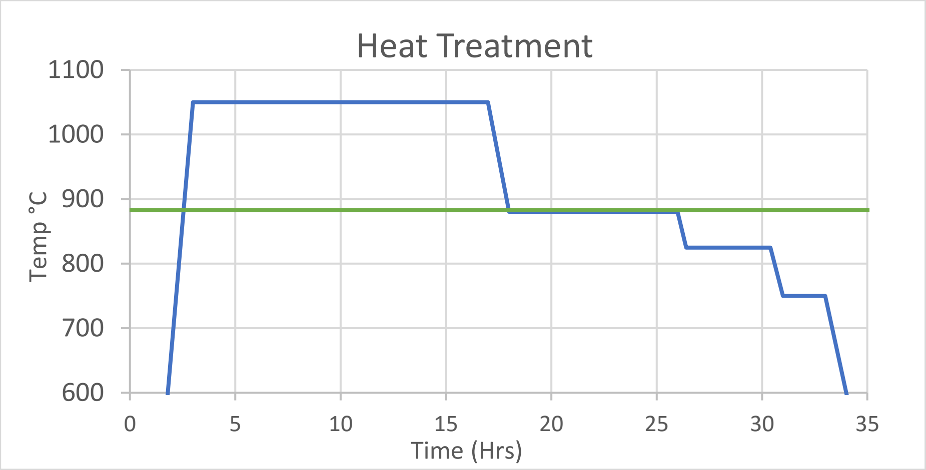

Figure 28: Heat treatment applied to Titanium before LSP.

3.1.2 Surface Preparation

This sample was lightly ground and polished with SiC paper of 1200 grit before being electropolished at 40V in a solution of 5% perchloric acid, 35% butanol and 60% methanol for 30s at room temperature.

After electropolishing (Figure 29a), electron backscattered detection (EBSD) was performed over the sites selected for the LSP study. This was used to study the microstructure before LS processing. The locations of the laser spot sites can be seen in Figure 29c, overlayed onto a stitched SEM backscattered electron image. This also shows the location of where TEM specimens were taken to study the pre-deformed material and verify the heat treatment removed existing deformation.

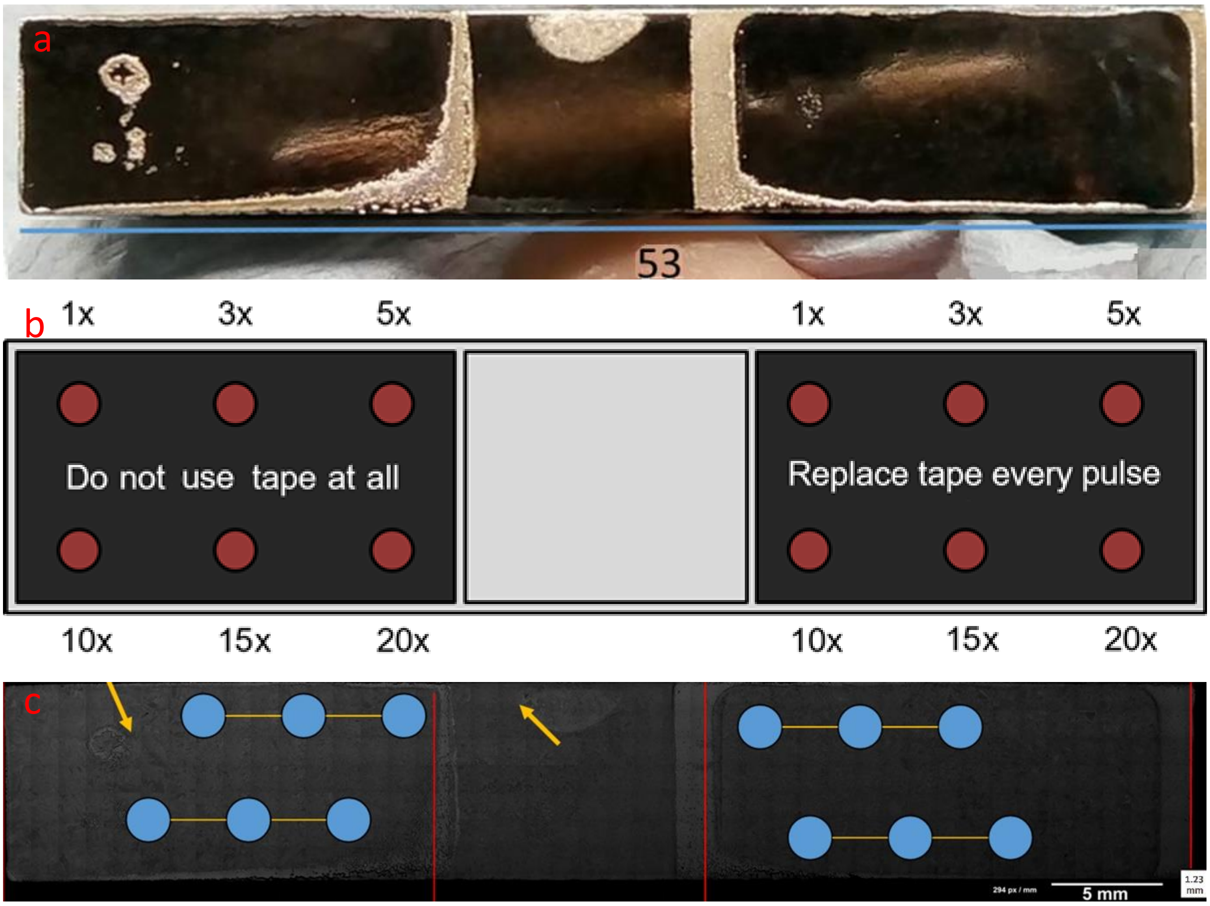

Figure 29: a) Optical image of CP Ti after electropolishing. b) Schematic describing CP Ti sample and intended LSP routine. c) SEM image with overlayed LSP site locations in blue. LSP spots are 2 mm in diameter, separated with 3 mm yellow lines. Orange arrows indicate TEM specimen locations for unprocessed testing. Red lines indicate separate electropolishing sites.

3.1.3 Laser Shock Processing

Laser Shock Peening was performed at *The MTC Coventry* using a *Litron LPY* 2 J laser operating at 1064 nm. The circular spot size was set to 1.5 mm diameter with pulse duration of 10 ns giving a power density of 11.32 GW/cm^2. The water confining medium was made to pour with a laminar flow of thickness 2-4 mm. The material was shocked in the locations indicated from 1 to 20 shocks, with the left side undergoing LSPwC and the right side undergoing LSP with a 160 µm PVC tape coating, which was replaced after each shock for consistency. This is schematically described in Figure 29b.

Images and schematics of the LSP process can be found in Figure 30. The laser beam exits the laser with a circular beam of diameter 25.4 mm (1”). This is converged using a lens, which focuses 234 mm away, leading to a beam between 1 and 2.5 mm, with a footprint between 2 and 5 mm depending on the target. The real size of the beam is therefore challenging to determine, even with the use of burn paper.

The sample was housed in a container of water held by clamps on a stand. This also held a smaller container that regulated the water flow rate and ensured a laminar flow over the shock site, filled by a recirculation pump. The sample itself was, depending on the experiment, covered with black PVC tape after glue on the region in contact with the surface was removed using alcohol, and a silicone mask was placed on the outside with coloured markers indicating the x and y co-ordinates marking the pre-determined shock sites. The laser was aligned according to a guidance beam and by eye, which was able to provide an accuracy to well within 300 µm. For safety considerations, the user may not attend the laser during operation; the sample was moved to perform the shocking on different sites. This was simple enough for LSPwC, however as the ablative layer was re-applied between shocks, there are possible minor errors associated with the position of these successive shocks even if care was taken to keep the sample position constant. Further testing regarding ablative materials and the optimal focal distance was performed and can be found in [*Appendix, 8.1 Experimental procedures carried out in MTC*]. A summary of the data can be found in Table 8.

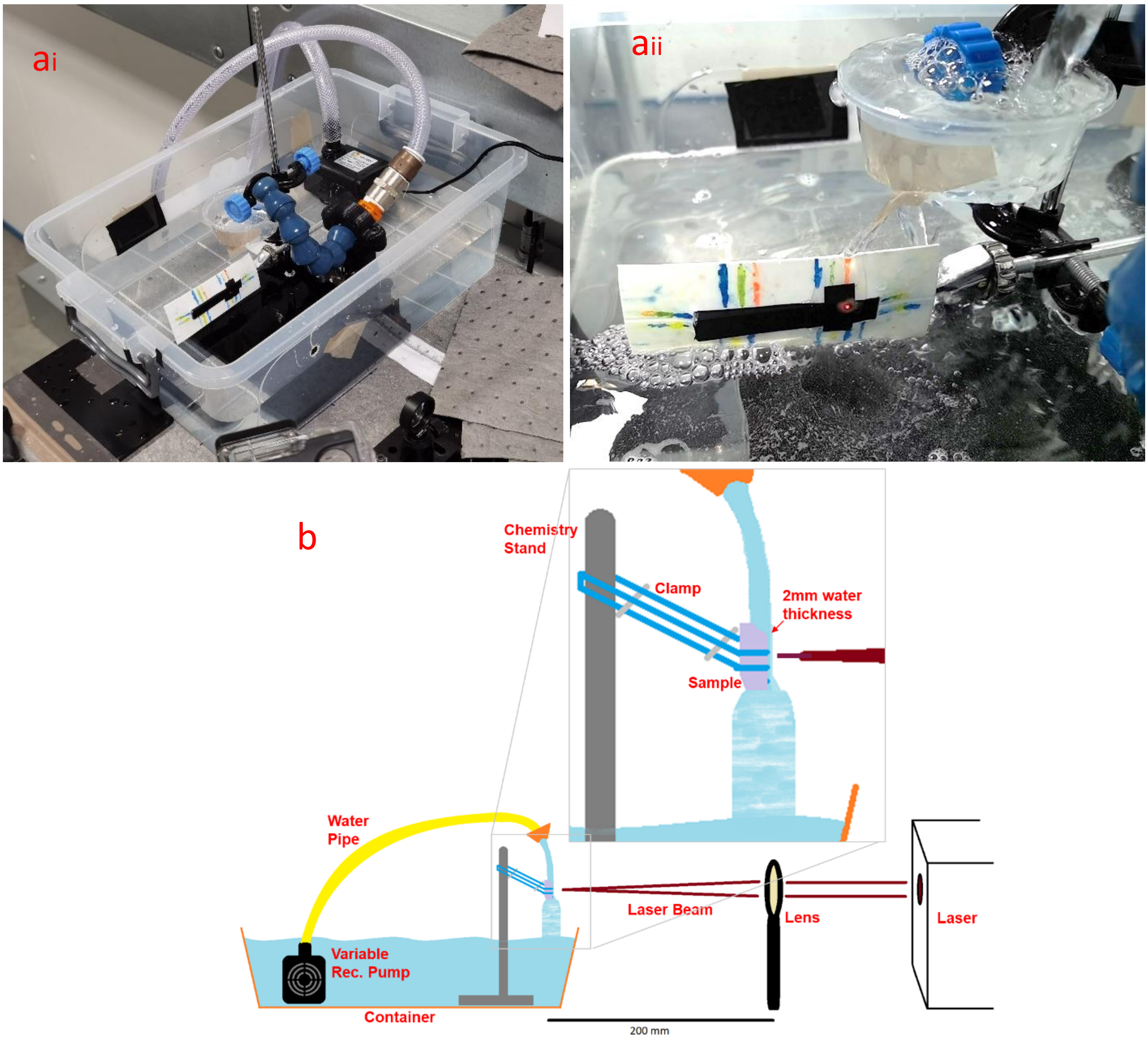

Figure 30: Experimental setup a) images showing the equipment used i) without and ii) with the confining water layer, and b) a schematic of all pieces required for use.

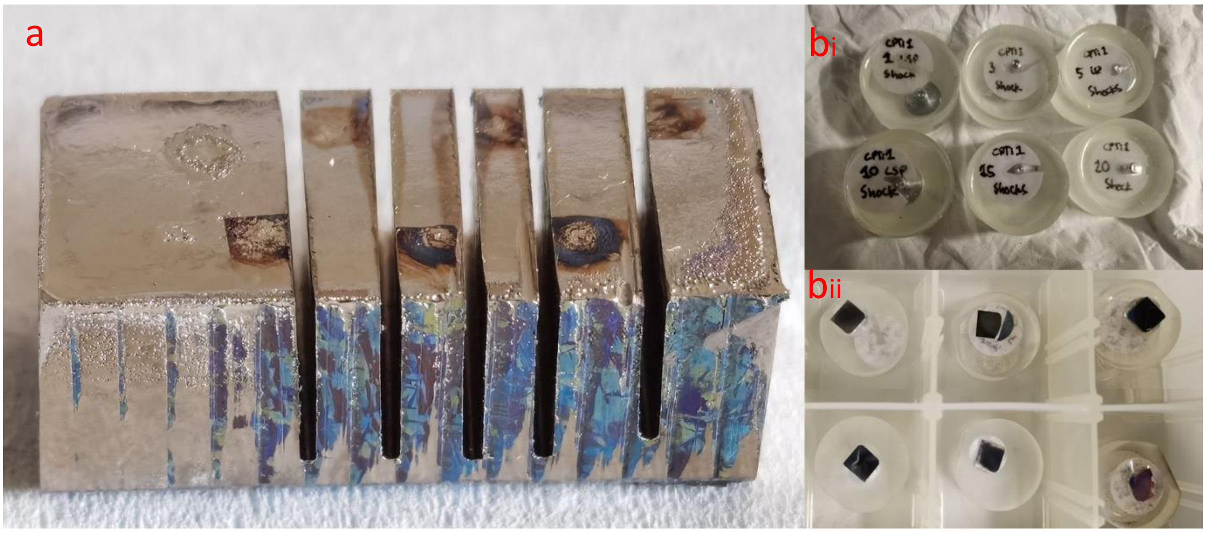

Figure 31: Laser shock peening sample a) during cross-sectional cutting and b) after cutting and mounting in transparent resin, i) bottom, labelled view and ii) surface view.

Table 8: Compilation of laser parameters used in this study.

Parameter	Default	Unit	Detail
1 Laser			
Dwell Time	5 to 10	s shock^-1	Time between laser pulses (per shock)
Power	2	J	Laser Energy
Power Density	~11.32	GW/cm^2	Power / (Pulse Duration x Area)
Pulse Duration	10	ns	FWHM of Laser Pulse
Repetition Rate	~0.3	s^-1	How often laser shocks occur
Spot Diameter / Length	~1.5	mm	Spot Size
Spot Shape	Circular		Can use mask to change shape
Temporal Pulse Shape	Gaussian		Shape of the laser energy profile
Wavelength	1064	nm	Laser operating wavelength
2 Material Choice			
Ablative Layer	Tape		Opaque layer to absorb laser energy
>Thickness	160	um	Measured via optical microscopy
Confining Medium	Water		Transparent ovelay
>Thickness (approx)	2 to 4	mm	Water thickness is uncontrolled
Substrate / Target	Titanium	99.5+%	The material to be processed
3 Practical Parameters			
No. of Laser Shocks	1-20		
Overlap	N/A	%	Distance between pulses / diameter
Material Geometry	Bulk Specimen		
Material Thickness	9	mm	

3.2 Procedure after laser shock peening

The surface profile was imaged using a *Sensofar S mart* optical sensor using white light interferometry for precise surface measurements before and after LSP. Although the protected side showed little to no visible changes, the LSPwC demonstrated significant changes. The step size for the optical profilometry was 1.4 µm, with a vertical resolution of 5 nm. This enabled extraction of surface roughness parameters and quantified the lower hit-rate for severely shocked material. This reduction sometimes occurred due to the colour change induced after oxidation of the material surface post-processing.

EBSD was repeated on the same regions for the right side protected by tape under the same conditions. There was enough protection to prevent major loss of EBSD signal on the surface. The left-hand side (without protection) underwent thermal changes which prevented electron diffraction techniques from picking up any signal. EBSD was therefore repeated on the right (tape-protected) side and ignored on the left (unprotected) side.

The following work pertains only to the left side where LSPwC was performed. The sample was cut cross-sectionally, separating each shock site before being mounted perpendicular to the shock direction, seen in Figure 31. These were mounted in transparent resin, shown in Figure 31b, which allowed for characterisation along the sample depth. A schematic of this extraction can be seen in Figure 32. These were carefully ground to the point of the cross section, being careful to not grind past the centre of the laser spots. These were ground according to the following procedure.

Samples were prepared via silicon carbide paper up to 4000 grit accompanied by a 3 µm diamond polish and 40 nm OPS polishing for 90 minutes. Many samples were also broad beam polished with argon using a *Hitachi IM4000* Ion Milling system, for 25 minutes, 4kV acceleration voltage and 20° tilting angle. Ion milling was found to add limited improvement to characterisation effectiveness.

3.2.1 Cross-Sectional Characterisation

SEM imaging was performed along the cross-section of the sample. Although secondary electron imaging did not reveal significant information, backscattered electron imaging revealed the location of twins. The distance over which twins can be found was recorded to understand the damage profile left by the LSP procedure.

TEM samples were extracted from different depths away from the shock surface, primarily 0 µm, 250 µm and 500 µm. Additional samples were extracted if the LSP effect was found or expected to be found deeper, or in order to assist with the identification of twins and other features. The 250 µm and 500 µm TEM samples were taken perpendicular to the shock direction (and parallel to the shock surface). The 0 µm samples are taken parallel to the shock direction and perpendicular to the shock surface, which allows characterisation of the near-surface microstructure, observing regions which may have been mechanically and/or thermally affected through LSP. These TEM locations have been illustrated through Figure 32.

TKD has been applied to many of the TEM samples procured, mainly to corroborate the twinning identification performed in the TEM. The details of these electron microscopy techniques will be elucidated in the following sections.

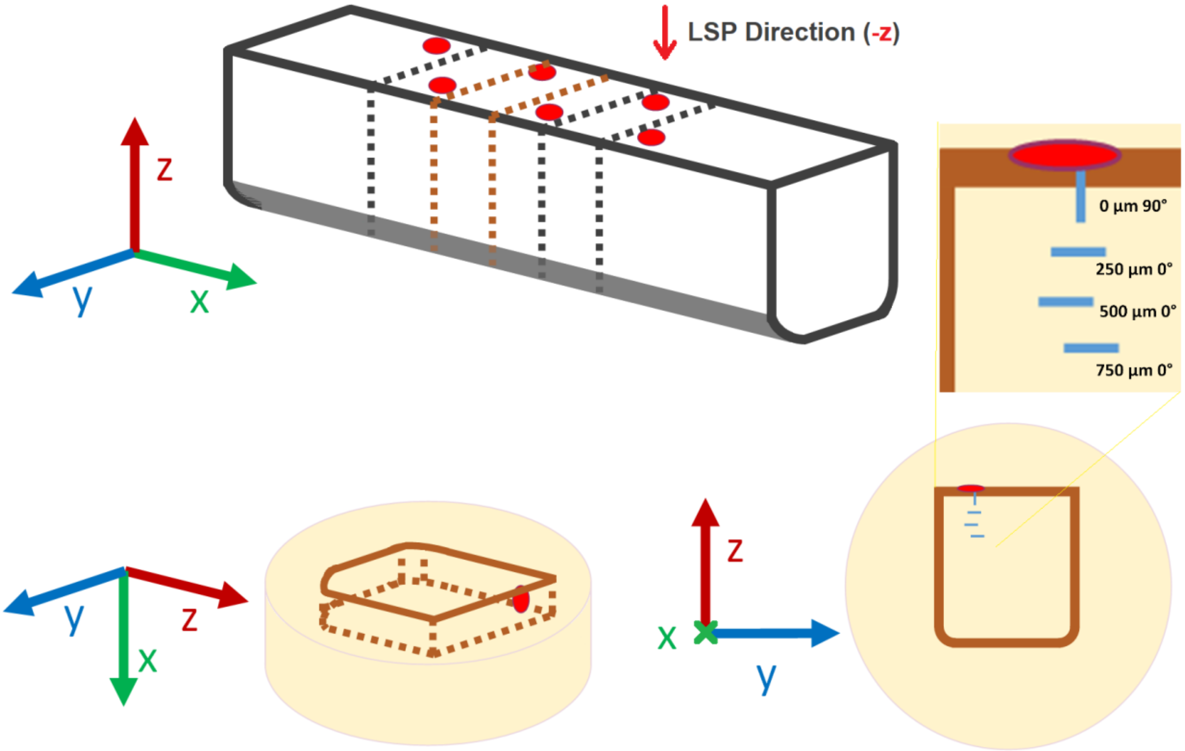

Figure 32: Schematic describing the sample extraction from bulk material. The SEM samples can also be seen in *Figure 31b*. Examples of common TEM lift-out locations have been shown with blue lines, along with description notation, as seen in the top right corner.

3.3 Electron Microscopy

3.3.1 Scanning Electron Microscopy & Ion Beam Preparation

The majority of SEM images were taken on a *TESCAN Mira3* system. These were often stitched together using the in-software faculties, or manually where required. This was needed when attempting to obtain the required resolution for feature identification on an approximately 1 mm^2 region. This SEM was also used for all EBSD and TKD micrographs using an attached *Oxford Instruments* detector. EBSD was performed at a 70° tilt angle at 20-30 kV with a step size of 20 µm before LSP. Although EBSD was attempted on the LSPwC sample after LS processing, the pattern quality reduction resulted in a poor indexing rate.

Electropolishing was avoided due to the worry that material removal if unsuccessful would potentially damage the sample and prevent extraction of accurate TEM results. TKD was performed off-axis with a -20° tilt angle, at 30 kV with a step size of 50 nm, unless otherwise stated.

A *Helios™ G4 PFIB CXe DualBeam™ FIB/SEM* was used for TEM lamella preparation. Some imaging was performed before and during the lamella preparation procedure, using secondary and BSE electrons and the ion beam. Electron images were taken at a 20 kV accelerating voltage. Ion beam images were taken at 30 kV. The lamella preparation utilised the 30 kV Ion beam. The process begins with deposition of a thin platinum protective layer atop the sample site. Initial rough milling at 60 nA generates the trenches. This is followed by cross-sectional cleaning from 15 nA to 1 nA for sample extraction using an *FEI EasyLift NanoManipulator* needle. Samples were welded onto a copper grid via platinum deposition before thinning from 4 nA to 0.33 nA, going from a 3-6 µm thickness to a regular electron transparency which ranged from approximately 40 nm to 300 nm. A final clean was performed with a beam current of 0.33 nA-0.1 nA at 5 kV, in order to remove the majority of irradiation damage from the 30 kV Ions.

It is worth noting that some TEM samples were not taken purely due to their depth into the sample. For these, linear features were seen through BSE imaging, and after broad beam milling these could also be seen via SE imaging. In order to best identify the features, the samples were extracted perpendicular to the (linear) twin direction, to allow for edge-on analysis. Figure 33 shows the extraction of such a sample. Figure 33a shows an image close to the surface of the 10-shock sample, after the TEM sample has been extracted. Many twin features have been recognised from the BSE images and are overlayed in red lines. The TEM sample location has been highlighted with a box. The image in Figure 33b shows the protective platinum layer, and the beginning of rough milling has enabled recognition of the twins under secondary electron imaging, due to the difference in milling rates of grains with differing orientations. This ensures the TEM lamella is taken from the correct location. Once the lamella preparation has been completed, we see in Figure 33c that the TEM sample contains the previously recognised twins.

3.3.2 Transmission Electron Microscopy

Samples were studied with two transmission electron microscopes (TEM's), primarily a *FEI Tecnai G2 F30 TEM* (TF30) for 300 kV analysis and secondarily a *FEI (Thermofisher) Talos F200X* (Talos) for 200 kV analysis. These were used to perform feature analysis of the samples, including the identification of twinning, and a generalised dislocation density study. Dislocation analysis of different regions provided insight into the microstructural evolution of laser shock peened material.

The dislocation density study was performed by counting intercepts of dislocations with the sample surfaces and dividing the total by two to obtain the number of dislocations. This was challenging to perform in the dislocation-rich near-surface material, between 5 and 10 µm from the laser shock surface.

The twinning identification was performed using a method termed "edge-on" in which the boundary between the matrix and twin is minimised to a thin line via tilting. When the boundary is thinnest, the possible twinning plane is identified in diffraction mode, and the sample is further tilted to the nearest zone axis (whilst maintaining the thin boundary). When the boundary is thin, this means the beam is “edge-on,” as the beam direction is travelling along the twinning plane. When the zone-axis has been reached, the twinning state may be confirmed via study of the diffraction pattern.

The diffraction pattern at a twin boundary provides reflections in all diffraction spots excluding those formed from the (shared) twinning plane itself (see Figure 34). As a result, the twinning plane is revealed as the non-reflected plane. If all planes are reflected, then either the boundary is not “edge-on” or the orientation relationship between the grains is not that of a twin boundary.

The final proof of twinning may be obtained from real-space imaging, when taking a dark field (DF) image of the matrix (or twin) where the g-vector is not the twinning plane. This confirms that the matrix (or twin) diffraction spot has no (or little) contribution from the twin (or matrix), as seen in Figure 35, showing a significant difference in contrast between the matrix and twin.

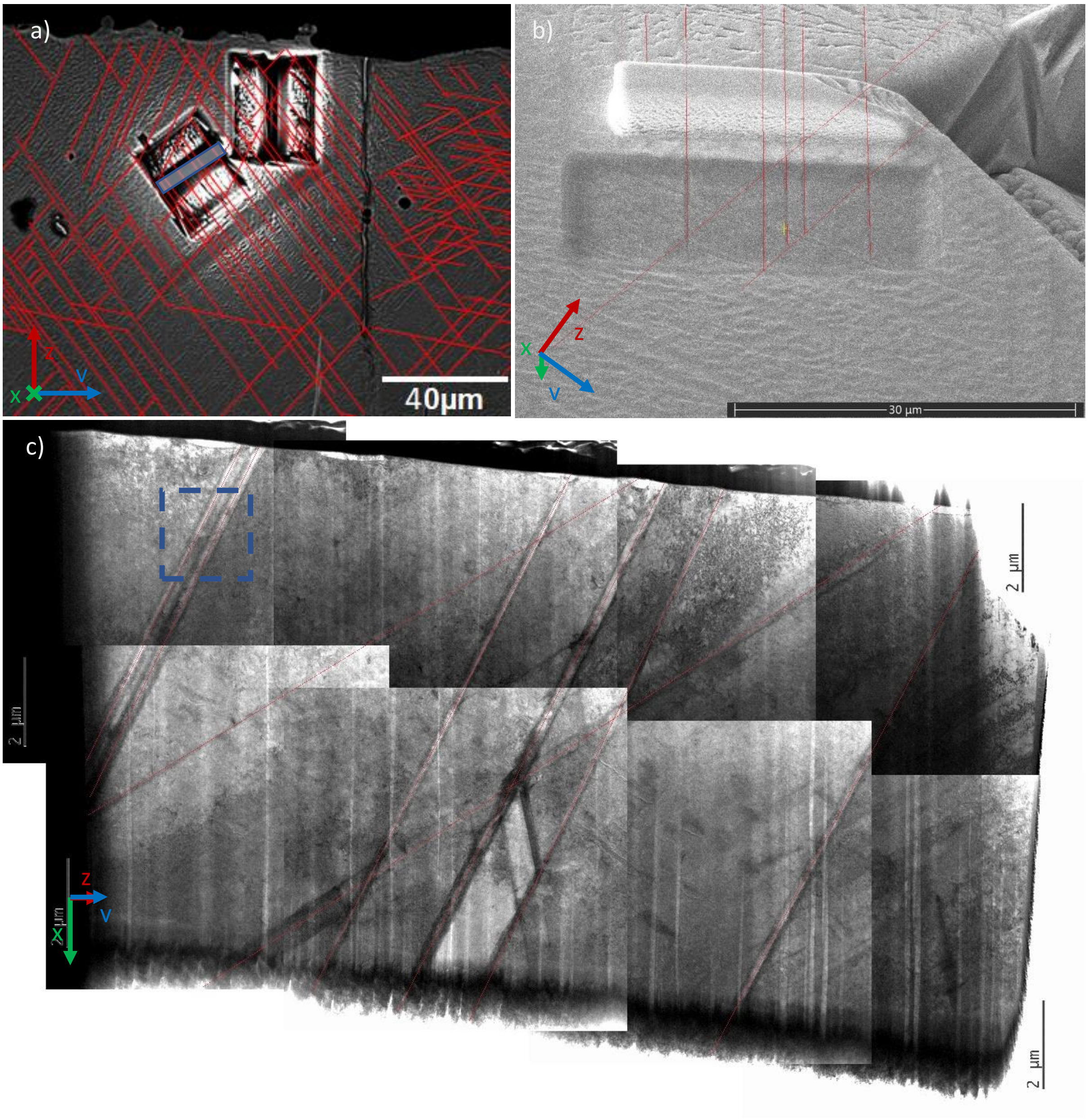

Figure 33: a) SEM, b) FIBSEM and c) TEM images of TEM specimen taken 40 µm from the surface of 10-shock specimen, within 100 µm of the spot centre. Twin locations are shown with red lines. The location of the sample is highlighted with blue in “a”, and correspondence can be seen between the majority of twins in each image. Twins in “c” share the orientation seen in “a” & “b”. Location of further study highlighted in dashed blue.

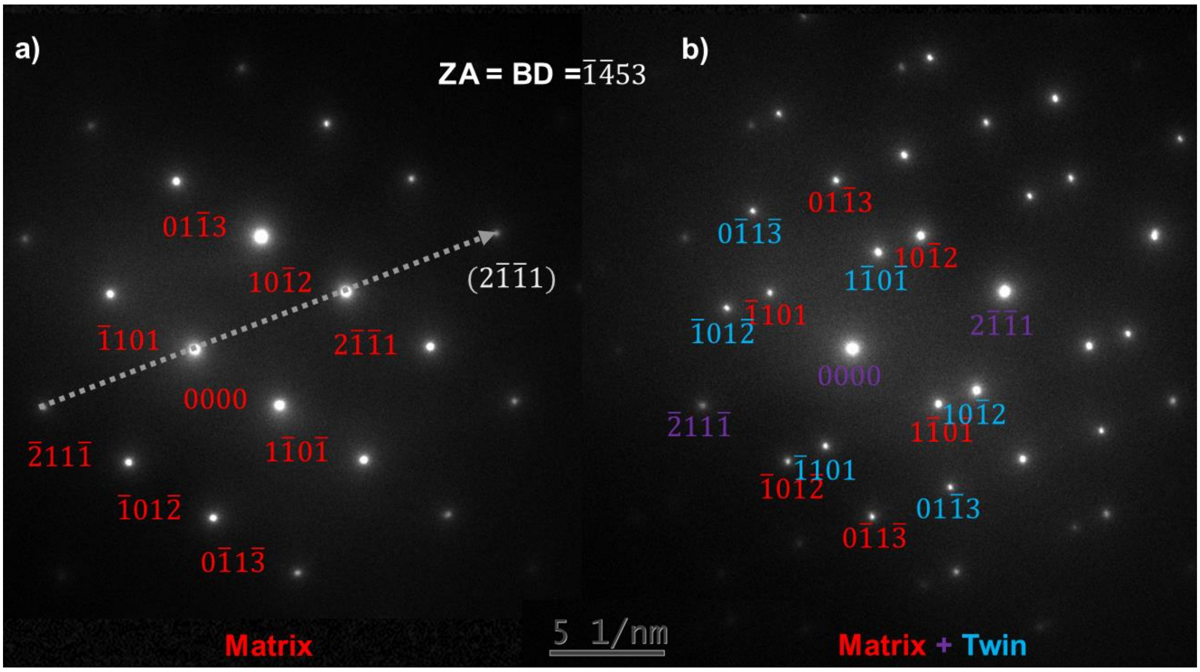

Figure 34: Diffraction patterns of the $[\bar{1}\bar{4}53]$ zone axis in HCP Titanium. a) shows that of the matrix alone, whilst b) shows the pattern over both the matrix and twin. Contribution from each of these is roughly equal, leading to similar intensity of diffraction spots. Matrix spots are labelled in red, twin spots labelled in blue, and shared spots (from the twin plane) are in purple.

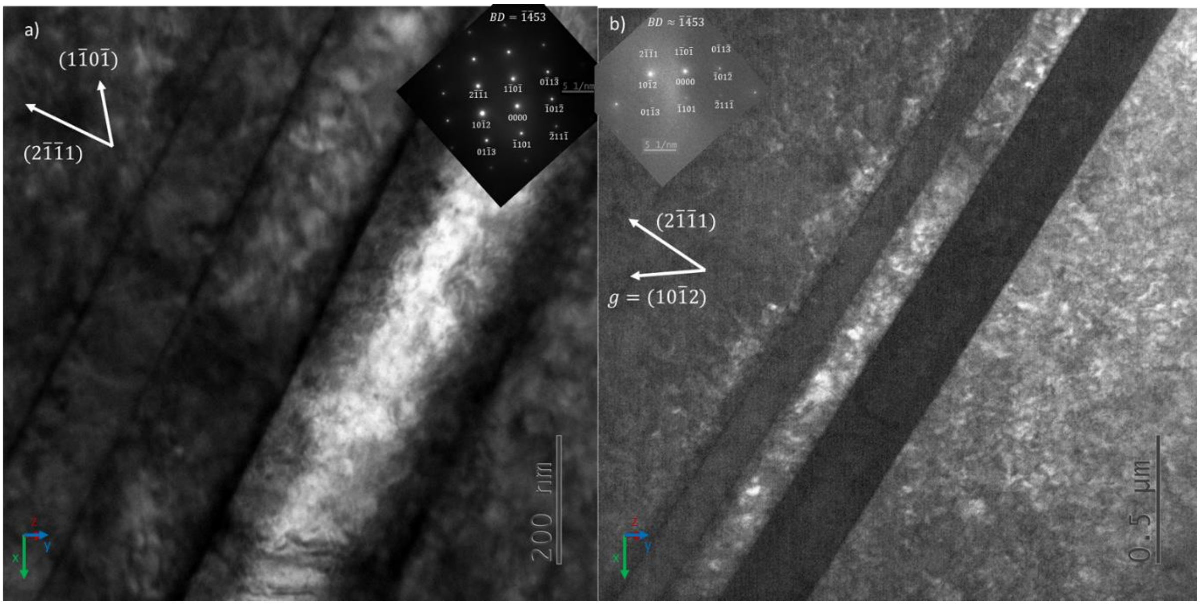

Figure 35: a) BF zone axis $[\bar{1}\bar{4}53]$ image of two $2\bar{1}\bar{1}1$ twins with accompanying diffraction pattern. b) Near zone axis $[\bar{1}\bar{4}53]$ DF image of two $2\bar{1}\bar{1}1$ twins with g=$10\bar{1}2$. Both images are of the same area as highlighted in dashed blue in *Figure 33*c, but having different magnification.

3.4 Nanoindentation

Nanoindentation was performed with a *Hysitron Triboindenter 950* via a 5-2-5 s load-hold-unload profile to a force of 5 mN (approximately 1 mN/s load rate) along the cross-section of the samples, around 150 µm away from the shock centre. 5 indents were taken across a 100 µm region for each depth. The error was calculated using the standard deviation of these 5 points. Any error margins given from the equipment that was larger than this value was disregarded, however all points utilised at least 4 indents.

4 Characterisation of LSP Induced Changes

In this chapter, our attention is directed towards a comprehensive examination of the changes induced in HCP α Titanium as a result of the Laser Shock Peening (LSP) process. The execution of the experimental methodology proved largely successful; nonetheless, subtle deviations were discerned, affecting the overall efficacy of the LSP procedure. These minor variations are an inherent aspect of tasks involving a multitude of variables, as is the case with LS processing. These are also discussed. As discussed in the methodologies section, two categories of samples were produced: the left-hand side undergoing LSPwC (laser shock peening without coating), and the right-hand side undergoing PVC-ablated LSP (seen before in Figure 29b). The LSPwC sample was also cross sectioned forming 6 individual samples, whilst the coated LSP sample was not pursued in the cross-sectional studies, as it exhibited no obvious signs of change compared with unprocessed material, as will be shown later in section [*4.2.1 With Coating*].

An image of the LSPwC sample after LSP, before completion of the cross-sectional cuts, can be seen in Figure 36. A square shape can be seen surrounding many of the spots (highlighted with dashed yellow lines for the 10-shock sample), which is due to the protective tape surrounding the shock site (not as part of the shocking procedure). Tape was used as a mask which allowed shocking on the site, whilst preventing debris and discolouration to influence the other shock sites. This protective layer slightly covered the 15-shock site, causing a reduction in the affected area, and a non-centralised footprint. This influences the optical profilometry of the 15-shock site.

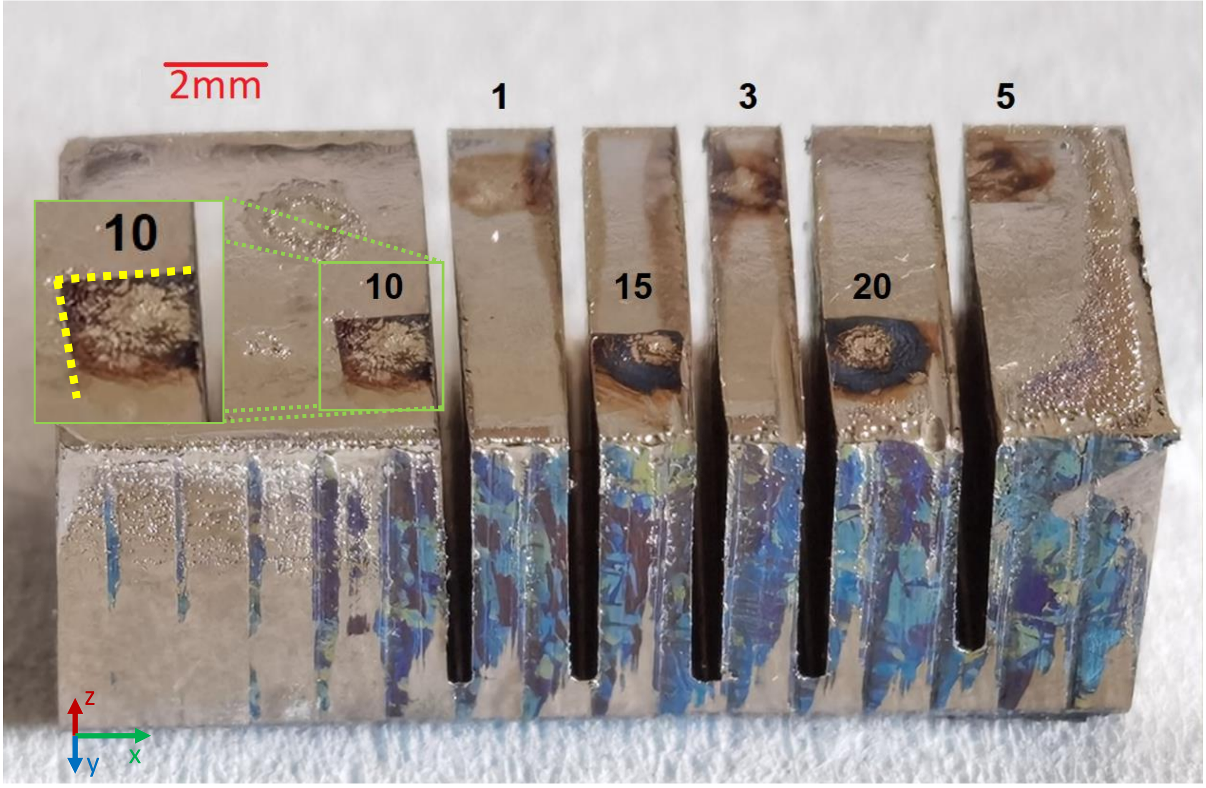

Figure 36: Left side of commercially pure titanium sample after LS processing, which was performed without coating. Six dark laser spots can be seen with numbers above them indicating the number of shocks performed at the site. The image seen in *Figure 29* displays the whole sample before LSP.

4.1 Optical

The optical images were taken after cutting the specimen shown in Figure 36 into smaller pieces, but before they were mounted and ground to the central cross-section of each laser shock. These are seen in Figure 37. All of these show a centralised region which is most affected (causing slight indentation), approximately 150-250 µm in diameter (dashed blue circles). This is surrounded by a larger region where a significant ripple emanates radially from the centre. This is around 1000 - 1200 µm (dashed green circles). This is difficult to identify on the 1-shock and 5-shock samples (Figure 37 a) and c) respectively). Finally, the total footprint ranges from 2000 - 2500 µm (dashed purple circles). An exception to this is the 5-shock sample, where it is possible that the water flow affected the edges of the footprint. This influences the optical profilometry of the 5-shock site. The discolouration increase is likely due to surface oxidation.

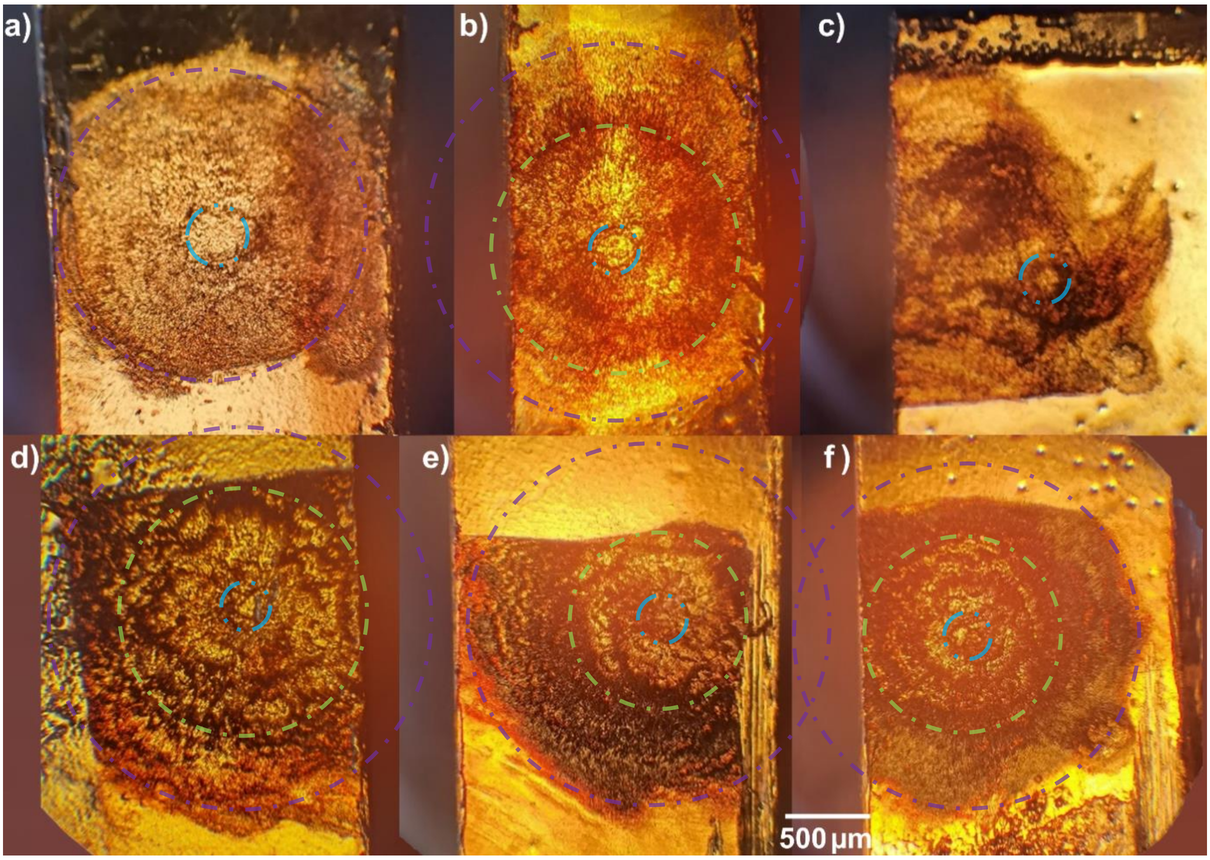

Figure 37: Optical images of laser footprints at shock sites after a) 1 b) 3 c) 5 d) 10 e) 15 and f) 20 shocks. Note the 5 and 15 shock samples were over-protected, changing the footprint shape.

4.2 Optical Profilometry

4.2.1 With Coating

The right hand side of the sample was laser shock peened whilst coated, and the before and after optical profilometry (for chronology, see [*3.2 Procedure after laser shock peening*]) can be seen in Figure 38 and Figure 39 respectively. In Figure 38 (before LSP), shallow scratches can be seen throughout each of the shock sites. The total range of depths is about 2.0 ± 0.2 µm. In Figure 39 (after LSP), these scratches can no longer be seen, and this is corroborated by slight reduction in the range of heights obtained from the scans, of 1.9 ± 0.1 µm.

It is also worth noting that a few regions were formed where the laser shocking permeated through the PVC coating, most easily seen in Figure 39c and Figure 39e on the 5-shock and 15-shock samples, circled in purple.

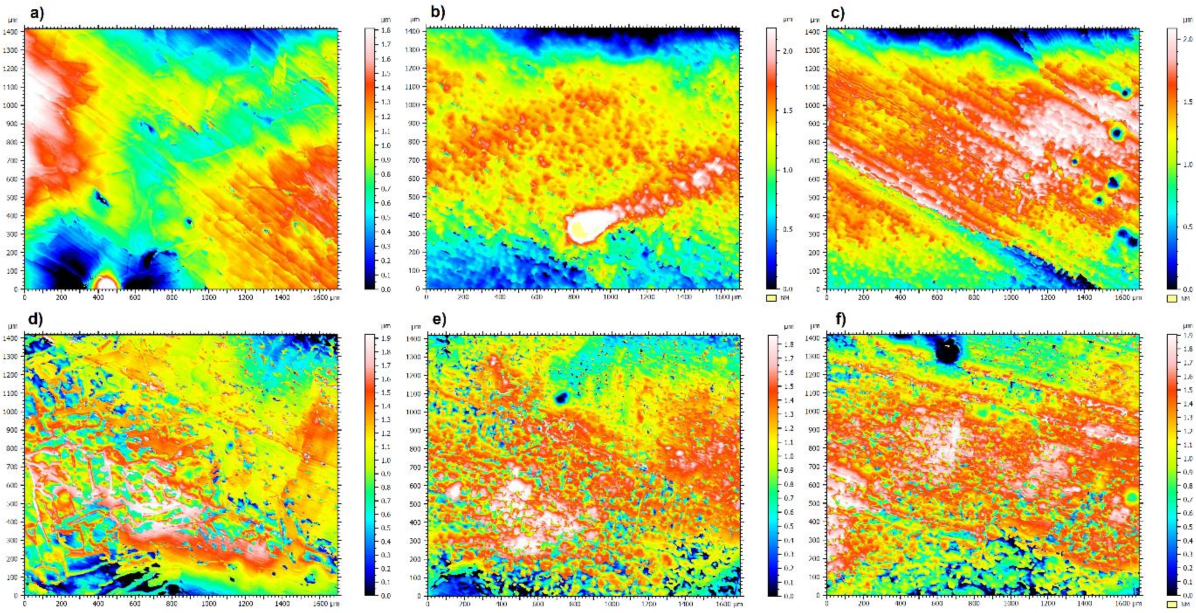

Figure 38: Optical profilometry of the right side of sample surface before a) 1 b) 3 c) 5 d) 10 e) 15 and f) 20 shocks. Colours indicate different heights; see individual colour keys at side.

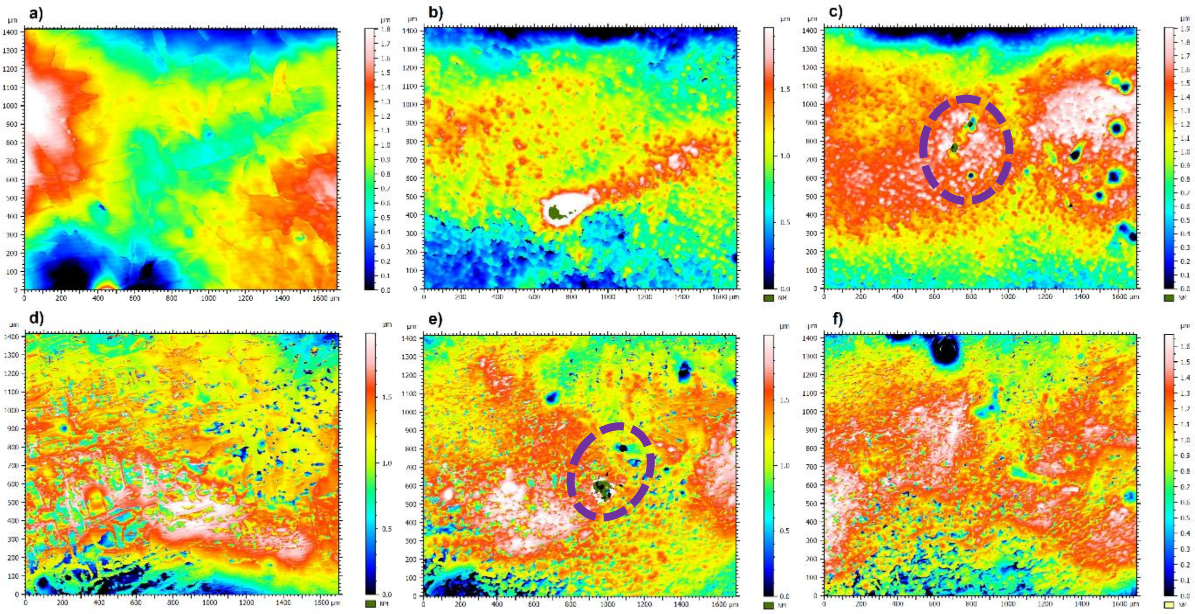

Figure 39: Optical profilometry of the coating-protected laser shocked surface after a) 1 b) 3 c) 5 d) 10 e) 15 and f) 20 shocks. Colours indicate different heights; see individual colour keys at side. Note, within the purple ovals where the laser has penetrated through the coating (three dots in each), causing surface changes (these are not visible in the corresponding scans in *Figure 38*).

4.2.2 Without Coating

The before and after optical profilometry of the LSPwC sample can be seen in Figure 40 and Figure 41 respectively. Figure 40 shows that there was slightly more pitting in this region than on the coated LSP sample (Figure 38) resulting in differences in the original surface profile. As the change after LSP is significant, as seen from Figure 41, this has a minor effect on the results shown in Figure 42, which collates the overall differences in surface roughness.

Figure 41 shows clearly from the profilometric scans, that the greater the number of shocks, the more extensive the surface changes. This can be determined not only from the general shape of the footprint, but also the number of regions for which the hardware is unable to ascertain the depth (i.e.: no result, appearing as dark green). This is due to the changes in absorbed light due to the discolouration caused by the laser. This is difficult to accurately determine for the 15-shock sample, due to the misplaced protective mask used during the experimental procedure.

Figure 42 shows the increase in the mean height changes of the shock surface with increasing shock number. The initial geometric height (S_q^i) for the 5-shock is above average, which has led to a minor difference between 3 and 5 shocks. The arithmetic mean height change (S_a^f-S_a^i) is a measure of surface roughness which uses the difference between each point and the average height, squared (minus the initial arithmetic height calculated before shocking). As a result, this is affected significantly by the unintentionally protected area on the 15-shock sample, as seen in Figure 41e.

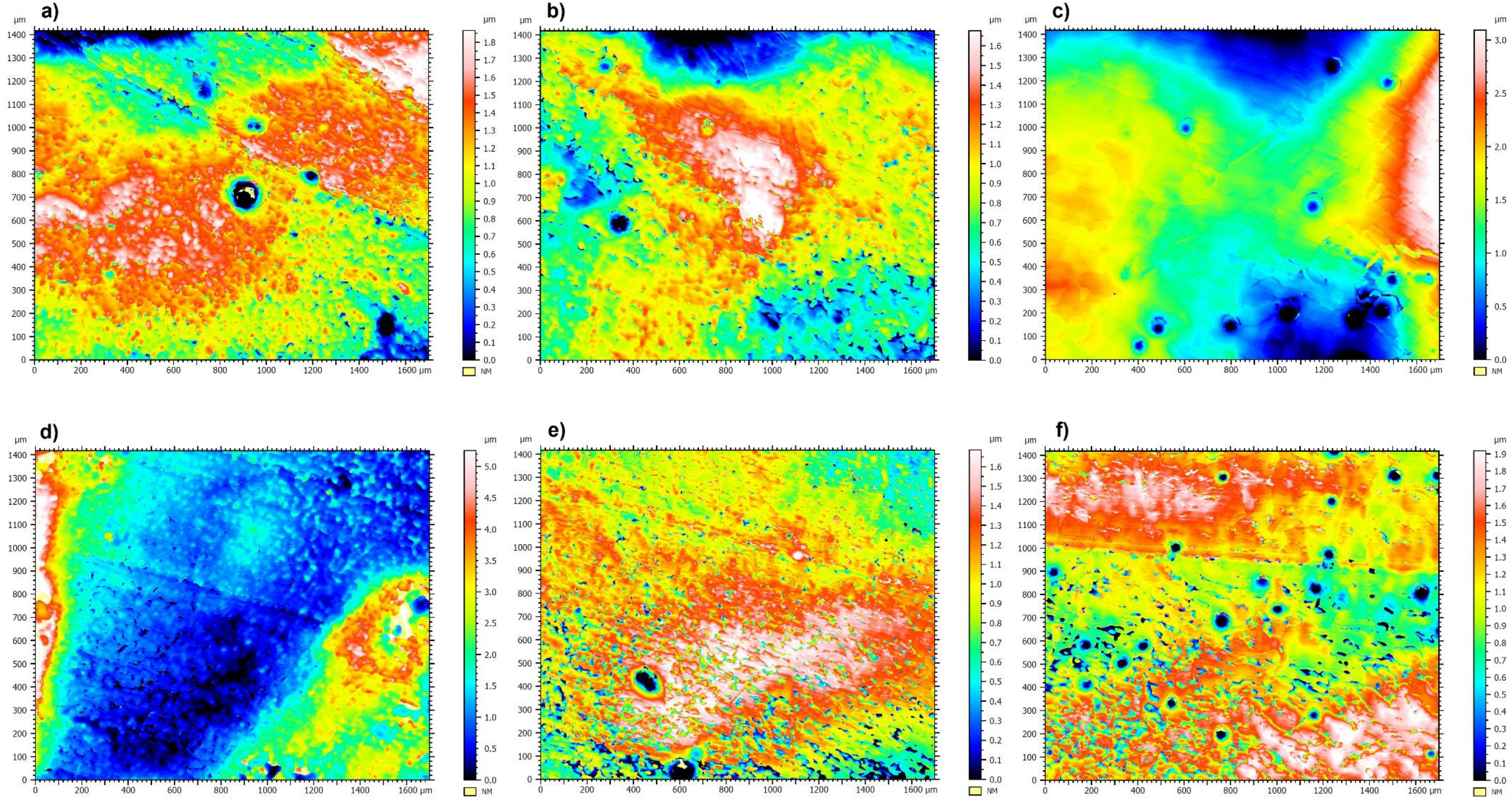

Figure 40: Optical profilometry of the left side of sample surface before a) 1 b) 3 c) 5 d) 10 e) 15 and f) 20 shocks. Colours indicate different heights; see individual colour keys at side.

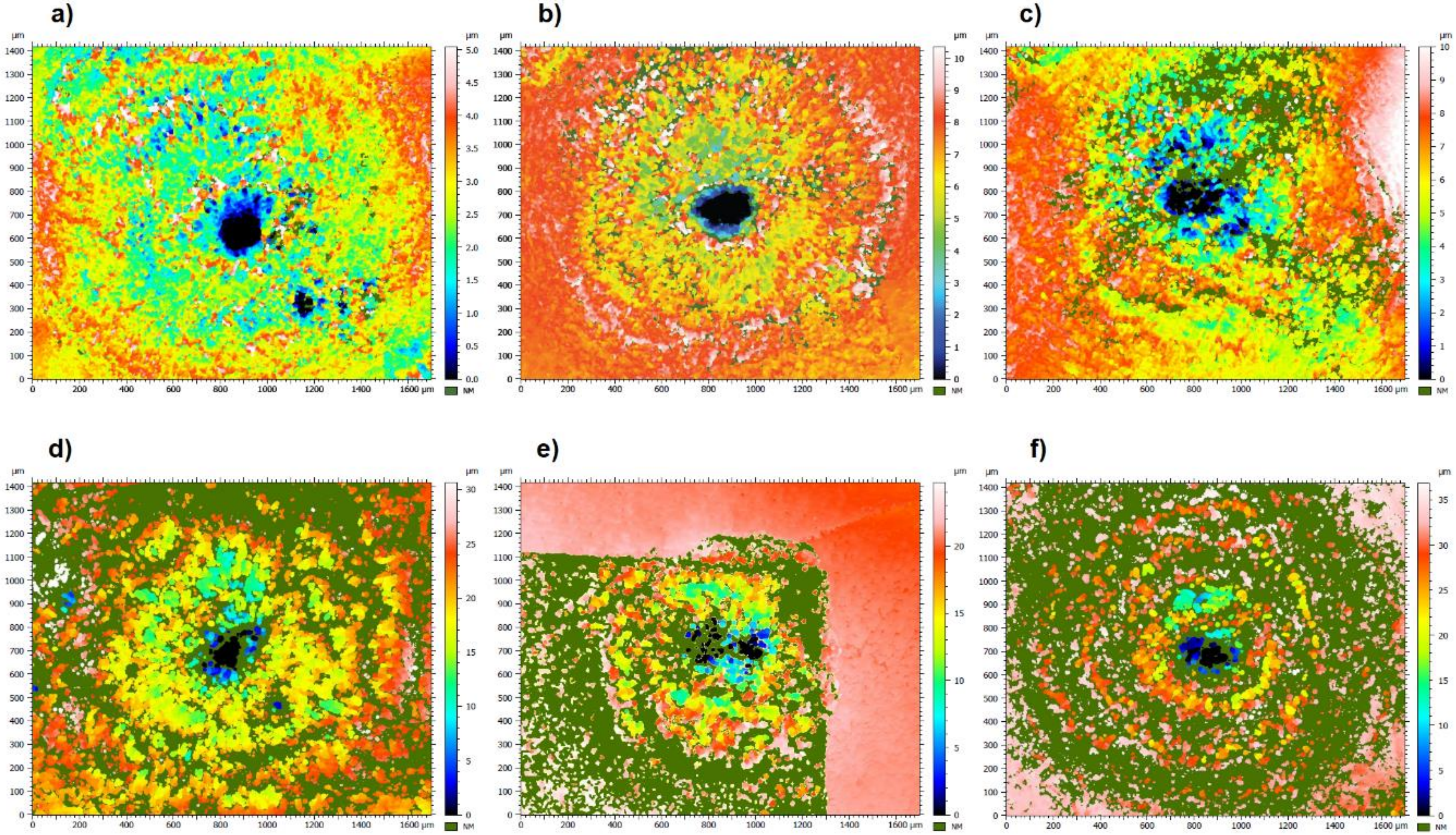

Figure 41: Optical profilometry of the laser shocked surface after a) 1 b) 3 c) 5 d) 10 e) 15 and f) 20 shocks. Colours indicate different heights; see individual colour keys at side. Minimum height for all LSP spots is in the shock center. The height gradually increases away from this point. The maximum heights tend to be on the unaffected region, not accounting for the absent results.

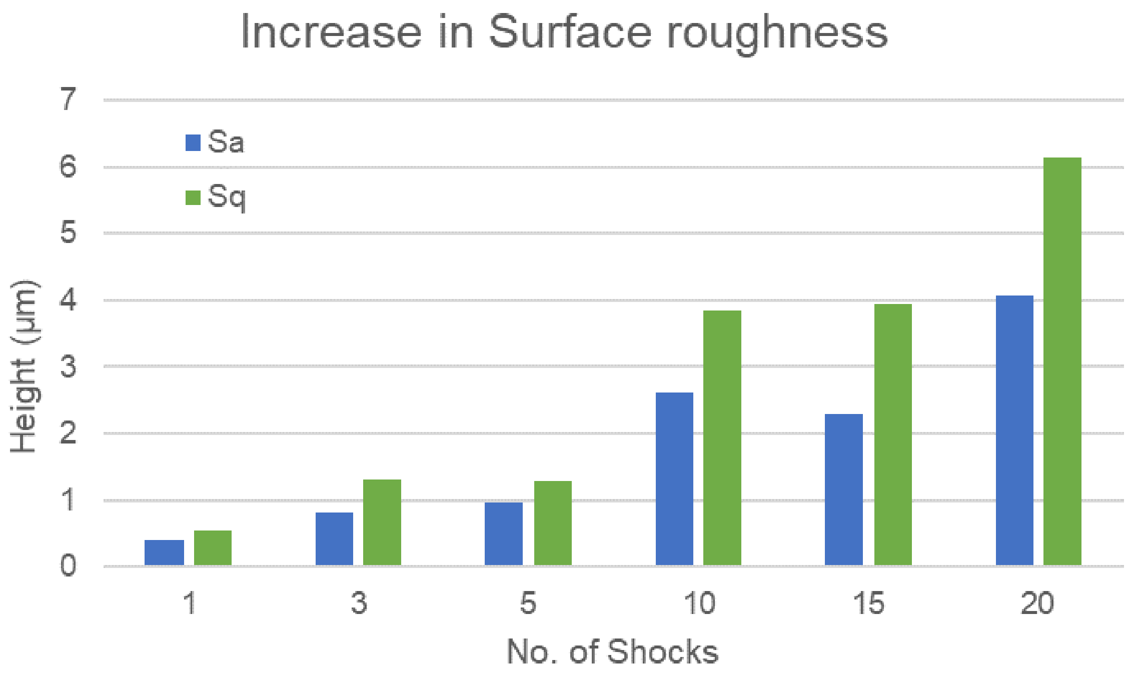

Figure 42: Chart comparing the arithmetic ($S_a = S_a^f - S_a^i$) and geometric ($S_q = S_q^f - S_q^i$) mean height changes of the laser shock sites and areas.

4.3 Scanning Electron Microscope Electron Backscattered Diffraction (EBSD)

Figure 43, which did not undergo LSP, has been set as a control region. This sustained minor surface changes from repeated covering and uncovering with black PVC tape, both as part of masking for protection when shocking adjacent sites and as the ablative coating when shocking the site itself. EBSD of the coated LSP material can be seen in Figure 44. There are no significant changes, probably due to the (large) thickness and (small) density of the PVC tape; this is due to the pressure functions as determined by the equations laid out in section [*2.1.2.2.2* Ablative layer]. The coated specimens were therefore not examined further in this study.

It is noted that after LSPwC (Figure 45), the surface condition was such that EBSD could not be performed successfully due to the melting effect of the laser. The region outside the laser footprint did index, but this was not considered to be worth the resources required to map each laser footprint with EBSD, as this provided no additional information when compared with data from the optical profilometry.

The EBSD results show that the majority of grains are lath-like, at least 50 µm in width, and many hundreds of micrometres long. These form in colonies of select orientations, likely formed from the β grains (which may be found above the α - β transus temperature of ~882 °C). These large grains reduce the complexity of the system and allows for orientation-sensitive analysis of the deformation systems involved. Small quantities of β-Ti are found, likely due to the (< 0.5 wt %) impurities in the CP Ti, typically iron.

The 10-shock site, shown in Figure 45, is seen to be a very large grain, being well over 2 mm in diameter at the surface. This was corroborated with the TEM results taken from the cross section.

With coating:

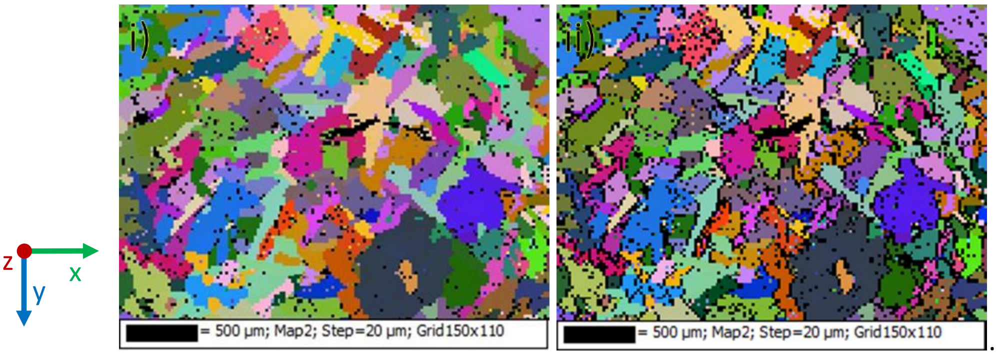

Figure 43: EBSD (Euler colours) of coated LSP sample (right side) as a control (0 shock) site i) before and ii) after application and removal of PVC tape (part of the laser shock peening procedure).

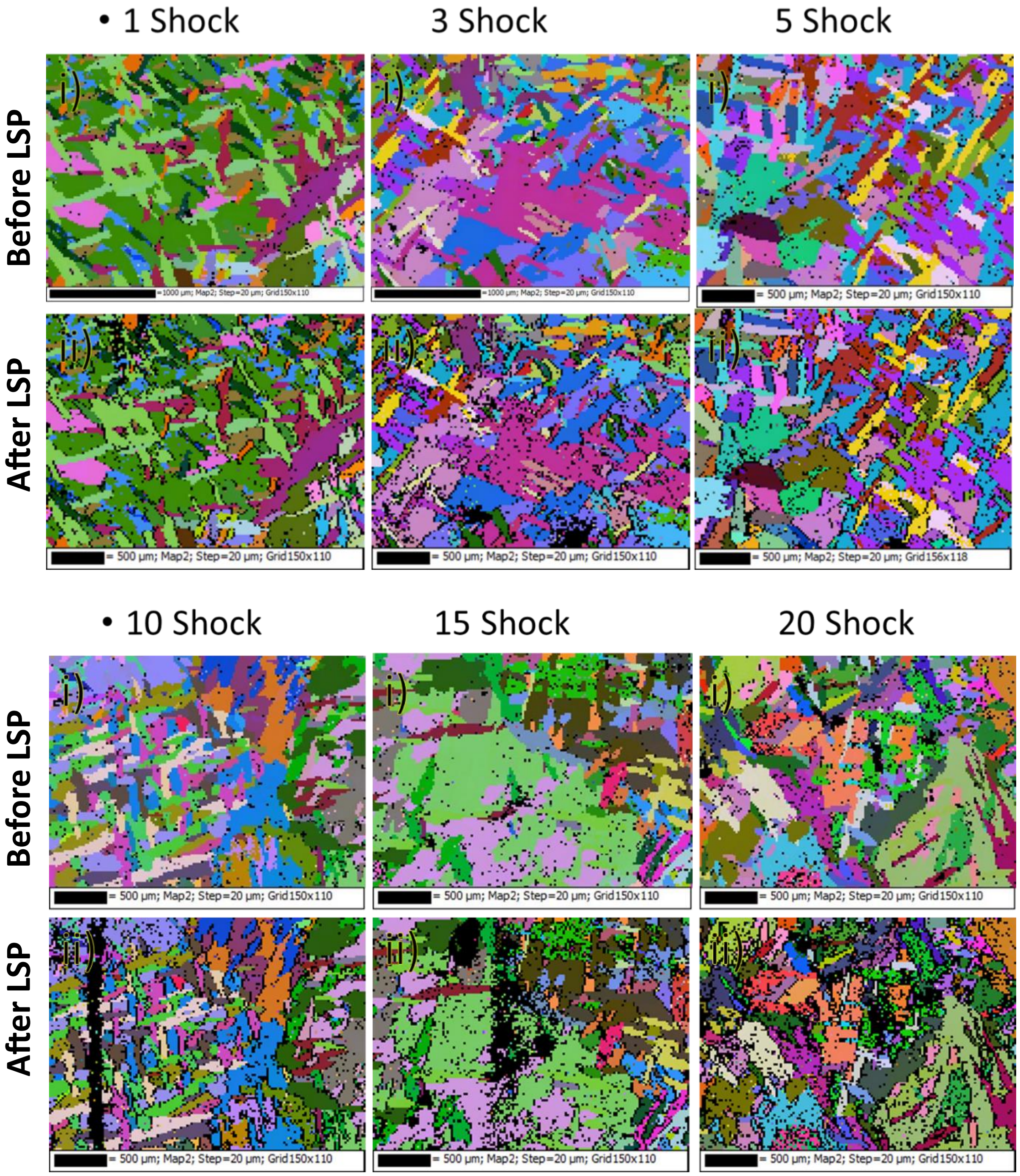

Figure 44: EBSD (Euler colours) of coated LSP sample (right side) at different sites with indicated shock numbers i) before and ii) after laser shock peening.

Without Coating:

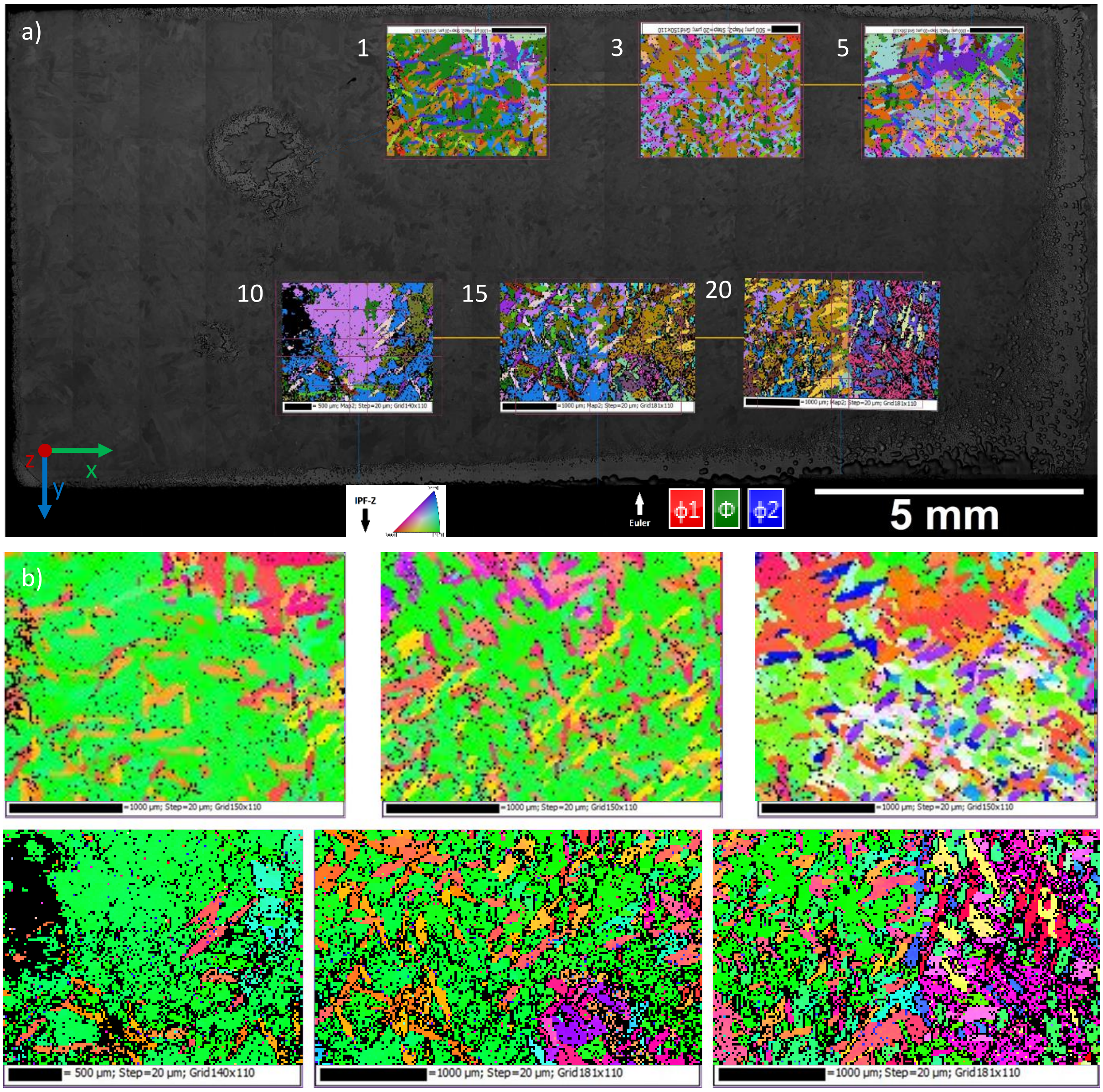

Figure 45: a) EBSD mapping in Euler colours of LSP sites, before laser processing, with corresponding number of subsequent shocks, superimposed on a backscattered electron SEM image taken at 30 kV (to see this more clearly, zoom in). These are the same locations as for the optical profilometry. The EBSD maps are b) enlarged below in IPF-Z convention for ease of viewing, with the upper sites (corresponding to 1, 3 and 5-shocks) also having been oriented appropriately.

4.4 Scanning Electron Microscope Backscattered Imaging (BSE)

No further study was performed on the coated sample due to the lack of changes seen as compared with the previous results. The surface changes as a result of LSPwC can be seen in Figure 46, as imaged with secondary electrons. This provides some information regarding the changes caused by LSP. The differences seen between shocks are less pronounced than in the optical imaging, however more ripples are seen emanating from the larger shock number sites. The tape mask lines can also be seen bordering the shock sites.

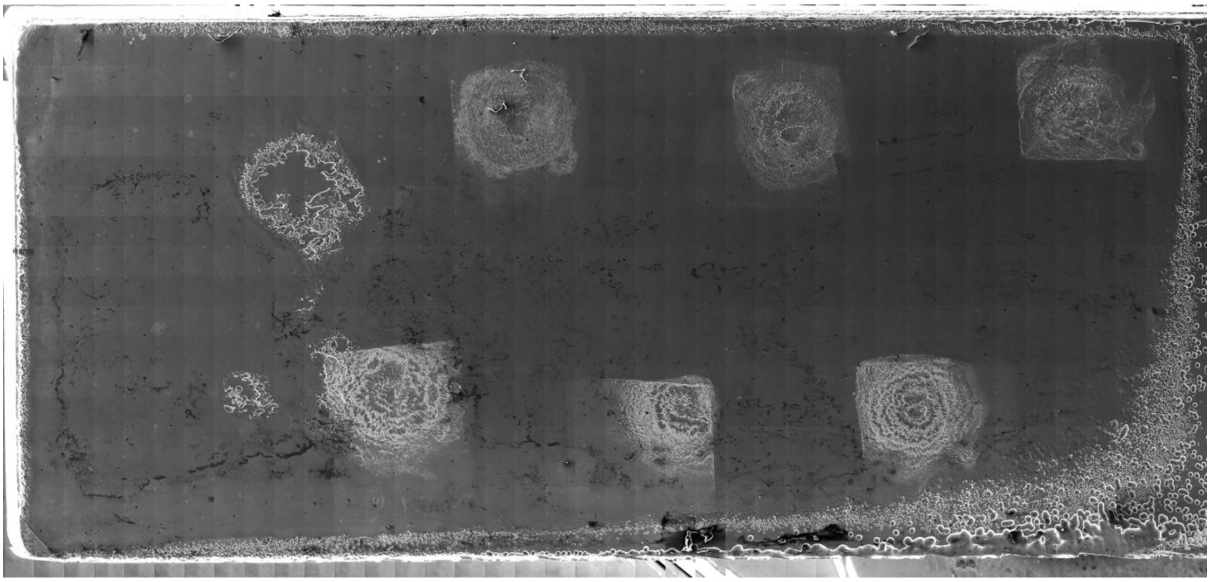

Figure 46: Stitched SEM image taken after LSP of uncoated material (left side of sample). Sample locations are as seen in *Figure 45*.

4.5 Cross-Sectional Backscattered Electron imaging

4.5.1 Twin Area Mapping

After cross sectioning, the 3, 5, 10 and 15 shock samples were prepared for imaging, as illustrated in Figures 47. Various linear features, later found to be twins, are seen. More twins are seen closer to the surfaces of the samples. Twins are found over a larger total area on samples that experienced more shocking. Figures 47.3-shock demonstrates how the area was determined, based on the location of twins highlighted in red. Although this was repeated for other samples, the red overlays used to highlight twins have not been included in these images. This 3-shock sample was re-imaged due to poor quality on previous imaging attempts. A balance was struck between imaging time and image quality to obtain efficient results for all samples. The white boundaries highlight the *area* over which twins have been seen. These are compiled and summarised in Figure 48, which shows there is a consistent increase in twinned area with increasing shock number. The blue line is used to show the *depth* over which twins have been seen. These have been compiled and summarised in Figure 49, which shows there is a consistent increase in maximum twin depth with increasing shock number.

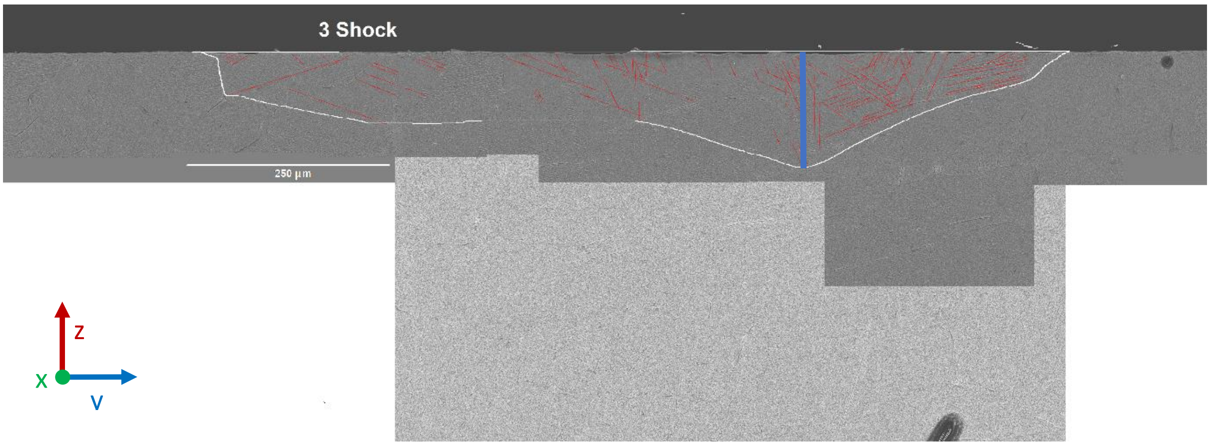
3 Shock
250 µm
Z
X
V

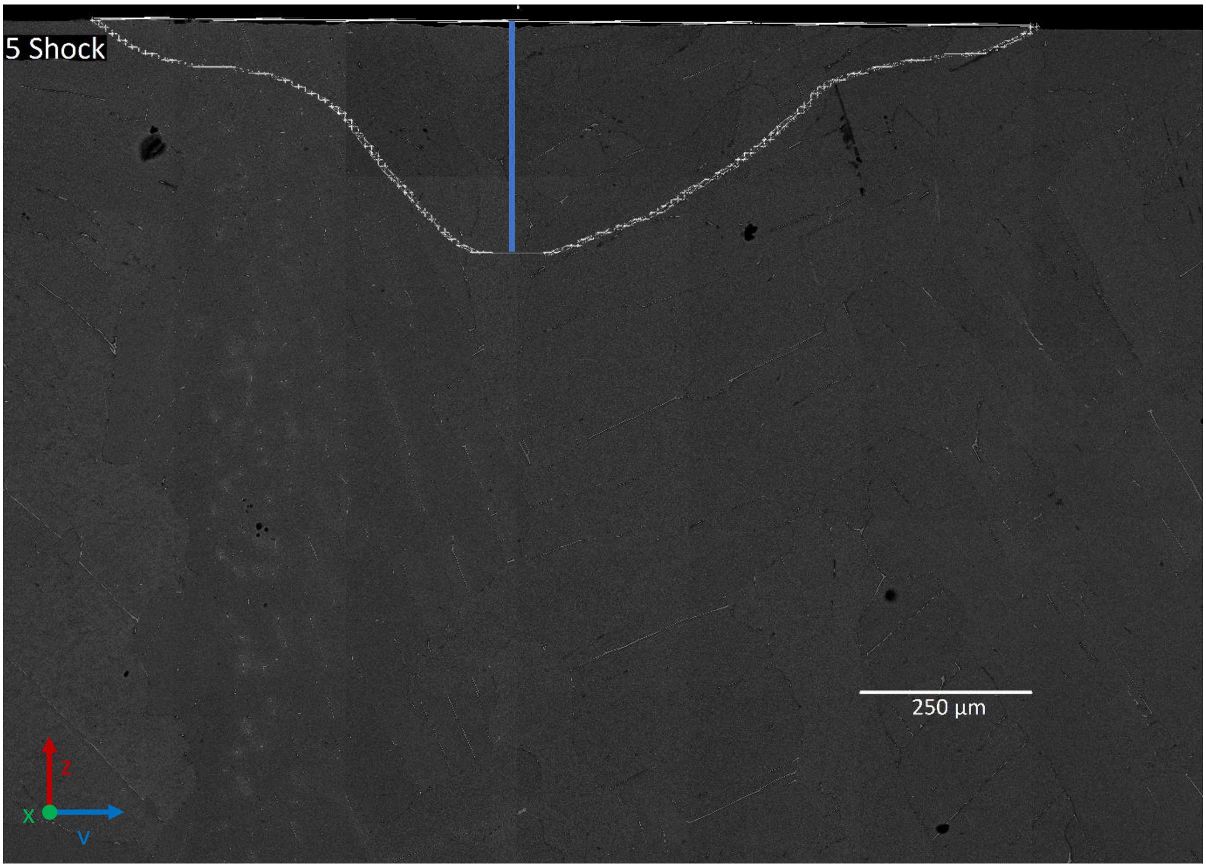
5 Shock
250 µm
Z
X
V

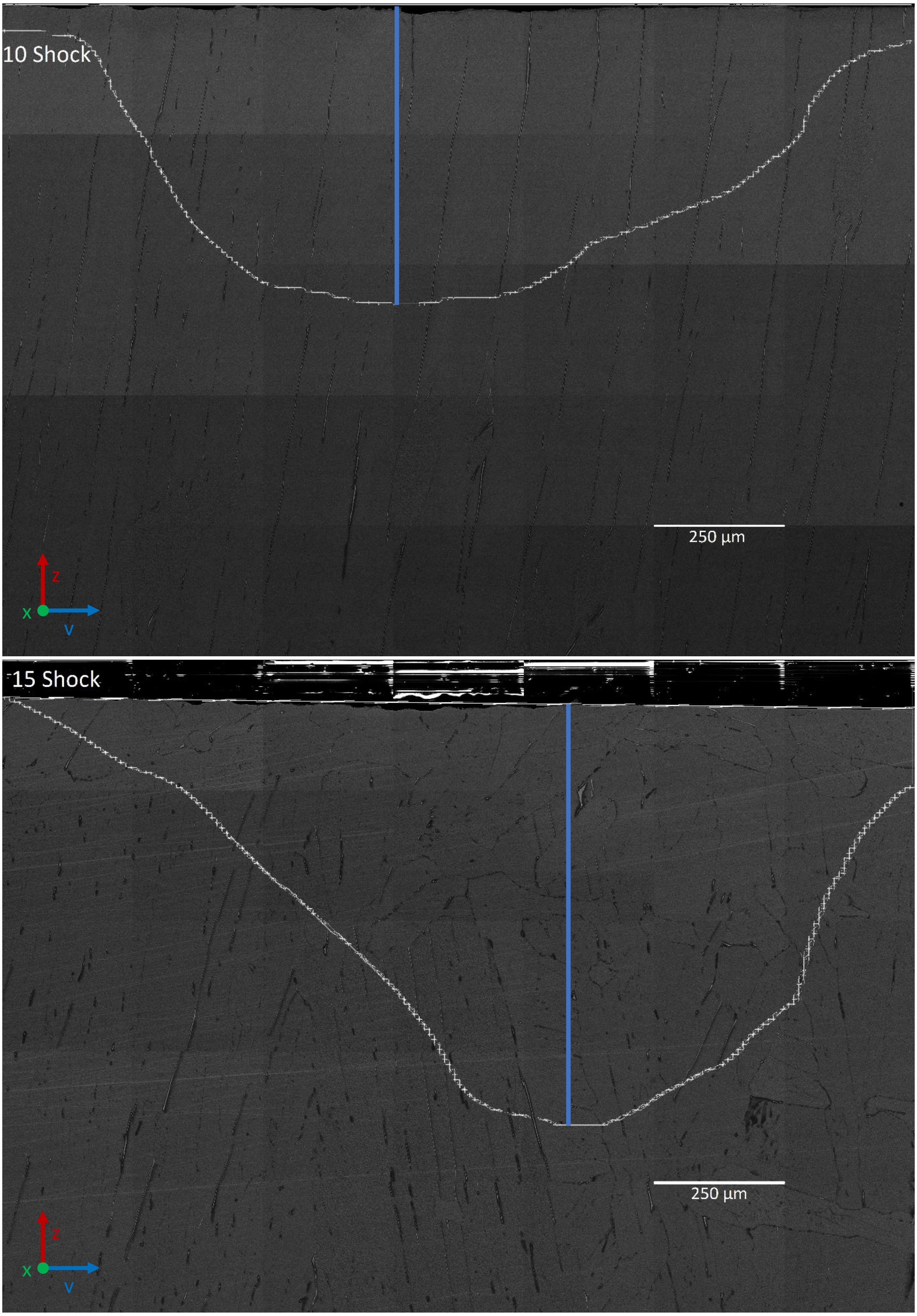

Figures 47: BSE SEM stitched images of central cross sections of LSP sites shocked 3, 5, 10 and 15 times as indicated, with white line signifying the twinning limit. Images are taken with backscattered electrons at 20 kV. For the 3 shock sample, twins have been highlighted with red lines.

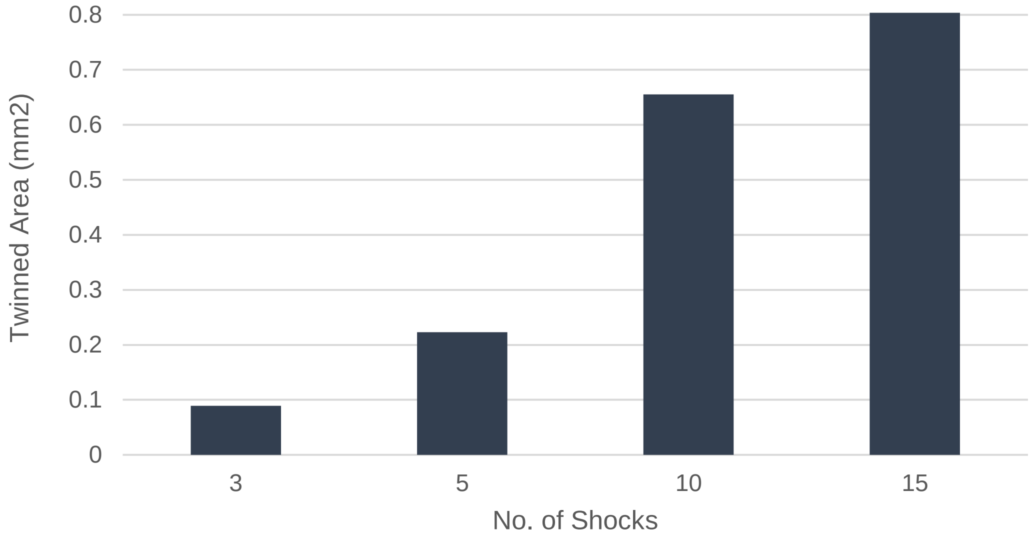

Figure 48: Chart showing the twinned area beneath the laser shock site on the sample cross-sections.

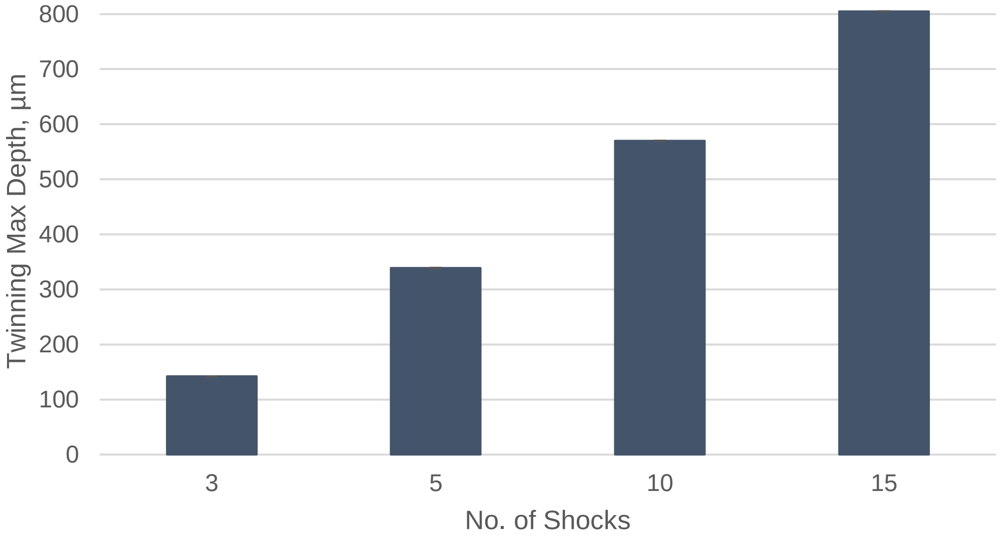

Figure 49: Chart showing the maximum depth over which twinning can be seen on the samples cross-sections.

4.5.2 10-Shock Area Analysis

The 10-shock area corresponded to a large grain, which made it very convenient to study based on orientation. It is therefore examined in more detail here.

Figure 50a and Figure 50b show the cross-section through the 10-shock sample. From EBSD attempts (not included) and later TEM results, this was found to be consistent with the EBSD from Figure 45, in that most of the shock-affected region is of a single grain, although divided by sub-grain boundaries (low angle grain boundaries) forming lamellae. This large grain enabled easy analysis of the sample to judge the types of twins produced and their relationship with the shockwave direction. These twins were grouped together according to their orientation relative to the shock surface and 6 different orientations were identified. A helpful schematic to describe this grain is seen in Figure 51. This schematic shows the orientation of the shock surface, the cross-sectional surface, and the perpendiculars to both of these directions; these are found above the primary schematic, which shows the laser footprint and the SEM sample surface (the cross-sectional surface) as a cutout of the sample going through the centre of the shock site, as was performed for all of the samples as laid out in [*3.2.1 Cross-Sectional Characterisation*]. Some readers may find this visual aid to be a hinderance, and as such has not been made critical to understand for future discussion.

These groups of twins have been provisionally identified, and their orientations predicted via corroborating with a stereographic projection (Figure 52), many of which have later been confirmed using TEM samples and Kikuchi analysis, and / or transmission Kikuchi diffraction (TKD). The use of the stereographic projection is detailed below. A summary of the results of these interpretations can be found in Table 9.

The shock direction for the 10-shock sample is very close to (within 5° of) $[11\bar{2}0]$. This means that the LSP process imposes compression of the a-axis. The expected twins would therefore be extension twins. Recalling Figure 20, these twins would be of the $\{10\bar{1}2\}$ and $\{11\bar{2}1\}$ types, with the $\{10\bar{1}1\}$ and $\{11\bar{2}2\}$ type twins being the c-axis contraction (or compression) twins (for α-titanium). After confirming the EBSD orientation using TEM Kikuchi diffraction, the $(\bar{1}10\bar{2})$ plane normal direction was identified as the cross-section surface. The possible 6 twin groups, as identified through the angle they made with respect to the shock surface, were compared with all possible twins, and the closest twin was assigned to each group. These were found to be predominantly of $\{11\bar{2}1\}$ type twins, of which there are 6 possibilities (namely, $(11\bar{2}1)$, $(1\bar{2}11)$, $(\bar{2}111)$, $(11\bar{2}\bar{1})$, $(1\bar{2}1\bar{1})$ and $(\bar{2}11\bar{1})$). The $(11\bar{2}\bar{1})$ twin was not found, and has been replaced with a much closer fit, the $(\bar{1}\bar{1}22)$ twin. The stereographic projection shown in Figure 52a shows the great circles corresponding to the $\{11\bar{2}1\}$ type twins. These great circles intersect the edges of the stereographic projection when they would be visible in the $(\bar{1}10\bar{2})$ plane (i.e., the SEM sample plane). Figure 52b shows the additional $(\bar{1}\bar{1}22)$ twin. The yellow lines correspond to the twin groups identified. They are seen to nearly correspond precisely with the great circle "points" (i.e., the intersections with the current projection, the $(\bar{1}10\bar{2})$ plane). Table 9 includes the difference between the theoretical angles and the experimental angles. Angles of less than 5° can reasonably be considered within experimental error.

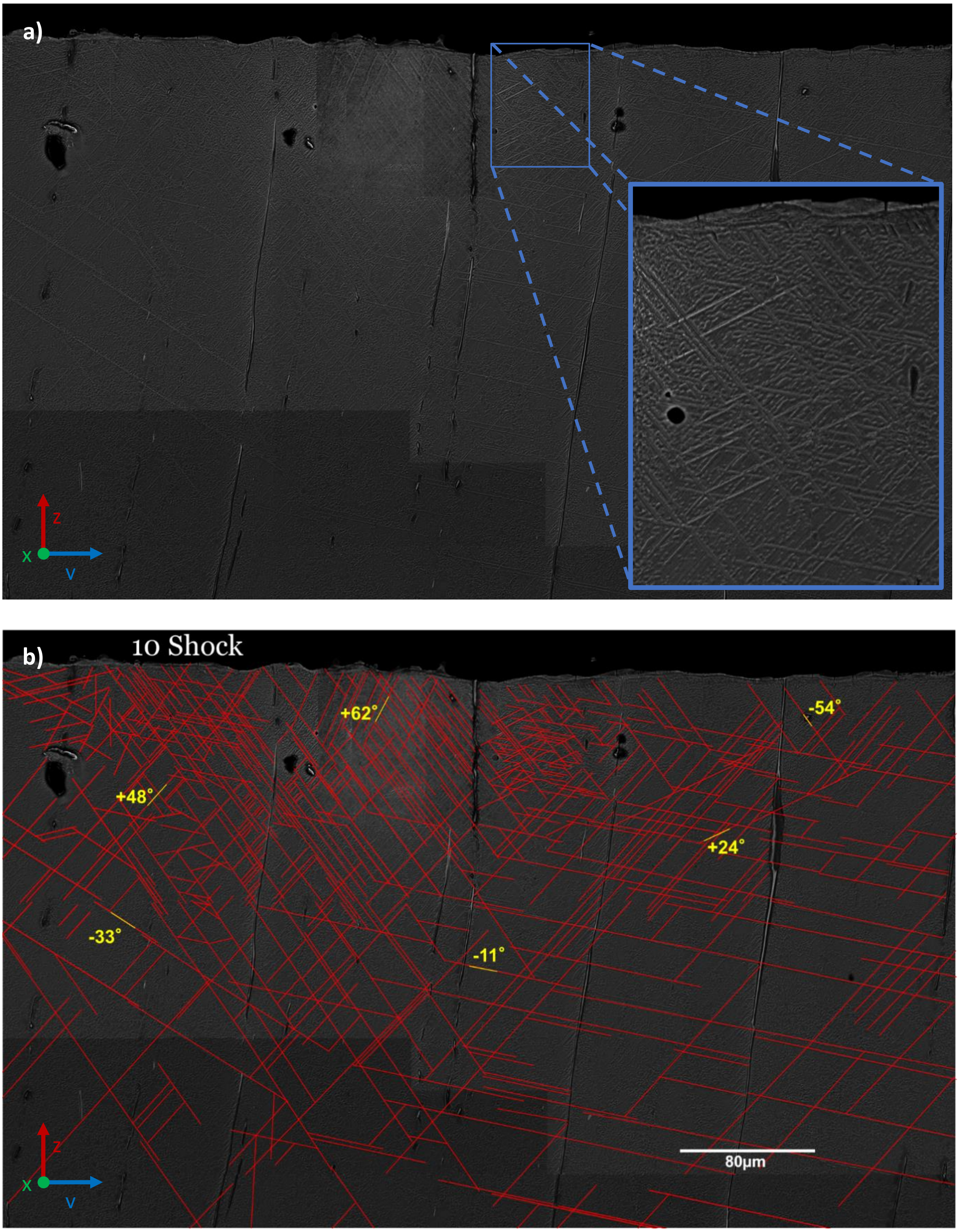

Figure 50: 10-Shock sample cross-sectional BSE a) before and b) after highlighting twins in red across the central shock site. A cutout in blue is seen which clearly shows the twins at increased magnification. The short yellow lines are superimposed on some of the red twins, indicating a group of twins of the same type, with a similar angle relative to the shock surface. These twin groups are summarised in *Table 9*.

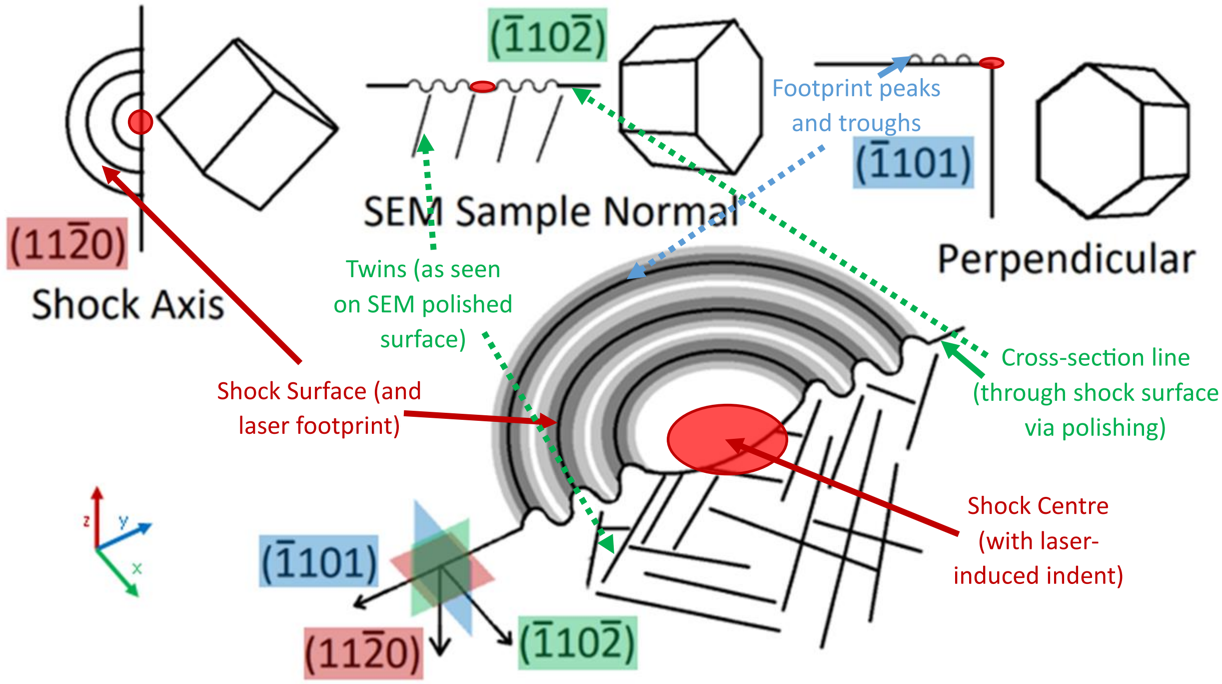

Figure 51: Schematic of the 10-Shock sample with crystallographic orientation. The schematic shows the cross-sectional cut, with the axes identified, complementing the axis system; the normals to $(\bar{1}10\bar{2})$, $-(\bar{1}101)$ and $-(11\bar{2}0)$ correspond to the x, y and z directions, respectively. Label colours are according to the primary plane on which the feature is seen.

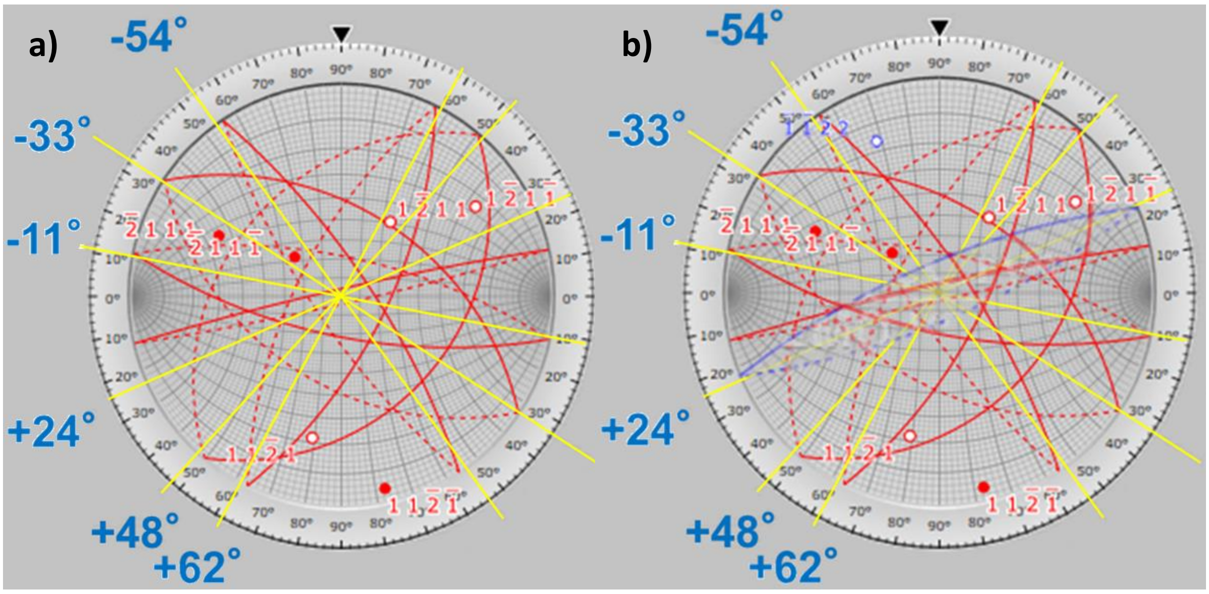

Figure 52: Stereographic projection of the SEM sample with a) all $\{11\bar{2}1\}$ type twins and b) including the most probable alternative twin, $(\bar{1}\bar{1}22)$. This is taken from the cross-sectional surface, as confirmed through TEM Kikuchi diffraction, to be near the perpendicular of the $(\bar{1}10\bar{2})$ plane. Also note some of the $(11\bar{2}\bar{1})$ twins can be seen in the top left of *Figure 50b*, unlabelled, mentioned at an angle of +11° in *Table 9*.

Table 9: Table of 10-Shock sample twins, according to angle from the horizontal, as pictured in *Figure 50b*. The cross-sectional plane is near $(\bar{1}10\bar{2})$. The frequency assessments and region descriptions correspond to those seen in *Figure 50b.*

Twin Angle	**Frequency**	**Primary Regions**	**Secondary Regions**	**Corresponding Theoretical Twin**	**Contraction / Extension (in c)**
-54°	Very Common	Left Surface	Left Deep, Right Surface	-54° $(1\bar{2}1\bar{1})$ **-2°**	Extension
-33°	Uncommon	Left Surface	Left	-33° $(1\bar{2}11)$ **±0°**	Extension
-11°	Common	Deep	Left Surface	-11° $(11\bar{2}1)$ **-1°**	Extension
+24°	Uncommon	Right Surface	Right	+24° $(11\bar{2}\bar{1})$ **-13°** +23° $(\bar{1}\bar{1}22)$ **-1°**	Extension Contraction
+48°	Very Common	Surface	All	+48° $(\bar{2}11\bar{1})$ **+2°**	Extension
+62°	Uncommon	Surface	None	+62° $(\bar{2}111)$ **+2°**	Extension

4.6 Transmission Electron Microscopy (TEM)

Many of the TEM samples made have features that contribute to the understanding of the mechanism behind the microstructural evolution of LS processed commercially pure titanium. The following section is separated according to distance from surface, and in some cases separated by the identification of twins and dislocation analysis. An example of unprocessed material can be seen in Figure 53, which exhibits a few features which pertain to the original microstructure. At the surfaces of the 3, 5, 10 and 15-shock SEM samples, Figure 54, Figure 58, Figure 63 and Figure 64 with Figure 65 can be seen, taken perpendicular to the respective shock surfaces. Both figures Figure 64 and Figure 65 are of 15-shock samples. 250 µm from the shock surfaces, Figure 67, Figure 68, Figure 69 and Figure 71, can be seen, with samples having been taken parallel to the 3, 5, 10 and 15-shock SEM sample surfaces, respectively. Similarly for 500 µm, Figure 75, Figure 76, Figure 77, and Figure 78 samples were taken. Many additional relevant samples are included particularly of the 5 and 10-shock samples as part of general characterisation. Higher magnification images are also found in each section, which highlight some of the features of interest seen in the afore-mentioned samples.

4.6.1 Unprocessed sample (0-Shock)

Of the many TEM samples made from unshocked material, the sample shown in Figure 53 is representative. There is a very low density of dislocations, along with occasional Low Angle Grain Boundaries (LAGBs), one of which appears in Figure 53. These can often be seen in the SEM data, such as in Figures 47.

A few other features are found in the unprocessed sample. These include the small amounts of residual β due to the impurities in the CP Ti. Many of these also appear in the BSE imaging (Figures 47) in thin bright areas between the large α lathes. It is also known that in pure titanium, there may be formation of titanium hydrides, particularly on TEM samples created during and after FIB preparation of TEM samples [109], which may become larger as the samples age. These may be confused with twins due to their morphology, although using accurate TEM imaging, diffraction analysis, and TKD, the distinctions can be made with confidence.

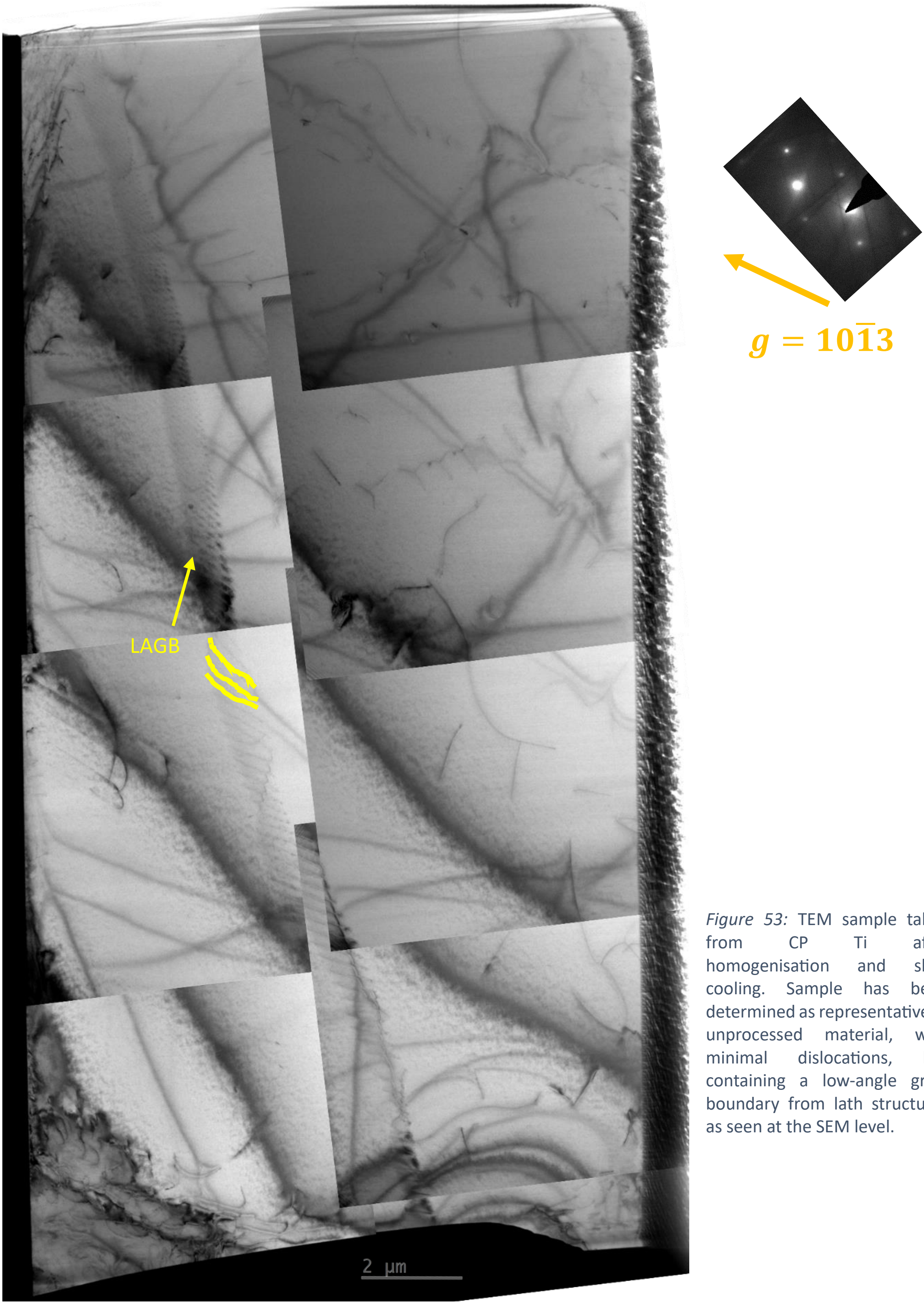

Figure 53: TEM sample taken from CP Ti after homogenisation and slow cooling. Sample has been determined as representative of unprocessed material, with minimal dislocations, but containing a low-angle grain boundary from lath structures as seen at the SEM level.

4.6.2 Depth-based sampling

4.6.2.1 *0 µm, Perpendicular to surface (90°)*

These samples are perpendicular to the surface, with the surface being at 0 µm and the bottom varying in depth depending on the sample. In general, the 0 µm samples are characterised by two main regions, not including the thin layer of amorphous resin or deposited platinum. The region closest to the surfaces (regions A) contain a complicated network most commonly containing twins, but also containing areas which are not identifiable as either twins or part of the main matrix. It is possible that these areas are very densely deformed and could contain nanocrystalline or amorphous regions, although these are insignificant when compared with the twinned regions themselves. The second regions (regions B) begin below (further away from the surface when compared to) region A. This is most notable for how it is densely populated with dislocations, and also contains many long twins, much more sparsely located when compared to region A. These regions, along with a difficult to categorise transition region, are highlighted at the surfaces of the 3, 5, 10 and 15-shock SEM samples taken perpendicular to the respective shock surfaces, seen in Figure 54, Figure 58, Figure 63 and Figure 64 with Figure 65 respectively. It is worth noting that region A also contains many dislocations, but they are much harder to identify in the TEM due to the small twin sizes and difficulty in identifying the matrix in the region compared with other twins (using diffraction methods). Figure 59 depicts region A well. Region B may be characterised by the fact that it is mostly of a single grain (on the scale of the TEM samples produced) in that any grain boundaries may be assumed to be part of the existing microstructure. This matrix is only broken up by twins that are thin and long, and arguably through the nature of the dislocation networks, which will be discussed in future sections [*5.2 Dislocation Networks*].

In the case of the 3-shock sample in Figure 54, region A twinning is very ordered, and appears to have twins forming between larger twins at a sharp angle. This is highlighted in Figure 55, where the twins are identified as $\{10\bar{1}1\}$ -type contraction twins. Additional twins are seen in Region B, with the largest one being of $\{11\bar{2}2\}$ -type, from Figure 56. It will later be discovered that this is the second most common twin type in region B, far outnumbered by $\{11\bar{2}1\}$ -type twins.

Figure 57 depicts a series of SAED patterns found close to the surface of the 3-shock sample, in the afore-mentioned region A. In this figure, the diffraction pattern from area D shows a diffraction pattern of the $1\bar{1}01$ zone axis. Area C depicts the diffraction by the matrix and recently identified (Figure 55) $(10\bar{1}\bar{1})$ twin. Area B shows a complex region containing some twins and other crystal structures, and area A shows diffraction over a twin array, containing multiple reflections, consistent with diffraction patterns of twinning. The SAED from area B clearly shows nanocrystallisation, due to the number of diffraction spots revealed, however as this is positioned below the nano-twinned region, it suggests that a more complicated situation has arisen.

In the case of the 5-shock sample in Figure 58, there is a complicated twinning network in region A which extends to around 5 µm into the sample. Many different twins are seen, and within these some features that appear to be nano-twins are seen (Figure 59), although these are too small to identify within the severely deformed matrix. There are only a few twins seen in region B, and their general structure is the same as that in the 3-shock; they extend very far, usually ending at either the region A boundary (TEM results) or sub-grain boundaries (more commonly seen in the SEM results). Their thicknesses vary from around 20 nm to 300 nm.

A number of dislocation structures seen in the 5-shock samples are highlighted in Figure 60. Dislocation tangles have formed from the high dislocation density in the matrix (Figure 60b). Many of these tangles loop around or join with other tangles to form dislocation cells (Figure 60c). These types features are seen in samples of greater shock numbers also, but have not necessarily been included as separate results. Other features seen include those highlighted in Figure 61. In addition to the twin and dislocation cell found boundaried by both dislocation tangles and the twin itself, we also see a series of lines inside the twins. These lines have been seen in literature to be twin arrays, but it is also possible these are simply Moiré fringes. They present a little differently to the confirmed twin arrays seen in Figure 57A, however we do not wish to discount the possibility that further twin arrays have been seen.

In the case of the 10-shock sample in Figure 63, region A type features extend to approximately 5 µm on the left side of the sample, and around 2 µm on the right of the sample. The sample was ion milled from a region on the shock surface that was on the edge of a ripple i.e. containing both a peak and a trough of the surface profile, formed from the laser shockwave. This explains the reason for the variation in the region A profile, and how it varies by 3 µm in this case. Some variation in this was seen in the 3-shock sample (Figure 54). Many twins of various types are seen in region B.

In the case of the 15-shock sample in Figure 64, the region A type features extend to approximately 3 µm on the left side of the sample, and around 5 µm on the right of the sample. The region A features vary somewhat from previous samples, in that there are some areas between twins that contain further twinning, although not as uniform as those shown in Figure 55 from the 3-shock sample. Many twins of a few types are seen in region B. An additional 15-Shock sample is shown in Figure 65. Although the surface has been milled away through the ion beam preparation, making the size of region A difficult to identify, this sample depicts an interesting feature between 12 µm and 20 µm from the shock surface, as highlighted in Figure 66. The twin structures are similar to those in Figure 55 (of 3-shock material) in both type ($\{10\bar{1}1\}$) and presentation (at an angle between a twin above and below). This is a small area of region A features found in region B.

The identification of the twins in regions A and B will be investigated using transmission Kikuchi diffraction (TKD) more comprehensively than the current isolated TEM investigations. This will be discussed later in [*4.7.1 0 µm, Perpendicular to surface (90°)*], which will enable greater understanding of the twins and their significance in the laser shocked material.

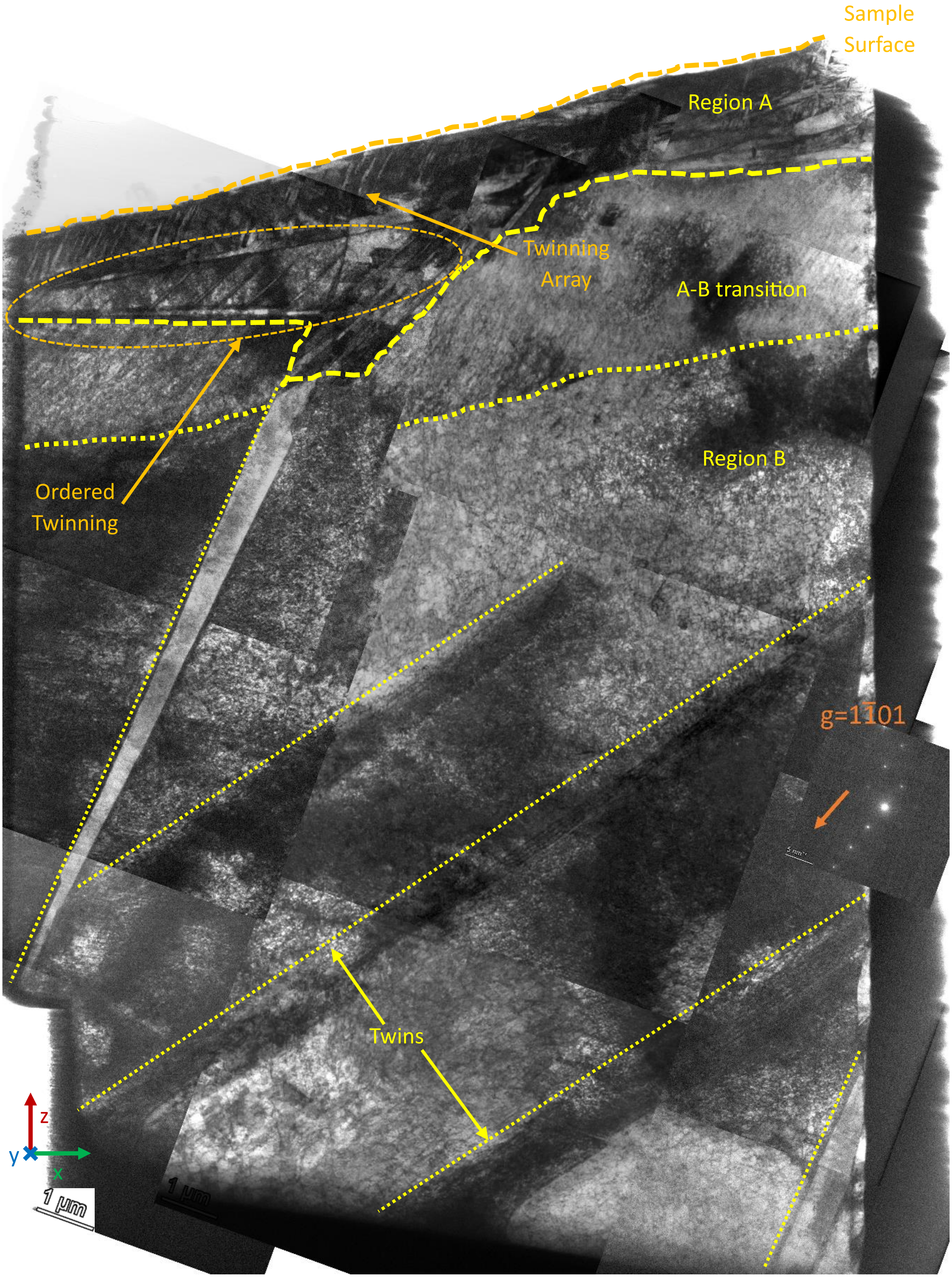

Figure 54: 3-Shock TEM sample taken at the shock surface perpendicular to this surface. Imaged using $g = 1\bar{1}01$. Further analysis can be seen in *Figure 103*. Boundaries are superimposed and labelled. Twins are highlighted in yellow.

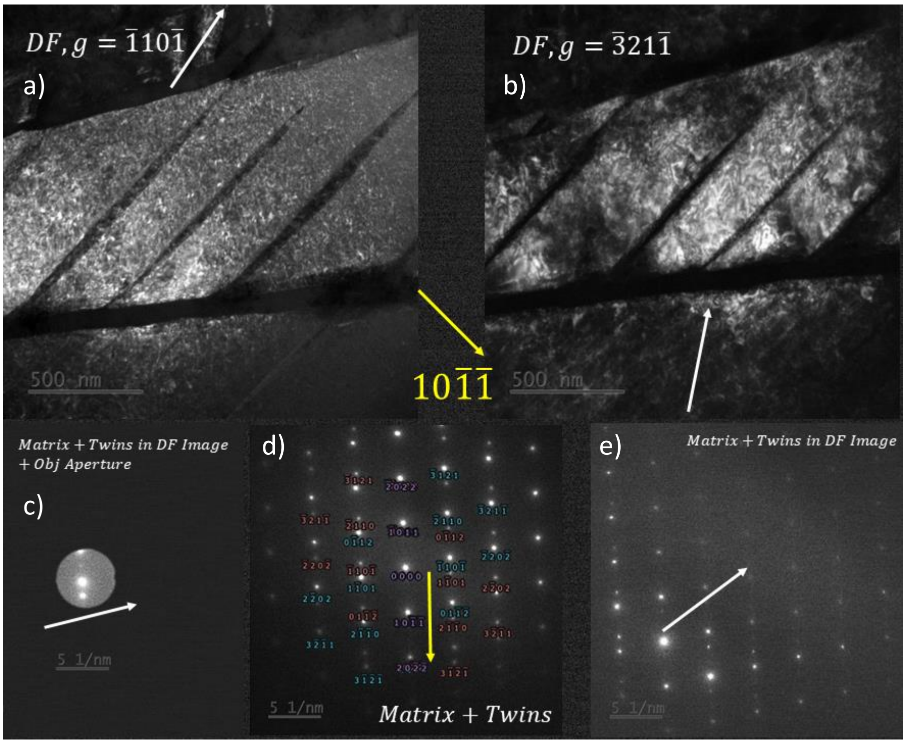

Figure 55: Increased magnification of *Figure 54*. This focuses on the imaging and diffraction of the twins seen near the surface. Imaging conditions and zone axis are labelled where appropriate. Twin type and direction in yellow. Zooming into images may be required.

a) DF image with $g = \bar{1}10\bar{1}$ and c) corresponding diffraction pattern. b) DF image with $g = \bar{3}21\bar{1}$ with e) corresponding diffraction pattern. d) The $01\bar{1}1$ zone axis diffraction pattern with spots corresponding to the matrix in blue, twins in red, and shared spots (along twin plane) in purple.

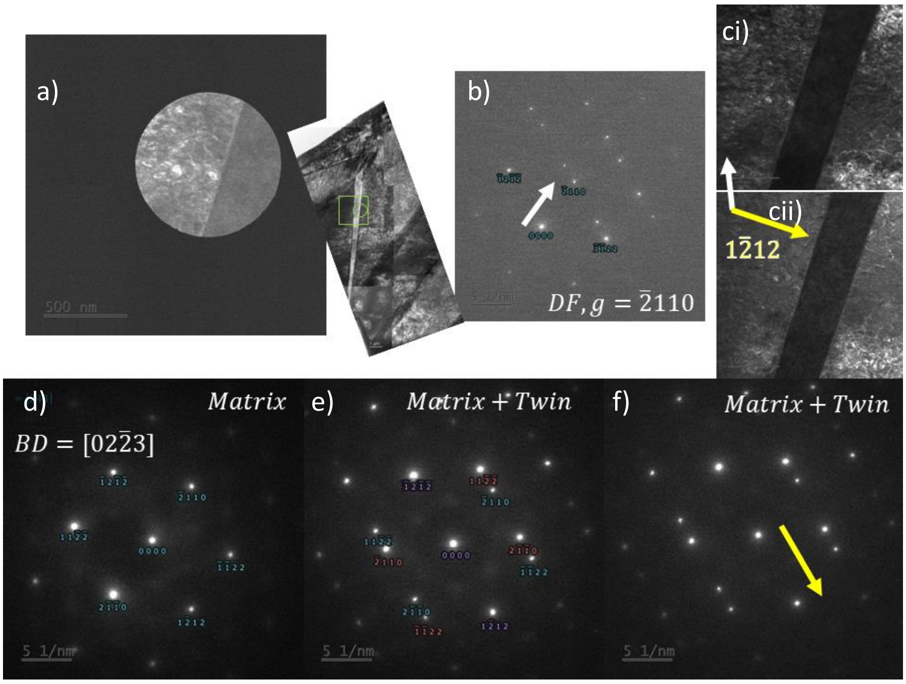

Figure 56: Increased magnification of *Figure 54*. This focuses on the imaging and diffraction of the single large twin starting near the surface. Imaging conditions and zone axis are labelled where appropriate. Twin type and direction in yellow.

a) Selected area aperture over twin and matrix, with cutout of location in main image (*Figure 54*). b) DF diffraction condition of c) DF images where $g = \bar{2}110$. d) Matrix with $BD = 02\bar{2}3$ labelled in blue, and e) twin contribution in red, with shared spots in purple. f) shows the twin direction $(1\bar{2}12)$ on the unlabeled DP.

Figure 57: SAED patterns taken from the 3-Shock surface close to the imaging condition of the matrix $BD = 1\bar{1}01$. A) shows the diffraction in a surface twin array with B) showing a similar location also covering regions outside the twin array. C) Depicts the diffraction pattern of the matrix and a thin twin (also seen in *Figure 54*) whilst D) shows the zone axis pattern within the matrix.

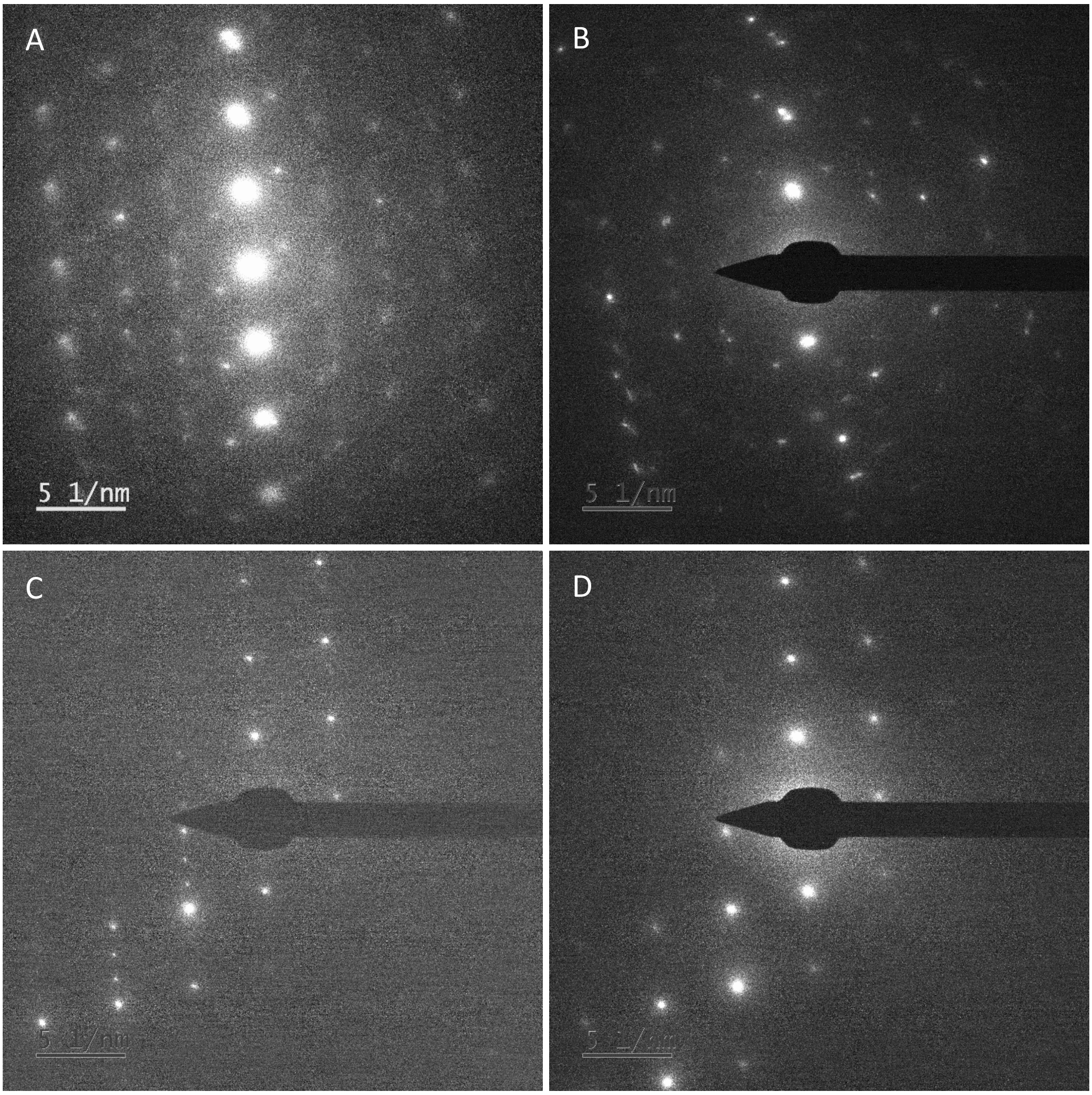

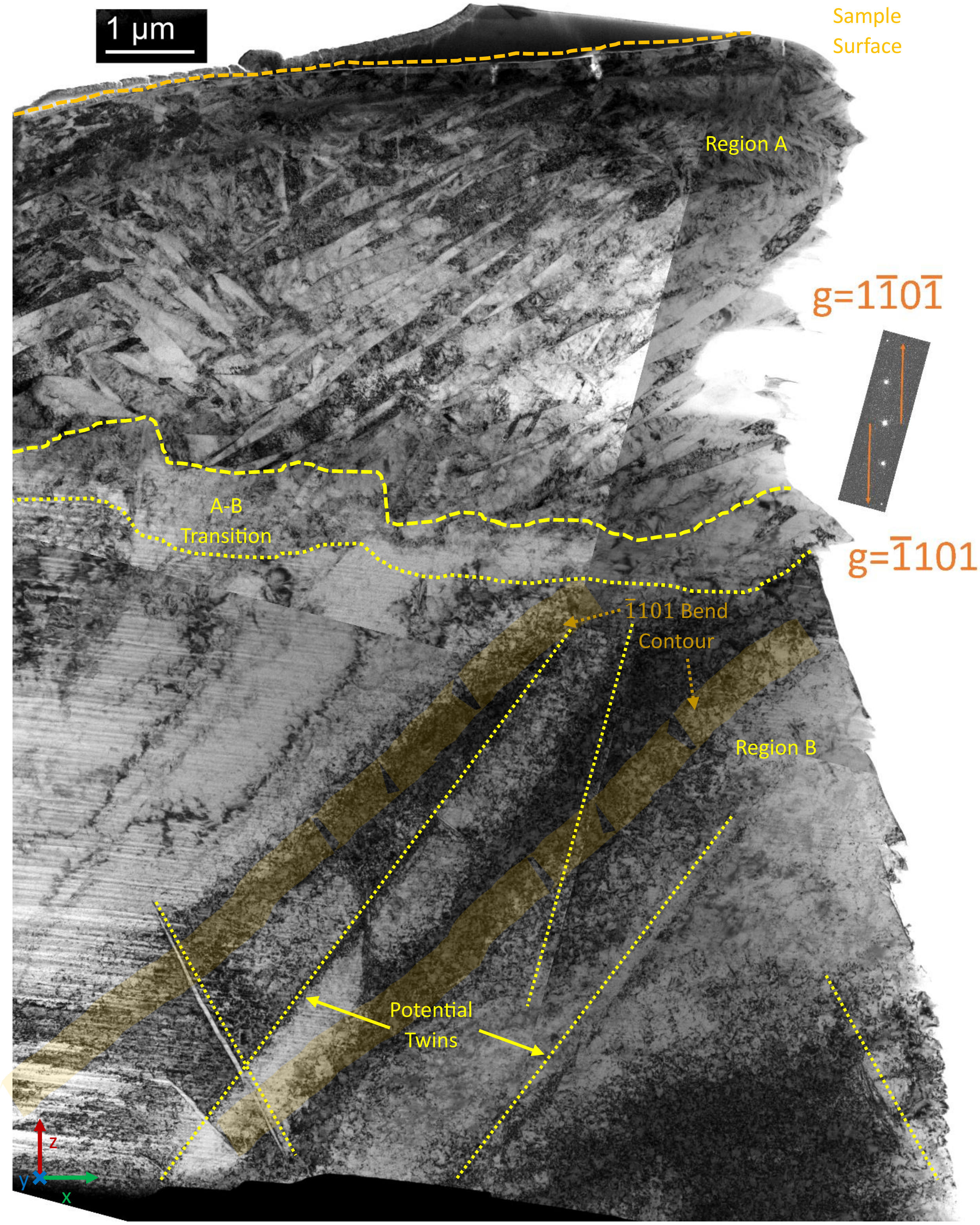

Figure 58: 5-Shock TEM sample taken at the shock surface perpendicular to this surface. Imaged using $g = \bar{1}101$ (below) and $g = 1\bar{1}0\bar{1}$ (above), with approximate bend contour boundaries labelled in translucent orange. Further analysis can be seen in *Figure 104*. Regions are labelled. Potential region B twins are labelled in yellow.

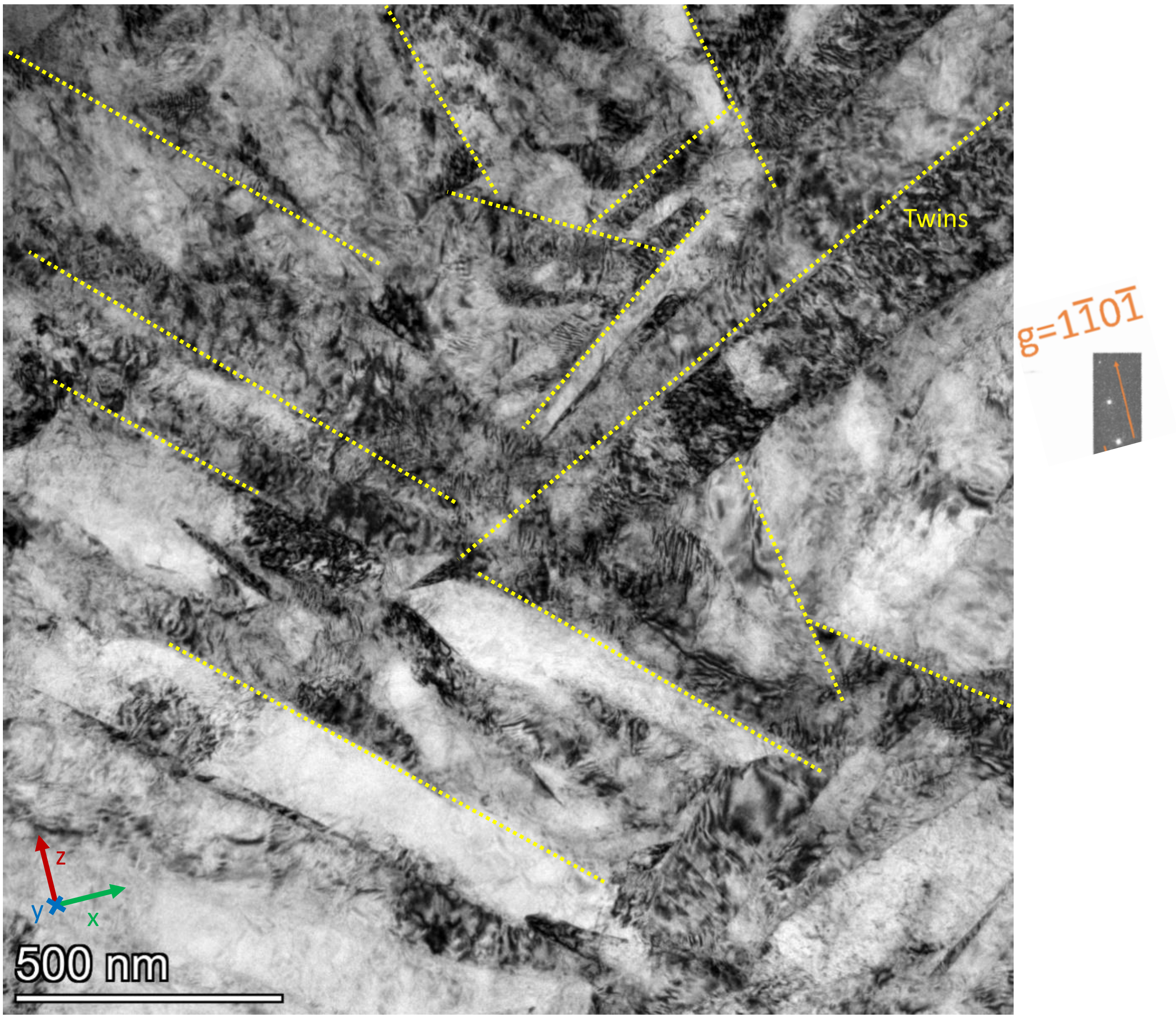

Figure 59: Enlarged image of the heavily twinned area (region A) at the laser shocked surface of the 5-shock specimen, as seen in *Figure 58* (Imaged using $g = \bar{1}10\bar{1}$. Some twins have been highlighted with dotted yellow lines (i.e. labelling is non-exhaustive).

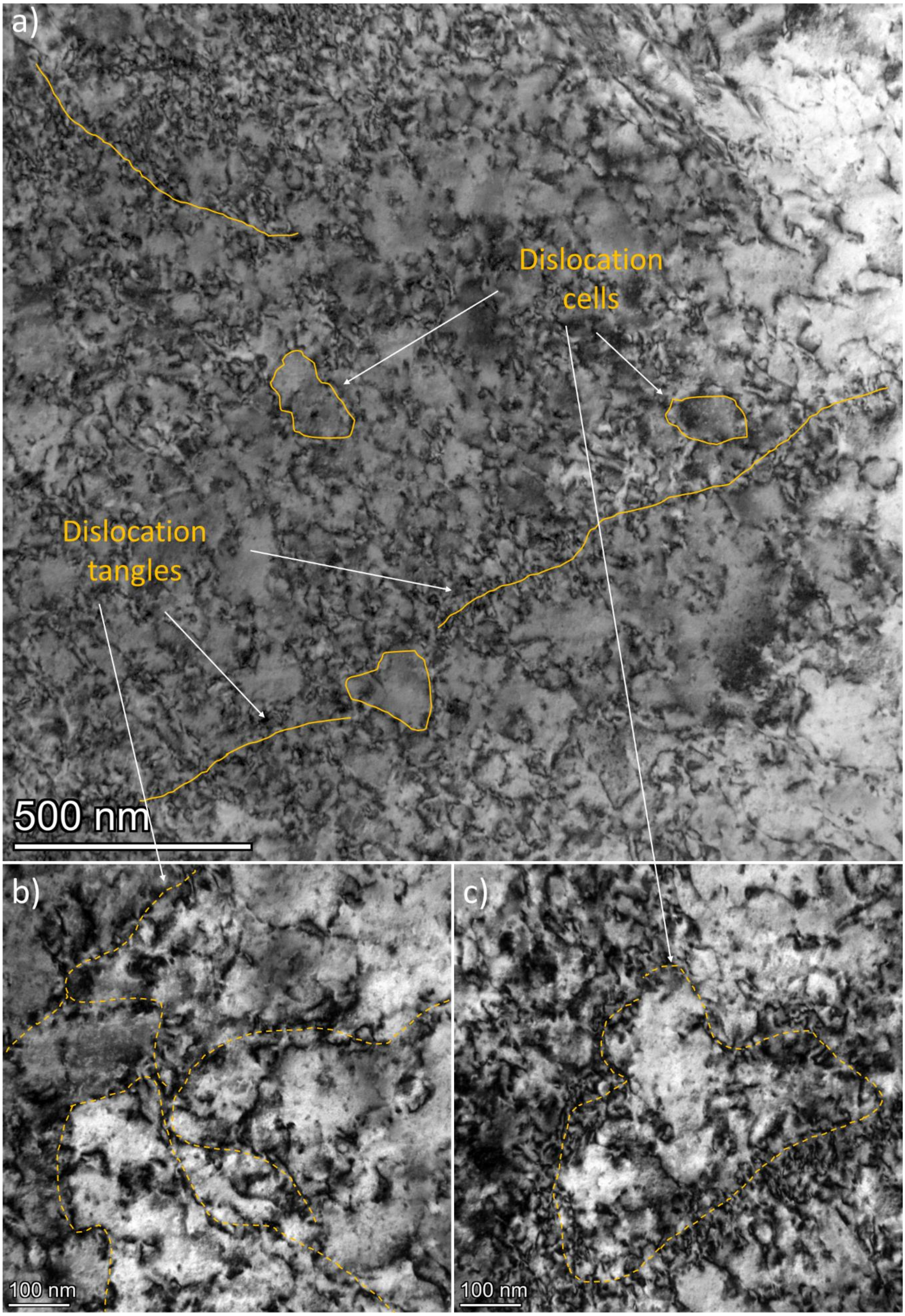

Figure 60: Increased magnification of 5-shock surface sample (*Figure 58*) dislocations with a) both b) dislocation tangles and c) dislocation cells, as highlighted in orange (non-exhaustive).

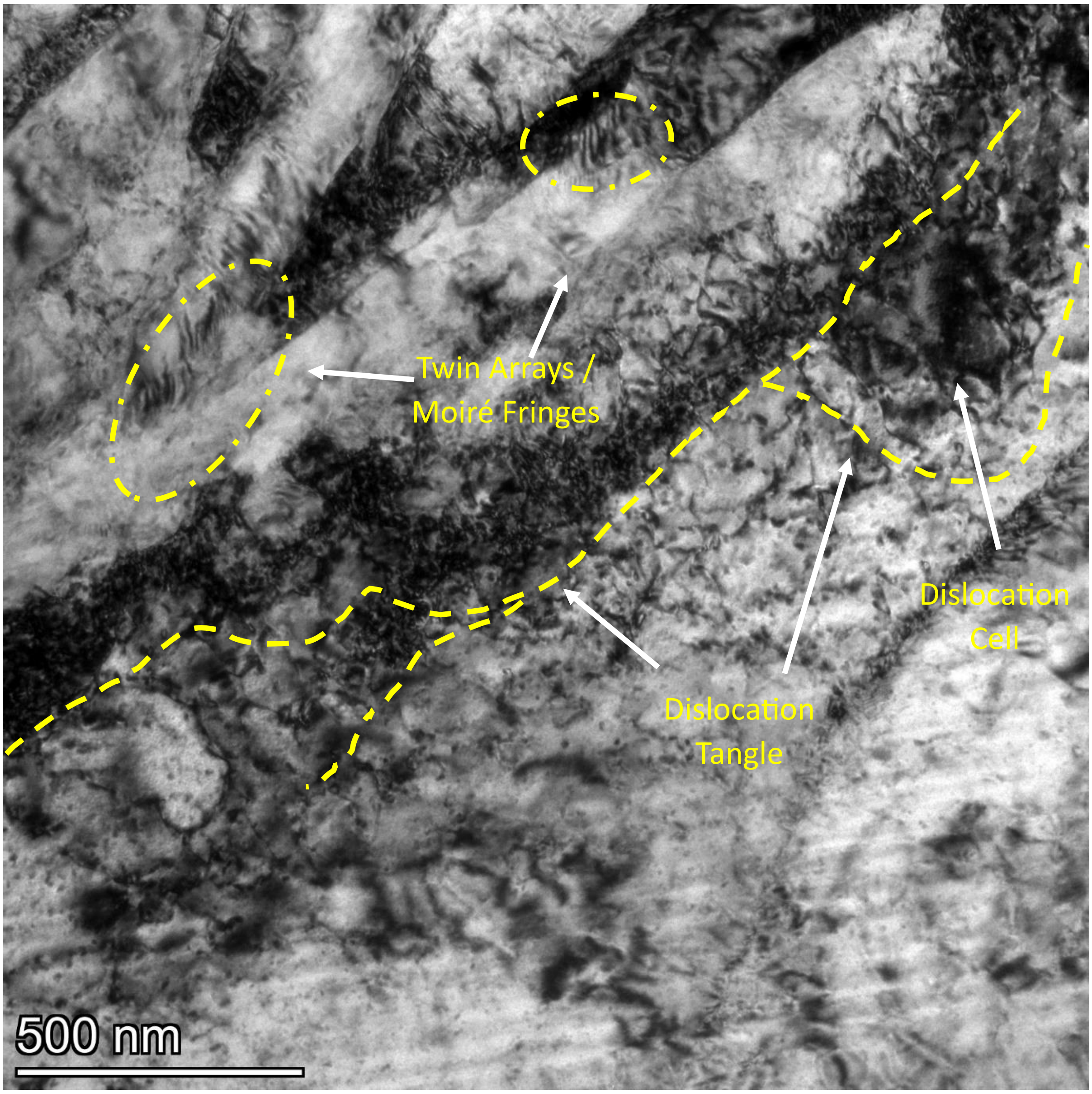

Figure 61: Increased magnification of the 0 µm sample of 5-shocks (*Figure 58*) between region A and B, with twin array's, dislocation tangles and a dislocation cell highlighted.

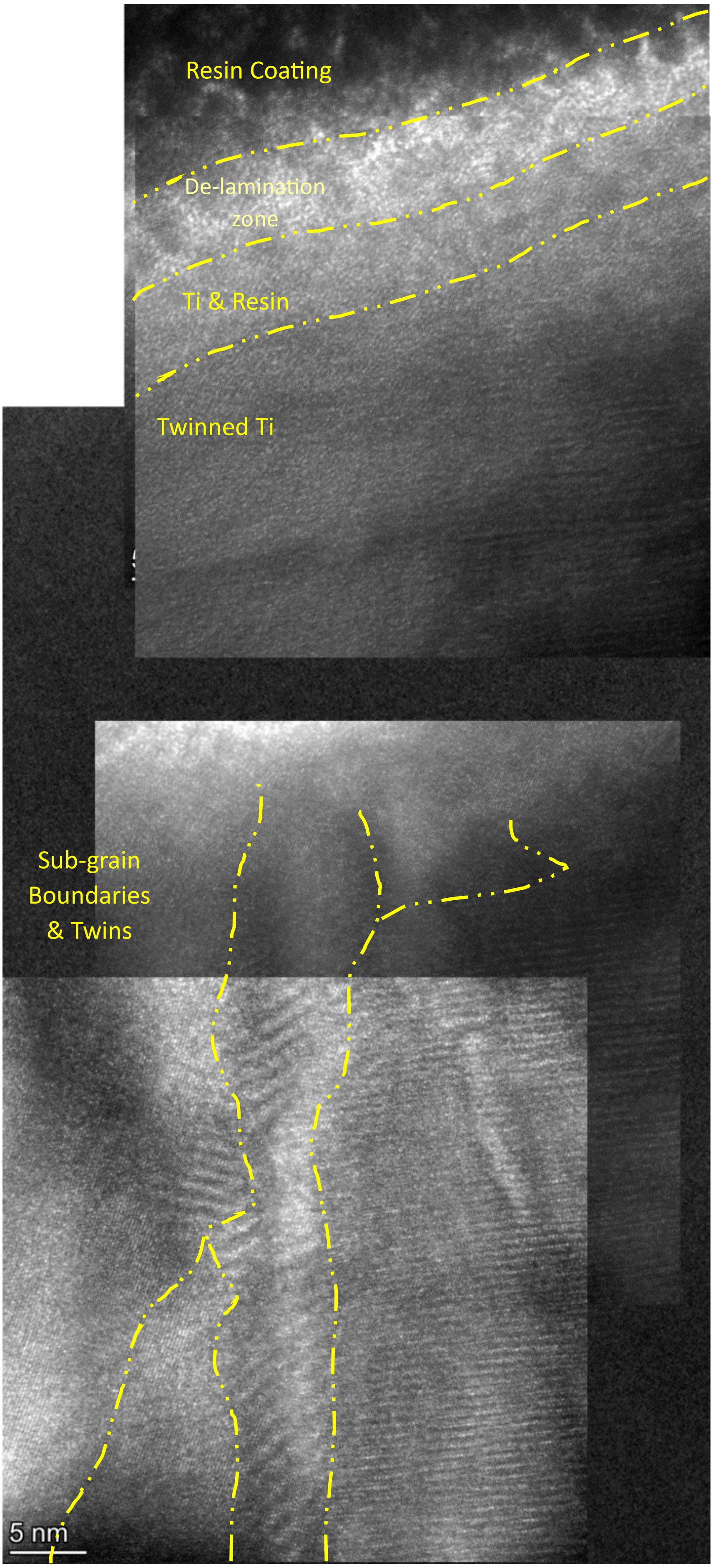

Figure 62: High resolution TEM imaging at the surface of the 5-Shock sample. This shows the resin coating, the region between the resin and titanium, the region containing majority titanium, and the purely titanium region. Some grain boundaries are seen clearer approximately 30 nm deep into the sample. This is shown to be predominantly compromised of twinned areas according to the low magnification images in *Figure 58* and *Figure 59*.

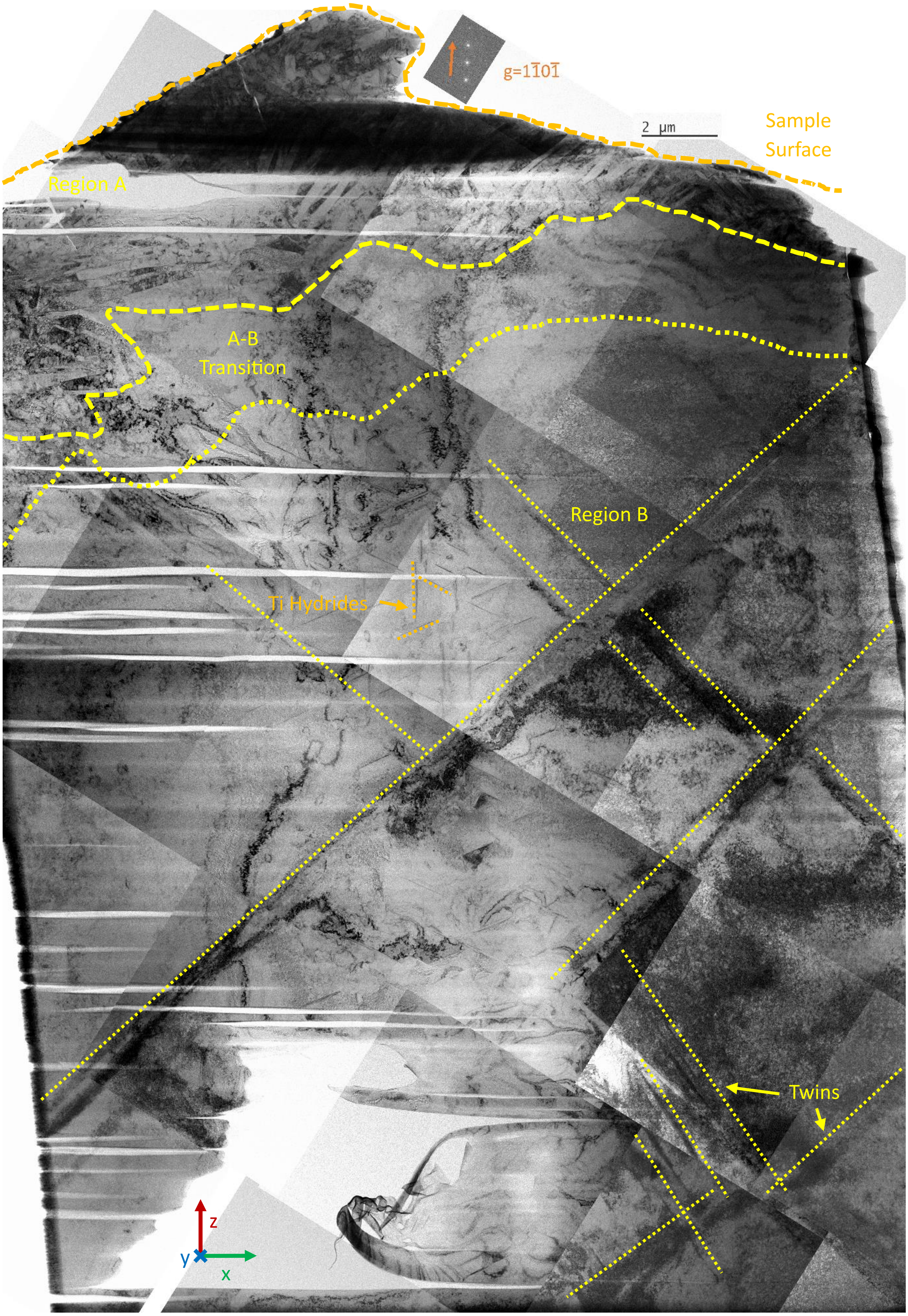

Figure 63: 10-Shock TEM sample taken at the shock surface perpendicular to this surface. Imaged using $g = 1\bar{1}0\bar{1}$. Further analysis can be seen in *Figure 105*. Many twins are seen in yellow, with a few hydrides labelled in orange.

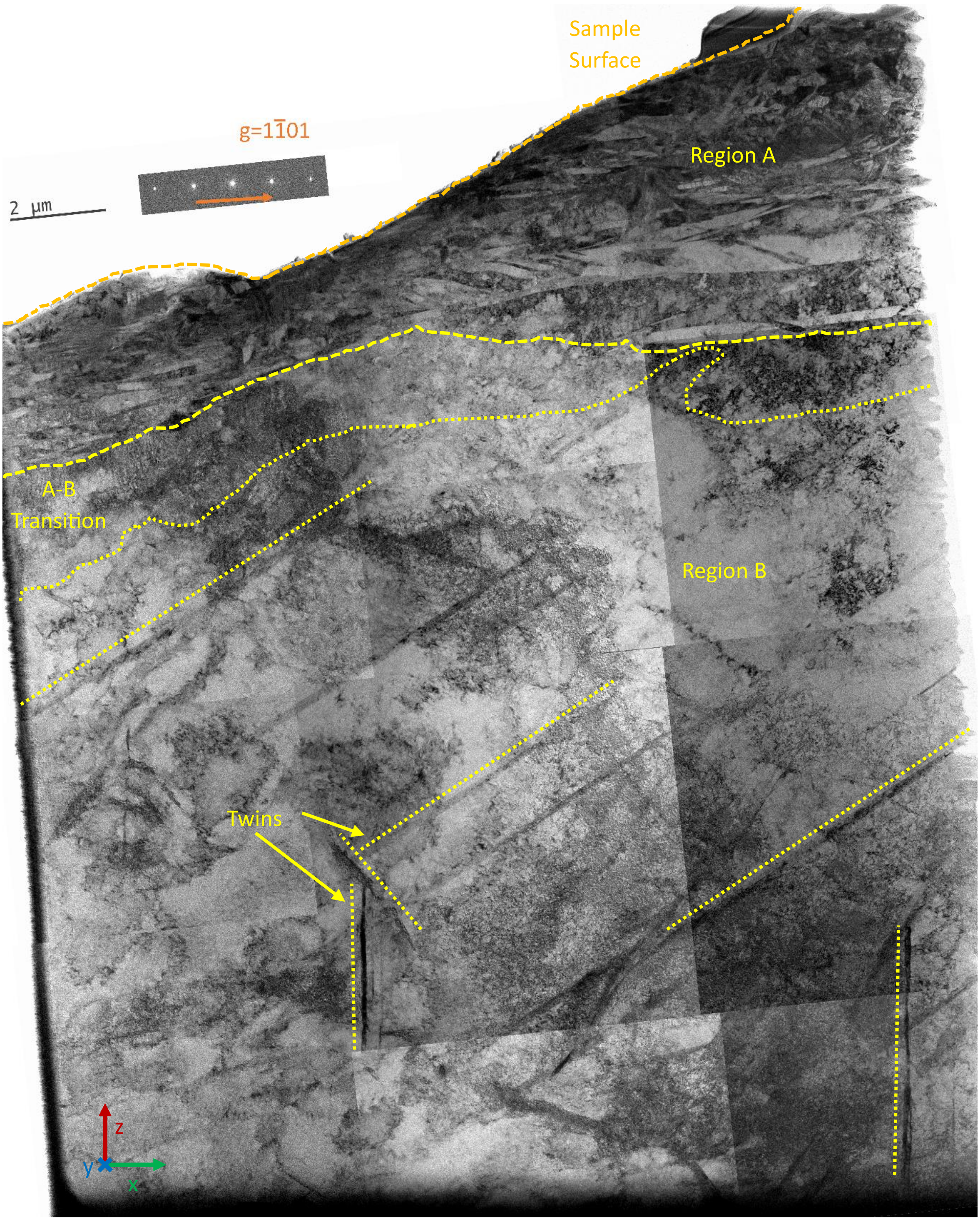

Figure 64: 15-Shock TEM sample taken at the shock surface perpendicular to this surface. Imaged using $g = 1\bar{1}01$. Further analysis can be seen in *Figure 106*. A few twins of the many twins seen are highlighted in yellow.

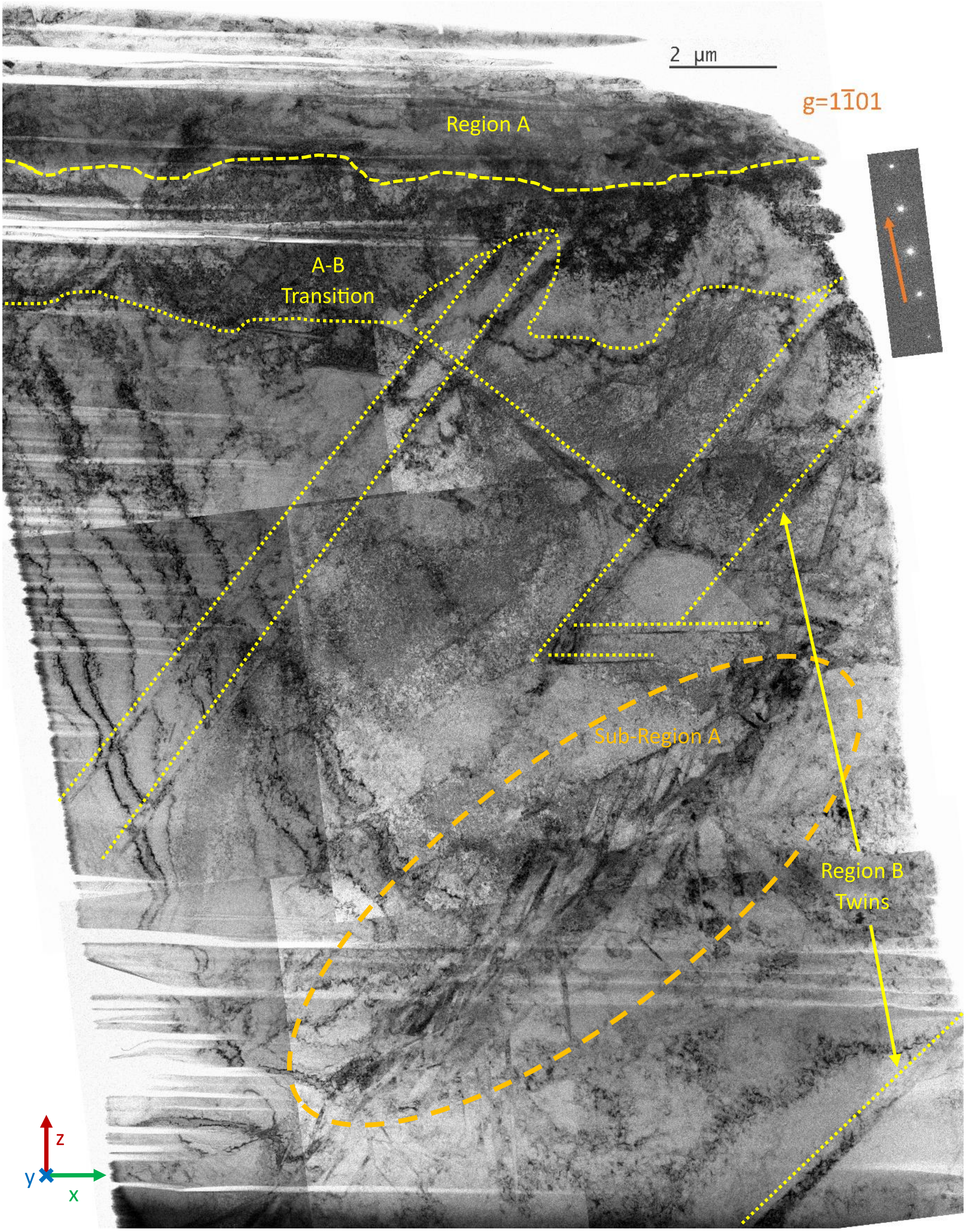

Figure 65: Additional 15-Shock TEM sample taken at the shock surface perpendicular to this surface. Imaged using $g = 1\bar{1}01$. The very surface of the sample has been milled away due to FIB preparation, and as a result begins at an estimated 2 μm away from the surface.

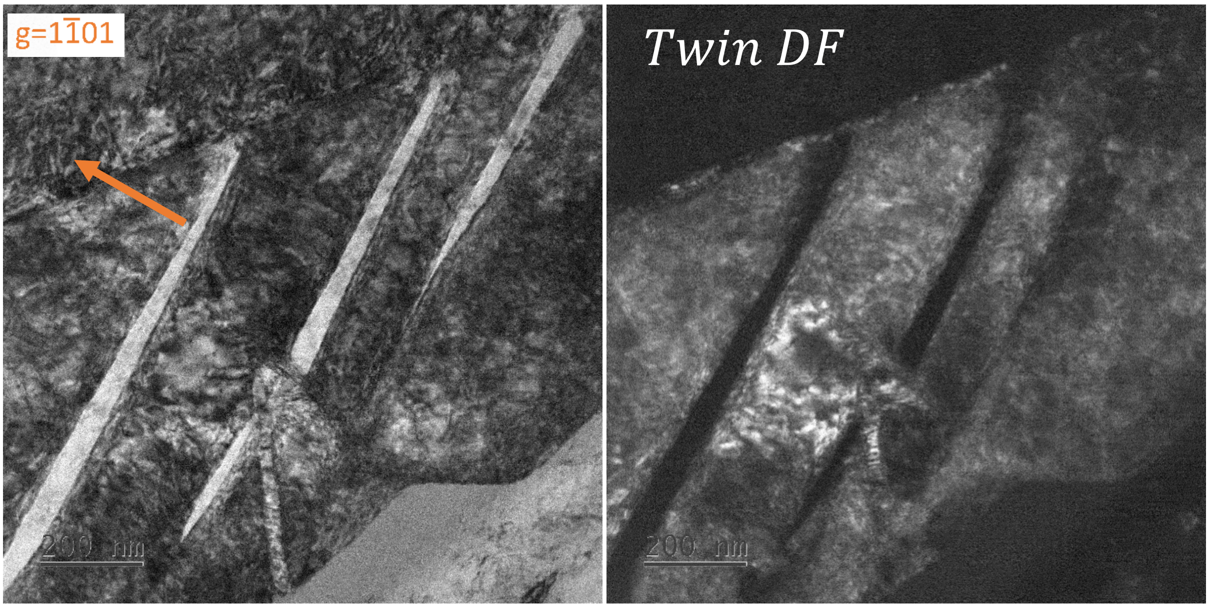

Figure 66: Greater magnification images in BF (Left, $g = 1\bar{1}01$) and DF image (Right, $g = 1\bar{1}01$) of double twinning phenomena (formation of twins between other twins at sharp angle) approximately 13 µm from the 15-Shock surface. This feature is seen in *Figure 65*.

4.6.2.2 250 µm, Parallel to surface (0°)

The 250 µm samples are taken parallel to the surface, such that the entire sample is the same depth from the surface (approximately 250 µm). These are found in Figure 67, Figure 68, Figure 69 and Figure 71, representing the 3, 5, 10 and 15-shock SEM sample surfaces, respectively. The 3 shock sample does not fall within the area over which twinning was seen according to the SEM results (summarised in Figure 49), whilst the other 3 are expected to contain twinning. There are varying numbers of dislocation structures such as tangles and cells, and varying numbers of twins. Some samples were damaged slightly near the cross-sectional surfaces; this is likely due to the mechanical preparation of the SEM samples. These influences have been accounted for and removed, based on other samples and the expected changes induced through LS processing compared to those induced through grinding and polishing.

The 3-Shock sample shown in Figure 67 shows a few dislocations of three regular orientations. In some cases, dislocations appear as dipoles. A dislocation analysis performed on this sample can be found in [*4.6.4.1 Analysis of Dislocations*]. This sample contains a few low angle grain boundaries (LAGBs), which are unlikely to be from the LSP. The 5-shock sample in Figure 68 shows a few groups of dislocations (which is lower than expected, for unknown reasons), however the more significant structures are the 3 to 4 twin-like features.

The 10-Shock sample (Figure 69) dislocations group together into bands, with a much greater density than the undeformed sample. These are found throughout the sample, either side of the low angle grain boundary. Some of these are highlighted in Figure 70, where dislocation lines forming within the bands can be seen. No twins happen to be seen in this sample, however the SEM results and other samples taken from the region show they are there.

The 15-shock sample (Figure 71) contains a large twin (Figure 73), and is surrounded by many dislocations above (Figure 72) and below (Figure 74). Some of these dislocations are grouped into bands, particularly those found beneath the twin. The difference either side of the twin is worth noting, as the dislocation density below the twin seems to be greater than that above the twin, making the dislocation bands more obvious. However, there are many more dislocations located outside of these bands than above the twin. This difference in dislocation density is a possible indication that the twin has influenced the laser shockwave, reducing the amplitude of the shockwave, thereby decreasing the dislocation density in the sample after the twin. This is challenging to confirm, as we are unsure which side of the twin on the Figure 71 micrograph is closer to the shock surface.

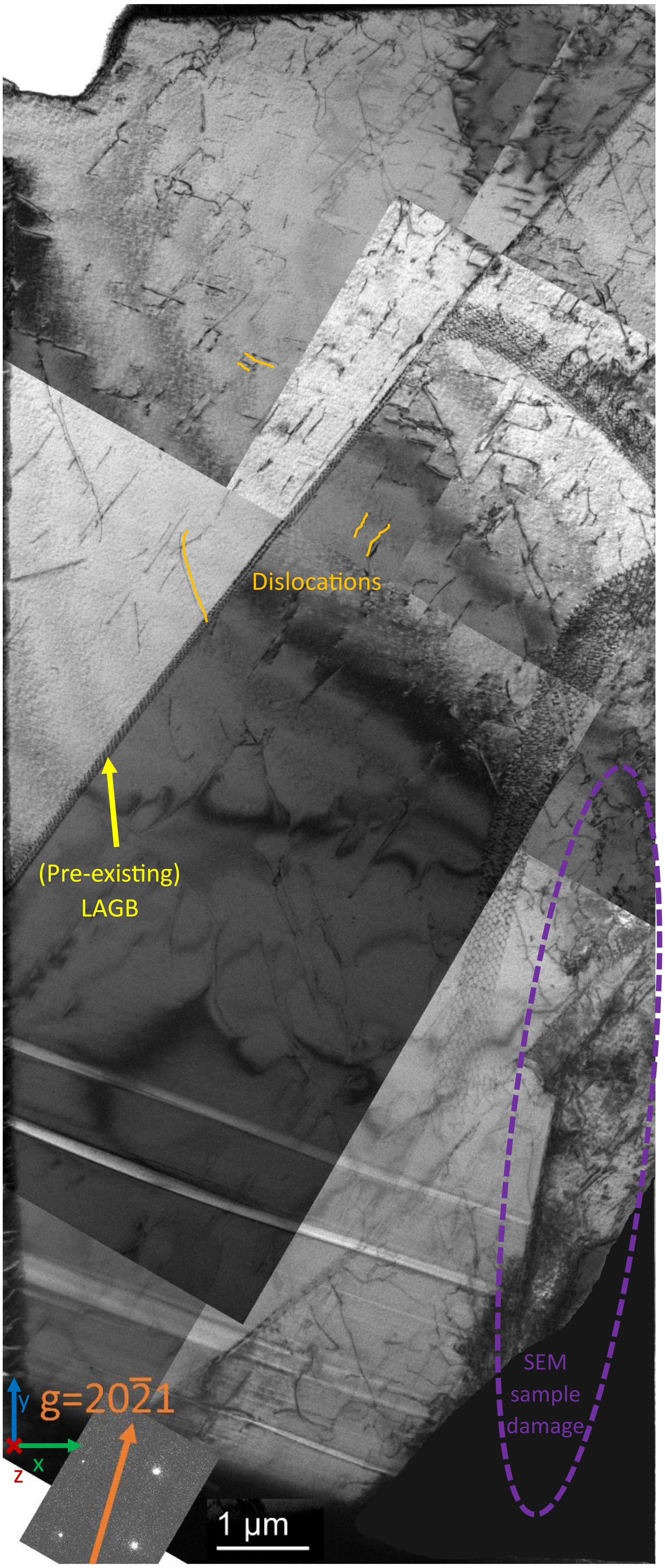

Figure 67: 3-Shock TEM sample taken 250 μm from the shock surface parallel to this surface. Imaged using $g = 20\bar{2}1$. Further analysis can be seen in *Figure 107*. This sample has also been used to perform dislocation analysis of dislocation lines seen away from sample's surfaces, as seen in Section *4.6.4.1*. Dislocations are non-exhaustively labelled in orange, many of which are dipoles. SEM sample damage can be found to be most significant towards the surface on the right side of the image, with the most obvious region indicated with purple oval.

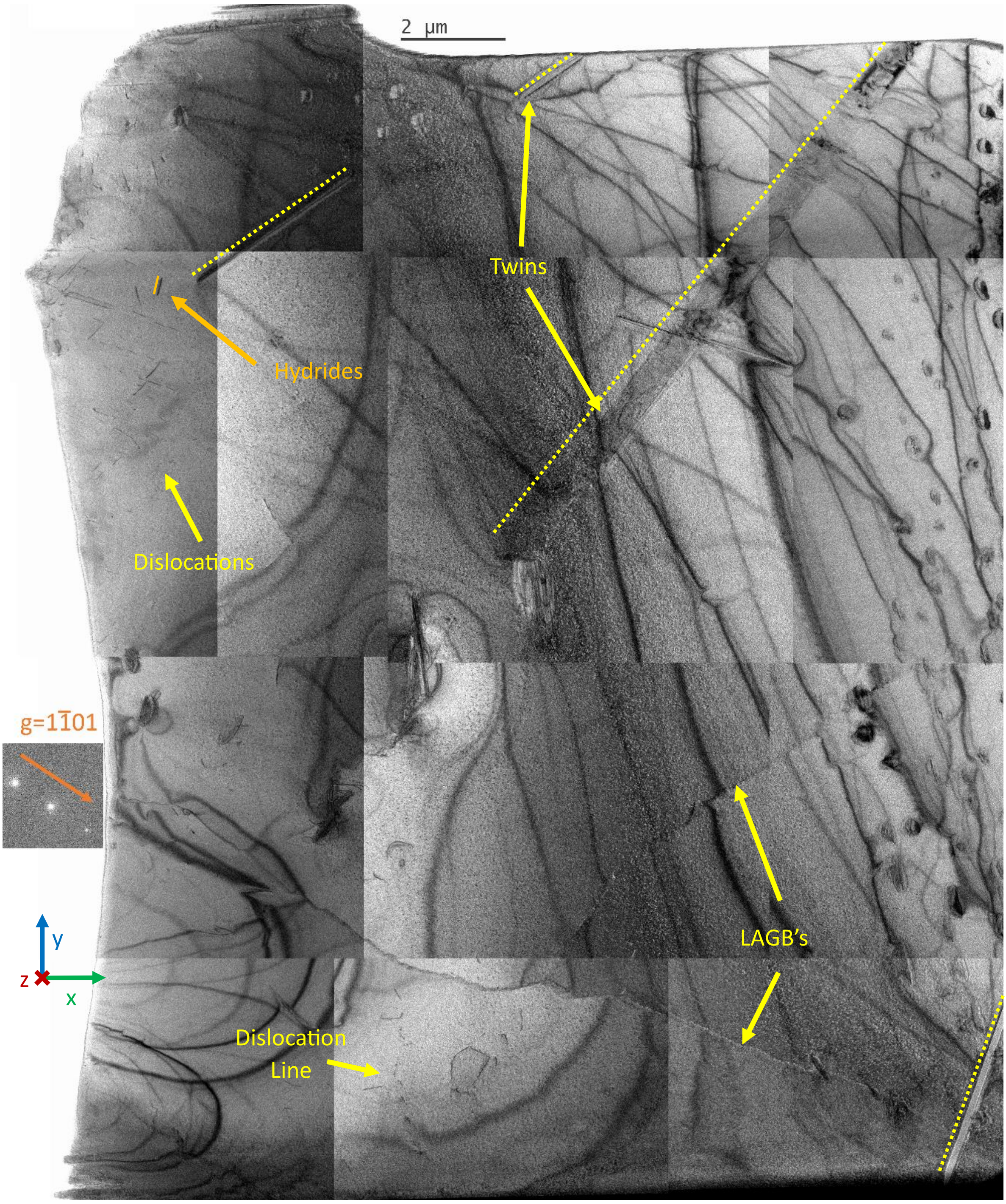

Figure 68: 5-Shock TEM sample taken 250 µm from the shock surface parallel to this surface. Imaged using $g = 1\bar{1}01$. Further analysis can be seen in *Figure 108*. Some dislocations are labelled, and although hydrides were found it is difficult to separate them from dislocations due to how small they are. LAGB's are assumed to be pre-existing. 4 possible twins are identified.

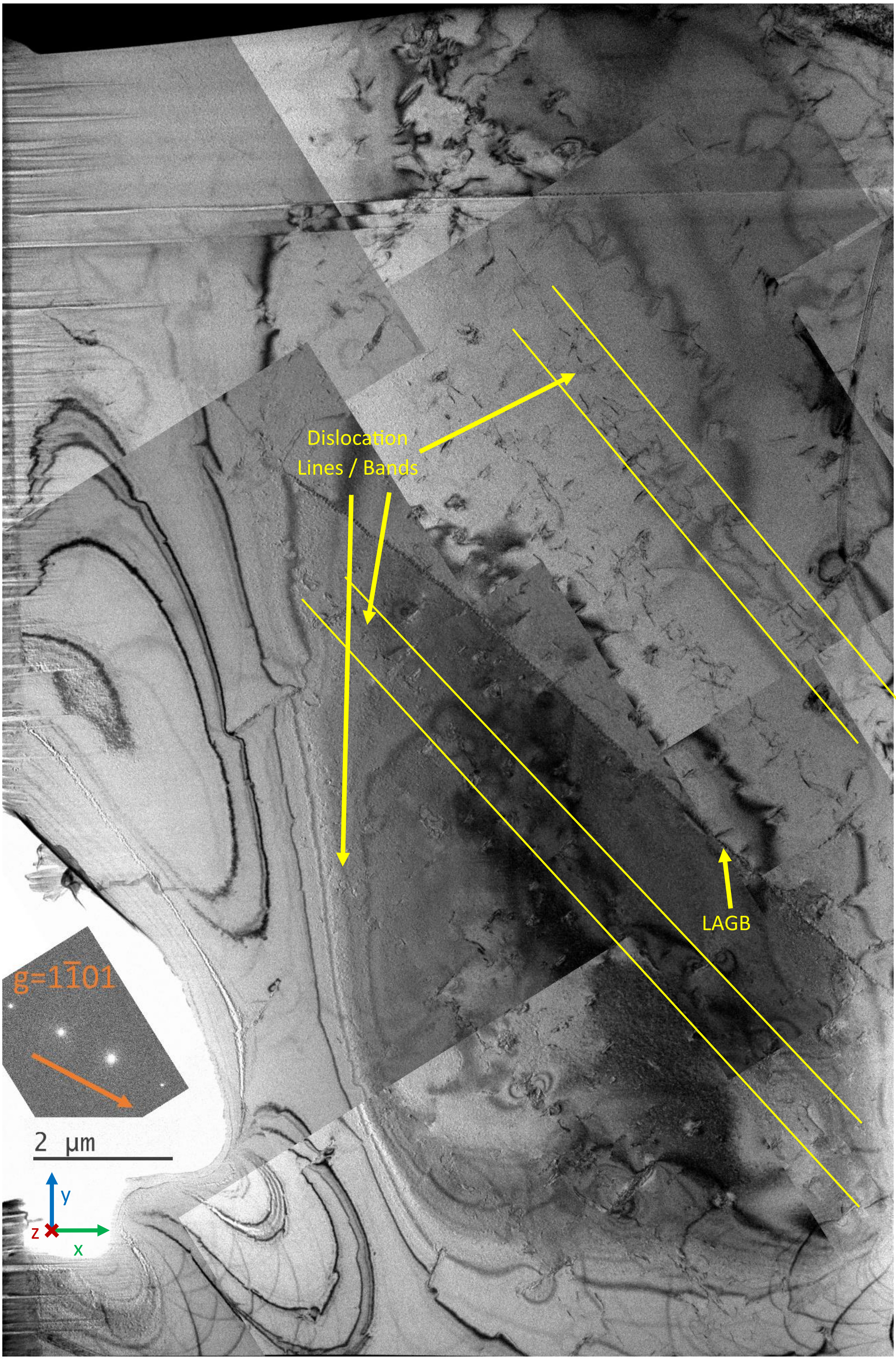

Figure 69: 10-Shock TEM sample taken 250 µm from the shock surface parallel to this surface. Imaged using $g = 1\bar{1}01$. Further analysis can be seen in *Figure 109*. Dislocation bands are labelled non-exhaustively.

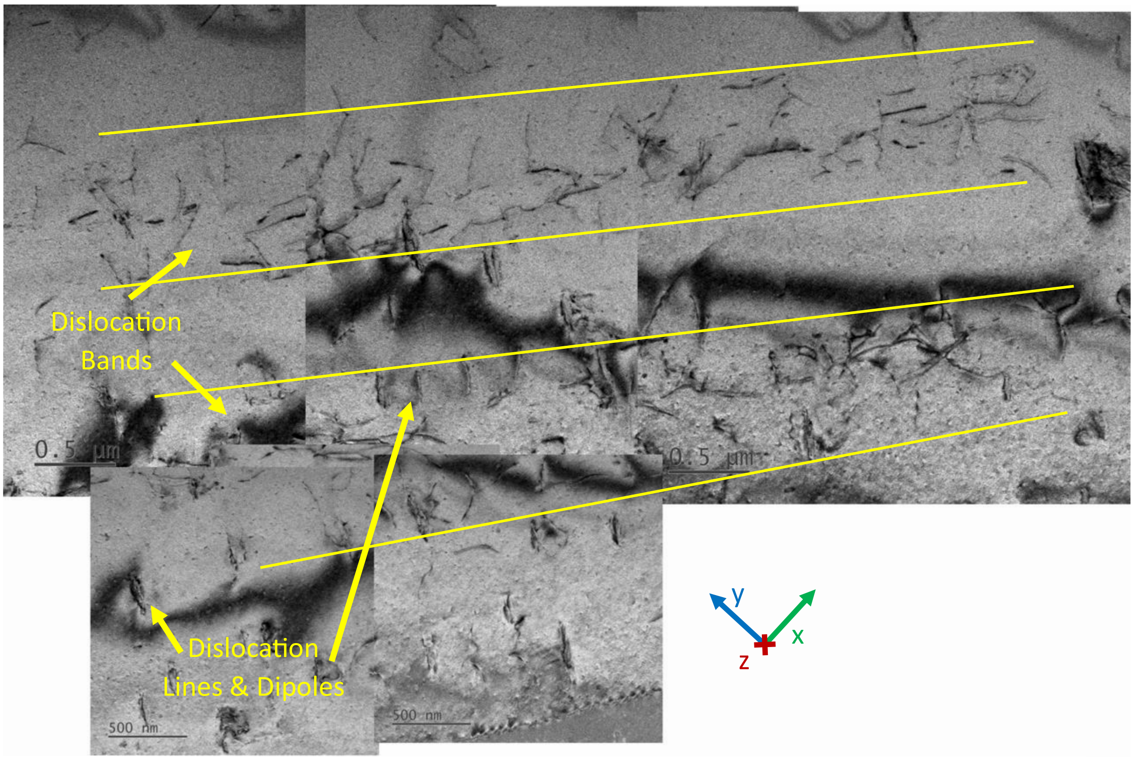

Figure 70: Greater magnification images of dislocation lines seen in the 10-Shock specimen at 250 µm depth. LM image seen in *Figure 69*.

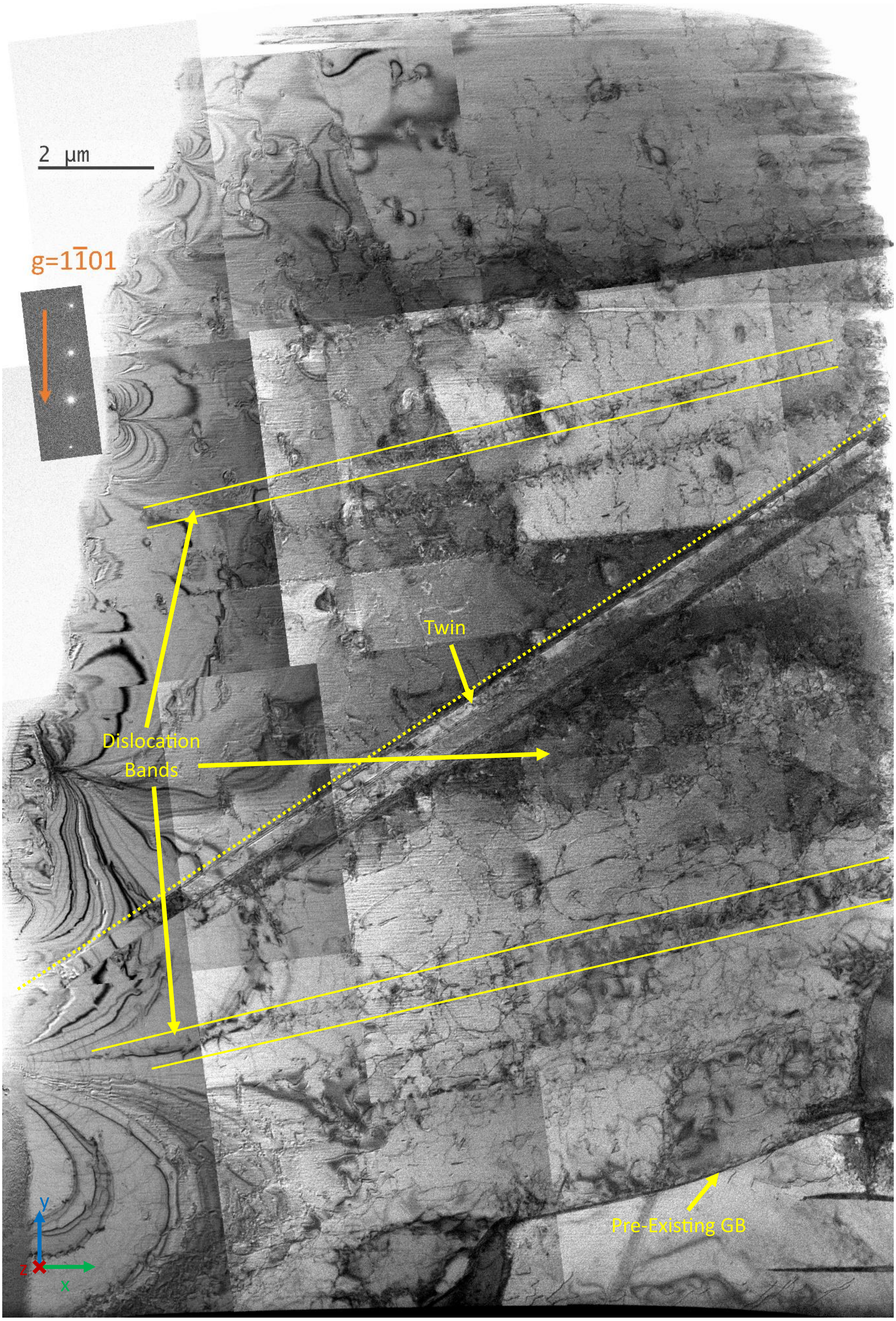

Figure 71: 15-Shock TEM sample taken 250 µm from the shock surface parallel to this surface. Imaged using $g = 1\bar{1}01$. Further analysis can be seen in *Figure 110*. Dislocation bands are labelled non-exhaustively.

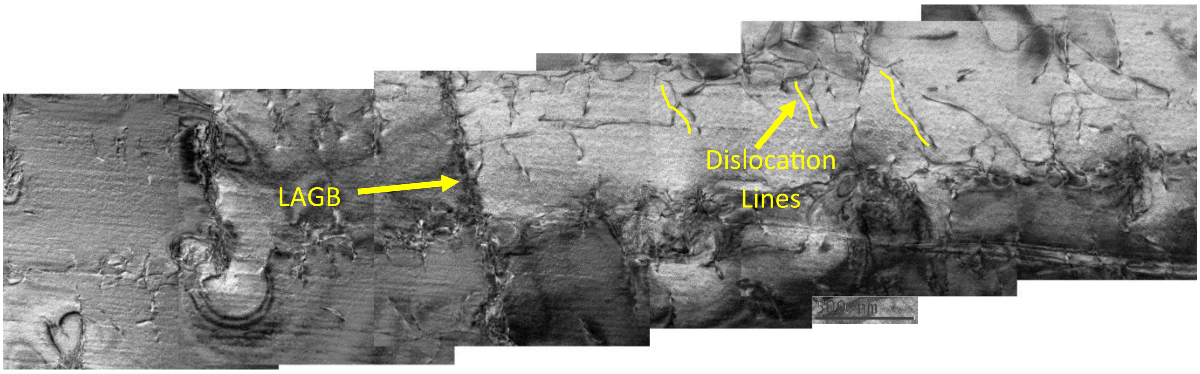

Figure 72: Increased magnification image of *Figure 71*, taken above the twin. This highlights a series of dislocation lines, and how they pass through the low angle grain boundary (lamella boundary).

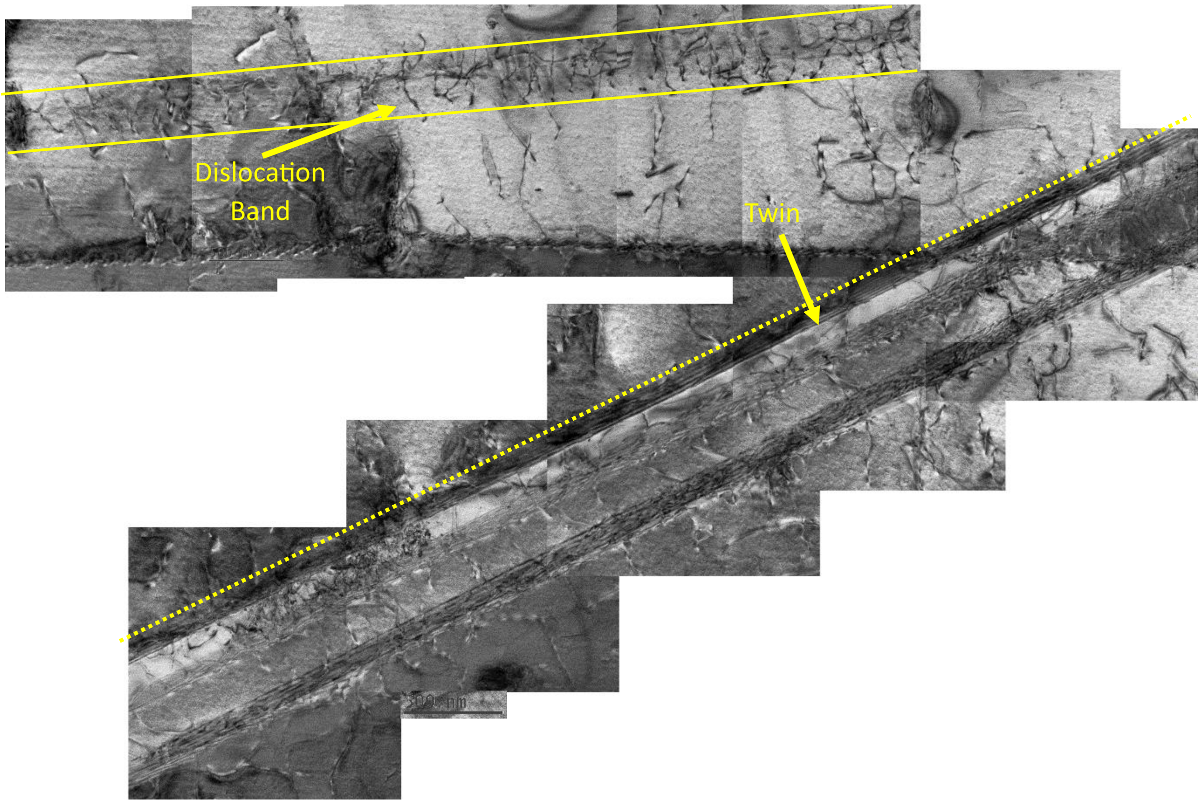

Figure 73: Increased magnification image of *Figure 71*, taken just above the twin and of the twin itself. This highlights a series of dislocation lines, and depicts some of the dislocations found within the twin. Dislocations can be seen above and below the twin.

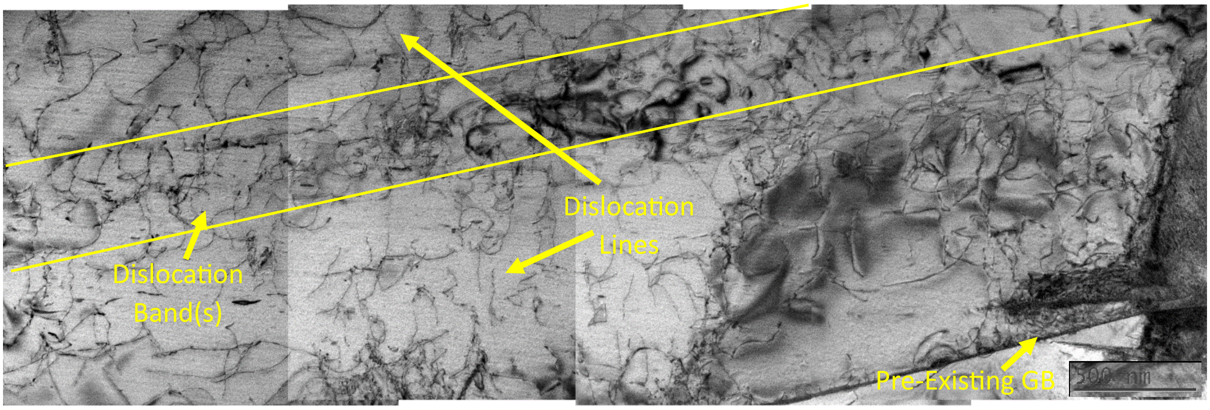

Figure 74: Increased magnification image of *Figure 71*, taken below the twin. This highlights a series of dislocation lines, although the uniformity exhibited above the twin is lost, showing that the microstructure can vary significantly over short distances. This may indicate the twin has affected the shockwave progression.

4.6.2.3 500 µm, Parallel to surface (0°)

The 500 µm samples are very similar to the 250 µm samples (as opposed to the 0 µm samples) however, the LSP induced dislocation and twin features seen are fewer. Figure 75, Figure 76, Figure 77, and Figure 78 correspond to the 3, 5, 10 and 15-shock samples, respectively. The 3-shock sample (Figure 75) contains very little of interest, with a few dislocations near the cross-sectional surface due to sample polishing, and a small quantity of residual β Ti phase. It is safe to assume neither of these were induced through LSP, leaving the region unaffected. As a reminder, Figure 49 illustrates that the SEM results show twinning in the 10 and 15-shock samples but not in the 3 or 5-shock samples.

The 5-shock sample (Figure 76) did contain a twin. It is not known how this occurred, however, as this was not seen clearly with the SEM imaging. This sample was affected by hydridation in the bulk specimen, which made the identification of dislocation structures challenging. This region already demonstrated differences to the bulk specimen (hydridation of many different sizes), so it is possible this location contains unusual pre-existing damage of other forms (twinning), or has been affected unexpectedly by the shockwave progression. In either instance, the assertion that the twin was produced through LSP is unreliable. The reason why this is still included, is because if the twin was produced as a result of both existing damage and the shockwave progression, it is an example of how the microstructural evolution resulting from LSP is complex and twin production requires nucleation sites within the matrix. Hydrides may provide such nucleation sites, however this would require significantly more work to confirm. The twin type was not reliably identified due to the high angle required to provide the edge-on condition in the SEM, however diffraction patterns taken did indicate twinning.

Another far simpler explanation, is that the SEM imaging was inadequate in determining the boundaries of the area over which twins are seen. However, this is the only sample that does not match reasonably well with the cross-sectional micrograph results procured.

The 10-shock sample (Figure 77) also contained dislocations, some possibly in the form of dislocation lines. This is corroborated by another sample taken at the same depth but at a -11° angle to the shock surface (see Figure 82 and Figure 83). This sample was subjected to similar challenges in analysis as the 5-shock sample due to the significant hydridation. Twins were seen in this and other samples (see [*4.6.3 Twin Identification and Analysis*]), as expected from the SEM results.

The 15-shock sample (Figure 78) clearly shows many dislocation lines, highlighted in Figure 79 and Figure 80. It is argued that these dislocation lines either are dislocation bands, or are proto-dislocation bands, most evidenced by the other dislocations collecting at the dislocation line depicted in Figure 79. The dislocation lines continue through most LAGB's, although there can be a minor change in dislocation density or spacing. At the bottom of the sample (Figure 78) a different grain is seen. The direction of the progression of the dislocation lines changes in the new grain.

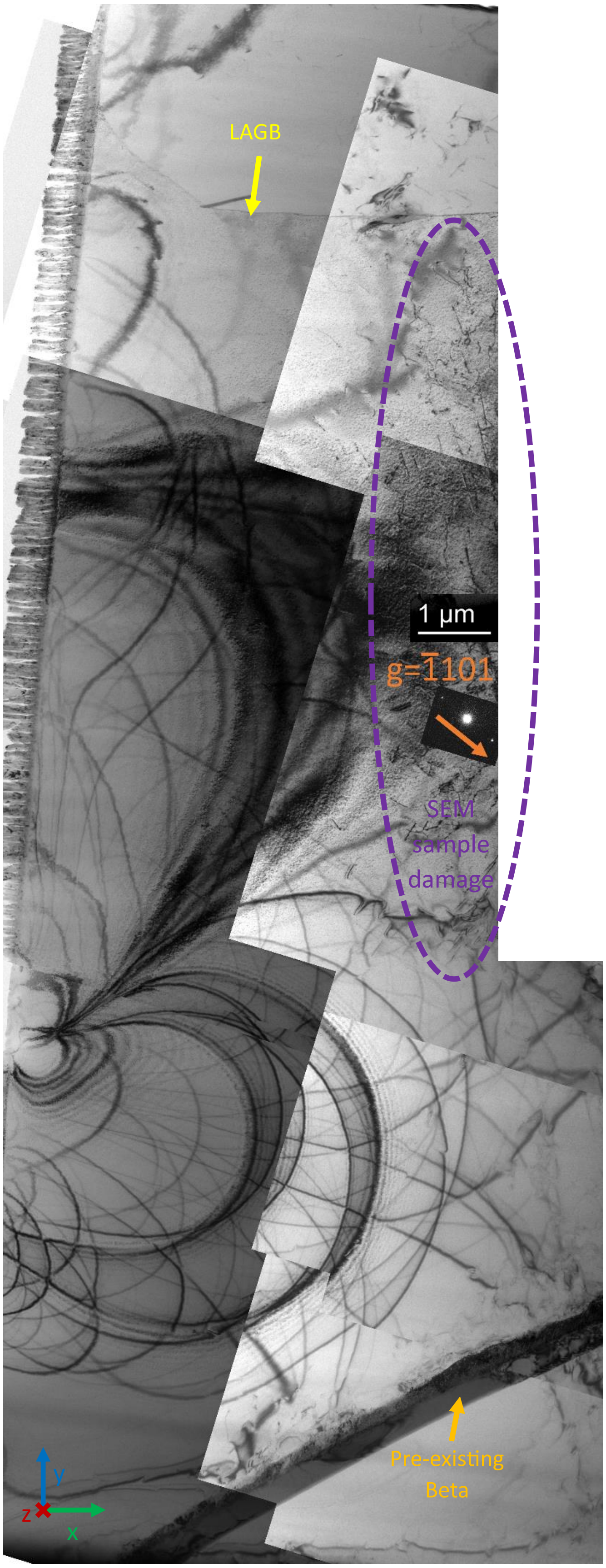

Figure 75: 3-Shock TEM sample taken 500 µm from the shock surface whilst parallel to this surface. Imaged at the condition $g = \bar{1}101$. The sample sustained some mechanical damage from grinding/polishing stage, circled in purple. This sample shows no new signs of deformation.

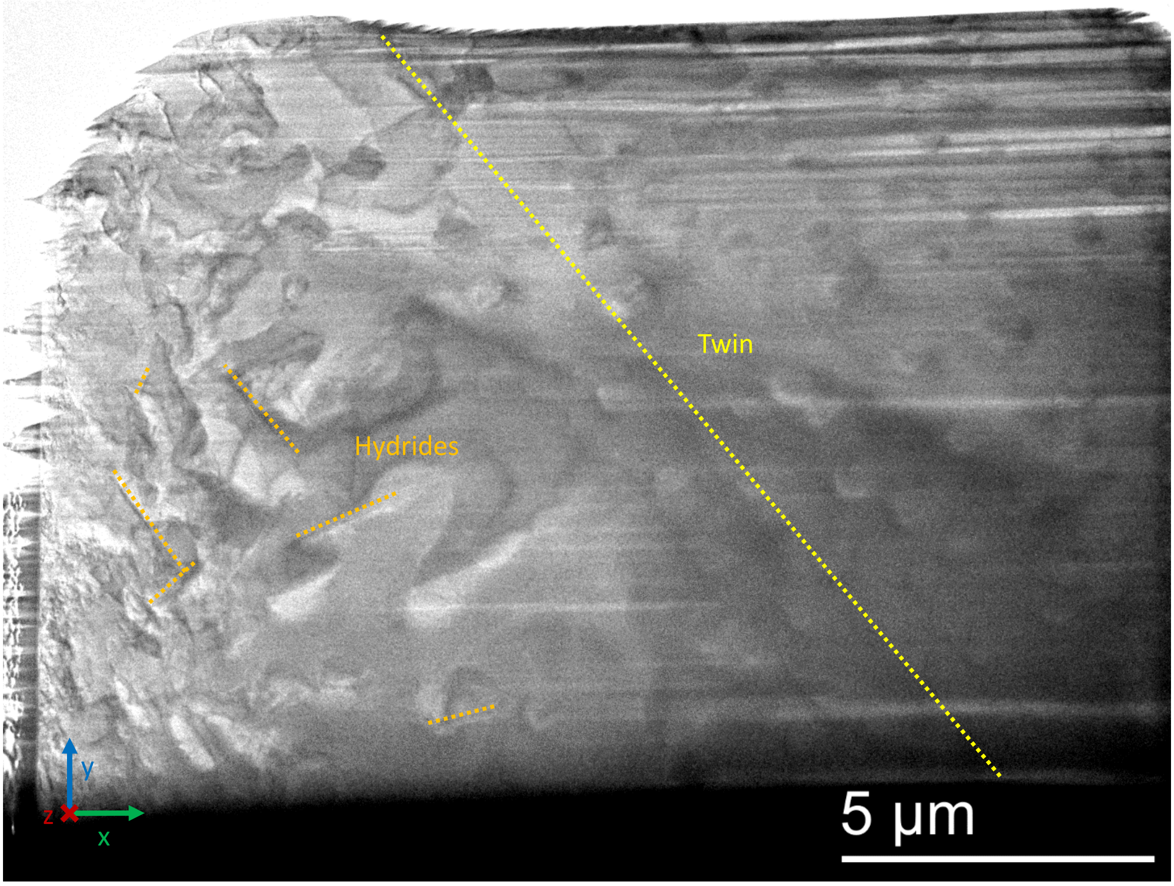

Figure 76: 05-Shock TEM sample taken 500 µm from the shock surface whilst parallel to this surface. Imaged at an unknown condition. This sample is unusual compared with other samples, as discussed in the main body of text.

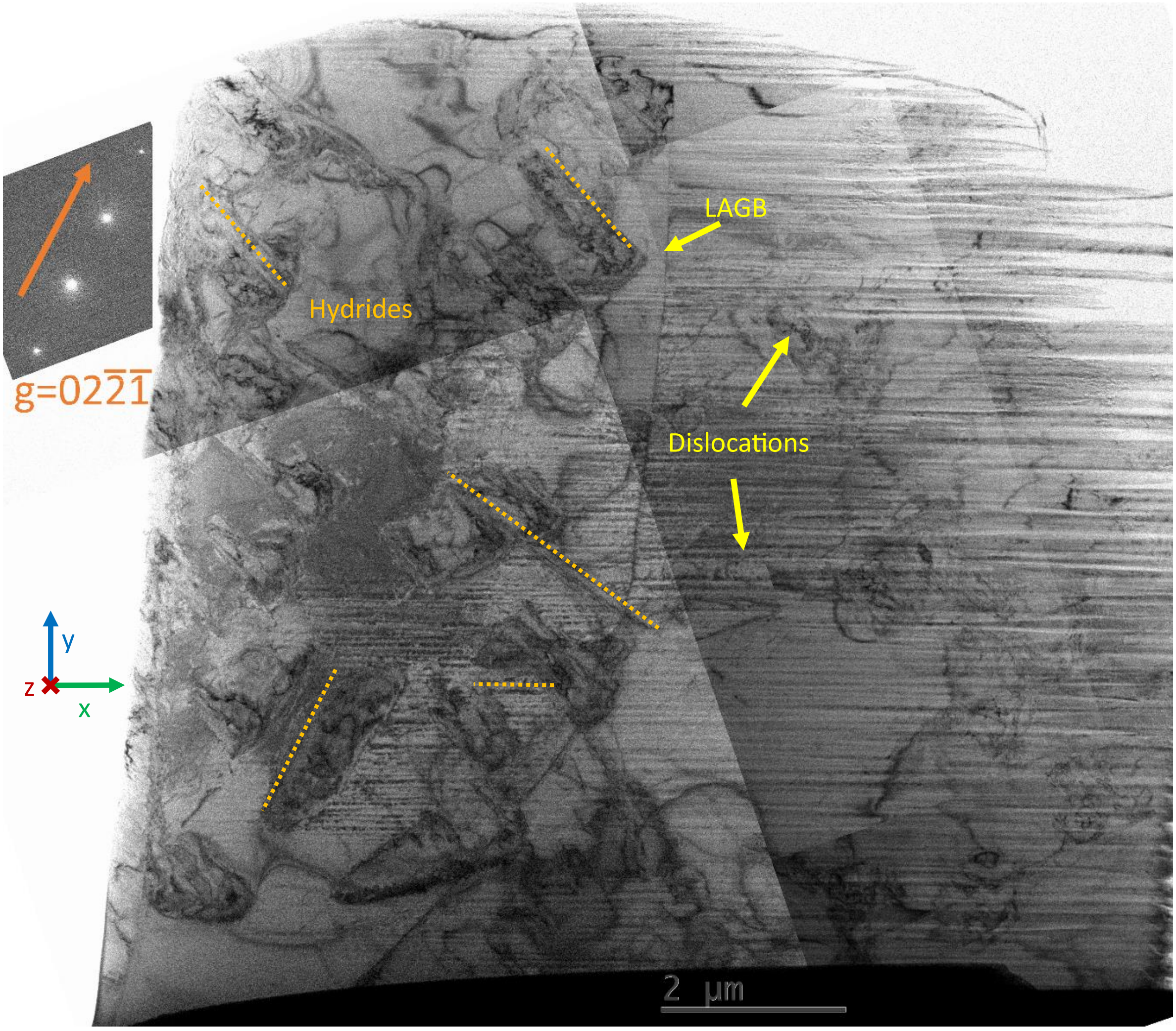

Figure 77: 10-Shock TEM sample taken 500 µm from the shock surface whilst parallel to this surface. Imaged at the condition $g = 02\bar{2}\bar{1}$. Many hydrides are seen, but there are also some dislocations which are likely induced through LSP.

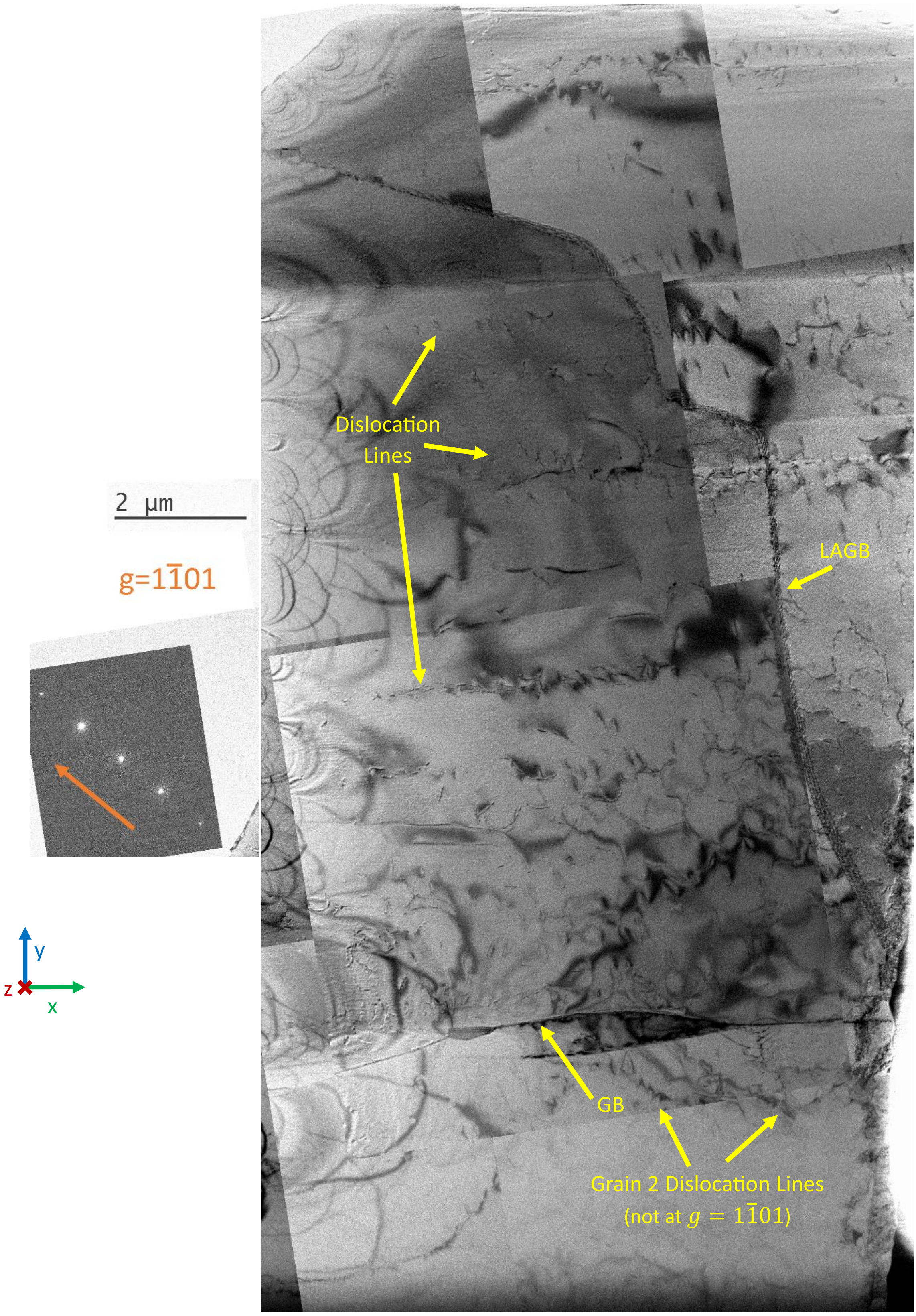

Figure 78: 15-Shock TEM sample taken 500 µm from the shock surface whilst parallel to this surface. Imaged at the condition $g = 1\bar{1}01$. Many Dislocation lines are seen throughout the sample. They are seen either side of the LAGB, and are even seen in an adjoining grain (confirmed through EBSD, not included), which is not close to the same imaging condition.

Figure 79: Increased magnification images of 500 µm depth 15-shock specimen. This depicts a set of dislocation lines as seen in *Figure 78*. Imaging condition is the same, where $g = \bar{1}101$.

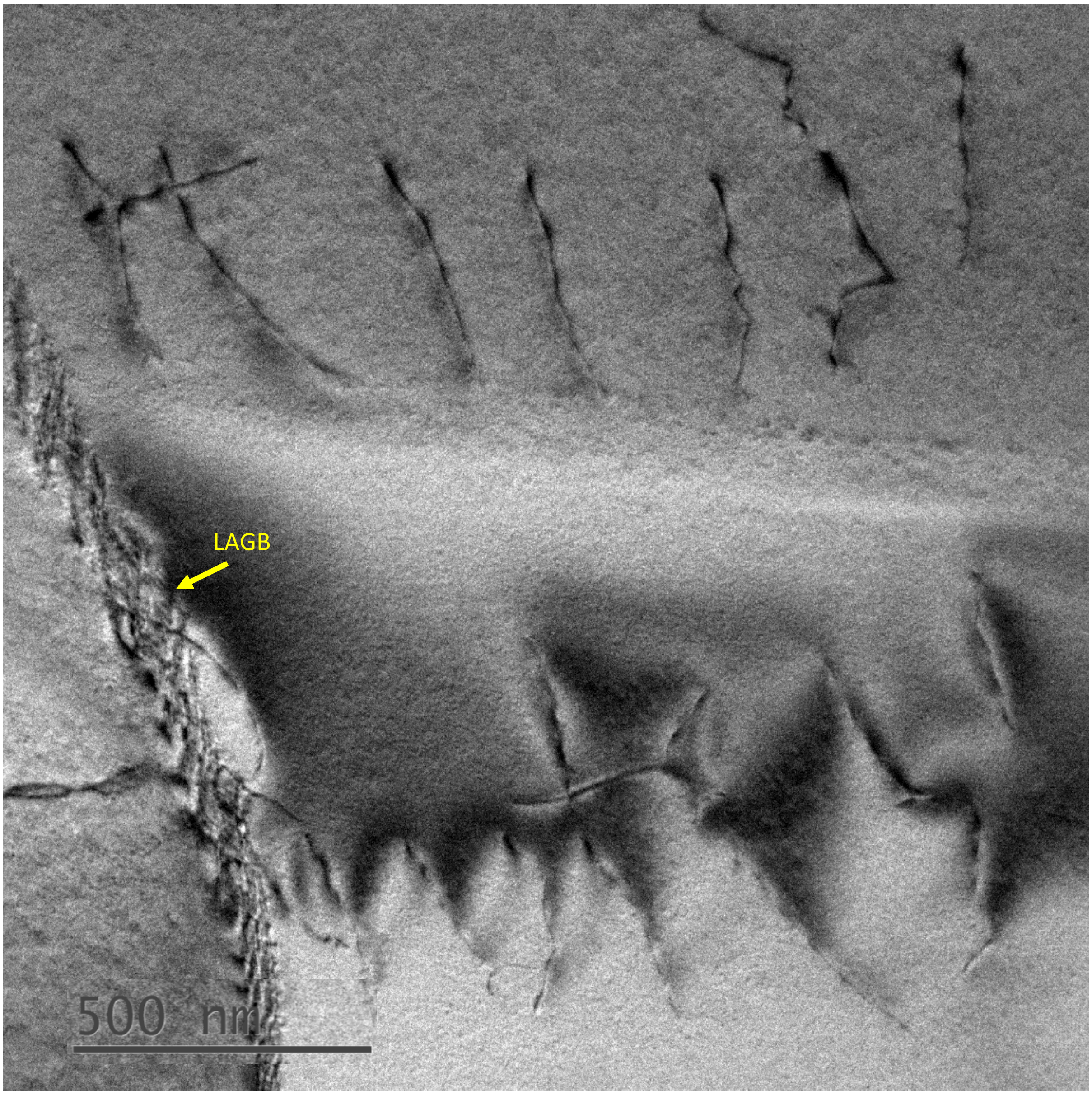

Figure 80: Increased magnification images of 500 µm depth 15-shock specimen. This depicts another set of dislocation lines as seen in *Figure 78*. These change slightly as they reach the low angle grain boundary. Imaging condition is the same, where $g = \bar{1}101$.

4.6.2.4 Miscellaneous

Additional samples have been included to illustrate some key points. Firstly, the level of deformation seems to be greatest a short distance away from the surface. Figure 86 Shows the microstructure about 10°µm away from the 10-shock surface, and similar to the sample in Figure 63, this sample is parallel to the shock surface. This sample intersects with many twins, which also shows that working out the twin density is challenging due to the variation at different depths and angles relative to the shock surface. As already shown based on the 500 µm 5-shock sample (Figure 76) the SEM results may not pick up every twin, perhaps due to how thin they are and reliance on the SEM sample finish (argon ion milling).

Aside from re-establishing the large amount of hydridation in the 10-shock sample, Figure 82, taken at a depth of 500 µm and angle of 79° to the shock surface, the sample features dislocation lines, imaged in greater magnification in Figure 83.

10 Shock, 10 µm, 0°

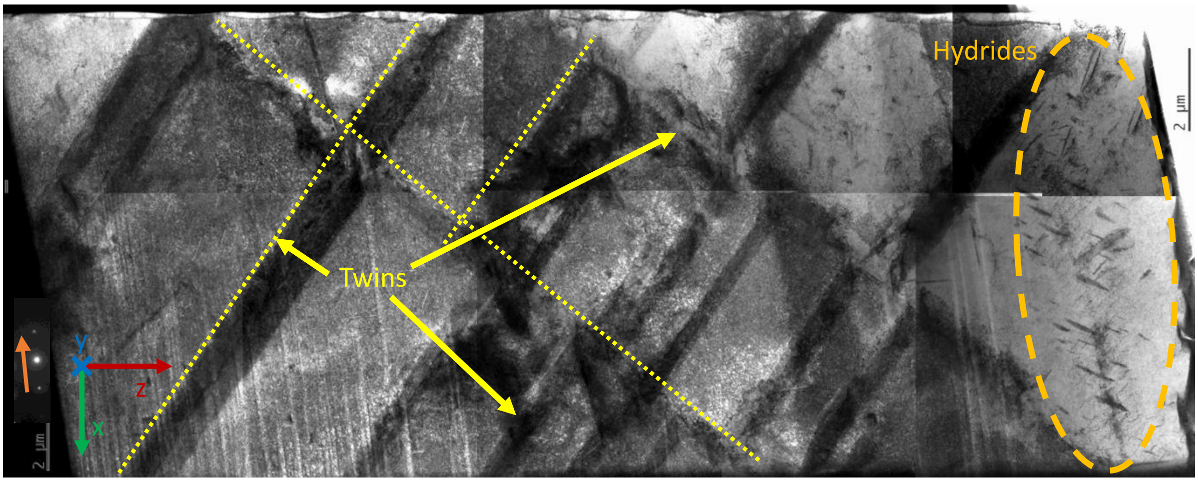

Figure 81: 10-Shock TEM sample taken 10 µm from the shock surface, perpendicular to this surface. Imaged at the condition $g = \bar{1}101$. Many twins are seen throughout the sample, some of which are labelled in yellow. Hydrides are seen towards the right, as indicated in orange.

10 Shock, 500 µm, -11d°

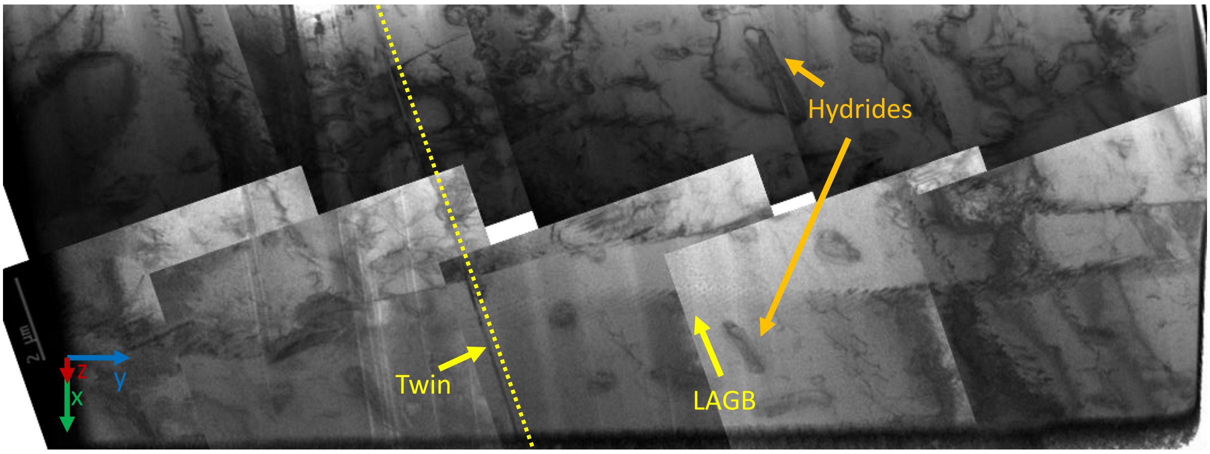

Figure 82: 10-Shock TEM sample taken 500 µm from the surface, at a 79° angle from the surface. This is supplementary to the other 500 µm 10-shock sample seen in *Figure 77*.

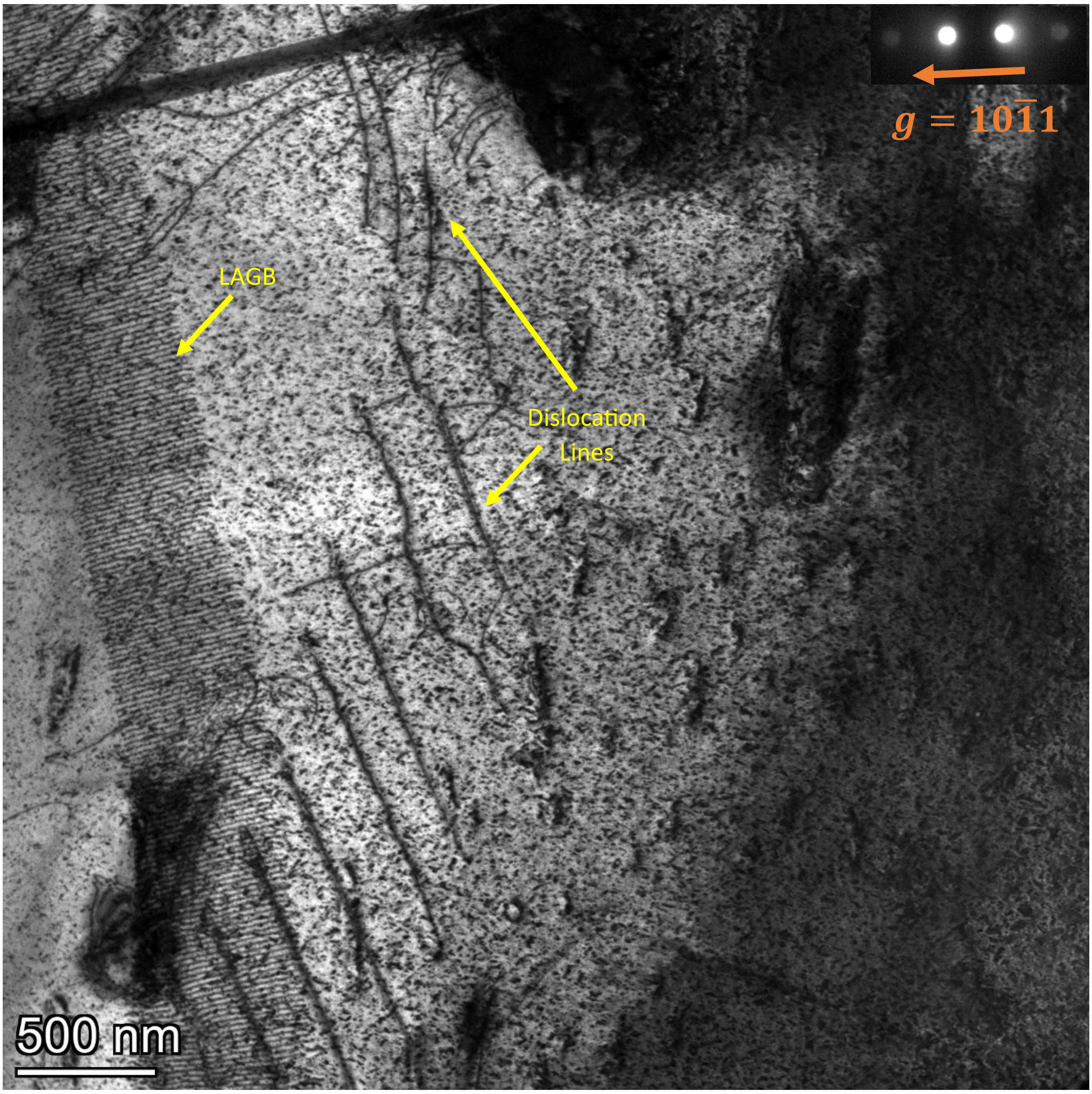

Figure 83: Increased magnification images of 500 µm depth 10-shock specimen. This depicts a set of dislocation lines as seen in *Figure 82*. Imaging condition, $g = \bar{1}101$.

4.6.3 Twin Identification and Analysis

Many of the twins were identified through the edge-on method seen in [*3.3.2 Transmission Electron Microscopy*]. This allowed for further characterisation. These are seen in Figure 84 (70 µm from surface, -70° angle from the shock surface, identifying twins that made a 20° angle with the surface) and Figure 85 (80 µm from surface, -57° angle from the shock surface, identifying twins that made a -33° angle with the surface) from the 5-shock sample, each yielding $\{11\bar{2}1\}$ type twinning, and Figure 86 (25 µm from surface, 36° angle from the shock surface, identifying twins that made a -54° angle with the surface) and Figure 87 (500 µm from surface, -79° angle from the shock surface, identifying twins that made a -11° angle with the surface) from the 10-Shock sample, also each yielding $\{11\bar{2}1\}$ type twinning. These are additional to those seen in previous sections, namely Figure 55 and Figure 56, both from the 3-shock sample at the surface, which yielded $\{10\bar{1}1\}$ and $\{11\bar{2}2\}$ type twinning, respectively. These results are either corroborated with the TKD results, or the TKD results were not adequate to make a judgement, often due to the resolution required for the thin twins.

5 Shock, 70 µm, +20° twins:

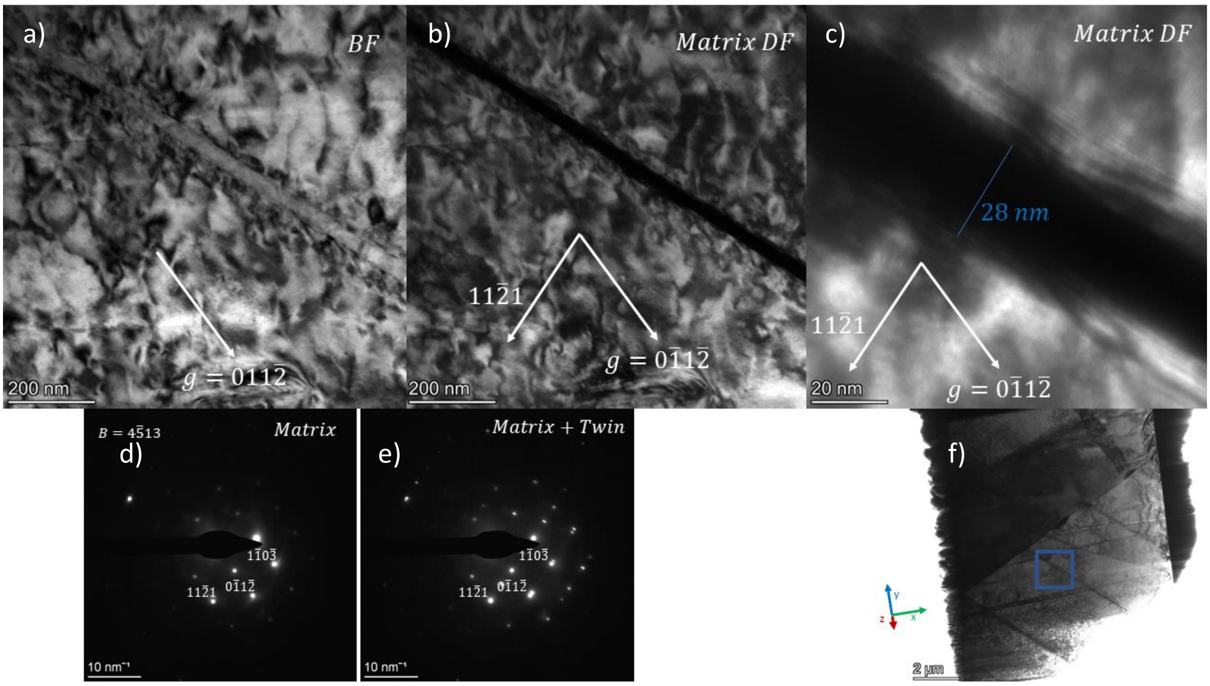

Figure 84: 5-Shock TEM sample taken 70 µm from the surface, at a 70° angle from the surface parallel. This focuses on the imaging and diffraction of the twins seen perpendicular to this angle, at 20°. Imaging conditions and zone axis are labelled where appropriate. Images with $g = 0\bar{1}1\bar{2}$ taken in a) BF and b) Matrix DF c) with greater magnification. Twin thickness indicated is 28 nm. DP's from the d) matrix and e) matrix and twin are shown with $B = 4\bar{5}13$. f) Original sample.

5 Shock, 80 µm, -33° twins:

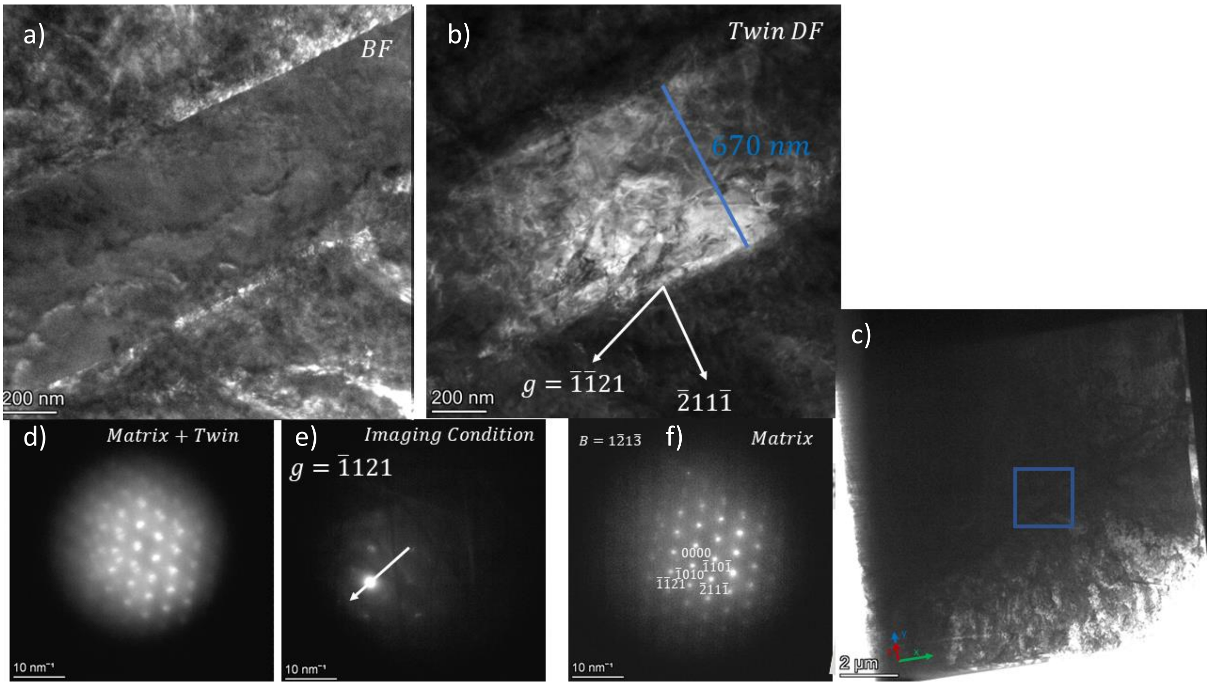

Figure 85: 5-Shock TEM sample taken 80 µm from the surface, at a 57° angle from the surface parallel. This focuses on the imaging and diffraction of the twins seen perpendicular to this angle, at -33°. Imaging conditions and zone axis are labelled where appropriate. Images with $g = \bar{1}\bar{1}21$ taken in a) BF and b) Twin DF. Twin thickness indicated is 670 nm. c) Original sample. DP's from the d) matrix and twin and e) at imaging condition $g = \bar{1}\bar{1}21$ in BF and f) matrix only with labels. $B = 4\bar{5}13$.

10 Shock, 25 µm, -54° twins:

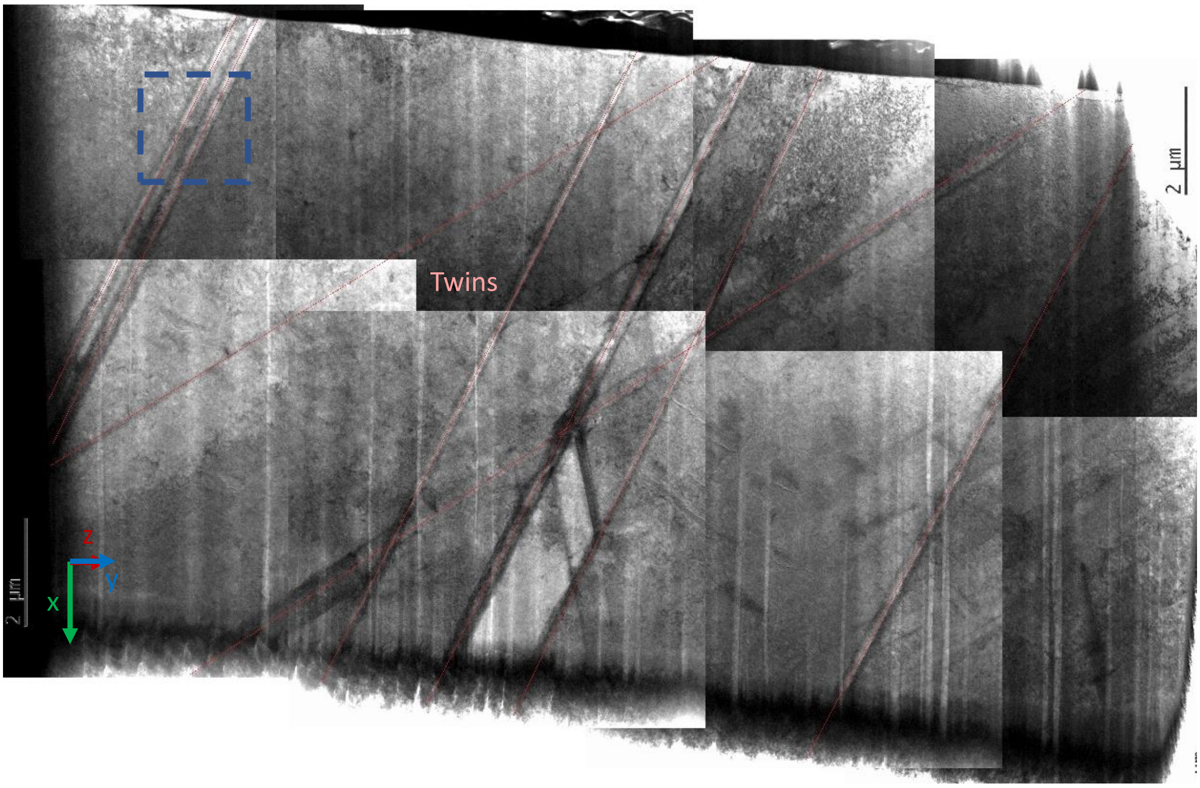

Figure 86.1: 10-Shock TEM sample taken 25 µm from the surface, at a 36° angle from the surface parallel. This focuses on the imaging of the twins seen perpendicular to this angle, at -54°. Greater magnification images are taken from region in blue, top left.

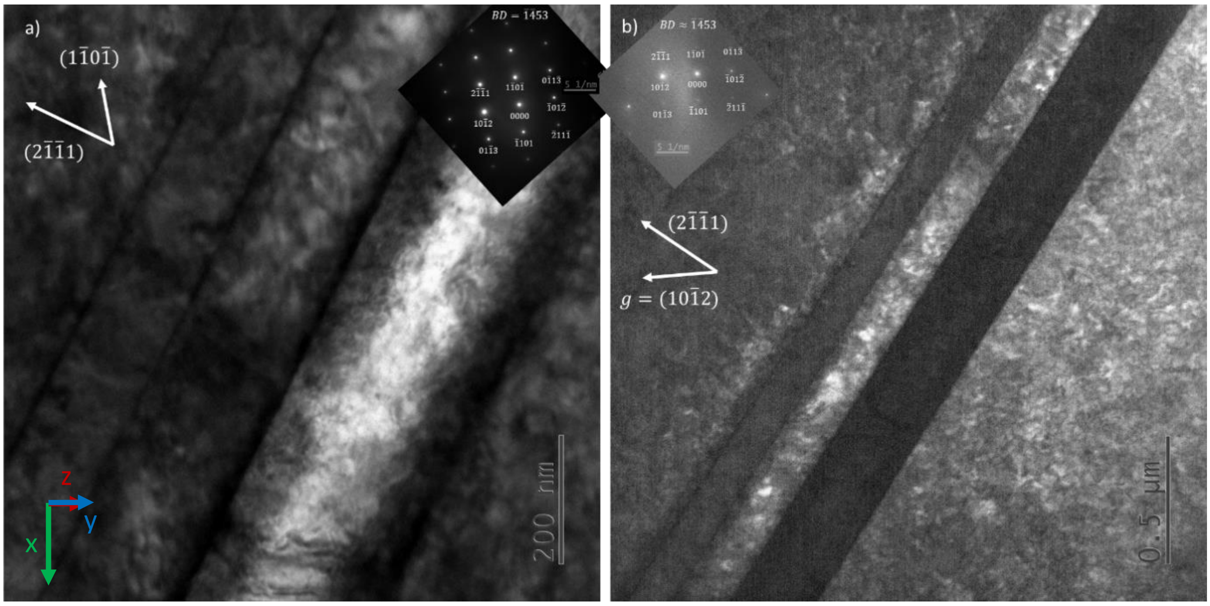

Figure 86.2: 10-Shock TEM sample taken 25 µm from the surface, at a 36° angle from the surface parallel. This focuses on the imaging and diffraction of the twins seen perpendicular to this angle, at -54°. a) is a bright field image at the zone axis $B = \overline{14}53$, with b) being imaged under dark field with $g = 10\bar{1}2$.

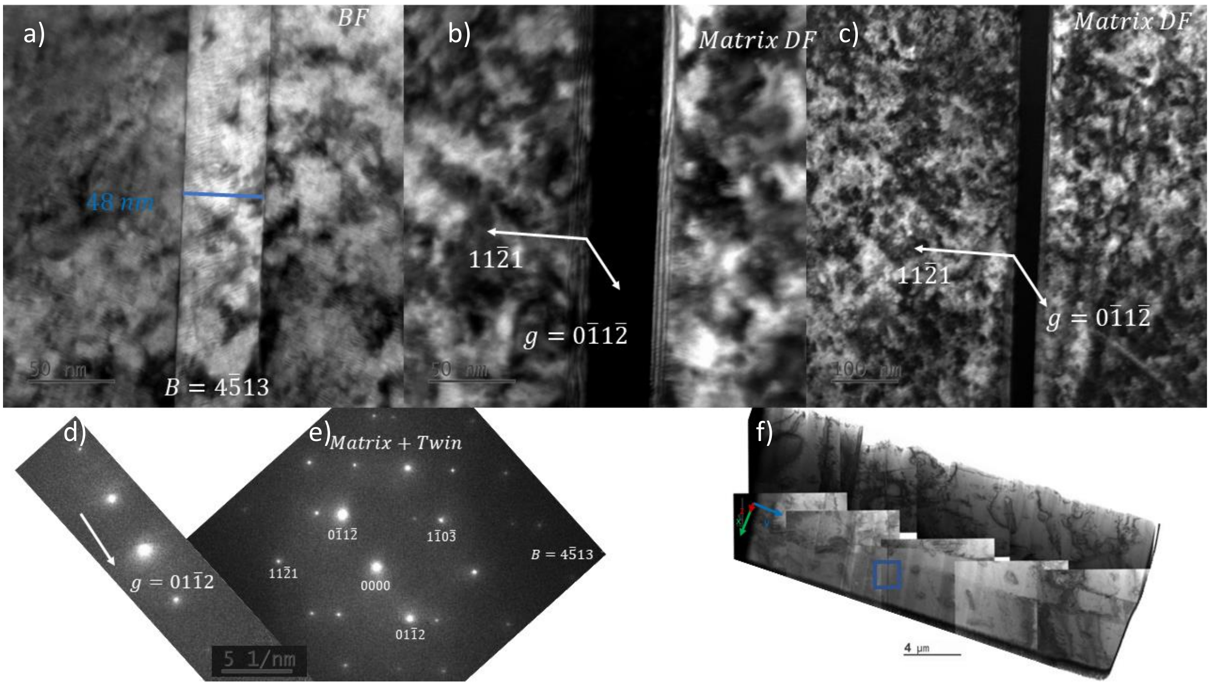

Figure 87: 10-Shock TEM sample taken 500 µm from the surface, at a 79° angle from the surface parallel. This focuses on the imaging and diffraction of the twins seen perpendicular to this angle, at -11°. Imaging conditions and zone axis are labelled where appropriate. Images taken with $B = 4\bar{5}13$ in a) BF and b+c) matrix DF with diffraction patterns d) $g = 01\bar{1}2$ and of the e) matrix and twin, where the matrix spots are labelled. f) Original sample, as seen in *Figure 82*.

4.6.4 Dislocation Studies

4.6.4.1 Analysis of Dislocations

Dislocation analysis was conducted on the 3-Shock sample as the simplest form of dislocation lines seen throughout the samples, given the low density and few dislocation-dislocation interactions. These are seen in Figure 88 as the background for all remaining figures in this section, to map the locations of the dislocations accurately. Figure 89, Figure 90, Figure 91, Figure 92 and Figure 93 have imaging conditions noted. A summary of the conclusions from these images can be found in Table 10. The Burgers vectors of dislocations are identified to be of the $\pm\frac{1}{3} < 11\bar{2}0 >$ type, i.e. $\boldsymbol{a}$-type dislocations.

Figure 88: 3-Shock TEM sample displaying Dislocation lines. Imaging condition $B = \bar{1}102$ (at zone axis). This serves as the background to *Figure 89*, *Figure 90*, *Figure 91*, *Figure 92* and *Figure 93* for locational accuracy. These are all near $B \cong \bar{1}102$.

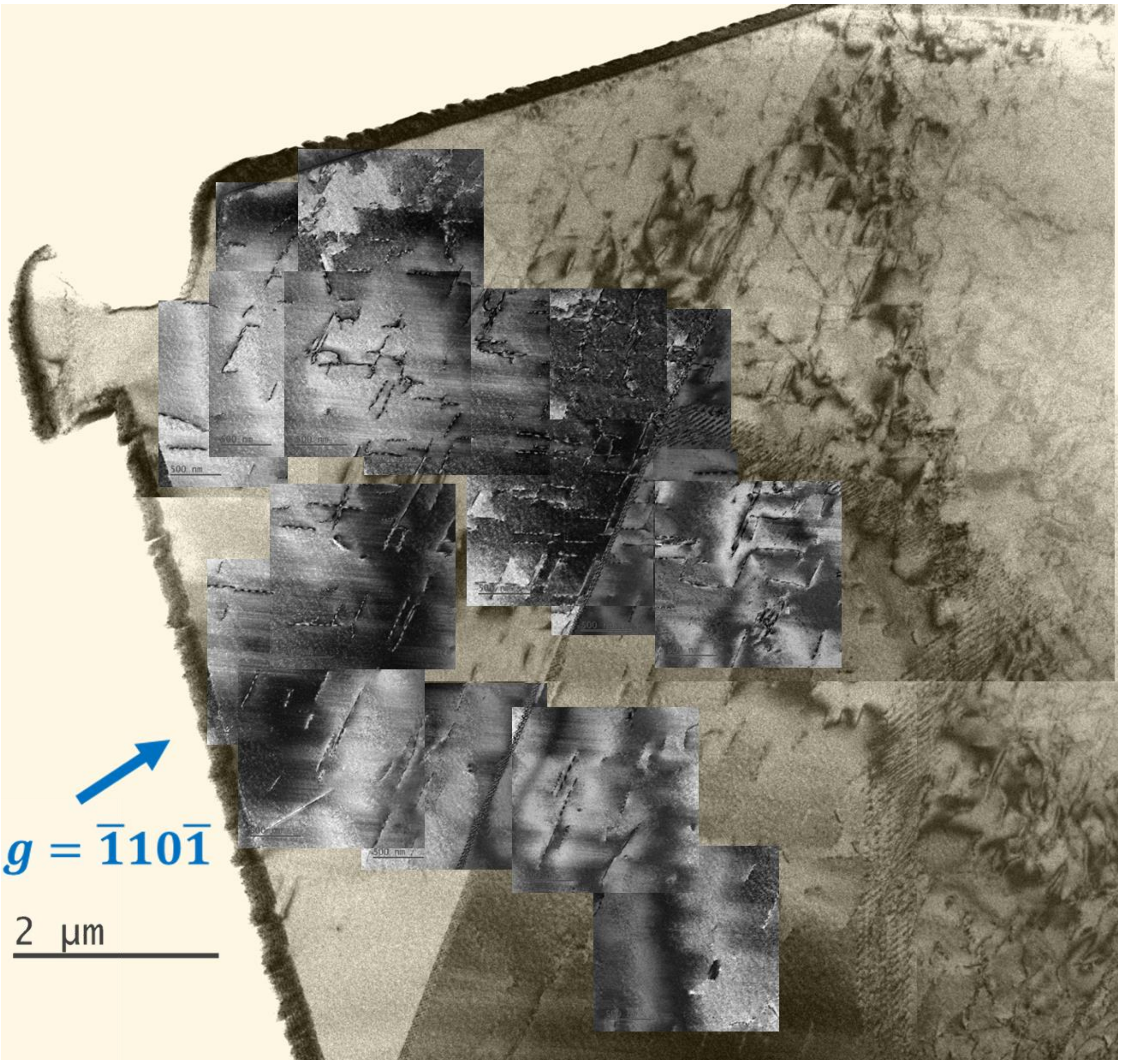

Figure 89: 3-Shock TEM sample displaying Dislocation lines. Imaging condition $g = \bar{1}10\bar{1}$ with yellowed background of $B = \bar{1}102$.

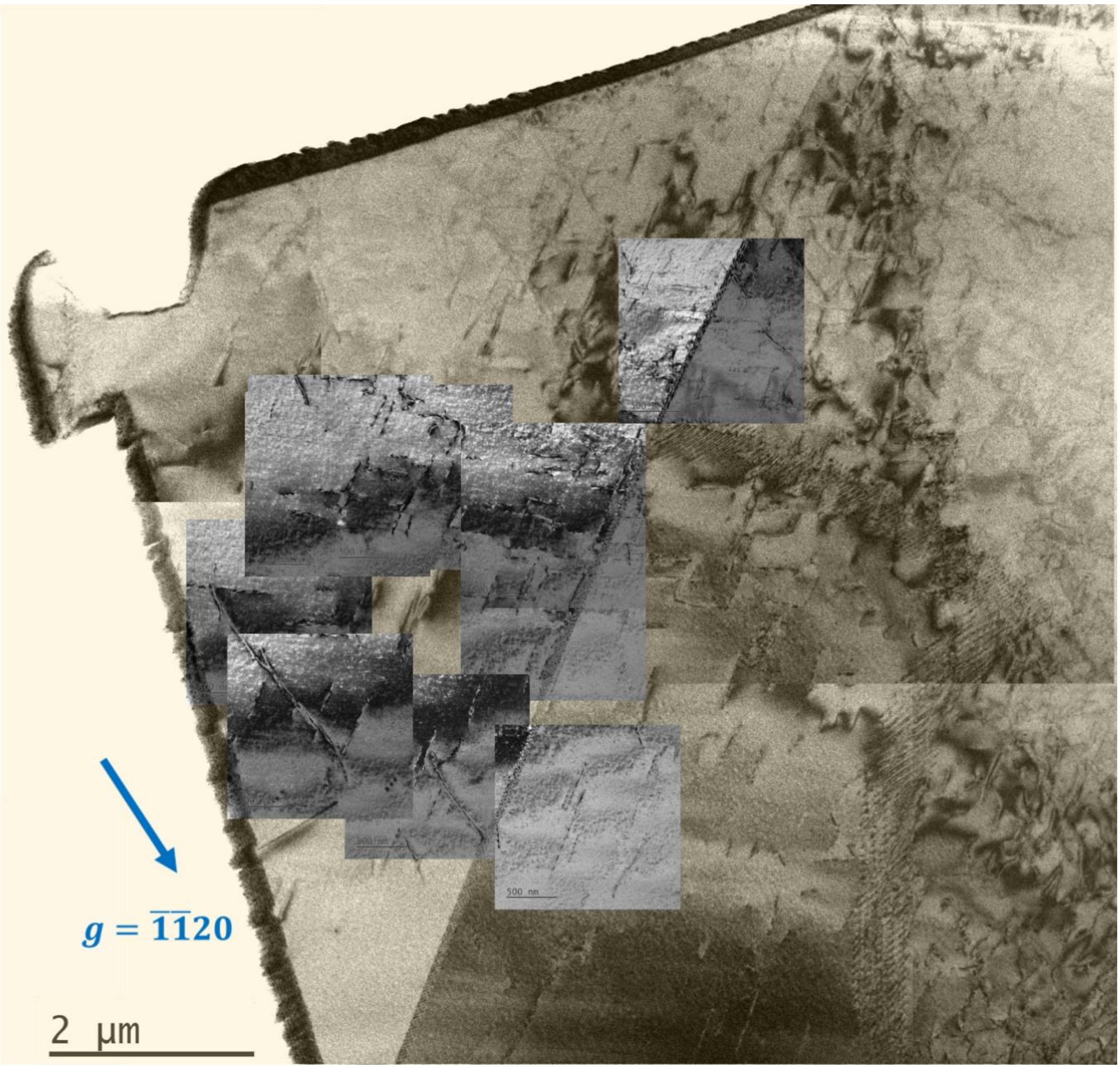

Figure 90: 3-Shock TEM sample displaying Dislocation lines. Imaging condition $g = \bar{1}\bar{1}20$ with yellowed background of $B = \bar{1}102$.

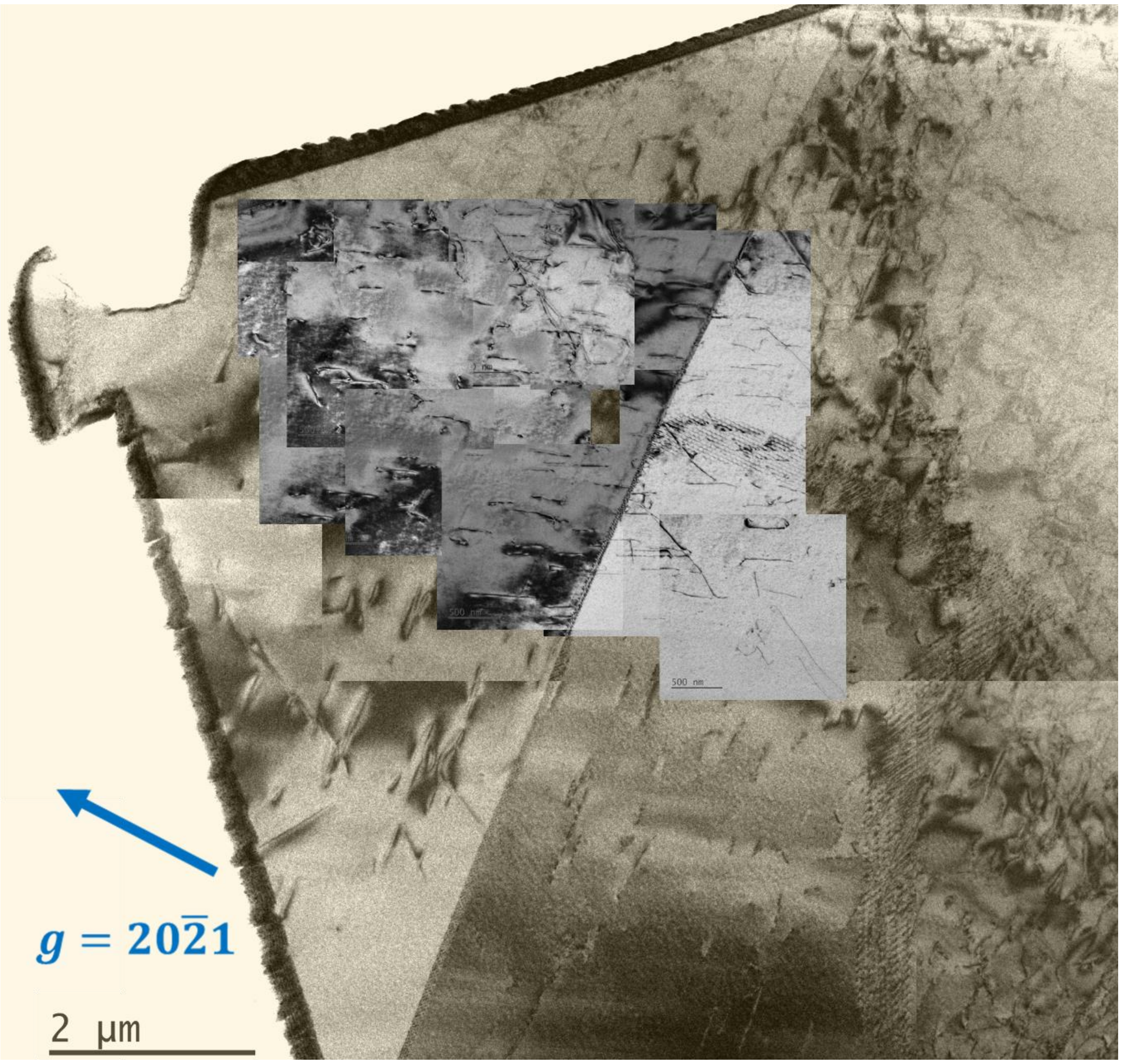

Figure 91: 3-Shock TEM sample displaying Dislocation lines. Imaging condition $g = 20\bar{2}1$ with yellowed background of $B = \bar{1}102$.

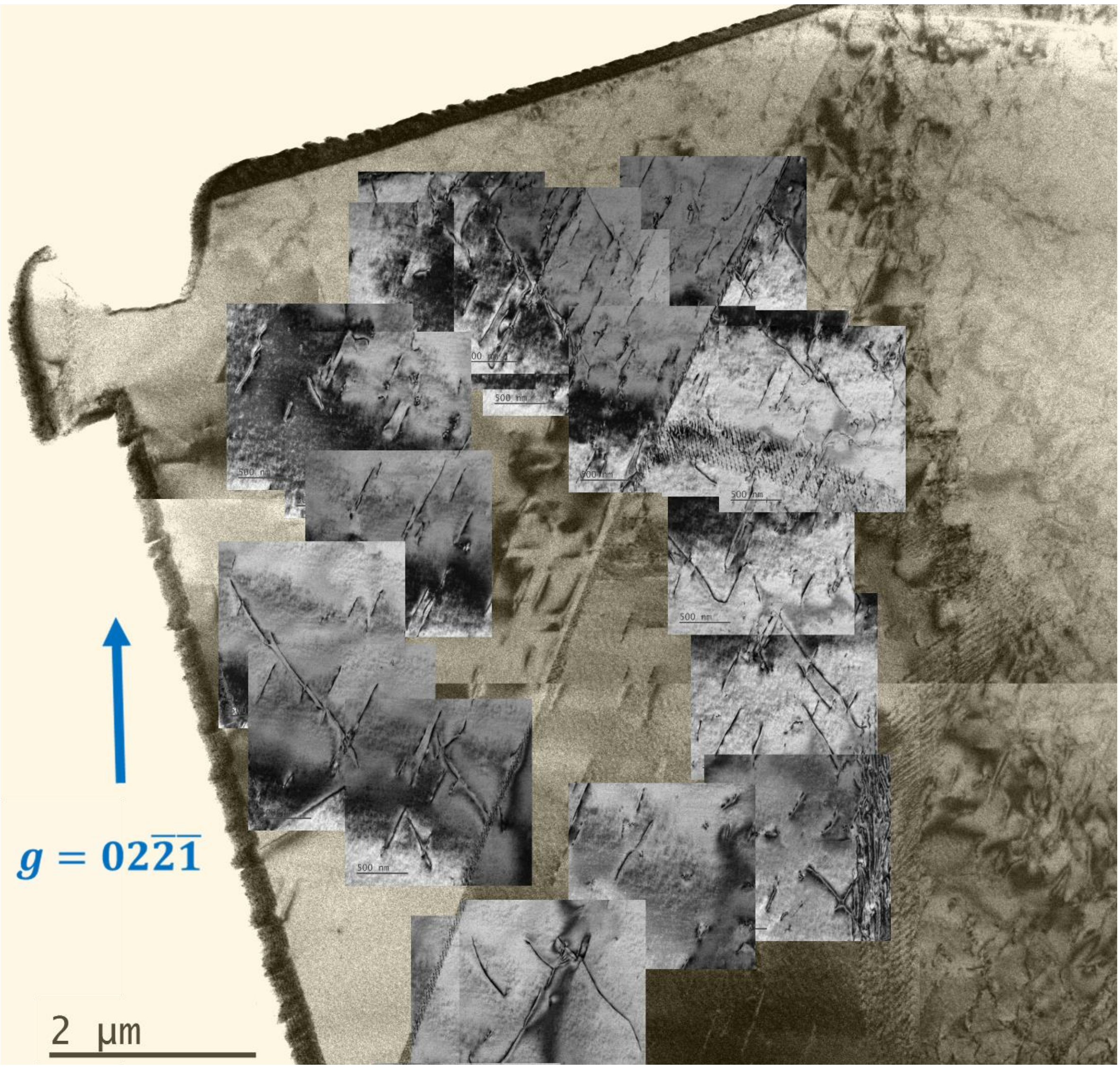

Figure 92: 3-Shock TEM sample displaying Dislocation lines. Imaging condition $g = 02\bar{2}\bar{1}$ with yellowed background of $B = \bar{1}102$.

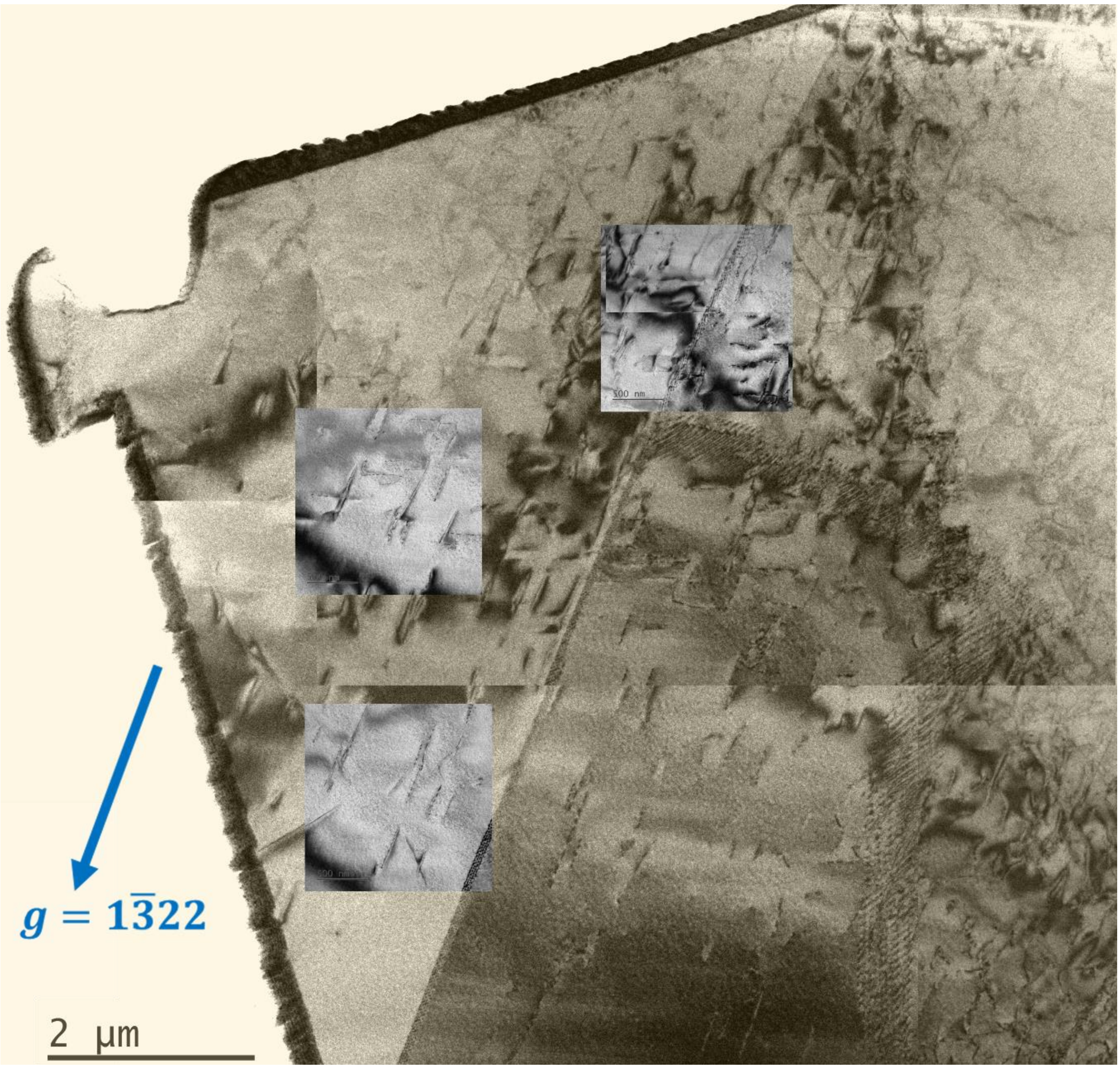

Figure 93: 3-Shock TEM sample displaying Dislocation lines. Imaging condition $g = 1\bar{3}22$ with yellowed background of $B = \bar{1}102$.

Table 10: Summary of 3-shock TEM sample data in identification of Burgers vectors of dislocation types seen. 3 common dislocation types have been seen, as indicated on *Figure 88*.

g	a_2 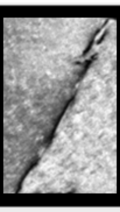	a_1 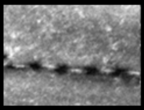	a_3 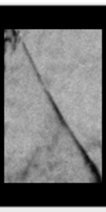
$\bar{1}10\bar{1}$	Visible	Visible	Invisible
$\bar{1}\bar{1}02$	Visible	Visible	Visible
$20\bar{2}1$	Invisible	Visible	Visible
$02\bar{2}\bar{1}$	Visible	Invisible	Visible
$1\bar{3}22$	Visible	Weak	Weak
Burgers Vector	$\pm\frac{1}{3}[1\bar{2}10]$	$\pm\frac{1}{3}[\bar{2}110]$	$\pm\frac{1}{3}[11\bar{2}0]$

4.6.4.2 *Dislocation Density Study (5 – 10 µm Depth)*

The images taken for dislocation analysis (Figure 94 and Figure 95 for 3-shock, Figure 96 and Figure 97 for 5-shock, Figure 98 and Figure 99 for 10-shock, Figure 100 and Figure 101 for 15-shock) are all at the $g = \bar{1}101$ type imaging condition. This allows for a comparative study. They were selected to be representative of the dislocation density between 5 µm and 10 µm from the shock surfaces, which describes part of region B closest to the surface, which was seen to have the greatest number of dislocations in each sample. In the case of the 10 and 15-shock samples in particular, the vast number of dislocations caused a difference in the imaging condition from one part of the image to the other. In practice, more images were taken at the same location with incremental changes to the tilt angle, which gave more confidence in the identification of dislocations. The dislocations seen in the 3-shock sample were long and showed some entanglement. The 5-shock sample shows an increase in the number of entangled dislocations, and they are shorter than in the case of the 3-shock. The 10-shock sample appears to have similar dislocation structures to the 5-shock sample, and in each of these it appears as though the dislocations form dislocation cells in various regions. The 15-shock sample has a multitude of dislocations, and the matrix shows significant variation in contrast making it difficult to apply the same imaging condition to the whole image. These dislocations are regularly entangling leading to the formation of dislocation cells.

A summary of these resulting dislocation density counts is found in the graph, Figure 102. The dislocation density increased significantly from 3-shock to 5-shock, and from 10-shock to 15-shock. There was no significant change in the dislocation density from 5-shock to 10-shock.

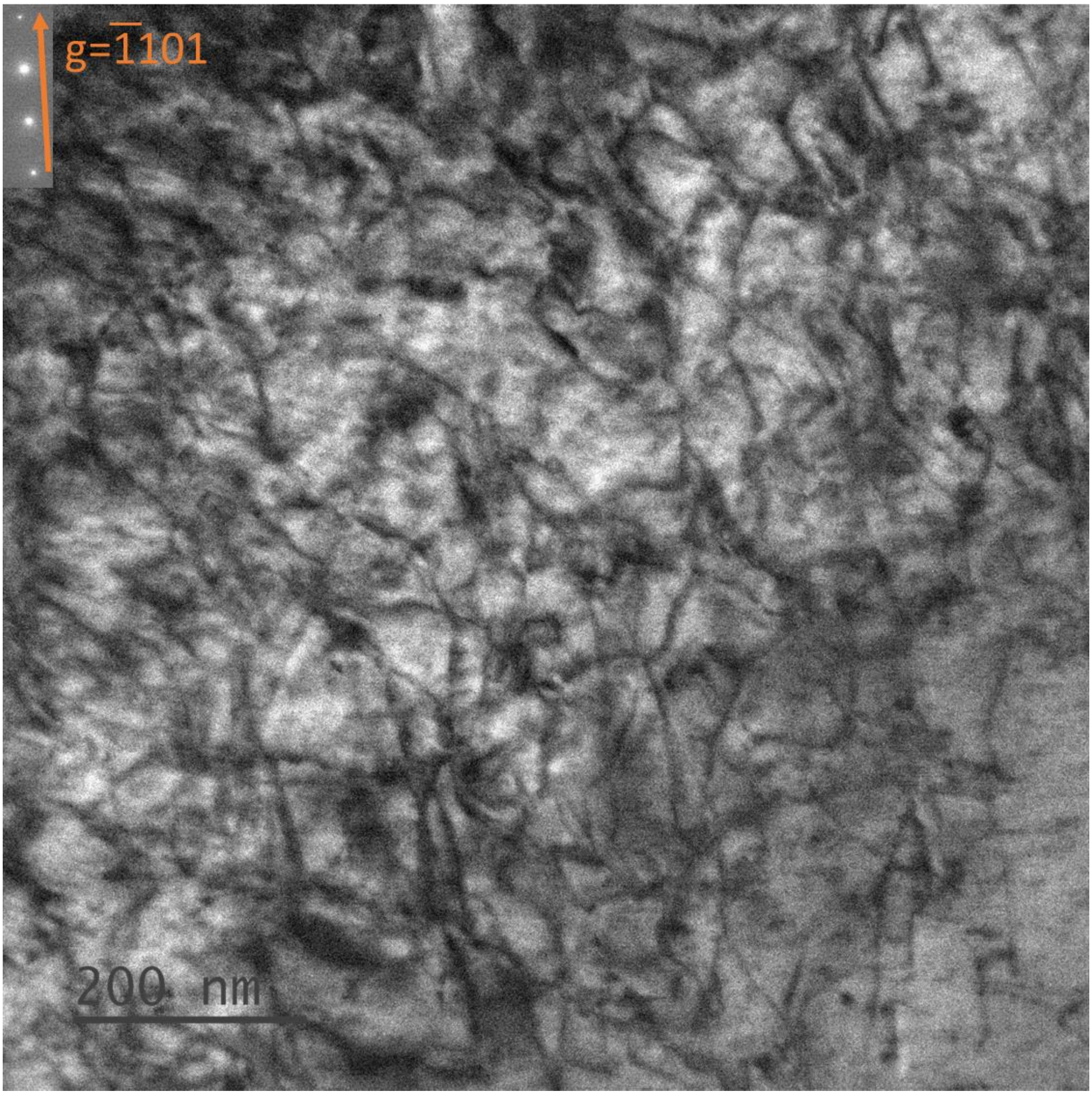

Figure 94: 3-Shock image taken perpendicular to the shock surface, between 5 and 10 µm from the surface, after the initial heavily twinned region. Imaging condition of $g = \bar{1}101$.

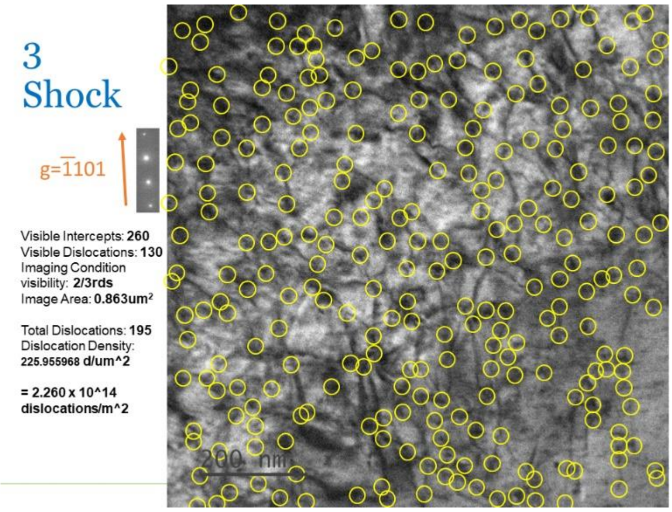

Visible Intercepts: **260**
Visible Dislocations: **130**
Imaging Condition visibility: **2/3rds**
Image Area: **0.863um^2**

Total Dislocations: **195**
Dislocation Density: **225.955968 d/um^2**

= 2.260 x 10^14 dislocations/m^2

Figure 95: 3-Shock image taken from *Figure 94* with overlayed highlighting in yellow circles, the perceived ends of dislocations. This has been factored into a dislocation density calculation as written to the left of the image.

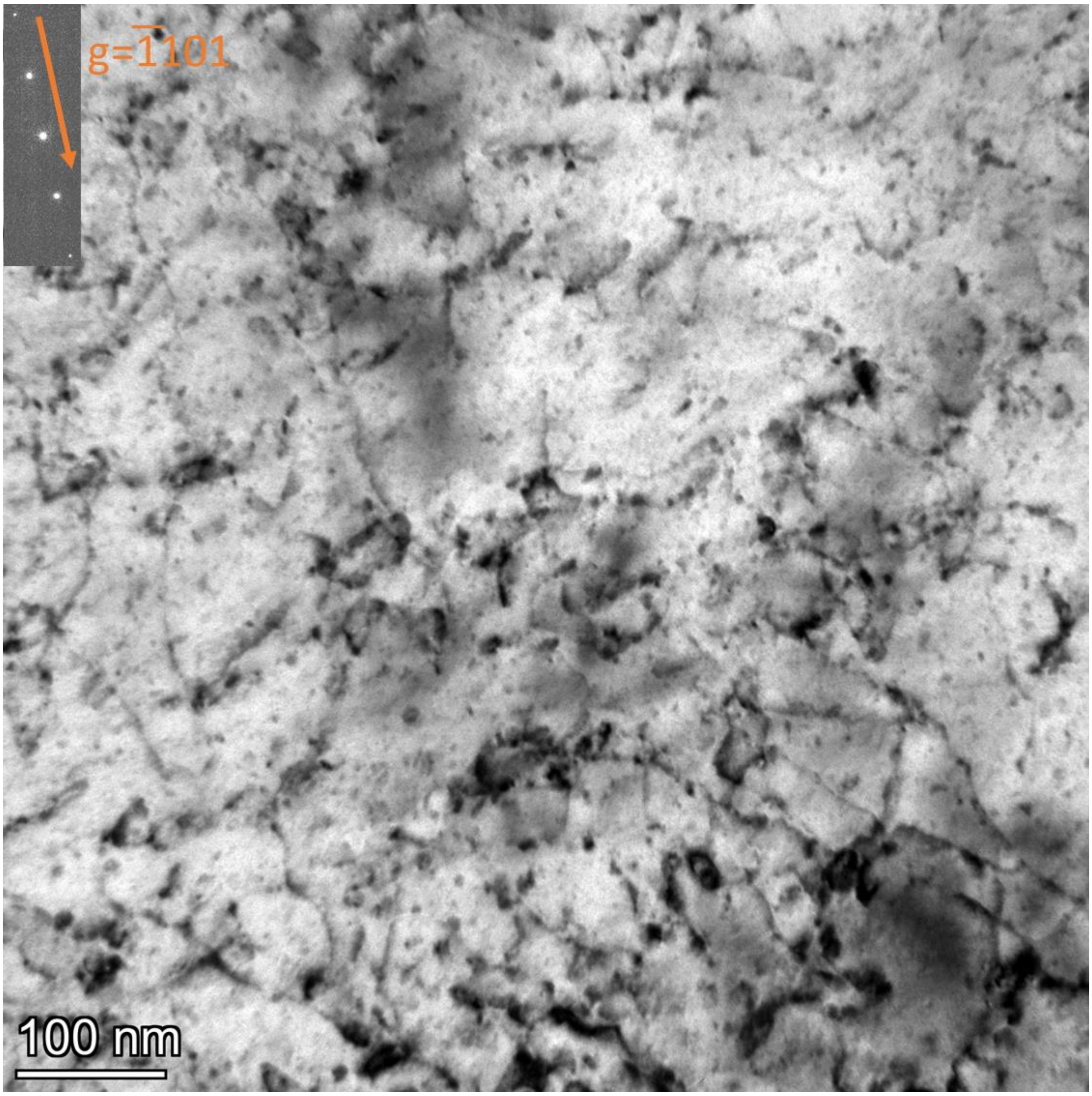

Figure 96: 5-Shock image taken perpendicular to the shock surface, between 5 and 10 µm from the surface, after the initial heavily twinned region. Imaging condition of $g = \bar{1}101$.

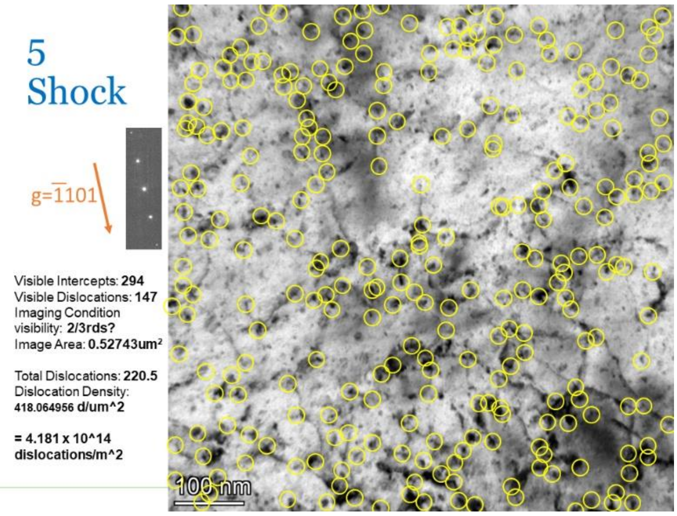

Figure 97: 5-Shock image taken from *Figure 96* with overlayed highlighting in yellow circles, the perceived ends of dislocations. This has been factored into a dislocation density calculation as written to the left of the image.

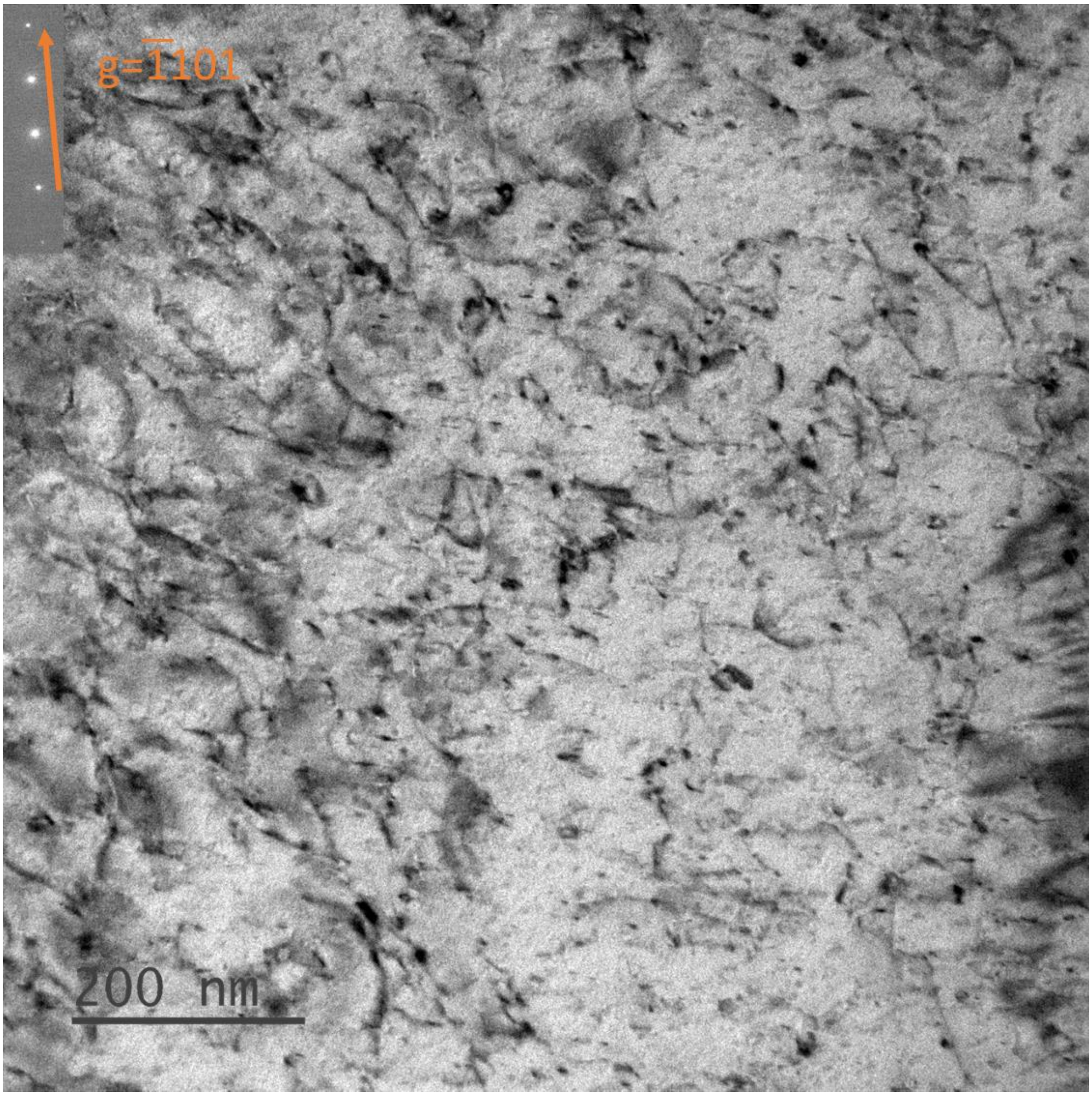

Figure 98: 10-Shock image taken perpendicular to the shock surface, between 5 and 10 µm from the surface, after the initial heavily twinned region. Imaging condition of $g = \bar{1}101$.

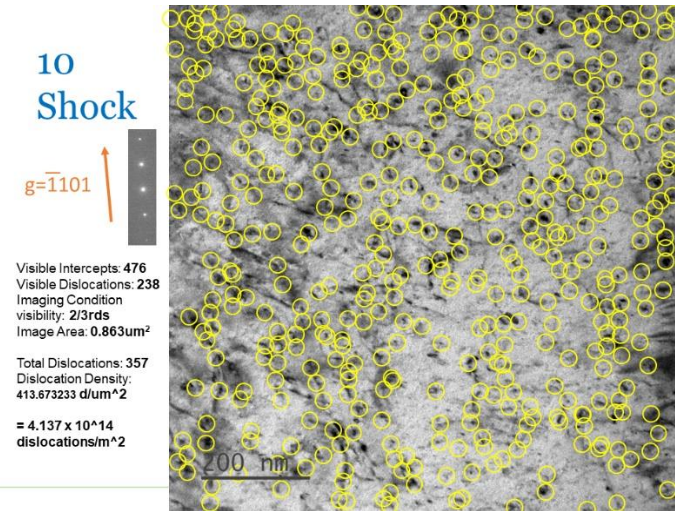

Visible Intercepts: **476**
Visible Dislocations: **238**
Imaging Condition visibility: **2/3rds**
Image Area: **0.863um^2**

Total Dislocations: **357**
Dislocation Density:
413.673233 d/um^2

= 4.137 x 10^14 dislocations/m^2

Figure 99: 10-Shock image taken from *Figure 98* with overlayed highlighting in yellow circles, the perceived ends of dislocations. This has been factored into a dislocation density calculation as written to the left of the image.

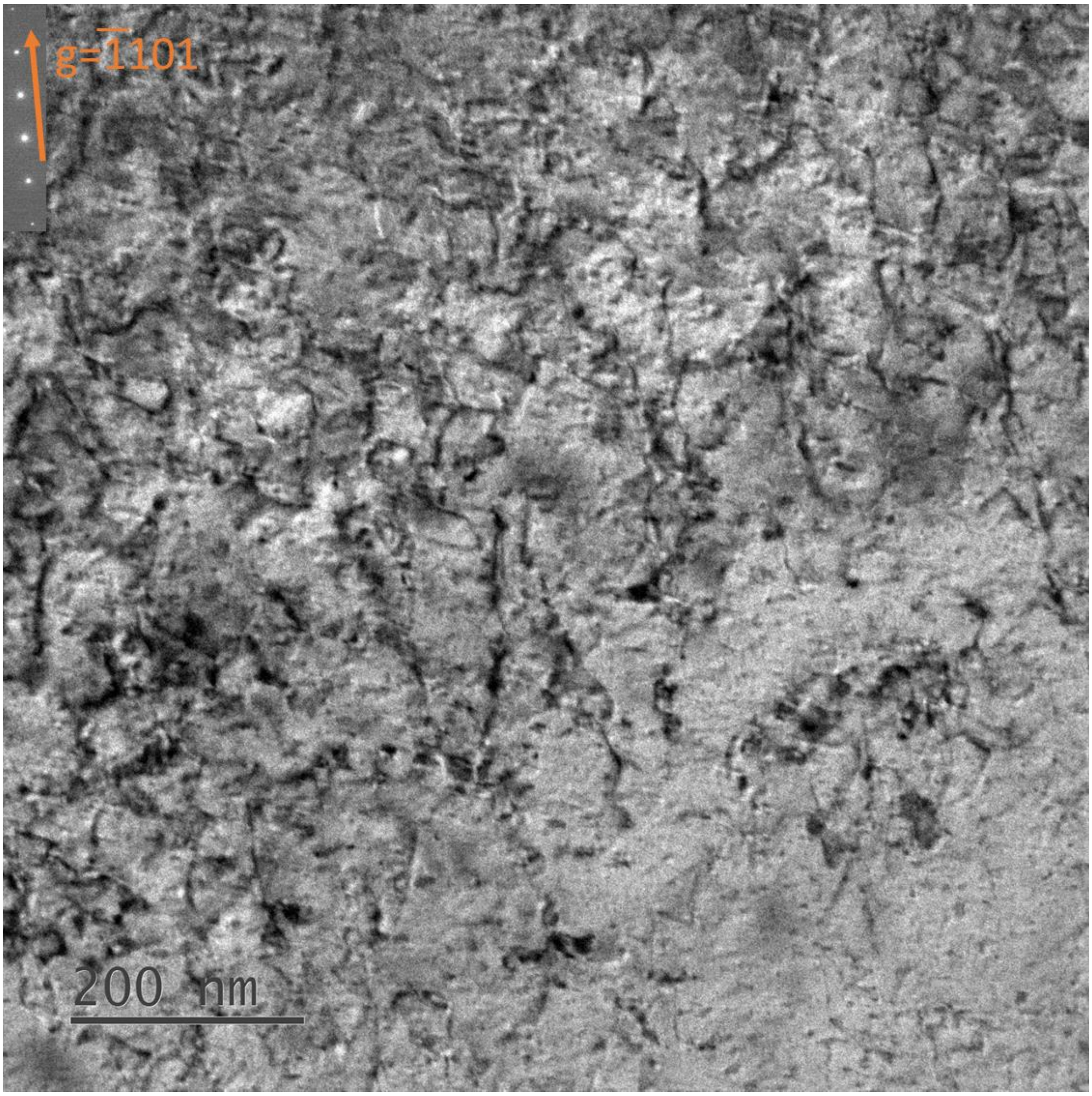

Figure 100: 15-Shock image taken perpendicular to the shock surface, between 5 and 10 μm from the surface, after the initial heavily twinned region. Imaging condition of $g = \bar{1}101$.

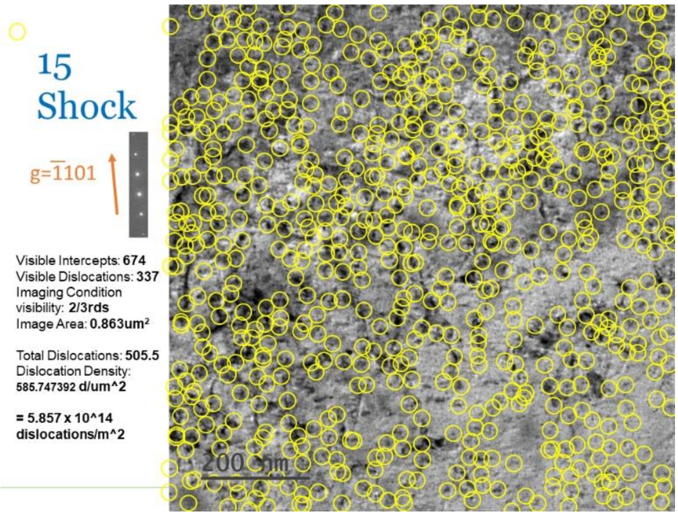

Visible Intercepts: **674**
Visible Dislocations: **337**
Imaging Condition visibility: **2/3rds**
Image Area: **0.863um²**

Total Dislocations: **505.5**
Dislocation Density: **585.747392 d/um^2**

= 5.857 x 10^14 dislocations/m^2

Figure 101: 15-Shock image taken from *Figure 100* with overlayed highlighting in yellow circles, the perceived ends of dislocations. This has been factored into a dislocation density calculation as written to the left of the image.

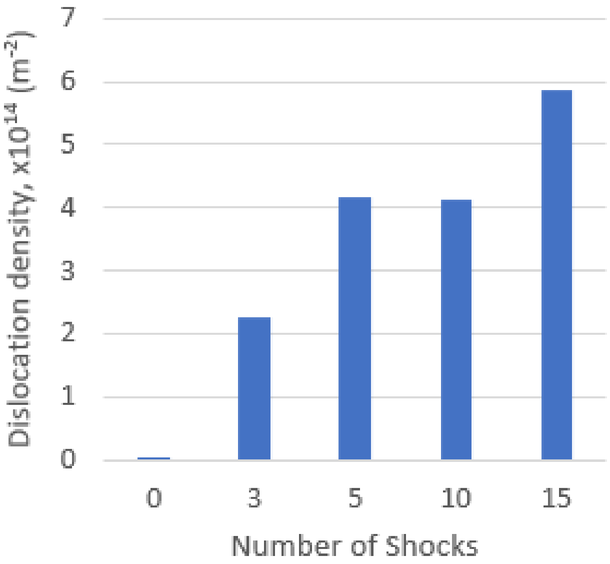

Figure 102: Summarised graphical data representing the dislocation density of the LS processed samples. Note, 0 shocks is calculated at between 10^{10} and 10^{11} dislocations m^{-2}.

4.7 Transmission Kikuchi Diffraction (TKD)

Many of the figures seen above have been further analysed with transmission Kikuchi diffraction (TKD). This is used to corroborate the twin types seen in the TEM (legend visible in Table 11) and perform this at a more efficient rate; the edge-on method is not always possible if the required tilting angle deviates greatly from the angle the sample is loaded into the TEM (zero tilt). TKD of the 3, 5, 10 and 15-shock samples at 0 µm are seen in Figure 103, Figure 104, Figure 105, and Figure 106, respectively, and those at 250 µm are seen in Figure 107, Figure 108, Figure 109, and Figure 110, respectively. The calculations used to determine these based on the orientation data from pole figures are found in the appendix [*8.2 Twin Analysis from TKD*].

Table 11: Key describing the notation used for different twinning types, with accompanying twinning shear. TKD lines describe twins identified via the SEM diffraction studies, whilst TEM describes those identified only through TEM, either through TEM twinning identification (using the edge-on method (*3.3.2 Transmission Electron Microscopy*) or through extrapolation from parallel twins identified through the TKD.

Type	Sense	Twinning Shear	Line	Type
1011	Compression	0.0933	= = = = = = = = = = = = = = = = ································	TKD TEM
1012	Tension	0.1802	= = = = = = = = = = = = = = = = ································	TKD TEM
1121	Tension	0.6317	= = = = = = = = = = = = = = = = ································	TKD TEM
1122	Compression	0.2131	= = = = = = = = = = = = = = = = ································	TKD TEM

4.7.1 0 µm, Perpendicular to surface (90°)

TKD of the 3, 5, 10 and 15-shock samples at 0 µm are seen in Figure 103, Figure 104, Figure 105, and Figure 106, respectively. Using the same terminology as in section [*4.6.2.1 0 µm, Perpendicular to surface (90°)*], Region A of the 3-shock sample contains many $\{10\bar{1}1\}$ type twins, with a single $\{11\bar{2}1\}$ twin near the transition to region B. Inside region B, there are many $\{11\bar{2}1\}$ twins of the same type, and one twin of $\{11\bar{2}2\}$.

The 5-shock sample contains many surface twins of $\{10\bar{1}1\}$ twins. Additional to this in region A are found $\{11\bar{2}1\}$ type twins, however although this is the closest fit according to the diffraction data, it is possible that these are actually $\{10\bar{1}1\}$. A reminder that this data is found in appendix ([*8.2 Twin Analysis from TKD*], AFigure 5).

The 10-shock sample contains exclusively $\{10\bar{1}1\}$ twins in region A, and $\{11\bar{2}1\}$ twins in region B, the latter containing two different types. The vast majority of twins in region A of the 15-shock sample are $\{10\bar{1}1\}$ type twins, with a few registering as $\{11\bar{2}1\}$ and $\{11\bar{2}2\}$ type twins. Region B contains many $\{11\bar{2}1\}$ twins of the same type, but also contains the only $\{10\bar{1}2\}$ twins found throughout all of the recorded data of all samples. These also happen to be perpendicular to the shock surface, and hence parallel to the shock direction.

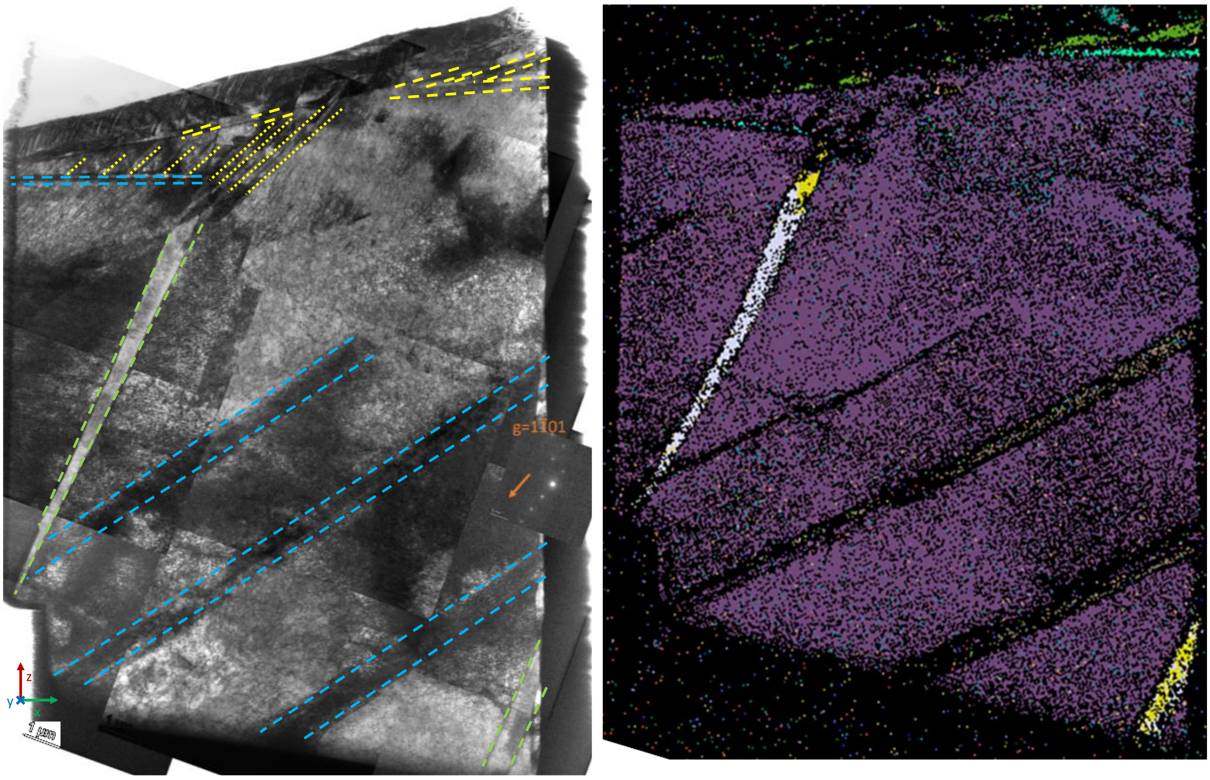

Figure 103: 3-Shock sample, *Figure 54* (3-Shock, 0 µm) with overlayed twins (Left) as identified through the TKD Euler colours (Right).

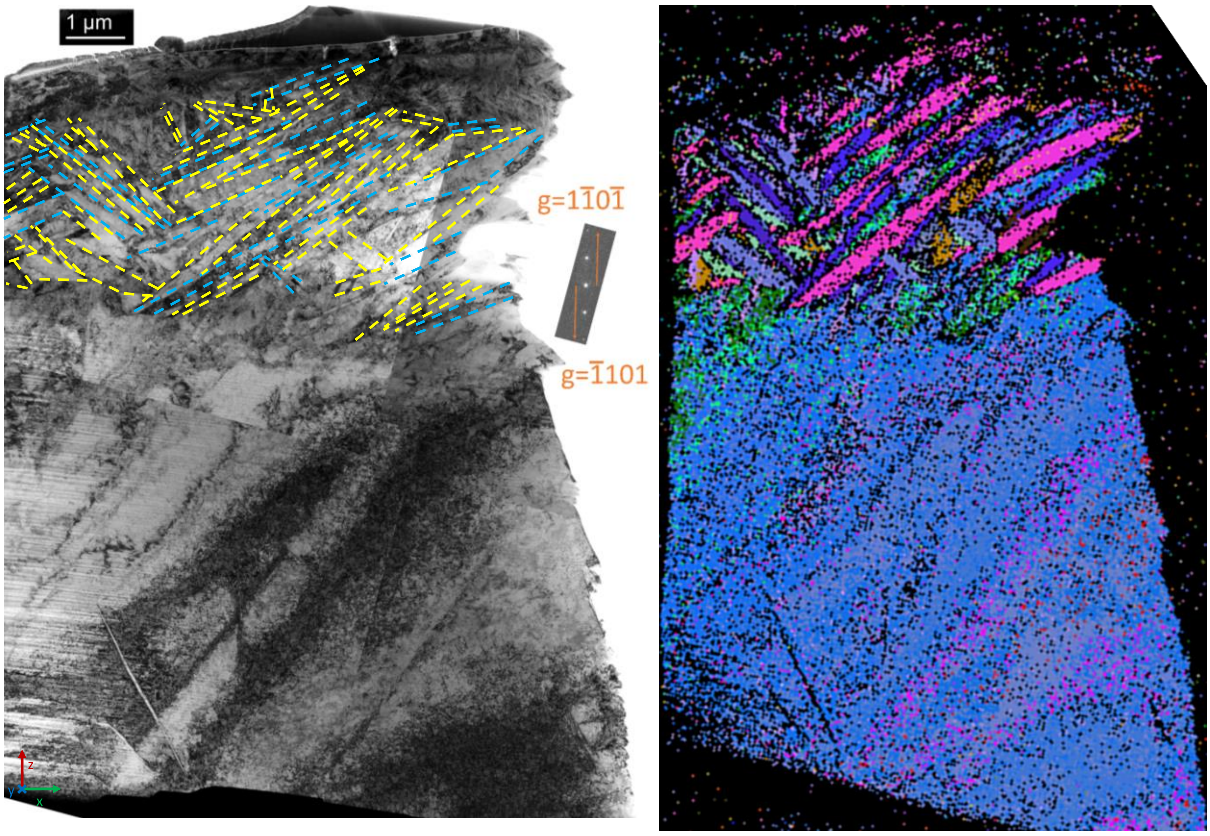

Figure 104: 5-Shock sample, *Figure 58* (5-Shock, 0 µm) with overlayed twins (Left) as identified through the TKD Euler colours (Right).

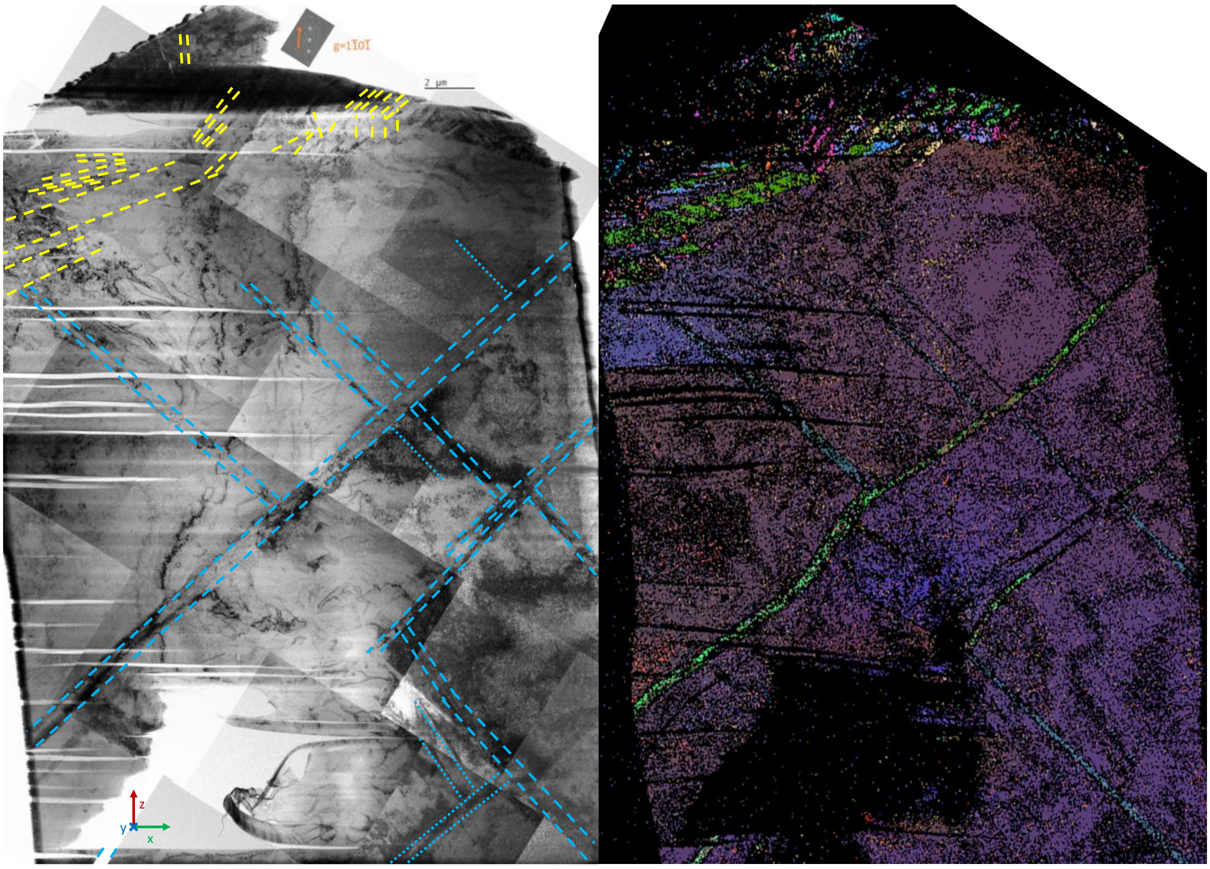

Figure 105: 10-Shock sample, *Figure 63* (10-Shock, 0 µm) with overlayed twins (Left) as identified through the TKD Euler colours (Right).

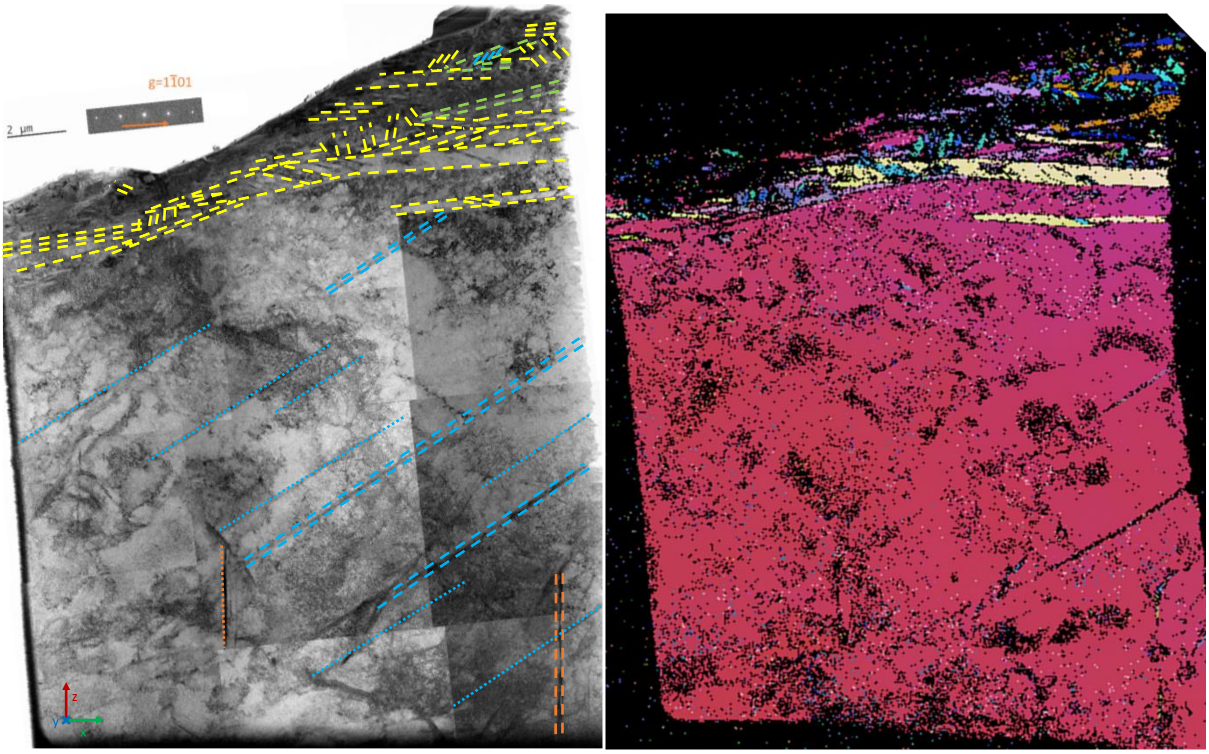

Figure 106: 15-Shock sample, *Figure 64* (15-Shock, 0 µm) with overlayed twins (Left) as identified through the TKD Euler colours (Right).

4.7.1 250 µm, Parallel to surface (0°)

TKD of the 3, 5, 10 and 15-shock samples at 250 µm are seen in Figure 107, Figure 108, Figure 109, and Figure 110, respectively. The 3-shock TKD confirms the absence of twinning, and the colour within each grain shows little variation implying low misorientation. The 5-shock specimen reveals the the possible location of three twins, but is only able to identify two of them as being of $\{11\bar{2}1\}$ and $\{10\bar{1}2\}$ type. The 10- shock and 15-shock each show a single $\{11\bar{2}1\}$ twin. The 5 and 10-shock twins seen are not so obvious to identify, whilst the 15-shock twin happens to be unmistakeable due to its thickness, and that it travels through the entire length of the sample.

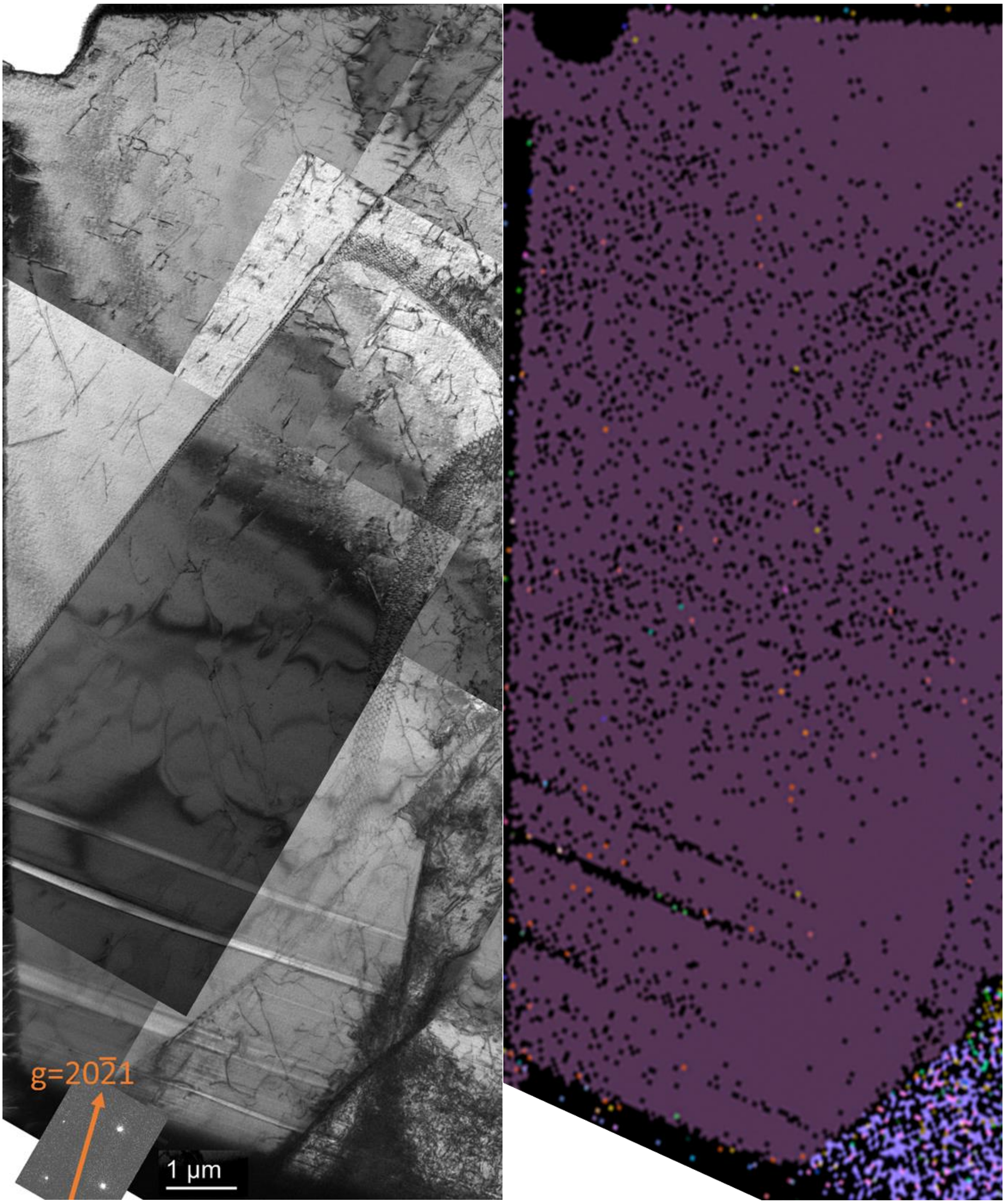

Figure 107: 3-Shock sample, *Figure 67* (3-Shock, 250 µm) with overlayed twins (Left) as identified through the TKD Euler colours (Right).

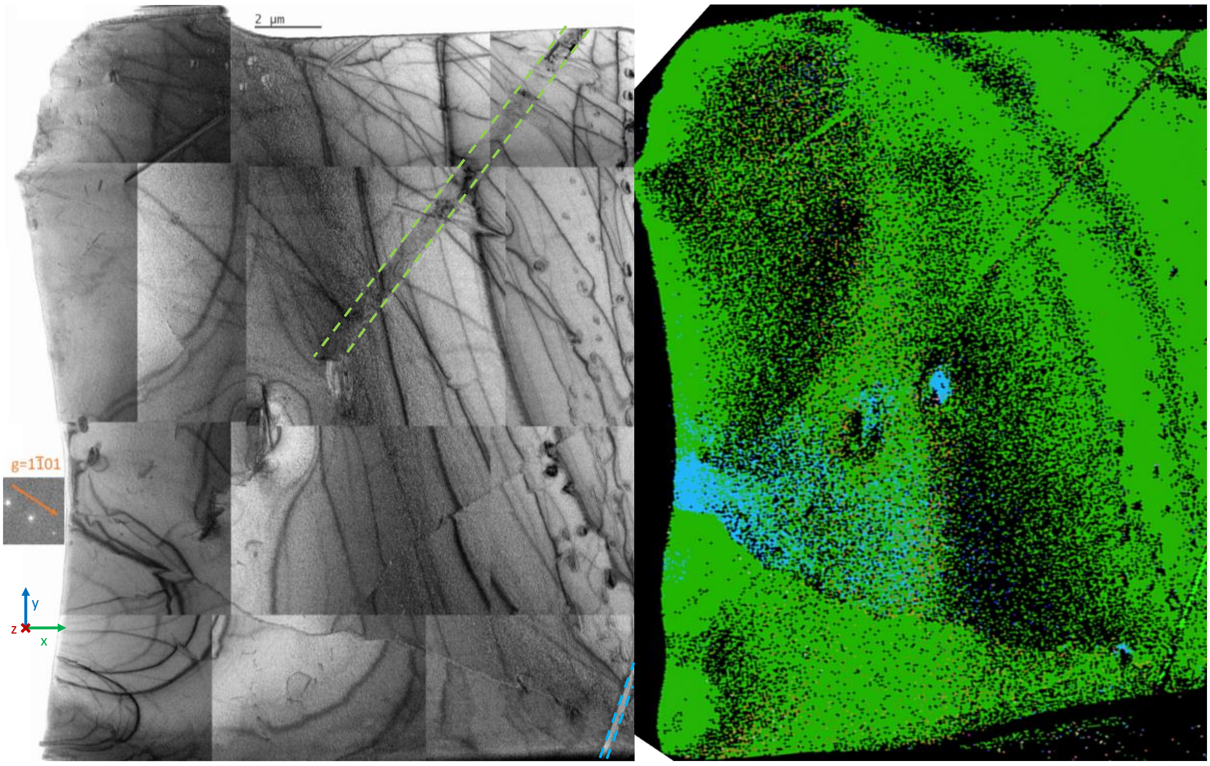

Figure 108: 5-Shock sample, *Figure 68* (5-Shock, 250 µm) with overlayed twins (Left) as identified through the TKD Euler colours (Right).

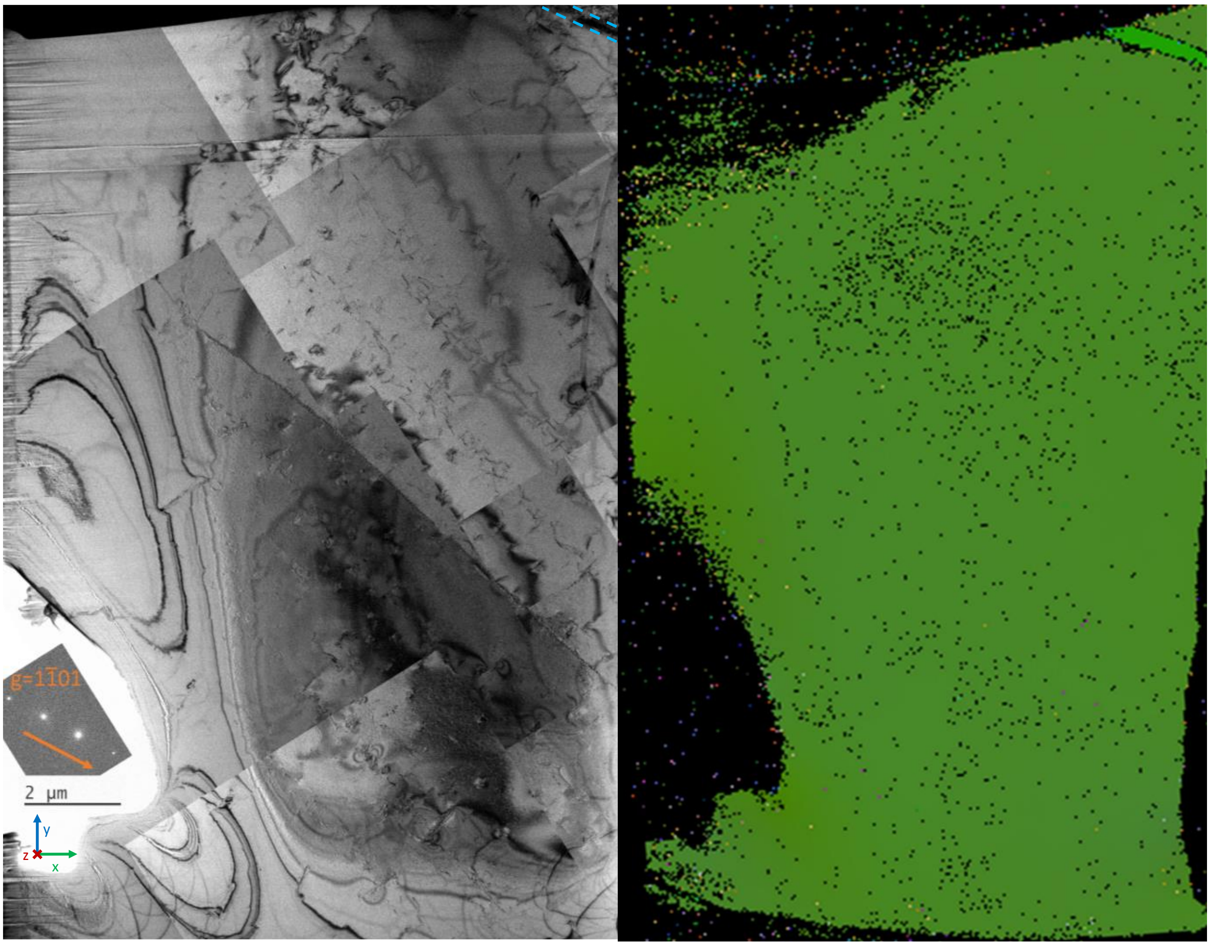

Figure 109: 10-Shock sample, *Figure 69* (10-Shock, 250 µm) with overlayed twins (Left) as identified through the TKD Euler colours (Right).

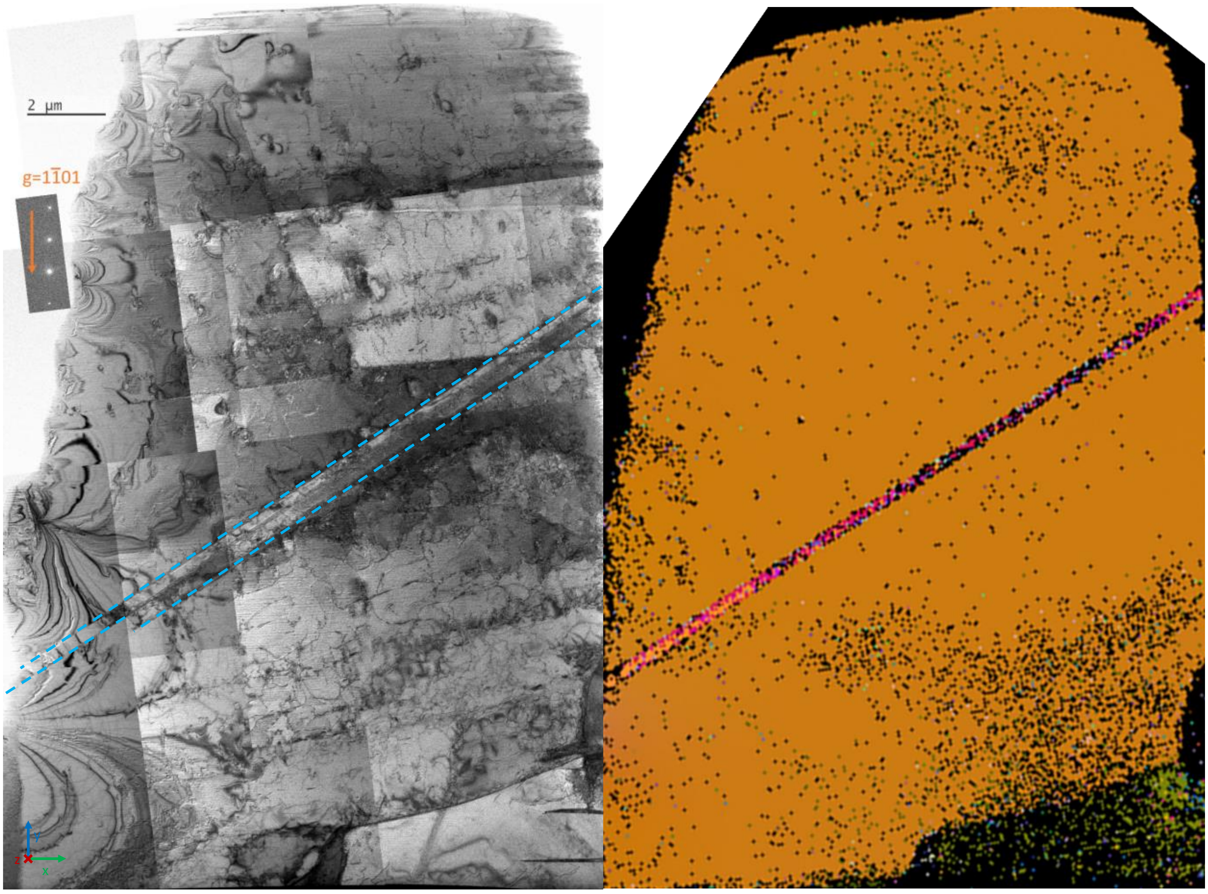

Figure 110: 15-Shock sample, *Figure 71* (15-Shock, 250 µm) with overlayed twins (Left) as identified through the TKD Euler colours (Right).

4.8 Nanoindentation

The nanoindentation results were collected via indentation at a force of 5 mN along the cross-section of the samples, around 150 µm away from the shock centre. 5 indents were taken across a 100 µm region for each depth. These results were collected to form the Figure 111 for 3, 5 10 and 15-shocks as indicated, with Figure 112 presenting these on the same graph for ease of comparison. The results of these indentation tests show little information. This is likely due to influence of large grains and their different orientations causing more significant changes than those as a result of the LSP process. These do not corroborate the results shown in other works which demonstrate an increased hardness at the surface of LSP samples.

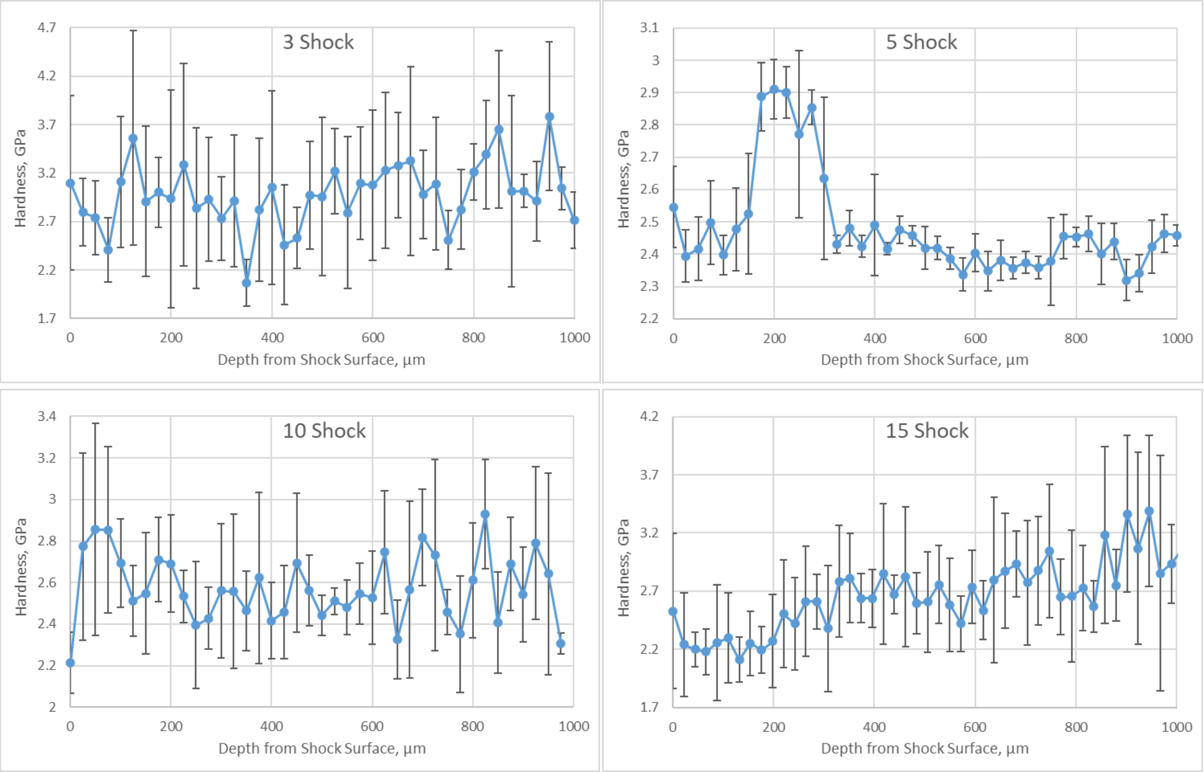

Figure 111: Nanoindentation results taken from the surfaces of the respective samples that were prepared to cross-section. Each point represents 5 indents. Array was performed within 200 µm from the shock centre.

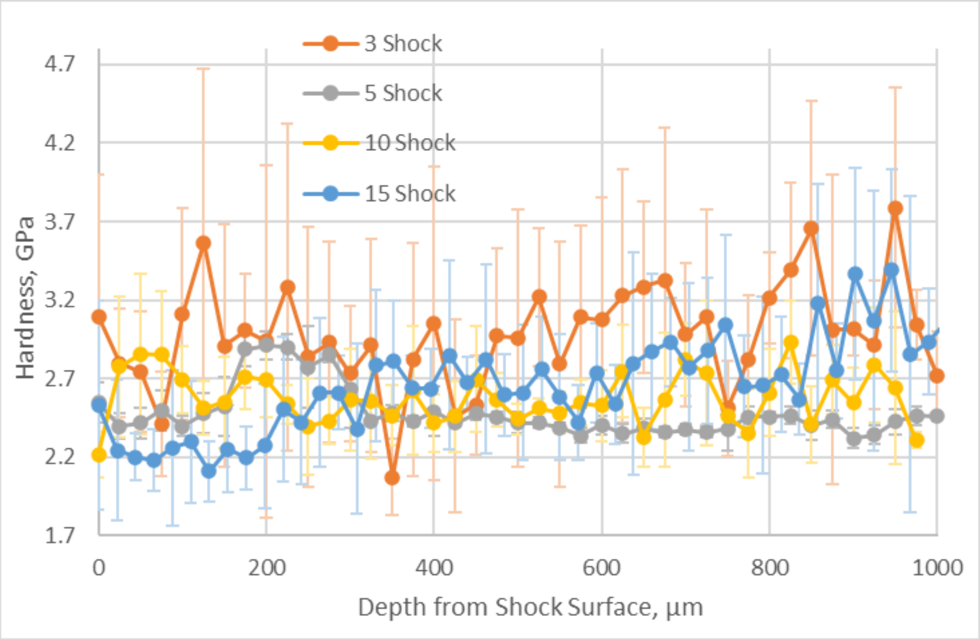

Figure 112: Summarised results of *Figure 111*.

4.9 Summary of Results

The EBSD taken before and after shocking of coated commercially pure titanium shows there are minimal recognisable changes to these samples.

The optical microscopy demonstrates the surface changes of the LSPwC material, increasing with shock number. This is supported by the SEM surface imaging.

BSE Imaging of cross-sectioned LSPwC samples after argon milling revealed twin boundaries. The area over which twinning can be seen increases with shock number, along with the depth of these twins. This matches reasonably well with the TEM results, which show twins in all the expected areas. The TEM results also show a series of dislocation-based features, which increase in quantity with increasing shock number. Dislocation lines are seen with low shocks. Dislocation cells are observed with moderate shock numbers and above close to the shock surface with the formation of dislocation tangles. Dislocation bands and tangles are seen further into the sample at greater shock numbers, and bands are seen clearly at 15-shocks in the 500 µm sample.

The types of twins seen in the SEM were predicted and confirmed with the use of TEM and TKD. The near-surface "region A" shows an abundance of $\{10\bar{1}1\}$ twins. This typically is contained within 10 µm, with no strong dependence on shock number, apart from a notable exception in the 15-shock sample. The area beyond region A typically extending to the maximal twin area depths is termed "region B," which is characterised predominantly by the presence of long $\{11\bar{2}1\}$ twins. A modest number of $\{11\bar{2}1\}$ twins are also observed here, with the usually common $\{10\bar{1}2\}$ twins not seen (with one exception). The TKD results corroborate absolutely with the TEM results.

5 Study of the Changes Induced from further Laser Shock Processing

The results shown prior demonstrate the changes introduced to the HCP system. We shall now discuss these changes in relation to other similarly compressive procedures, as well as discuss the mechanism by which the microstructure adapts from low shock numbers to high shock numbers. This constitutes an explanation of the dislocation networks and types of twins produced, and how these evolve with increased LS processing.

5.1 Surface Analysis

The Optical (Figure 37) and SEM (Figure 46) imaging shows the increase in region affected by the LSP process, as determined by the size and colour of the shock sites. The severely dark brown and black parts of the spots cannot be measured using light due to the limited reflection. This darker discolouration contributes to the fewer hits on the optical profilometry results (Figure 41) and is indicative of oxidation during superheating and cooling of titanium.

5.2 Dislocation Networks

The predominant microstructural changes induced in the CP Ti samples as a result of LSP are a substantial increase in dislocations, and subsequent formation of HCP twins. The relationship between these two mechanisms is complicated and as such we shall begin with an assessment of the dislocation distributions. It should be added that dense dislocation structures are typically found in the first 50 - 100 µm of material.

The dislocations seen in the 3-shock sample surface (0 µm, Figure 54) have formed in substantial numbers (Figure 94), however these are long and have fewer interactions between each other when compared with the 5-shock sample. The 5 and 10-shock samples (Figure 96 and Figure 98, respectively) are similar in number, with an increase in the number of triple points demonstrating the presence of dislocation tangles and cells, seen clearer in Figure 60. Any differences between the 5 and 10-shock dislocation morphologies are not easily identified.

The 15-shock sample (Figure 100) demonstrated a notable increase in the quantity of dislocations, as well as the challenge in imaging such an affected region under the same imaging condition (due to the change in imaging condition as a result of the severe plastic deformation). The dislocations seen are very short and are mostly collected in tangles. Dislocation cells are on some occasions harder to identify due to the vast number of dislocations inside the prospective dislocation cells. The dislocation structures produced are comparable to those seen in literature, such as in Lu *et al*. [82]. Gaoli *et al*. [90] depicts a very clear dislocation cell, partially bounded by existing grain boundaries and from dislocation tangles, with a significant reduction in internal dislocation density, and a change in imaging condition producing good contrast (Figure 25). Similar dislocation features are seen in Jia *et al*. and Pan *et al*. [91,99]. Although this study identifies dislocation cells, there is a smaller number of them, or they are harder to identify, probably due to the large grain size and strain-free dislocation network prior to LSP. This has reduced the number of nucleation sites for dislocation tangles, resulting in sparser tangles and fewer tangle-tangle interactions, which in turn reduces the number of identifiable dislocation cells.

5.3 Twin Analysis

When α-titanium is compressed, the commonly produced twinning types are $\{10\bar{1}2\}$ and $\{11\bar{2}2\}$ [47]. These twin types are seen the least in this study. The common twins seen in the afore-mentioned region A (near the surface of the samples) contains an abundance of $\{10\bar{1}1\}$ twins, with a few twins of other types which in some cases may be contested according to the TKD results, found in appendix section [*8.2 Twin Analysis from TKD*]. These, as contraction twins, are indicative of tensile residual stresses, according to the direction of shockwave compression being close to along the a-axis. It is likely that region A has been affected both mechanically as a result of the high amplitude shockwave, but also thermally due to the superheating and supercooling of the surface titanium, as expected in the LSPwC regime. This region typically extends less than 10 µm into the sample. In contrast to region A, region B contains many $\{11\bar{2}1\}$ twins. These are extension twins, and are indicative of compressive residual stresses (CRS) in the samples. This is the expected condition of LSP samples, and why the technique is employed. We can understand that this region has been affected purely from the mechanical effect of the shockwave, but not the thermal effects of the surface ablation. This region extends many hundreds of micrometres into the sample and would contribute towards desired mechanical properties. It is worth noting that these twins are the least commonly seen in HCP materials.

5.3.1 "Region B" Twinning

The presence of $\{11\bar{2}1\}$ twins in the absence of a large number of other twins is unusual, with literature available amongst greater numbers of other twin types [110,111]. The main difference between twin types than LSP may affect is the twinning shear, s. Twinning shear is the shear stress required to produce the twin. As summarised in Table 11, the twinning shear is obtained from the equations outlined in Table 5. It shows that the $\{11\bar{2}1\}$ has the greatest twinning shear, with $s = 0.632$, significantly larger than the $\{10\bar{1}2\}$ extension twin at $s = 0.180$. LS processing induces one of the highest strain rates in surface processing, even reaching over 10^7. This would clearly be enough to introduce the $\{11\bar{2}1\}$ contraction twins. This is made more significant by the absence of $\{10\bar{1}1\}$ and $\{10\bar{1}2\}$ twins in region B, (with a few exceptions that shall be clarified shortly). This implies that for the short duration over which the shockwave progresses through the sample (as a vast simplification using ultrasonic shear wave measurements in polycrystalline Ti-6Al-4V where the speed of sound is $4.95\ km\ s^{-1}$ [62], $v \approx 5000\ ms^{-1}$, so $1\ mm$ corresponds to $\approx 200\ ns$) the energy imparted to the system can only be accommodated through this twinning type, and not through twins that correspond to reduced free energy. Similar observations were made regarding these twins by *Gray and Morris* [62].

A few additional $\{11\bar{2}2\}$ twins (with $s = 0.213$, the second largest value) have also formed, which can be explained as the twin type is of opposite sense (contraction twinning, when compared to $\{11\bar{2}2\}$ extension twinning) which can adjust for any minor misalignment of the compressed grains (as deviation from the a-axis). Thereby, these are also likely to contribute to the CRS.

There is one contrition of a single group of $\{10\bar{1}2\}$ type twins, as seen in the 15-shock sample in Figure 106. This can be explained, due to the angle these twins make with the shock axis. They are perpendicular to the shock surface, parallel to the shockwave direction. This means that the amplitude of stress acting upon these regions which formed the twins was small. They may have formed from reflection or release waves caused by grain or sub-grain boundaries.

5.3.2 “Region A” Twinning

In this location in each sample, there is an abundance of $\{10\bar{1}1\}$ type contraction twins. This suggests the presence of tensile stresses. A few other twins are seen in region A, which could either be the result of misidentification of the TKD software, but is more likely explained by release waves and minor deviations in the compression direction of the a-axis. Release waves are more likely, as in the case of the 15-shock sample (Figure 106). The primary exception is seen in the 5-shock sample (Figure 104) which appears to show many $\{11\bar{2}1\}$ type twins. This is almost certainly a misidentification of the TKD software, as all of these possible twin planes also had possible matches with $\{10\bar{1}1\}$ type twins (within about 10° range) (see Appendix, AFigure 5).

Figure 65 and Figure 66 show that there is a region similar to region A in the bulk structure (region B) at a depth of around 16 m from the shock surface. This is a similar feature to that seen in the 3-shock sample at the surface (Figure 54 and Figure 55). The inference is that this space is a zone of tensile residual stresses. This area is surrounded by compressive region B. This gives credence to the idea that increased laser shocking past the point of saturation, "over-processing," starts to increase tensile stresses deep into LS processed samples, leading to internal rupture [3,12,112].

$\{10\bar{1}1\}$ twins are seen throughout literature. Examples of their formation purely through deformation via cold rolling can be seen in Zhang *et al*. [113]. Examples of their formation through annealing can also be seen [43], as well as through mixed thermomechanical means in the case of additive manufacturing [114]. A contact explosion study of Ti6321 Ti alloy from Yan *et al*. [115] provides similar conditions to LSP, which also demonstrates the abundance of $\{10\bar{1}1\}$ twins. Morris *et al.* also surmises that in contrast to $\{11\bar{2}2\}$ twins, which readily form at low temperatures even though it has a greater formation energy requirement, the $\{10\bar{1}1\}$ twins are only formed at higher temperatures [116]. These conditions explain the thermomechanical dependence of $\{10\bar{1}1\}$ twins in this study.

5.3.3 Understanding Twins

To summarise section [*5.3.1 "Region B" Twinning*] regarding $\{11\bar{2}1\}$ twins; they are produced due to the high twin shear ($s = 0.632$) required to produce them. An explanation why these twins are preferentially produced is that this is the only twin able to accommodate the strain induced from the high-amplitude shockwave are the $\{11\bar{2}1\}$ twins. The other possible twins do not accommodate the strain over the shockwave time.

Twin nucleation and growth is a major contribution of plastic deformation in HCP alloys, with early attempts in the 1990's to work out the twin boundary energies [116]. There is still much research required to understand this mechanistically [117]. Papers that have investigated this phenomenon typically do not cover the rarest of these twins, the $\{11\bar{2}1\}$

type. Hui *et al.* discusses the twin boundary energy sustained by $\{10\bar{1}1\}$ and $\{10\bar{1}2\}$ twinning [118]. This states that an increased shear strain closely relates to increased twin formation energy, with the greater twin energy formation requirement leading to an increased twin boundary energy. The paper focuses on segregation energy in reducing the free energy requirement to stabilise twins. Zahiri et al., concentrates on mediation phases which reduce the energy requirement to produce twins of each type, suggesting a HCP-BCC-HCP phase transformation reduces the twinning shear, s from 0.632 to 0.514 [117].

As this study does not observe any intermediate phases, the precise mechanism by which the $\{11\bar{2}1\}$ twins form cannot be precisely ascertained, however there is enough indication that the $\{11\bar{2}1\}$ twins have a greater twin boundary energy, allowing the HCP-Ti to accommodate greater strain resulting from the laser pulses.

5.3.4 Implications of $\{11\bar{2}1\}$ Twins

The topics of CRSS and TCRSS have been discussed extensively in section [*2.3.3.1 CRSS and TCRSS*]. The assumed twin production in TCRSS models [48,49] are $\{11\bar{2}2\}$ in the case of contraction twinning, and $\{10\bar{1}2\}$ in the case of extension twinning. These assumptions are made due to the commonly seen twins produced in α-titanium. We have shown from the abundance of $\{11\bar{2}1\}$ and even $\{10\bar{1}1\}$ twinning, that this lower threshold does not predict the types of twinning produced. It is possible that LSP can be used, after varying the laser parameters, to control the compression force incident on substrates. Experimentally, this can provide a method by which the compression of samples may be systematically performed to study the strain response of materials at variable compression rates, to assess which deformation mechanisms are produced at various strains, at the ultra-high strain rate produced by LSP exceeding 10^6. The Pressure calculated according to Equation 3, assuming $\alpha = 0.3$, is 16.2 GPa (per shock) for pure titanium (without coating).

5.4 Comparison with Shock-Loading Experiments

Looking at work performed by *Los Alamos National Laboratory*, it has been shown that in high purity titanium (HP Ti) a roughly 10 GPa pressure [62] is required to induce an α-ω phase transformation. In this work, no such transformation was observed. Firstly, the 16.2 GPa value for the pulse pressure is an approximation, as we were unable to measure the shock-wave profile in-situ. As the shock surface was well polished, much of the energy may have been reflected.

A second, more likely reason, relates to the oxygen concentration in the sample. The analysis tool used to verify the O% in this work was SEM-EDX, attaining a value of O% < 0.1. This is well known to provide low resolution data for elements with low atomic mass, such as carbon, nitrogen and oxygen. Using a comparative study from *Cerreta et al.* [61], we see that although the α-ω phase transformation was shown at 10.4 GPa for a HP Ti of O = 360 ppm, no such transformation was found up to 35 GPa for a commercial purity alloy of O = 3700 ppm. An elemental analysis experiment for accurate determination of the proportion of oxygen in the samples would be beneficial for further studies.

5.5 Shock Number Comparison

Overall, the level of LSP-induced microstructural changes increases with an increase in the shock number. This is primarily summarised in Figure 48 and Figure 49 from the SEM data, in relation to the visible twins. The increase in twinning depth and area elucidates the principle stated by Lou *et al*. as seen in Figure 24 [70]. This shows that regions closer to the surface often exhibit later stages of microstructural changes than deeper regions, i.e. the dislocation tangles seen at the surface after moderate laser shocking are seen slightly deeper into the material after many laser shocks. Similarly, twinning is seen in the surface of 3-shock sample, but seen much deeper into the remaining samples, particularly the 15-shock sample.

A similar effect is shown from the dislocations seen in the TEM results. The dislocations seen in the surface of the 3-shock sample, Figure 54 are longer with fewer interactions with each other, reducing the tangling effect clearly visible throughout the remaining 5, 10 and 15-shock samples. The dislocation densities summarised in Figure 102 have shown the dislocation density between 5 and 10-shocks is almost the same. This is probably due to the shockwave energy dispersed through rearrangement of existing dislocations, and through formation of twins further into the sample. This is also an indication that the dislocation density in these samples have reached saturation, through which an increase in the number of dislocations will not contribute towards an increase in the local CRS. This is why the twin depth must increase - to accommodate the energy imparted to the system from the laser.

The changes are more obvious at a depth of 250 µm. In the 3-shock sample no twins can be seen, and the few dislocations found are sparsely distributed. These dislocations are identified to be a-type dislocations, with prismatic $< a >$ slip (Table 10) consistent with common twinning in HCP materials [48]. Twins are seen in the 5-shock sample, with a negligible amount of dislocations. The dislocations in the 10-shock sample have collected into dislocation lines, with regular intervals to the next dislocation line. This progression suggests that dislocations have rearranged with successive shocks into dislocation lines, highlighted in Figure 70. These dislocation lines / bands increase in dislocation density in the 15-shock sample, seen in Figure 72, Figure 73 and Figure 74. This particular TEM sample of 10-shocks happens to not show a twin, however the SEM has demonstrated 10-shock twins at this depth. The 15-shock sample shows an obvious twin in the centre. The dislocation lines above and below the twin in Figure 73 have slightly different directions and densities, as well as the dislocation density outside of the lines. This shows that the twin itself has influenced the shockwave progression, most likely reducing the shockwave amplitude above the twin.

These observations imply that the microstructural changes introduced are as a function of absorbed shockwave energy, because the shockwave energy decreases as a function of distance into the material. A summary of the observed and inferred microstructural changes in the increasing shock samples can be seen in Figure 113.

Based on these results, the process parameters recommended in this study would be around 10-shocks, which could be accommodated on a larger sample through a 90 % overlap ratio in one dimension. This is due to the observation of significant positive microstructural changes in this sample, and a large depth of “Region B” (570 µm) indicating successful introduction of compressive residual stresses, as intended. Although these are observed even more in the 15-shock sample, the presence of internal “Region A,” which is indicative of tensile residual stresses, renders the sample dangerous and unpredictable. It is probable that a component treated under these conditions would experience failure before the 10-shock equivalent, and there is also a chance such a component would perform worse than an unprocessed component.

This assessment is given assuming the same 2 J pulse energy, 1.5 mm spot size, 10 ns pulse duration (thereby corresponding to a power density of ~11.2 GW cm^{-2}) and keeping all other parameters constant (see Table 8). It should be noted that any changes to any of the parameters may have a significant effect on the resulting sample, as discussed extensively in *Chapter 2 Literature Review*.

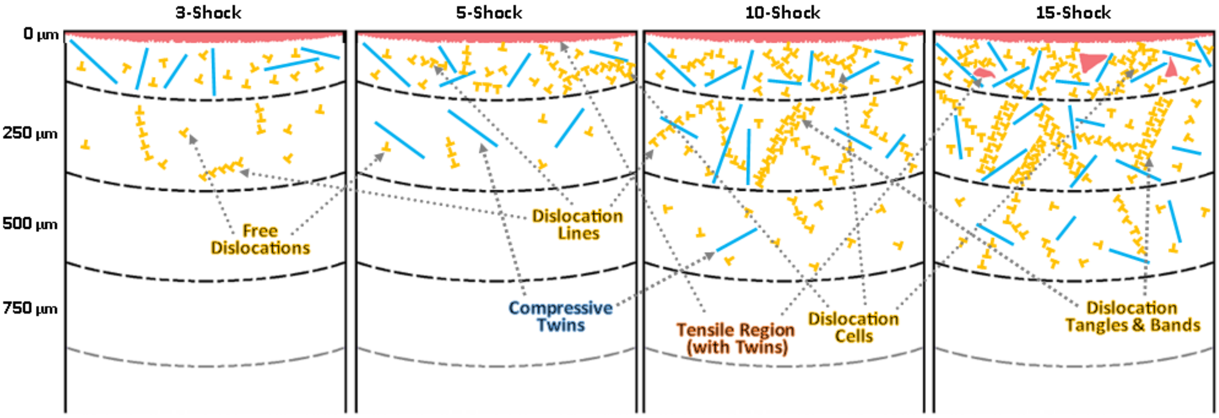

Figure 113: Summary of twinning and dislocation features found in LSP samples studied from cross-sectional SEM and depth-based TEM study. Dislocation commentary in yellow, tensile region and twins in red, with compressive twins in blue.

5.6 Grain Refinement

The dislocation networks seen close to the surface of the sample (but still within "region B", not the absolute surface) constitute dislocation cells. At earlier stages, dislocation cells can be seen forming from dislocation lines, which later increase in density to cause dislocation tangles. The cells are bounded primarily by dislocation tangles, but sometimes are bounded by twins and low-angle grain boundaries (along with dislocation tangles, as the size of the twins and grain boundaries are too great to allow tangles to consistently stretch from one to the other in this study, unlike those observed in literature [79,91,106]). As a result of the increased deformation, it is possible to consider some of these cells to be sub-grains. There is no hard definition in the literature to separate dislocation cells and sub-grains. Here, we observe that some these dislocation cells observe a contrast difference from the matrix, suggesting some misorientation. The misorientation observed with increasing shock sizes increases the likelihood of sub-grain formation. Changes in contrast are seen in the 15-shock sample when comparing different parts of the image shown in Figure 100, where the top left of the image appears darker than the bottom right of the image. These changes are significant enough to change the visibility of dislocations in parts of the image.

In the near surface region of the samples ("region A"), the grain refinement seen appears very different. The twinning found is clearest in the 5-shock sample Figure 59. Many close twins are found, with thicknesses of 0.1 – 0.3 µm and lengths of over 0.5 - 2 µm. This sample also shows potential twinning arrays, seen in Figure 61, although as discussed previously, these are more likely to be Moiré fringes. A similar set of region A microstructure that is more likely to be a twin array is highlighted in Figure 57 using SAED patterns, which show the nanocrystallisation of the near surface regions (Figure 57A and Figure 57B). The diffraction pattern observed in Figure 57A has definitive symmetry, which is strongly indicative of twinning diffraction patterns. This region is not amorphous; an amorphous nanocrystalline compressive region has not been observed in this study, unlike some of the literature [29,30,81,96], but comparable to the (non-amorphous) nanocrystallisation seen in [71,92,96,104]. As mentioned previously, there is no indication that region A provides CRS, and therefore the nanocrystallisation observed here is unlikely to contribute towards improved mechanical properties, which may be characteristic of LSPwC.

6 Conclusions

6.1 Conclusion

LSPwC successfully induced changes to samples, proportional to the number of shocks incident on the sample surface. The level of deformation within the first 50 to 100 µm showed signs of severe plastic deformation. The dislocation densities taken approximately 10 µm from the shock surface show a sizeable increase from 3 to 5-shock and 10 to 15-shock with no significant change from 5 to 10-shock.

The near surface area (region A) often exhibited nanocrystalline behaviour, however the presence of an abundance of $\{10\bar{1}1\}$ twins despite a-axis compression indicates this region exhibits tensile residual stresses. This is accounted for given that in the LSPwC regime, surface material often exhibits a reduction in mechanical properties. This is localised to a layer averaging 5°µm. The 15-shock sample experienced patches of region A a small distance from the surface, which in fatigued components would provide prime locations for crack propagation or even initiation.

The area found beyond region A was termed “Region B” where $\{11\bar{2}1\}$ twins dominated, and some $\{11\bar{2}2\}$ twins were found. These indicate a vast compressively stressed area, reaching depths of over 500 µm in the 10 and 15-shocked samples. The presence of $\{11\bar{2}1\}$ twins and lack of other more common α-titanium twinning mechanisms is accounted for due to the ultra-high strain rate induced through LSP. It is asserted that the only twin type able to accommodate the large shockwave amplitude in the short time-scale over which LSP operates ($\sim$200 ns) are those corresponding to the greatest twinning shear, resulting in a greater twin boundary energy.

Regarding the (compressive) Region B features: Dislocation lines were observed throughout all the shock-affected areas; Dislocation cells were found from 5-shocks onwards in the surface samples, after region A; Dislocation tangles and bands have been observed up to 250 µm into the 10 and 15 shock samples; the primary twin introduced as a result of LSP were of $\{11\bar{2}1\}$ type.

6.2 Future work

The work completed in this study provides a good grounding into the microstructural characterisation of LSP HCP-Ti. This would be complimented with two primary pieces of evidence: Mechanical property data, and residual stress measurements that would conclusively support the microstructural observations. That being said, the literature on LSP-improved mechanical properties and residual stress data is vast. The reasons why this data extraction has been challenging is due to the large grains used in the experiments, which mitigates the comparisons possible from nanoindentation (given orientation data is lengthy to procure) and prevents XRD which relies on polycrystalline materials.

In this capacity, this experiment may now be attempted on samples with smaller grains. This would allow for a deeper understanding of the contributions of grain boundaries in the grain refinement mechanisms of the near surface (< 100 µm) areas. This description has been performed by some studies [79,107], however one would require working with samples of low prior deformation. This would allow for an easy separation between features observed as a result of LSP, over features caused by other means.

Bearing this necessary constraint in mind, the effect of solid solutions should also be studied. The oxygen content of titanium alloys is known for having strong effects on phase transformations [33], amongst other microstructural changes. Extending this to other commercially available alloys can take place at this point, which will then give context to the large numbers of studies performed on the alloys and components used in industry.

Once this is performed, we will have the tools needed to establish a laser input - component improvement relationship, making LSP a much more attractive technique for environments that are unfamiliar with it, such as the biomedical and manufacturing industries.

7 References

[1] B. Dhakal, S. Swaroop, Review: Laser shock peening as post welding treatment technique, J. Manuf. Process. 32 (2018) 721–733. https://doi.org/10.1016/j.jmapro.2018.04.006.

[2] C.S. Montross, T. Wei, L. Ye, G. Clark, Y.W. Mai, Laser shock processing and its effects on microstructure and properties of metal alloys: A review, Int. J. Fatigue. 24 (2002) 1021–1036. https://doi.org/10.1016/S0142-1123(02)00022-1.

[3] A.K. Gujba, M. Medraj, Laser peening process and its impact on materials properties in comparison with shot peening and ultrasonic impact peening, Materials (Basel). 7 (2014) 7925–7974. https://doi.org/10.3390/ma7127925.

[4] K. Ding, L. Ye, Laser shock peening, Woodhead Publishing Ltd, Cambridge, 2006. https://doi.org/10.1533/9781845691097.

[5] Y. Yang, K. Zhou, G. Li, Surface gradient microstructural characteristics and evolution mechanism of 2195 aluminum lithium alloy induced by laser shock peening, Opt. Laser Technol. 109 (2019) 1–7. https://doi.org/10.1016/j.optlastec.2018.07.041.

[6] C. Wang, L. Wang, C.L. Wang, K. Li, X.G. Wang, Dislocation density-based study of grain refinement induced by laser shock peening, Opt. Laser Technol. 121 (2020) 105827. https://doi.org/10.1016/j.optlastec.2019.105827.

[7] R. Fabbro, P. Peyre, L. Berthe, X. Scherpereel, Physics and applications of laser-shock processing, J. Laser Appl. 10 (1998) 265–279. https://doi.org/10.2351/1.521861.

[8] G. Gomez-Rosas, C. Rubio-Gonzalez, J.L. Ocaña, C. Molpeceres, J.A. Porro, M. Morales, F.J. Casillas, Laser Shock Processing of 6061-T6 Al alloy with 1064 nm and 532 nm wavelengths, Appl. Surf. Sci. 256 (2010) 5828–5831. https://doi.org/10.1016/j.apsusc.2010.03.043.

[9] L. Berthe, R. Fabbro, P. Peyre, E. Bartnicki, Wavelength dependent of laser shock-wave generation in the water-confinement regime, J. Appl. Phys. 85 (1999) 7552–7555. https://doi.org/10.1063/1.370553.

[10] A.S. Gill, Z. Zhou, U. Lienert, J. Almer, D.F. Lahrman, S.R. Mannava, D. Qian, V.K. Vasudevan, Erratum: High spatial resolution, high energy synchrotron x-ray diffraction characterization of residual strains and stresses in laser shock peened Inconel 718SPF alloy (Journal of Applied Physics (2012) 111 (084904)), J. Appl. Phys. 111 (2012). https://doi.org/10.1063/1.4718917.

[11] J.N. Johnson, R.W. Rohde, Dynamic deformation twinning in shock-loaded iron, J. Appl. Phys. (1971). https://doi.org/10.1063/1.1659750.

[12] M.J. Yadav, A.N. Jinoop, C. Danduk, S.K. Subbu, Laser Shock Processing: Process Physics, Parameters, and Applications, Mater. Today Proc. 4 (2017) 7921–7930. https://doi.org/10.1016/j.matpr.2017.07.128.

[13] D. Devaux, R. Fabbro, L. Tollier, E. Bartnicki, Generation of shock waves by laser-induced plasma in confined geometry, J. Appl. Phys. 74 (1993) 2268–2273. https://doi.org/10.1063/1.354710.

[14] J. Fournier, P. Ballard, P. Merrien, J. Barralis, L. Castex, R.. Fabbro, Détermination des contraintes résidelles par diffraction des raons X dans une couche mince de 1000A de ungstène, Society. (1991) 1467–1480. https://doi.org/10.1051/jp3.

[15] U. Trdan, J. Grum, Evaluation of corrosion resistance of AA6082-T651 aluminium alloy after laser shock peening by means of cyclic polarisation and ElS methods, Corros. Sci. 59 (2012) 324–333. https://doi.org/10.1016/j.corsci.2012.03.019.

[16] C. Rubio-González, G. Gomez-Rosas, J.L. Ocaña, C. Molpeceres, A. Banderas, J. Porro, M. Morales, Effect of an absorbent overlay on the residual stress field induced by laser shock processing on aluminum samples, Appl. Surf. Sci. 252 (2006) 6201–6205. https://doi.org/10.1016/j.apsusc.2005.08.062.

[17] P. Peyre, L. Berthe, X. Scherpereel, R. Fabbro, Laser-shock processing of aluminium-coated 55C1 steel in water-confinement regime, characterization and application to high-cycle fatigue behaviour, J. Mater. Sci. 33 (1998) 1421–1429. https://doi.org/10.1023/A:1004331205389.

[18] A. Telang, A.S. Gill, G. Ramakrishnan, V.K. Vasudevan, Effect of Different Ablative Overlays on Residual Stresses Introduced in IN718 SPF by Laser Shock Peening, Int.

Journ. Peen. Sci. Technol. 1 (2018) 75–86.

[19] Y. Zhang, J. You, J. Lu, C. Cui, Y. Jiang, X. Ren, Effects of laser shock processing on stress corrosion cracking susceptibility of AZ31B magnesium alloy, Surf. Coatings Technol. 204 (2010) 3947–3953. https://doi.org/10.1016/j.surfcoat.2010.03.015.

[20] C. Correa, A. Gil-Santos, J.A. Porro, M. Díaz, J.L. Ocaña, Eigenstrain simulation of residual stresses induced by laser shock processing in a Ti6Al4V hip replacement, Mater. Des. 79 (2015) 106–114. https://doi.org/10.1016/j.matdes.2015.04.048.

[21] G. Hammersley, L.A. Hackel, F. Harris, Surface prestressing to improve fatigue strength of components by laser shot peening, Opt. Lasers Eng. 34 (2000) 327–337. https://doi.org/10.1016/S0143-8166(00)00083-X.

[22] Q. Liu, S. Barter, G. Clark, Internal cracking during surface treatment of 7050-T74 aluminium alloy using laser shock peening., Struct. Integr. Fract. Proc. Int. Conf. SIF 2002, Perth, Aust. 25-28 Sept. 2002. (2002) 177.

[23] H. Lim, P. Kim, H. Jeong, S. Jeong, Enhancement of abrasion and corrosion resistance of duplex stainless steel by laser shock peening, J. Mater. Process. Technol. 212 (2012) 1347–1354. https://doi.org/10.1016/j.jmatprotec.2012.01.023.

[24] S. Kalainathan, S. Sathyajith, S. Swaroop, Effect of laser shot peening without coating on the surface properties and corrosion behavior of 316L steel, Opt. Lasers Eng. 50 (2012) 1740–1745. https://doi.org/10.1016/j.optlaseng.2012.07.007.

[25] D. Kumar, S. Nadeem Akhtar, A. Kumar Patel, J. Ramkumar, K. Balani, Tribological performance of laser peened Ti-6Al-4V, Wear. 322–323 (2015) 203–217. https://doi.org/10.1016/j.wear.2014.11.016.

[26] Z.P. Tong, X.D. Ren, W.F. Zhou, S. Adu-Gyamfi, L. Chen, Y.X. Ye, Y.P. Ren, F.Z. Dai, J.D. Yang, L. Li, Effect of laser shock peening on wear behaviors of TC11 alloy at elevated temperature, Opt. Laser Technol. 109 (2019) 139–148. https://doi.org/10.1016/j.optlastec.2018.07.070.

[27] P. Ganesh, R. Sundar, H. Kumar, R. Kaul, K. Ranganathan, P. Hedaoo, G. Raghavendra, S. Anand Kumar, P. Tiwari, D.C. Nagpure, K.S. Bindra, L.M. Kukreja, S.M. Oak, Studies

on fatigue life enhancement of pre-fatigued spring steel specimens using laser shock peening, Mater. Des. 54 (2014) 734–741. https://doi.org/10.1016/j.matdes.2013.08.104.

[28] X.C. Zhang, Y.K. Zhang, J.Z. Lu, F.Z. Xuan, Z.D. Wang, S.T. Tu, Improvement of fatigue life of Ti-6Al-4V alloy by laser shock peening, Mater. Sci. Eng. A. 527 (2010) 3411–3415. https://doi.org/10.1016/j.msea.2010.01.076.

[29] S. Luo, L. Zhou, X. Wang, X. Cao, X. Nie, W. He, Surface nanocrystallization and amorphization of dual-phase TC11 titanium alloys under laser induced ultrahigh strain-rate plastic deformation, Materials (Basel). 11 (2018). https://doi.org/10.3390/ma11040563.

[30] X. Nie, W. He, S. Zang, X. Wang, J. Zhao, Effect study and application to improve high cycle fatigue resistance of TC11 titanium alloy by laser shock peening with multiple impacts, Surf. Coatings Technol. 253 (2014) 68–75. https://doi.org/10.1016/j.surfcoat.2014.05.015.

[31] Y. WANG, X. PAN, X. WANG, Z. LIU, S. LIU, W. WAN, P. WANG, Influence of laser shock peening on surface integrity and tensile property of high strength low alloy steel, Chinese J. Aeronaut. 34 (2021) 199–208. https://doi.org/10.1016/j.cja.2020.09.004.

[32] Y. Shadangi, K. Chattopadhyay, S.B. Rai, V. Singh, Effect of LASER shock peening on microstructure, mechanical properties and corrosion behavior of interstitial free steel, Surf. Coatings Technol. 280 (2015) 216–224. https://doi.org/10.1016/j.surfcoat.2015.09.014.

[33] M.A. Meyers, O. Vöhringer, V.A. Lubarda, The onset of twinning in metals: A constitutive description, Acta Mater. 49 (2001) 4025–4039. https://doi.org/10.1016/S1359-6454(01)00300-7.

[34] H.J. Frost, M.F. Ashby, Deformation-Mechanism Maps, Oxford Pergamon Press. (1982) 44–45. https://searchworks.stanford.edu/view/1033654 (accessed May 29, 2023).

[35] G. Lütjering, J.C. Williams, Engineering Materials and Processes: Titanium, 2nd ed., Springer Berlin, Heidelberg, Berlin, Heidelberg, 2007.

https://doi.org/https://doi.org/10.1007/978-3-540-73036-1.

[36] M.H. Yoo, Slip, twinning, and fracture in hexagonal close-packed metals, Metall. Trans. A. 12 (1981) 409–418. https://doi.org/10.1007/BF02648537.

[37] F. Bridier, P. Villechaise, J. Mendez, Analysis of the different slip systems activated by tension in a α/β titanium alloy in relation with local crystallographic orientation, Acta Mater. 53 (2005) 555–567. https://doi.org/10.1016/J.ACTAMAT.2004.09.040.

[38] I.P. Jones, W.B. Hutchinson, Stress-state dependence of slip in Titanium-6Al-4V and other H.C.P. metals, Acta Metall. 29 (1981) 951–968. https://doi.org/10.1016/0001-6160(81)90049-3.

[39] X. Lu, IN - SITU TRANSMISSION ELECTRON MICROSCOPY STUDY OF DISLOCATION IN TI - 6AL - 4V by XINYU LU A thesis submitted to the University of Birmingham for the degree of DOCTOR OF PHILOSOPHY School of Metallurgy and Materials University of Birmingham MARCH 2017 P, University of Birmingham, 2017.

[40] S.J. Lainé, K.M. Knowles, P.J. Doorbar, R.D. Cutts, D. Rugg, Microstructural characterisation of metallic shot peened and laser shock peened Ti–6Al–4V, Acta Mater. 123 (2017) 350–361. https://doi.org/10.1016/j.actamat.2016.10.044.

[41] J.W. Christian, S. Mahajan, Deformation Twinning, Prog. Mater. Sci. 39 (1995) 1–157. https://doi.org/10.1007/BF00550122.

[42] M. Wronski, M. Arul Kumar, L. Capolungo, R.J. McCabe, K. Wierzbanowski, C.N. Tomé, Deformation behavior of CP-titanium: Experiment and crystal plasticity modeling, Mater. Sci. Eng. A. 724 (2018) 289–297. https://doi.org/10.1016/j.msea.2018.03.017.

[43] Z. Nishiyama, M. Oka, H. Nakagawa, {10-11} Transforamtion Twins in Titanium, Japan Inst. Met. 7 (1966) 1–4.

[44] A. Akhtar, Basal slip and twinning in α-titanium single crystals, Metall. Trans. A. 6 (1975) 1105–1113. https://doi.org/10.1007/BF02661366.

[45] D.R. Chichili, K.T. Ramesh, K.J. Hemker, D.R. Chichili, K.T. Ramesh, K.J. Hemker, The high-strain-rate response of alpha-titanium: experiments, deformation mechanisms and modeling, AcMat. 46 (1998) 1025–1043. https://doi.org/10.1016/S1359-

6454(97)00287-5.

[46] R.W. Armstrong, P.J. Worthington, CONSTITUTIVE RELATION FOR DEFORMATION TWINNING IN BODY CENTERED CUBIC METALS., in: Plenum Press (Metall Soc of AIME Proc), 1973: pp. 401–414. https://doi.org/10.1007/978-1-4615-8696-8_22.

[47] A.A. Salem, S.R. Kalidindi, R.D. Doherty, Strain hardening of titanium: Role of deformation twinning, Acta Mater. 51 (2003) 4225–4237. https://doi.org/10.1016/S1359-6454(03)00239-8.

[48] X. Wu, S.R. Kalidindi, C. Necker, A.A. Salem, Prediction of crystallographic texture evolution and anisotropic stress-strain curves during large plastic strains in high purity α-titanium using a Taylor-type crystal plasticity model, Acta Mater. 55 (2007) 423–432. https://doi.org/10.1016/j.actamat.2006.08.034.

[49] H. Qin, J.J. Jonas, H. Yu, N. Brodusch, R. Gauvin, X. Zhang, Initiation and accommodation of primary twins in high-purity titanium, Acta Mater. 71 (2014) 293–305. https://doi.org/10.1016/j.actamat.2014.03.025.

[50] A.H. Shapiro, The dynamics and thermodynamics of compressible fluid flow, 1st ed., Ronald Press, New York, 1953.

[51] M. a Meyers, Dynamic Behaviour of Materials, 1994.

[52] B. Pang, The Defect Evolution in Shock Loaded Tantalum Single Crystals, University of Birmingham, 2015.

[53] N. Bourne, Materials in Mechanical Extremes: Ch5 Metals, in: Mater. Mech. Extrem., Cambridge University Press, Cambridge, 2013: pp. 219–222. https://doi.org/10.14361/9783839452431-024.

[54] A.R. Kutsar, V.N. German, THE INVESTIGATION OF THE TITANIUM STRUCTURE AFTER SHOCK WAVE LOADING, (1982) 1633–1634.

[55] S.K. Sikka, Y.K. Vohra, R. Chidambaram, Omega phase in materials, Prog. Mater. Sci. 27 (1982) 245–310. https://doi.org/10.1016/0079-6425(82)90002-0.

[56] J.C. Jamieson, Crystal Structures of Titanium, Zirconium, Sci. Mag. 140 (1963) 72–73.

[57] M.P. Usikov, V.A. Zilbershtein, The Orientation Relationship between the a- and o -Phases of Titanium and Zirconium, Phys. Stat. Sol. 19 (1973) 53–58.

[58] Y.K. Vohra, S.K. Sikka, E.S.K. Menon, R. Krishnan, Direct evidence of intermediate state during alpha-omega transformation in TiV alloy, Acta Metall. 28 (1980) 683–685. https://doi.org/10.1016/0001-6160(80)90146-7.

[59] S.G. Song, G.T. Gray, Microscopic and crystallographic aspects of retained omega phase in shock-loaded zirconium and its formation mechanism, Philos. Mag. A Phys. Condens. Matter, Struct. Defects Mech. Prop. 71 (1995) 275–290. https://doi.org/10.1080/01418619508244356.

[60] D.R. Trinkle, R.G. Hennig, S.G. Srinivasan, D.M. Hatch, M.D. Jones, H.T. Stokes, R.C. Albers, J.W. Wilkins, New Mechanism for the alpha to omega Martensitic Transformation in Pure Titanium, Phys. Rev. Lett. 91 (2003) 2–5. https://doi.org/10.1103/PhysRevLett.91.025701.

[61] E. Cerreta, G.T. Gray, A.C. Lawson, T.A. Mason, C.E. Morris, The influence of oxygen content on the α to ω phase transformation and shock hardening of titanium, J. Appl. Phys. 100 (2006). https://doi.org/10.1063/1.2209540/983930.

[62] G.T.. I. Gray, C.E. Morris, Influence of peak pressure on the substructure evolution and shock wave profiles of Ti-6Al-4V, 6. World Conf. Titanium, Cannes, Fr. 6 Jun 1988. (1988). https://digital.library.unt.edu/ark:/67531/metadc1054259/ (accessed July 11, 2024).

[63] D.R. Jones, B.M. Morrow, C.P. Trujillo, G.T. Gray, E.K. Cerreta, The α-ω Phase transition in shock-loaded titanium, J. Appl. Phys. 122 (2017) 24. https://doi.org/10.1063/1.4987146/19789820/045902_1_ACCEPTED_MANUSCRIPT.PDF.

[64] H. Conrad, Effect of interstitial solutes on the strength and ductility of titanium, Prog. Mater. Sci. 26 (1981) 123–403. https://doi.org/10.1016/0079-6425(81)90001-3.

[65] Z. Zhang, S. Wendt, N. Cosentino, L.J. Bond, Nondestructive strain depth profiling with high energy X-ray diffraction: System capabilities and limitations, AIP Conf. Proc. 1949 (2018). https://doi.org/10.1063/1.5031635.

[66] S.S. Rajan, G. Manivasagam, M. Ranganathan, S. Swaroop, Influence of laser peening without coating on microstructure and fatigue limit of Ti-15V-3Al-3Cr-3Sn, Opt. Laser Technol. 111 (2019) 481–488. https://doi.org/10.1016/j.optlastec.2018.10.027.

[67] A.S. Gill, A. Telang, C. Ye, S.R. Mannava, D. Qian, V.K. Vasudevan, Localized plastic deformation and hardening in laser shock peened Inconel alloy 718SPF, Mater. Charact. 142 (2018) 15–26. https://doi.org/10.1016/j.matchar.2018.05.010.

[68] L. Chen, X. Ren, W. Zhou, Z. Tong, S. Adu-Gyamfi, Y. Ye, Y. Ren, Evolution of microstructure and grain refinement mechanism of pure nickel induced by laser shock peening, Mater. Sci. Eng. A. 728 (2018) 20–29. https://doi.org/10.1016/j.msea.2018.04.105.

[69] L. Zhou, W. He, S. Luo, C. Long, C. Wang, X. Nie, G. He, X. Shen, Y. Li, Laser shock peening induced surface nanocrystallization and martensite transformation in austenitic stainless steel, J. Alloys Compd. 655 (2016) 66–70. https://doi.org/10.1016/j.jallcom.2015.06.268.

[70] S. Lou, Y. Li, L. Zhou, X. Nie, G. He, W. He, Surface nanocrystallization of metallic alloys with different stacking fault energy induced by laser shock processing, Mater. Des. 104 (2016) 320–326. https://doi.org/10.1016/j.matdes.2016.05.028.

[71] W. Zhou, X. Ren, F. Liu, Y. Ren, L. Li, Nanocrystallization in the duplex Ti-6Al-4V alloy processed by multiple laser shock peening, Metals (Basel). 6 (2016) 1–10. https://doi.org/10.3390/met6120297.

[72] K.Y. Luo, J.Z. Lu, Y.K. Zhang, J.Z. Zhou, L.F. Zhang, F.Z. Dai, L. Zhang, J.W. Zhong, C.Y. Cui, Effects of laser shock processing on mechanical properties and micro-structure of ANSI 304 austenitic stainless steel, Mater. Sci. Eng. A. 528 (2011) 4783–4788. https://doi.org/10.1016/j.msea.2011.03.041.

[73] Y. Sano, M. Obata, K. Akita, K. Masaki, Y. Ochi, Characterization of Laser-peened Materials by Synchrotron Radiation and Neutron Diffraction Techniques, J. JSEM. 7 (2007) 61–67. http://japanlinkcenter.org/JST.JSTAGE/jjsem/7.s61?from=Google.

[74] A. Umapathi, S. Swaroop, Phase gradient in a laser peened TC6 titanium alloy analyzed using synchrotron radiation, Mater. Charact. 131 (2017) 431–439.

https://doi.org/10.1016/j.matchar.2017.07.036.

[75] S. Keller, S. Chupakhin, P. Staron, E. Maawad, N. Kashaev, B. Klusemann, Experimental and numerical investigation of residual stresses in laser shock peened AA2198, J. Mater. Process. Technol. 255 (2018) 294–307. https://doi.org/10.1016/j.jmatprotec.2017.11.023.

[76] A. Chahardehi, F.P. Brennan, A. Steuwer, The effect of residual stresses arising from laser shock peening on fatigue crack growth, Eng. Fract. Mech. 77 (2010) 2033–2039. https://doi.org/10.1016/j.engfracmech.2010.03.033.

[77] S. Van Staden, C. Polese, D. Glaser, S. Africa, Measurement of Residual Stresses in Different Thicknesses of Laser Shock Peened Aluminium Alloy Samples, Mech. Stress Eval. by Neutron Synchrotron Radiat. 4 (2018) 117–122. https://doi.org/10.21741/9781945291678-18.

[78] K.Y. Luo, X. Jing, J. Sheng, G.F. Sun, Z. Yan, J.Z. Lu, Characterization and analyses on micro-hardness, residual stress and microstructure in laser cladding coating of 316L stainless steel subjected to massive LSP treatment, J. Alloys Compd. 673 (2016) 158–169. https://doi.org/10.1016/j.jallcom.2016.02.266.

[79] J.Z. Lu, L.J. Wu, G.F. Sun, K.Y. Luo, Y.K. Zhang, J. Cai, C.Y. Cui, X.M. Luo, Microstructural response and grain refinement mechanism of commercially pure titanium subjected to multiple laser shock peening impacts, Acta Mater. 127 (2017) 252–266. https://doi.org/10.1016/j.actamat.2017.01.050.

[80] Y. Guo, S. Wang, W. Liu, Z. Sun, G. Zhu, T. Xiao, Effect of laser shock peening on tribological properties of magnesium alloy ZK60, Tribol. Int. 144 (2020) 106138. https://doi.org/10.1016/j.triboint.2019.106138.

[81] C. Ye, S. Suslov, X. Fei, G.J. Cheng, Bimodal nanocrystallization of NiTi shape memory alloy by laser shock peening and post-deformation annealing, Acta Mater. 59 (2011) 7219–7227. https://doi.org/10.1016/j.actamat.2011.07.070.

[82] H.F. Lu, K.Y. Luo, L.J. Wu, C.Y. Cui, J.Z. Lu, Effects of service temperature on tensile properties and microstructural evolution of CP titanium subjected to laser shock peening, J. Alloys Compd. 770 (2019) 732–741.

https://doi.org/10.1016/j.jallcom.2018.08.161.

[83] F. Wang, X. Yan, L. Liu, M. Nastasi, Y. Lu, B. Cui, Surface strengthening of single-crystal alumina by high-temperature laser shock peening, Mater. Res. Lett. 9 (2021) 155–161. https://doi.org/10.1080/21663831.2020.1862933.

[84] K.K. Liu, M.R. Hill, The effects of laser peening and shot peening on fretting fatigue in Ti-6Al-4V coupons, Tribol. Int. 42 (2009) 1250–1262. https://doi.org/10.1016/j.triboint.2009.04.005.

[85] S. Varin, M. Agarwal, A. Chugh, M. Manikandan, S. Prabhakaran, S. Kalainathan, P. Shukla, J. Lawrence, N. Arivazhagan, Effect of Laser Shock Peening on Commercially Pure Titanium-1 Weldment Fabricated by Gas Tungsten Arc Welding Technique, Trans. Indian Inst. Met. 72 (2019) 1569–1573. https://doi.org/10.1007/s12666-019-01704-1.

[86] K. Gurusami, D. Chandramohan, S. Dinesh Kumar, M. Dhanashekar, T. Sathish, Strengthening mechanism of Nd: Yag laser shock peening for commercially pure titanium (CP-TI) on surface integrity and residual stresses, Mater. Today Proc. 21 (2020) 981–987. https://doi.org/10.1016/j.matpr.2019.09.141.

[87] P. Peyre, I. Chaieb, C. Braham, FEM calculation of residual stresses induced by laser shock processing in stainless steels, Model. Simul. Mater. Sci. Eng. 15 (2007) 205–221. https://doi.org/10.1088/0965-0393/15/3/002.

[88] X.D. Ren, J.J. Huang, W.F. Zhou, S.D. Xu, F.F. Liu, Surface nano-crystallization of AZ91D magnesium alloy induced by laser shock processing, Mater. Des. 86 (2015) 421–426. https://doi.org/10.1016/j.matdes.2015.07.039.

[89] B. Mao, Y. Liao, B. Li, Gradient twinning microstructure generated by laser shock peening in an AZ31B magnesium alloy, Appl. Surf. Sci. 457 (2018) 342–351. https://doi.org/10.1016/j.apsusc.2018.06.176.

[90] L. Gaoli, Z. Lingfeng, X. Yi, Z. Baofeng, C. Xuepeng, Effect of Laser Shock Peening on Microstructure and Properties of Ti-6Al-3Nb-2Zr-1Mo Titanium Alloy, (2022).

[91] W. Jia, Y. Zan, C. Mao, S. Li, W. Zhou, Q. Li, S. Zhang, V. Ji, Microstructure evolution

and mechanical properties of a lamellar near-α titanium alloy treated by laser shock peening, Vacuum. 184 (2021). https://doi.org/10.1016/j.vacuum.2020.109906.

[92] J. Li, J. Zhou, L. Liu, A. Feng, S. Huang, X. Meng, High-cycle bending fatigue behavior of TC6 titanium alloy subjected to laser shock peening assisted by cryogenic temperature, Surf. Coatings Technol. 409 (2021) 126848. https://doi.org/10.1016/j.surfcoat.2021.126848.

[93] R. Sun, Z. Che, Z. Cao, S. Zou, J. Wu, W. Guo, Y. Zhu, Fatigue behavior of Ti-17 titanium alloy subjected to different laser shock peened regions and its microstructural response, Surf. Coatings Technol. 383 (2020) 125284. https://doi.org/10.1016/j.surfcoat.2019.125284.

[94] Y. Yang, K. Zhou, H. Zhang, H. Hu, H. Qiao, Thermal stability of microstructures induced by laser shock peening in TC17 titanium alloy, J. Alloys Compd. 767 (2018) 253–258. https://doi.org/10.1016/j.jallcom.2018.06.030.

[95] W. Jia, H. Zhao, Q. Hong, L. Li, X. Mao, Research on the thermal stability of a near α titanium alloy before and after laser shock peening, Mater. Charact. 117 (2016) 30–34. https://doi.org/10.1016/j.matchar.2016.04.019.

[96] L. Zhou, Y. Li, W. He, G. He, X. Nie, D. Chen, Z. Lai, Z. An, Deforming TC6 titanium alloys at ultrahigh strain rates during multiple laser shock peening, Mater. Sci. Eng. A. 578 (2013) 181–186. https://doi.org/10.1016/j.msea.2013.04.070.

[97] C. Xuepeng, Z. Lingfeng, X Yi, L Gaoli, W Yongli, Effect of Laser Shock Peening on Microstructure and Properties of Laser Additive Manufactured TC4 Titanium Alloy, (2022) 696–700.

[98] W. Bohan, C. Li, L. Dongchun, Microstructure Evolution and Nanocrystal Formation of TC4 by Laser Shock Peening, (2022).

[99] X. Pan, X. Wang, Z. Tian, W. He, X. Shi, P. Chen, L. Zhou, Effect of dynamic recrystallization on texture orientation and grain refinement of Ti6Al4V titanium alloy subjected to laser shock peening, J. Alloys Compd. 850 (2021) 156672. https://doi.org/10.1016/j.jallcom.2020.156672.

[100] J. Lv, K. Luo, H. Lu, Z. Wang, J. Liu, J. Lu, Achieving high strength and ductility in selective laser melting Ti-6Al-4V alloy by laser shock peening, J. Alloys Compd. 899 (2022) 163335. https://doi.org/10.1016/j.jallcom.2021.163335.

[101] H. Zhang, Z. Cai, J. Chi, R. Sun, Z. Che, L. Lin, P. Peng, H. Zhang, W. Guo, Gradient microstructure evolution in laser shock peened Ti6Al4V titanium alloy, Surf. Coatings Technol. 437 (2022) 128378. https://doi.org/10.1016/j.surfcoat.2022.128378.

[102] H. Lu, W. Deng, K. Luo, Y. Chen, J. Wang, J. Lu, Tailoring microstructure of additively manufactured Ti6Al4V titanium alloy using hybrid additive manufacturing technology, Addit. Manuf. 63 (2023) 103416. https://doi.org/10.1016/j.addma.2023.103416.

[103] J. Li, J. Zhou, A. Feng, Y. Huang, X. Tian, S. Huang, X. Meng, Twin formation and its strengthening mechanism of pure titanium processed by cryogenic laser peening, Opt. Laser Technol. 120 (2019) 105763. https://doi.org/10.1016/j.optlastec.2019.105763.

[104] L. Li, W. Jia, V. Ji, Effect of laser shock peening on α→ω phase transformation in high-purity titanium, Vacuum. 206 (2022). https://doi.org/10.1016/j.vacuum.2022.111510.

[105] J.Z. Lu, K.Y. Luo, Y.K. Zhang, G.F. Sun, Y.Y. Gu, J.Z. Zhou, X.D. Ren, X.C. Zhang, L.F. Zhang, K.M. Chen, C.Y. Cui, Y.F. Jiang, A.X. Feng, L. Zhang, Grain refinement mechanism of multiple laser shock processing impacts on ANSI 304 stainless steel, Acta Mater. 58 (2010) 5354–5362. https://doi.org/10.1016/j.actamat.2010.06.010.

[106] J. Li, J. Zhou, A. Feng, Y. Huang, X. Tian, S. Huang, X. Meng, Twin formation and its strengthening mechanism of pure titanium processed by cryogenic laser peening, Opt. Laser Technol. 120 (2019) 105763. https://doi.org/10.1016/j.optlastec.2019.105763.

[107] L. Li, W. Jia, V. Ji, Phase transformations mechanism in commercially pure titanium subjected to multiple laser shock peening, Surf. Coatings Technol. 450 (2022) 129010. https://doi.org/10.1016/j.surfcoat.2022.129010.

[108] G. Lütjering, J.C. Williams, 10 Titanium-10, Titanium. (2007) 383–415.

[109] R. Ding, I.P. Jones, In situ hydride formation in titanium during focused ion milling,

(2010). https://doi.org/10.1093/jmicro/dfq066.

[110] T. Hama, H. Nagao, A. Kobuki, H. Fujimoto, H. Takuda, Work-hardening and twinning behaviors in a commercially pure titanium sheet under various loading paths, Mater. Sci. Eng. A. 620 (2015) 390–398. https://doi.org/10.1016/j.msea.2014.10.024.

[111] P. Zhou, S. Xu, D. Xiao, C. Jiang, Y. Hu, J. Wang, Shock-induced {1121}→{1122} double twinning in titanium, Int. J. Plast. 112 (2019) 194–205. https://doi.org/10.1016/j.ijplas.2018.08.014.

[112] R. T.J., B. Mark S., A. Clarence A., U. Walter, Shock Processing of Aircraft Engine Components, Laser Focus World. (2008). https://www.laserfocusworld.com/industrial-laser-solutions/article/14216627/laser-shock-procesing-of-aircraft-engine-components.

[113] H. Zhang, B. Wei, X. Ou, S. Ni, H. Yan, M. Song, Atomic-level study of {101¯1} deformation twinning in pure Ti and Ti-5at.% Al alloy, Int. J. Plast. 153 (2022). https://doi.org/10.1016/j.ijplas.2022.103273.

[114] H. Wang, Q. Chao, L. Yang, M. Cabral, Z.Z. Song, B.Y. Wang, S. Primig, W. Xu, Z.B. Chen, S.P. Ringer, X.Z. Liao, Introducing transformation twins in titanium alloys: an evolution of α-variants during additive manufacturing, Mater. Res. Lett. 9 (2021) 119–126. https://doi.org/10.1080/21663831.2020.1850536.

[115] Z. Yan, L. Wang, Z. Ning, Y. Li, A. Liu, X. Cheng, Evolution of dislocations and deformation twins in Ti6321 titanium alloy under contact explosion, J. Mater. Res. Technol. 24 (2023) 1070–1075. https://doi.org/10.1016/j.jmrt.2023.03.027.

[116] J.R. Morris, Y.Y. Ye, K.M. Ho, C.T. Chan, M.H. Yoo, Structures and energies of compression twin boundaries in hcp Ti and Zr, Philos. Mag. A Phys. Condens. Matter, Struct. Defects Mech. Prop. 72 (1995) 751–763. https://doi.org/10.1080/01418619508243798.

[117] A.H. Zahiri, J. Ombogo, M. Lotfpour, L. Cao, Twinning in Hexagonal Close-Packed Materials: The Role of Phase Transformation, Metals (Basel). 13 (2023) 525. https://doi.org/10.3390/met13030525.

[118] J. Hui, X. Zhang, T. Liu, W. Liu, B. Wang, First-principles calculation of twin boundary energy and strength/embrittlement in hexagonal close-packed titanium, Mater. Des. 213 (2022) 110331. https://doi.org/10.1016/j.matdes.2021.110331.

8 Appendix

8.1 Experimental procedures carried out in MTC

8.1.1 Ablative layer comparisons

Many different experimental setups were considered before settling upon the schematic seen in the main body [*3.1.3 Laser Shock Processing*]. Firstly, confinement materials other than water such as silica glass, thermoplastic polyurethane and quartz were considered. This would have allowed for consistent thicknesses of the confining layer whilst also potentially removing the need for a water system. It was found, however, that the difficulty in firmly fixing the three layers (confining, ablative and substrate) while still allowing for ease of shifting the confinement and ablative layers between shocks, was greater than the challenges involved with creating a water circulation system. It was also judged that as a fluid, the water would be more effective at confining the plasma expansion during the LSP process.

It was also discovered that all solid confining materials suffered from damage when the concentrated laser passed through it, most likely as a form of dielectric breakdown (even on coated protective window glass invisible to 1064 nm photons, the operating wavelength of the laser used). This made it difficult to laser shock using the same confinement area, as the damage caused scattering of the laser beam, reducing the energy incident upon the shock site on the substrate. This was separate from the significant damage caused to the confinement layers as a result of the generation of a successful pressure pulse. Although this is rarely explicitly mentioned in the literature, it is obvious that the pressure pulses generated from LSP will destroy solid confinement layers.

Various ablative layers were tested for their absorption capability using qualitative methods (see AFigure 1), before it was decided that black PVC electrical tape was most suitable. It was seen that polypropylene tapes were too thin for adequate protection of the substrate. Electrical tape was shown to maintain overall integrity after LSP, with maximal absorption in black tape when compared to the brown and grey tapes as seen by the size of the laser footprint . This was further analysed to decide that glue on the tape may be removed on the location to be peened minimising the distance from the ablative layer (tape) to the substrate surface, increasing the chances of successful shockwave propagation and corresponding magnitude.

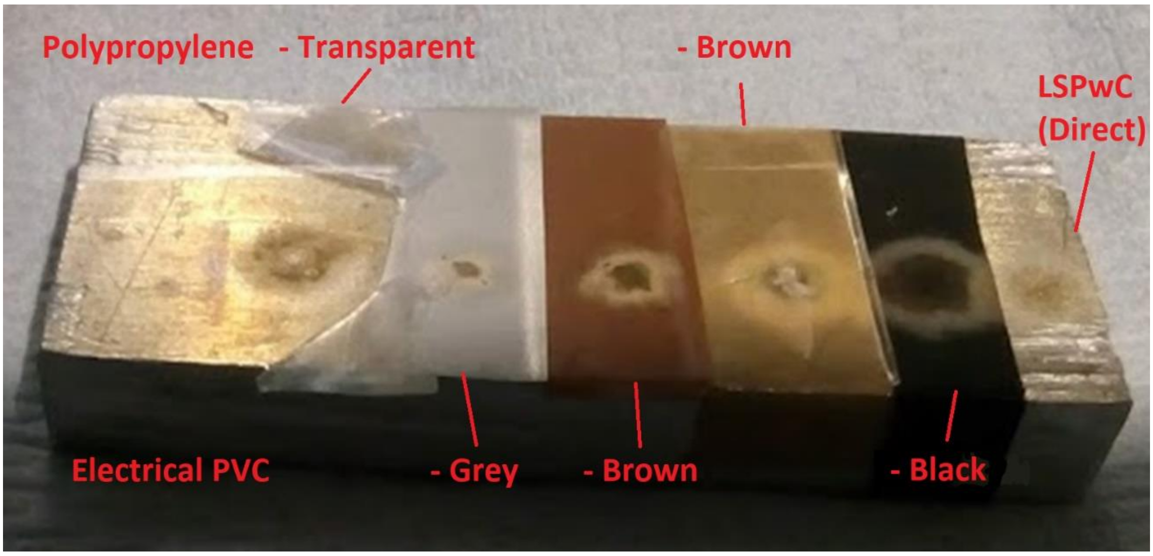

AFigure 1: Examples of ablative layers tested, shown after LSP. Substrate is Aluminium scrap metal.

8.1.2 Focal distance comparisons

A number of pulses were fired onto burn paper at varying distances to assess the size and area of the burn marks in an attempt to understand the laser profile away from the lens compared with the beam as it exits from the laser. A schematic can be seen in AFigure 2. The beam exits the laser at an inch in diameter. This is maintained until it reaches the converging lens, which causes a convergence at roughly 200 mm. The beam size at this point is 10.2 mm. The laser footprint on burn paper can be seen in AFigure 3. It was seen from this that the finest focus of less than 1.2 mm was between 200 mm and 210 mm which, from other experimentation was optimised to 203 – 204 mm, although this level of precision is challenging to implement due to practical restrictions when loading and setting up the sample. This is also difficult to confirm due to the variation on the burn paper. For this reason, the spot size is assumed to be 1.5 mm for all calculations.

The shape of the beam before the lens is constant and maintained by Litron engineers. The beam from the lens to the focal point reduces in diameter, but this magnifies some small aberrations. It can be seen in AFigure 3 that artifacts to the top left and the bottom right become more pronounced as the beam size is reduced. This is indicative that the beam has split and that some energy transfer will either be lost or will not impact the sample with a uniform distribution.

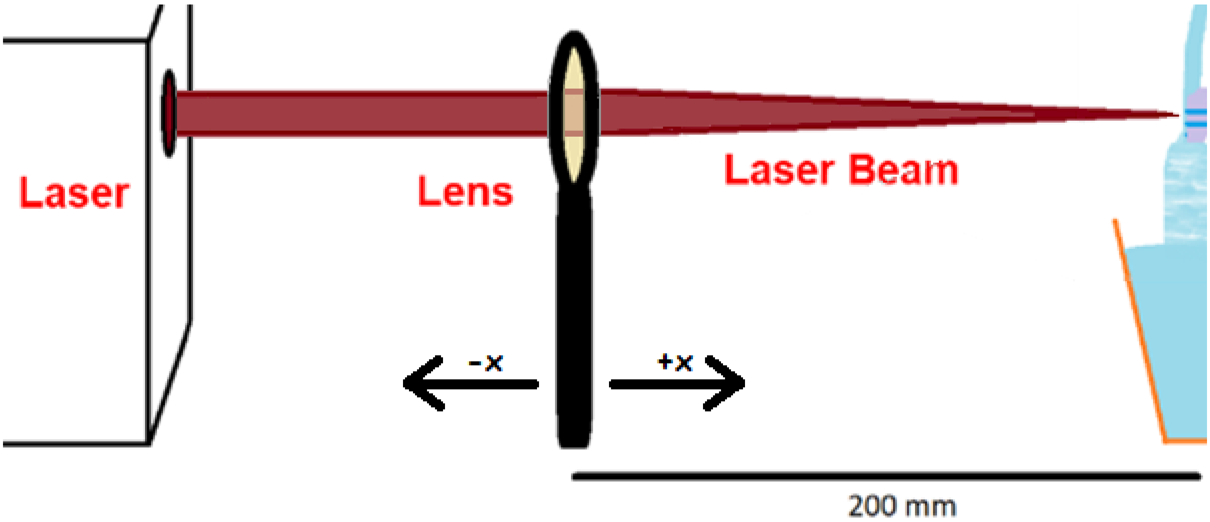

AFigure 2: Schematic of the laser beam as it exits the laser housing, with the focal distance after the lens approximating 200 mm.

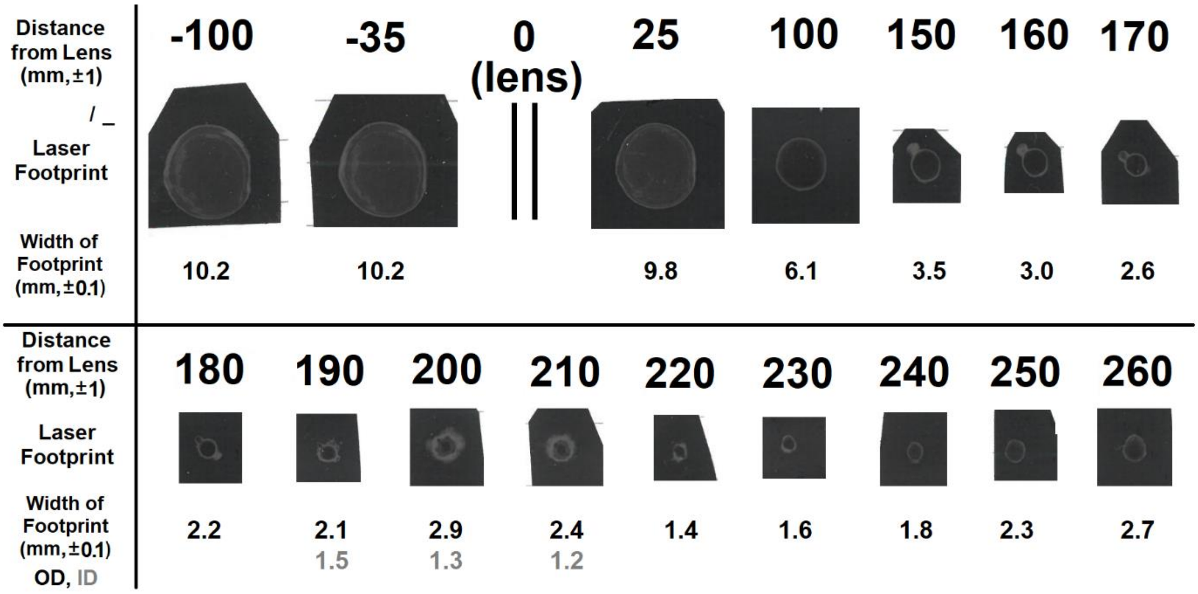

AFigure 3: Laser footprint at different distances from the lens. Negative numbers indicate closer to the laser source, and positive numbers indicate distance towards the target. When closer to the point of maximal focus, the footprint changes to give a smaller, dark circle in the centre. This has been characterised as the Inner diameter (ID), distinguishable from the existing outer diameter (OD) measurements. The grey region bordering the spot is typically not included.

8.2 Twin Analysis from TKD

Diffraction data from TKD based twin analysis from pole figures and directional correlation can be found below. Possible twin directions are taken from the perpendicular to the twinning plane as seen in the TKD mapping. This perpendicular line is in red. The most probable twins are circled in red. For those at the surface, AFigure 4 depicts 3-shock, AFigure 5 5-shock, AFigure 6 10-shock, and AFigure 7 15-shock. At a 250 µm depth, the 3-shock sample did not contain twins. For the rest, 5-shock is analysed in AFigure 8, 10-shock in AFigure 10, and 15-shock in AFigure 9. Where there are multiple options, the closest is picked. As in the case of the 5-shock sample at 0 µm (AFigure 5), it is quite likely that the $\{11\bar{2}1\}$ type twins near the surface are, in fact, $\{10\bar{1}1\}$ type twins (as seen in Figure 104) as this is a real possibility, whilst matching the other near-surface results.

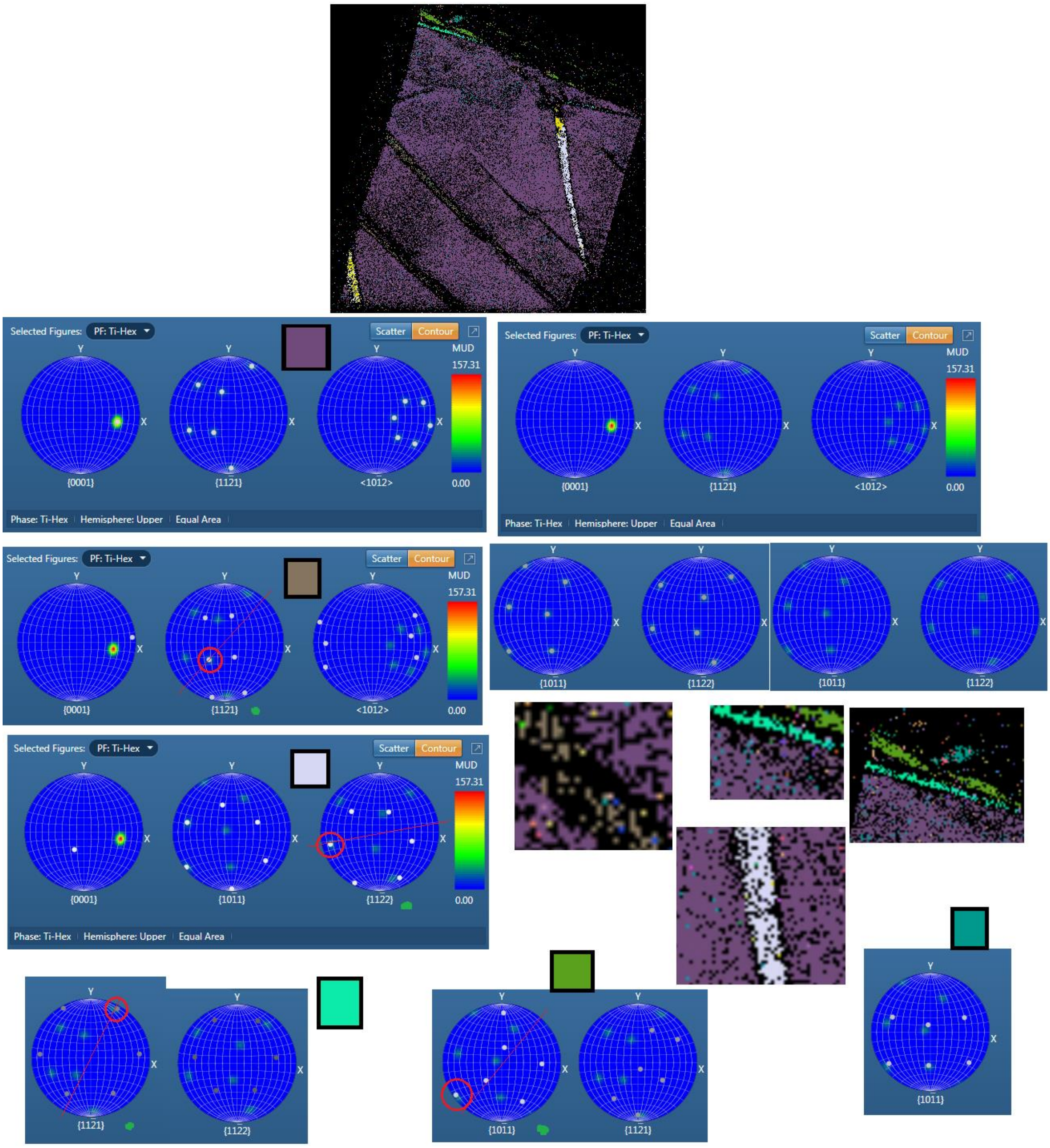

AFigure 4: Euler coloured TKD results of 3-shock TEM sample taken at 0 µm. This shows the analysis which identified the twin types seen in *Figure 103*.

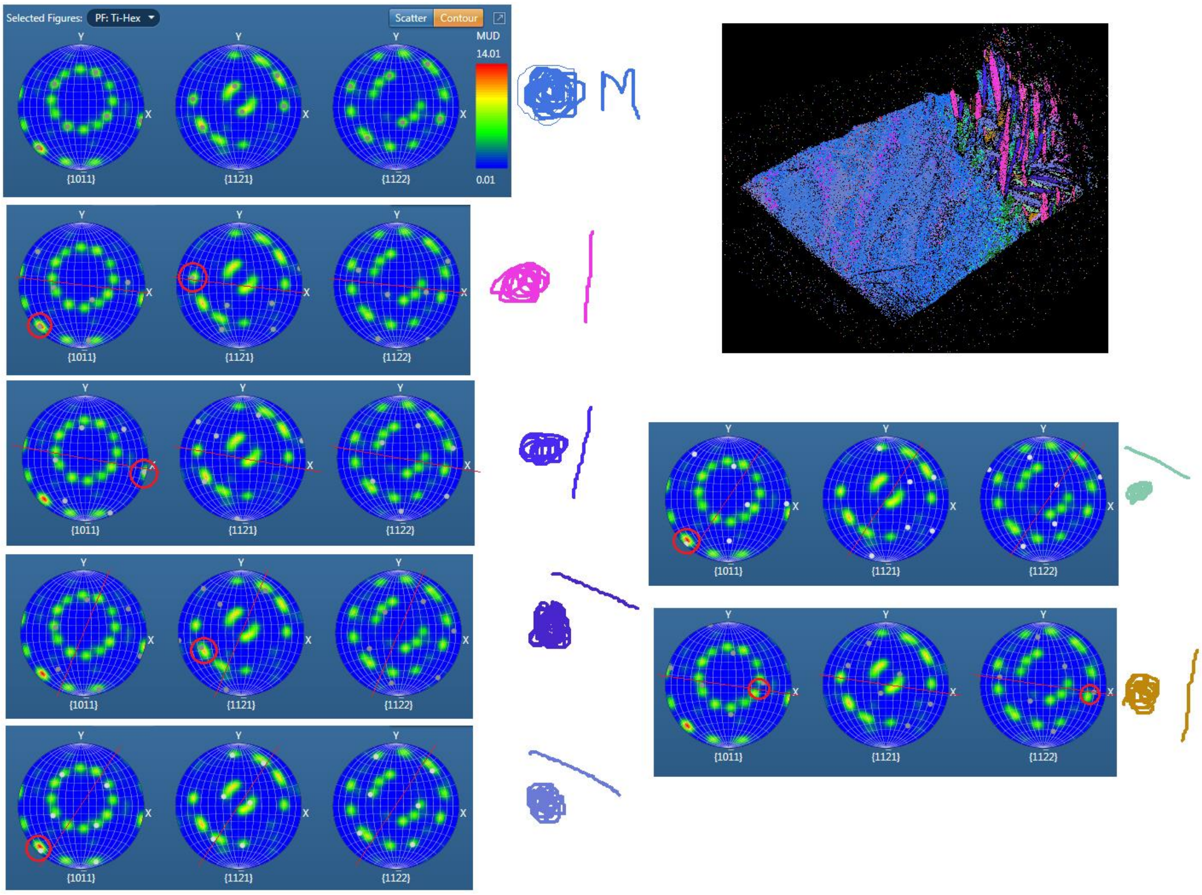

AFigure 5: Euler coloured TKD results of 5-shock TEM sample taken at 0 µm. This shows the analysis which identified the twin types seen in *Figure 104*.

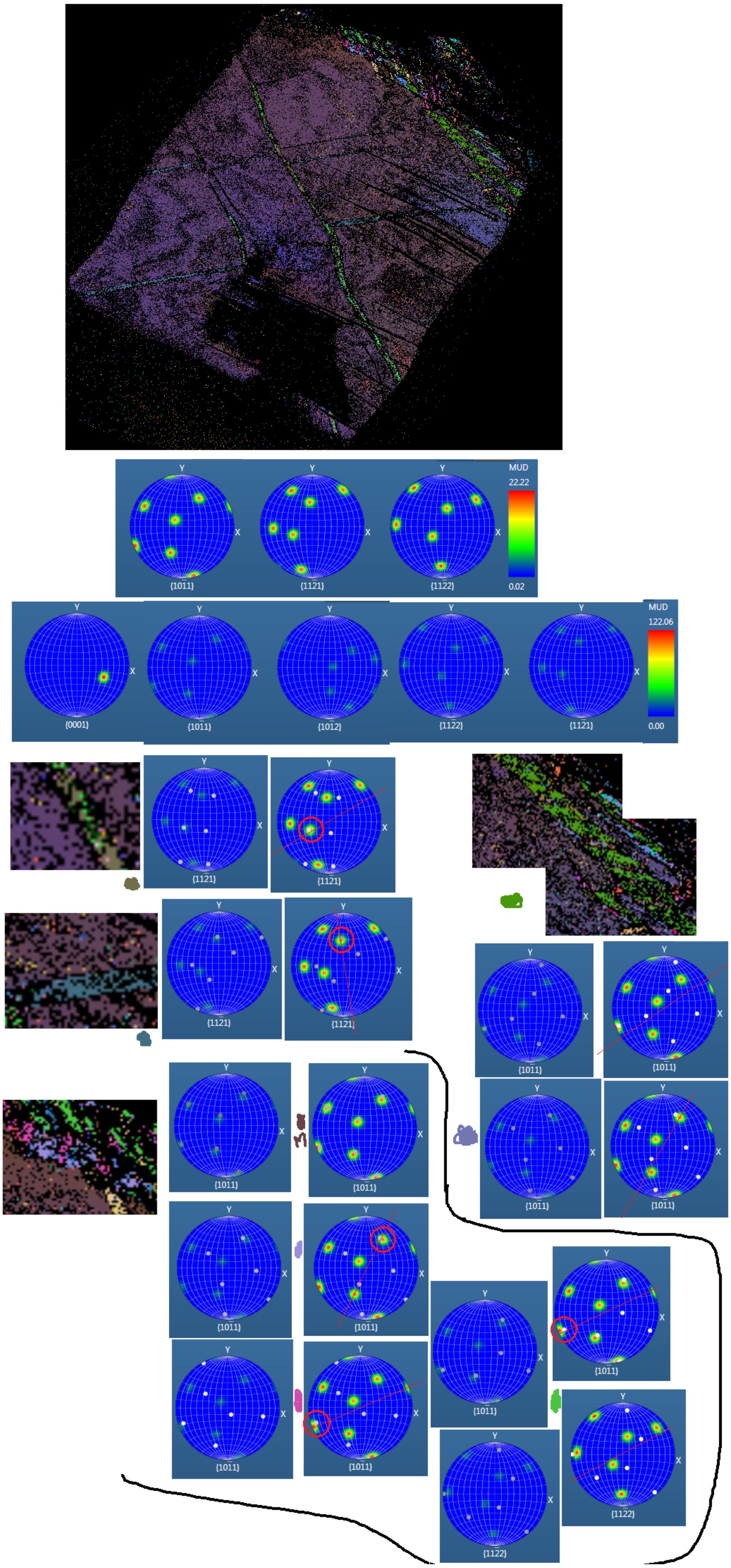

AFigure 6: Euler coloured TKD results of 10-shock TEM sample taken at 0 μm. This shows the analysis which identified the twin types seen in *Figure 105*.

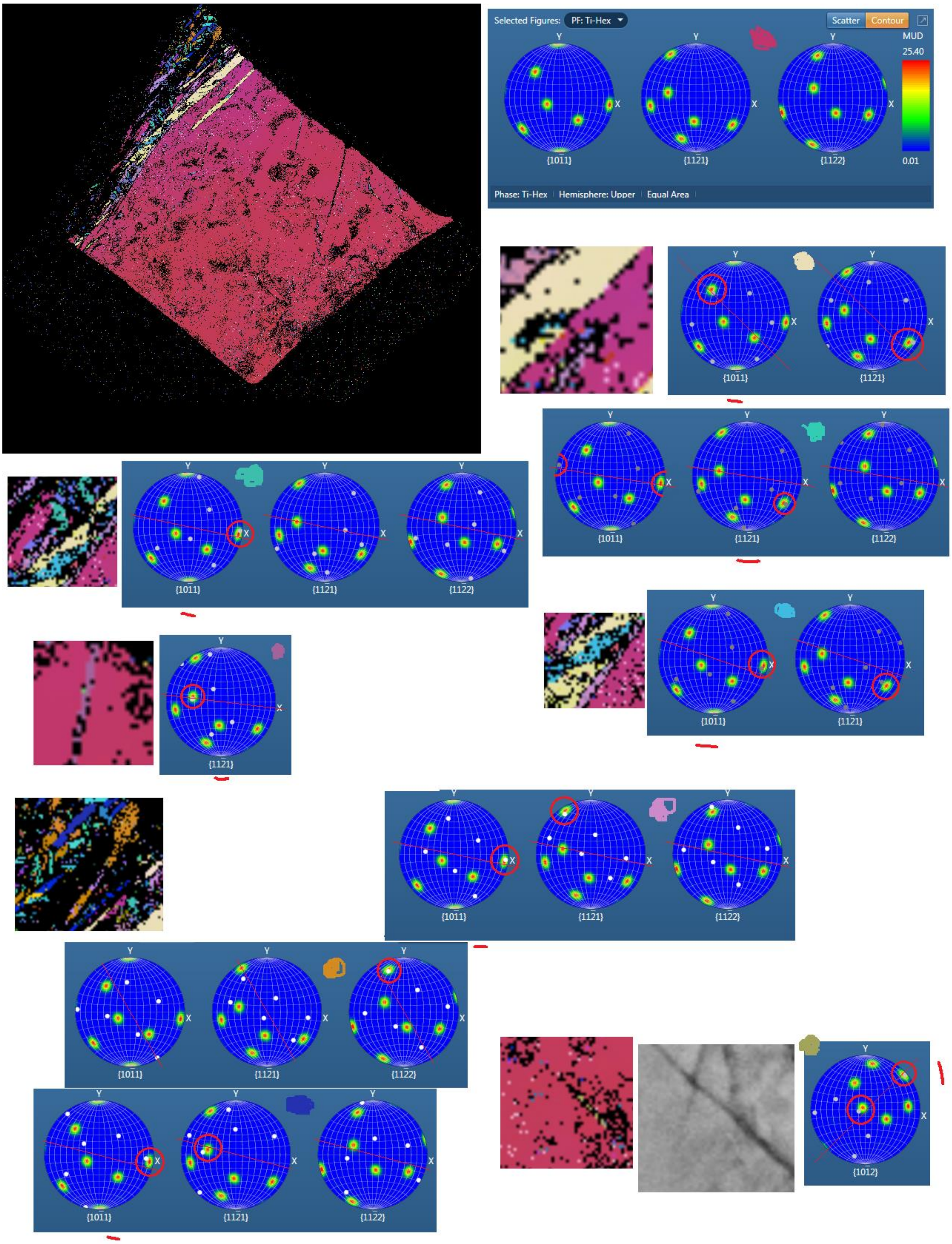
Selected Figures: PF: Ti-Hex

Phase: Ti-Hex | Hemisphere: Upper | Equal Area

AFigure 7: Euler coloured TKD results of 15-shock TEM sample taken at 0 µm. This shows the analysis which identified the twin types seen in *Figure 106*.

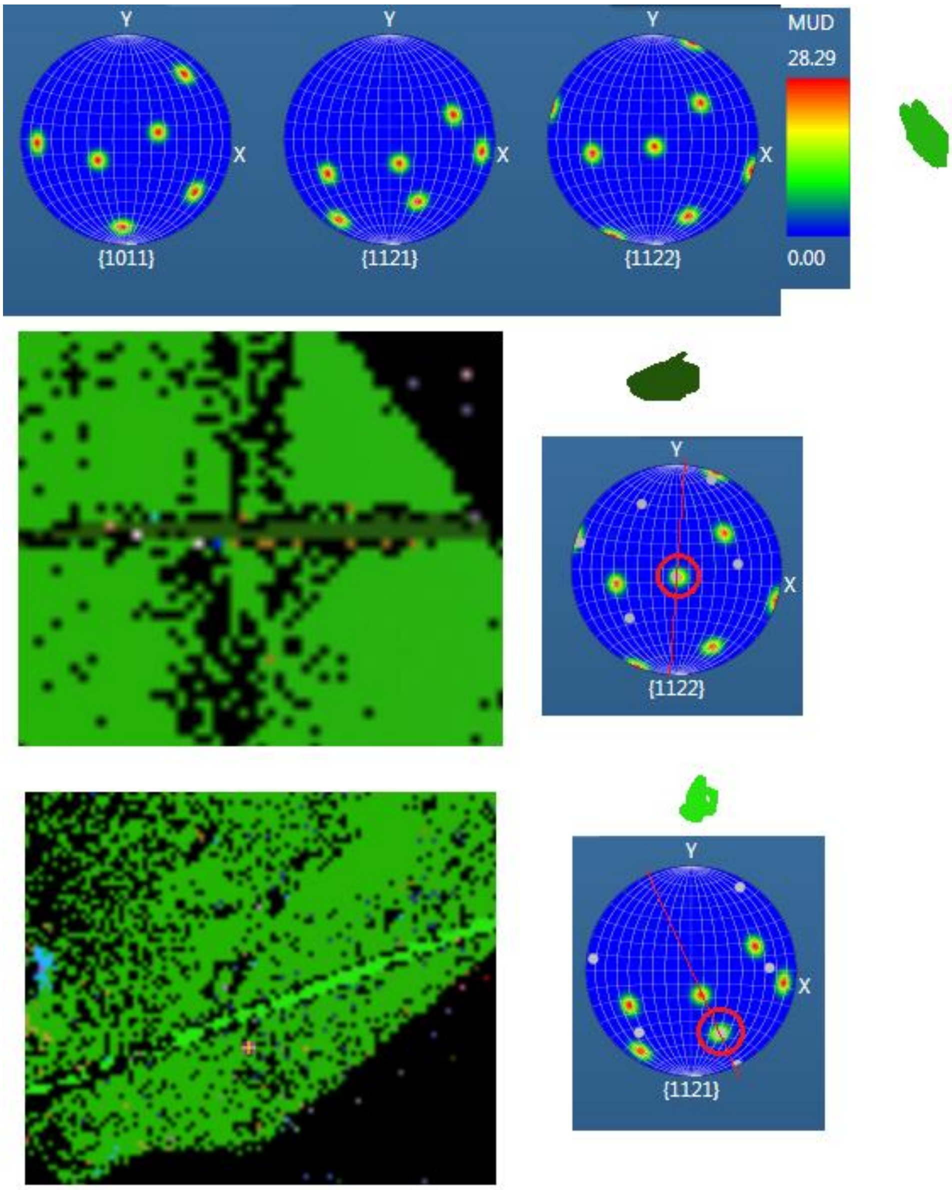

AFigure 8: Euler coloured TKD results of 5-shock TEM sample taken at 250 µm. This shows the analysis which identified the twin types seen in *Figure 108*.

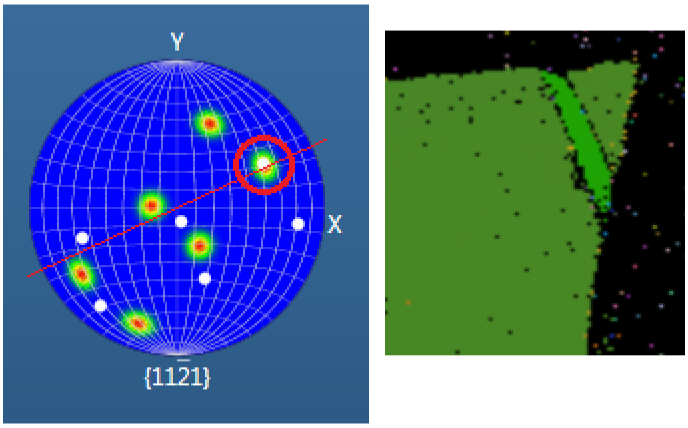

AFigure 9: Euler coloured TKD results of 10-shock TEM sample taken at 250 µm. This shows the analysis which identified the twin types seen in *Figure 109*.

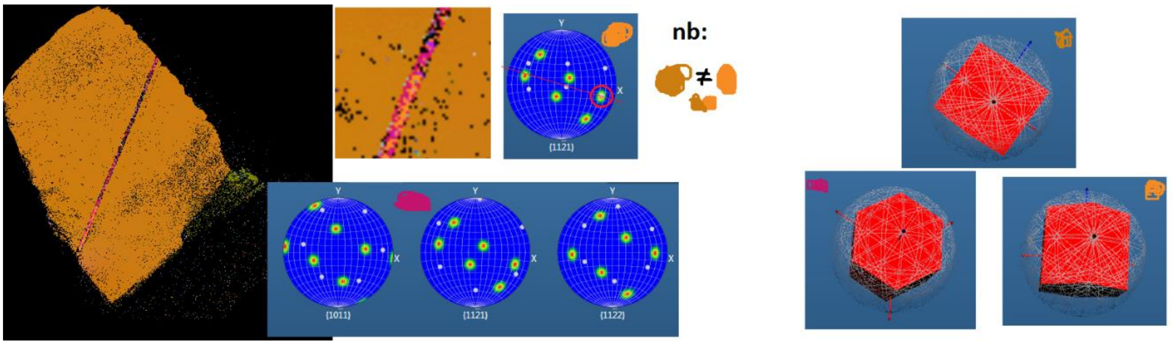

AFigure 10: Euler coloured TKD results of 15-shock TEM sample taken at 250 µm. This shows the analysis which identified the twin types seen in *Figure 110*.